Western Australia School of Mines: Minerals, Energy and Chemical Engineering
Fuels and Energy Technology Institute

Synthesis, Characteristics and Application of Single Atom Catalysts

Shiyong Zhao

This thesis is presented for the Degree of
Doctor of Philosophy
of
Curtin University

March 2020

Declaration

To the best of my knowledge and belief this thesis contains no material previously published by any other person except where due acknowledgement has been made.

This thesis contains no material which has been accepted for the award of any other degree or diploma in any university.

Signature:……

Date:…… 17/03/2020 ……...

Abstract

During the catalysis process, the size effect of metal catalyst will dramatically influence the catalytic performance. It has been becoming increasingly important to decrease the size of catalysts in order to maximize their utilization efficiency. The minimum of the catalyst size can be achieved is single atoms in the chemistry reaction. It is an ideal approach to maximize the efficiency through reducing the size of the metal nanocluster to single atoms, which can boost the electrocatalytic performance. Single-atom catalysts (SACs), consist of atomically dispersed metal atoms on different supports with high surface area, have been confirmed to exhibit high efficiency and good selectivity in energy-related chemical catalysis, surpassing those of metal nanoparticles-based catalysts. The maximized utilization and special coordination environments of metal atoms in SACs contribute to the excellent catalytic efficiency. Nevertheless, the great challenge in the practical application and commercialization of SACs is the development of facile synthesis methods of SACs with high mass loading of single atom and prevention of aggregation of the single atoms on the supports. Thus, the objective of the PhD project is on the synthesis, characterization and application of SACs.

Herein, a feasible one-pot pyrolysis approach has been developed to achieve high metallic single atoms embedded in nitrogen-doped carbon nanotube (MSA-N-CNT, M=Ni, Co，Fe, Pt). The X-ray absorption spectroscopy (XAS) and aberration-corrected scanning transmission electron microscopy (AC-STEM) were conducted to investigate the structure of single atoms in MSA-N-CNT. Among them, NiSA-N-CNT achieved single atom loading of 20.3 wt%, one of the highest SAC loadings reported in the literature. In addition, NiSA-N-CNT shows an excellent activity and selectivity for CO_2 reduction reaction (CO2RR) for the production of CO. A synthesis mechanism based on the solid-to-solid rolling process has been proposed for the one-pot synthesis of the structurally stable MSA-N-CNT catalysts with high SAC loading.

In order to increase the utilization efficiency of SACs, the one-pot synthesis method has been expanded to the SAC supported on 2D materials. In this case, nitrogen-doped microwave exfoliated graphene oxide (MEGO) was used as support to synthesize the Ni single atoms with SAC loading of ~6.9 wt% (Ni-N-MEGO). The atomically dispersed Ni atoms, coordinated with nitrogen, were demonstrated predominantly anchored along the edges of nanopores (<6 nm), as

showing by XAS and AC-STEM techniques. The Ni-N-MEGO indicates an onset overpotential of 0.18 V with a current density of 53.6 mA mg^{-1} under overpotential of 0.59 V for CO2RR. Density functional theory (DFT) simulations indicate that the electrochemical CO2RR occurs preferentially around the edge-anchored unsaturated nitrogen coordinated Ni single atoms, leading to improved activity toward CO2RR.

For practical application of SACs, the development of controllable, scalable and efficient synthesis method is most critical. To meet this challenge, a versatile seeding technique has been developed to synthesize SACs on various two-dimensional (2D) support materials such as graphene, boron nitride (BN) and molybdenum disulfide (MoS_2). This method has been demonstrated on the synthesis of Ni, Co, Fe, Cu, Ag, Pd single atoms as well as binary atoms of NiCu on 2D support materials with the single atomic loading in the range of 2.8-7.9 wt%. In particular, nickel SACs on graphene oxide (SANi-GO) exhibits excellent catalytic performance for CO2RR with a low overpotential of 0.63V and high selectivity of 96.5% for CO production.

In addition to CO2RR, the as-synthesized SACs were also applied to improve lithium−sulfur (Li−S) batteries performance. Li-S batteries have attracted much attention due to their high theoretical energy density, environmental friendliness, low cost and the promises as the next-generation energy storage technologies. However, the poor reversible conversion of Li polysulfides (LiPSs) to Li_2S in discharge hinders practical application. Herein, SACs synthesized based on the seeding approach have been applied to improve the performance of Li-S batteries. Theoretical calculation was employed to consider the forward and reverse catalytic reaction in the design of the efficient catalyst. The results show the significantly improved Li-S battery performance, demonstrating the effectiveness of the theoretical approach in the development of high-performance Li–S batteries.

Finally, the controlled synthesis of SACs was conducted on Ni single atoms on nitrogen doped carbon nanotube (NiSA-N-CNT) and graphene (NiSA-N-G). The formation of NiSA-N-CNT is due to the solid-to-solid rolling up mechanism during the high temperature pyrolysis from the stacked and layered g-C_3N_4-Ni structure to a bamboo-shaped tubular NiSA-N-CNT structure. Addition of citric acid interrupts the solid-to-solid rolling process, and result in NiSA-N-G. The electrochemical performance of NiSA-N-CNT and NiSA-N-G for CO2RR reveals that more exposed active sites owned in graphene structure achieves higher catalytic performance. The results demonstrate the feasibility in the control of the synthesis of single atom metal catalyst. This

PhD project produced 11 publications with 6 of them as first authored papers.

Acknowledgements

Over my past three years' PhD study at Curtin University, it is one of the most fantastic and memorable periods in my whole life. I would like to give my sincere thanks to my supervisor, Prof. San Ping Jiang, who supported me throughout the whole PhD project with great patience and expertise. Under his splendid guidance I carried out the progress in scientific research. He always can grab the highlight of the research and provide me great amount of help and opportunities for the developing of my academic career. Then I want to thank my co-supervisor Prof. Shaomin Liu for the meaningful discussion of my research work. Besides, I want to thank to the director of our institute, Prof. Chun-zhu Li for supplying us excellent research facilities.

I also want to thank to Ms. Angelina Rossiter and Mrs. Tasneem Dawood, Mrs. Lana McQueen for supporting me in safety and administrative issues. I would like to give my thanks to our current and previous group members for their great help (in no particular order): Dr.Yi Cheng, Dr. Shuai He, Dr. Jian Pan, Dr. Kongfa Chen, Dr. Na Ai, Dr. Yu Liu, Dr. Xiaoguang Duan, Mr. Haohua Kuang, Ms.Qi Zhang, Mr.Jingwei Li, and Ms.Xiao Zhang, Mr. Hongqi Wang, Ms. Yurong Liu, Ms. Weichen, Mr. Dechao Chen, Mr. Xiaomin Xu, Mr. Yijun Zhong, Mr.Xiaojie Li, Ms. Xiu Liu.

I also want to thank to the facilities, scientific and technical assistance of Ms. Elaine Miller, Ms. Veronica Avery, Dr Matthew of the Curtin University Scanning Probe Microscopy, Curtin X-Ray Laboratory, Department of Chemistry/Nanochemistry Research Institute, Curtin University, all of which are funded and supported by the University, State and Commonwealth Governments.

Thanks a lot to Prof. Roland De Marco from Sunshine Coast University for the synchron facility application, Dr. Bernt Johannessen from Australian Synchrotron for the XAS test, Dr. Jean-Pierre Veder from Curtin University for the great XPS and XAS tests, Prof.Huiming Cheng and Prof.Chang Liu, Prof. Pengxiang Hou, Prof.Lichang Yin, Dr.Min Cheng, Dr. Yongxin Cheng, Dr.Jincheng Li from Institute of Metal Research, Chinese Academy of Sciences for the results disscusion, Dr.Shize Yang from Oak ridge National Lab USA for the high resolution STEM and structure modelling, Dr.Ruopian Fang from Institute of Metal Research, Chinese Academy of Sciences for the collaboration on the Li-S batteries test, Dr. Guangmin Zhou, Dr. Guangxu Chen,

Prof. Yicui from Stanford University for the electrochemical tests and resutls discussion, Prof. Tianfan Zhang, Dr. Tianshuai Wang from Beihang University for the simulation work, Dr. Lianji Zhang from Zhengzhou University for the simulation work and many collaboraters who are not mentioned here due to the words limitation.

Besides these, I would like to thank my parents, my parents in law and younger sister for being such great support through my whole experiences. Last but not the least, my wife Mengyao Xue, one of the most important persons in my life deserves my special and sincere appreciation. I couldn't have made it without you all. Love you all.

List of Publications

1. Yi Cheng, **Shiyong Zhao**, Bernt Johannessen, Jean-Pierre Veder, Martin Saunders, Matthew R. Rowles, Min Cheng, Chang Liu, Matthew F. Chisholm, Roland De Marco, Hui-Ming Cheng, Shi-Ze Yang, and San Ping Jiang, Atomically Dispersed Transition Metals on Carbon Nanotubes with UltraHigh Loading for Selective Electrochemical Carbon Dioxide Reduction, **Advanced Materials**, **2018**, 30, 13, 1706287.(Y.Cheng and SY. Zhao contribute equally)
2. **Shiyong Zhao**, Guangxu Chen, Guangmin Zhou, Li-Chang Yin, Jean-Pierre Veder, Bernt Johannessen, Martin Saunders, Shi-Ze Yang, Roland De Marco, Chang Liu, A Universal Seeding Strategy to Synthesis Single Atom Catalysts on 2D Materials for Electrocatalytic Applications, **Advanced Functional Materials**, **2019**, 30, 6, 1906157.
3. Guangmin Zhou, **Shiyong Zhao**, Tianshuai Wang, Shi-Ze Yang, Bernt Johannessen, Hao Chen, Chenwei Liu, Yusheng Ye, Yecun Wu, Yucan Peng, Chang Liu, San Ping Jiang, Qianfan Zhang, Yi Cui ,Theoretical calculation guided design of single-atom catalysts towards fast kinetic and long-life Li-S batteries., **Nano Letters**, **2020**, 2019-04719g.(GM. Zhou, SY. Zhao and TS. Wang contribute equally)
4. Ruopian Fang, **Shiyong Zhao**, Zhenhua Sun, Da-Wei Wang, Rose Amal, Shaogang Wang, Hui-Ming , Cheng and Feng Li, Polysulfide immobilization and conversion on a conductive polar MoC@MoOx material for lithium-sulfur batteries, **Energy Storage Materials**, **2018**, 10, 56-

61. (RP. Fang and SY. Zhao contribute equally)

5. **Shiyong Zhao,** Ruopian Fang, Zhenhua Sun, Shaogang Wang, Jean-Pierre , Veder, Martin Saunders, Hui-Ming Cheng, Chang Liu, San Ping Jiang, Feng Li, A 3D Multifunctional Architecture for Lithium–Sulfur Batteries with High Areal Capacity, **Small Methods**, **2018**, 2, 6, 1800067.

6. Cheng, Yi, Veder Jean-Pierre, Thomsen, Lars, **Zhao Shiyong**, Saunders Martin, Demichelis, Raffaella, Liu Chang, De Marco, Roland, Jiang San Ping," Electrochemically substituted metal phthalocyanines, e-MPc (M = Co, Ni), as highly active and selective catalysts for CO2 reduction" **Journal of Materials Chemistry A**, **2018**, 6, 4, 1370-1375.

7. **Shiyong Zhao**, Yi, Cheng, Jean-Pierre Veder, Bernt Johannessen, Martin Saunders, Lianji Zhang, Chang Liu, Matthew F. Chisholm, Roland De Marco, Jian Liu, Shi-Ze Yang, San Ping Jiang, "One-Pot Pyrolysis Method to Fabricate Carbon Nanotube Supported Ni Single-Atom Catalysts with Ultrahigh Loading" **ACS Applied Energy Materials**. **2018**, 1, 10, 5286-5297.

8. Yi Cheng, **Shiyong Zhao**, Haobo Li, Shuai He, Jean-Pierre Veder, Bernt Johannessen[e], Jianping Xiao, Shanfu Lu, Jian Pan, Mattew F. Chisholm, Shi-Ze Yang, Chang Liu, Jingguang G. Chen, San Ping Jiang. "Unsaturated Edge-anchored Ni Single Atoms on Porous Microwave Exfoliated Graphene Oxide for Electrochemical CO_2 Reduction" **Applied Catalysis B Environmental. 2018,** 243, 294-303. (Y.Cheng and SY. Zhao contribute equally)

9. Ruopian Fang, Guoxian Li, **Shiyong Zhao**, Lichang Yin, Kui Du, Pengxiang Hou, Shaogang Wang, Hui-ming Cheng, Chang Liu, Feng Li. "Single-wall carbon nanotube network enabled ultrahigh sulfur-content electrodes for high-performance lithium-sulfur batteries". **Nano Energy**, **2017**, 42, 205-214. (RP. Fang, GX. Li and SY. Zhao contribute equally)

10. Ruopian Fang, **Shiyong Zhao**, Da-Wei Wang, Zhenhua Sun, Hui-Ming Cheng, Feng Li, Micro-Macroscopic Coupled Electrode Architecture for High-Energy-Density Lithium–Sulfur Batteries, ACS Applied Energy Materials, 2019, 2, 10, 7393-7402. (RP. Fang and SY. Zhao contribute equally)

11. **Shiyong Zhao**, Tianshuai Wang, Guanmin, Zhou, Liji Zhang, Chao Lin, Jean-Pierre Veder, Bernt Johannessen, Martin Saunders, Lichang Yin, Chang Liu, Roland De Marco, Shi-Ze Yang,

Qianfan Zhang, San Ping Jiang, Controlled One-pot Synthesis of Nickel Single Atoms Embedded in Carbon Nanotube and Graphene Supports with High Loading, **ChemNanoMat**, 2020, doi:10.1002/cnma.202000223.

Contents

Chapter 1: Introduction

1.1 Background

The size effect of the metal nanoparticles significantly influences the catalytic performance and it has been becoming increasingly important to reduce the size of catalysis in order to maximize the atom utilization efficiency [1-5]. Single-atom catalysts (SACs) [6-8], comprised of atomically dispersed single atoms supported on different substrates, have exhibited high efficiency and distinctive selectivity in energy catalysis, far exceeding conventional metal nanoparticles catalysts. The single site catalysis is not a new concept which can be date back to 1925 [9-11], when Taylor proposed the surface of a heterogeneous catalyst has certain catalytically active centers. The understanding of single site catalysis has been endowed especially the advanced development of atomic level investigation technique. The massive efforts have been devoted to the synthesis of SACs, which can be mainly divided into two approaches: the physical and chemical methods. The former methods have been proved to be feasible for synthesizing metal clusters and atoms such as the laser evaporation, electron beam evaporation, atomic layer deposition, thermal transport. However, the physical approaches cannot overcome the demerits such as low yield, limited yield, high technical requirements. The recent vast developments of chemical approaches promote the SACs research. The impregnation method has been applied to achieve SACs due to the feasible technique, low cost on the supports including g-C_3N_4, metal oxides, carbon materials and so on. Nevertheless, the method relies on the limited absorption sites, which restrains the SACs loading less than 2wt.% [9, 12-15]. The nitrogen atom coordination approaches have been developed well to synthesize the SACs, utilizing the strong nitrogen coordination in the substrate, which can achieve up high loading of 20 wt%. This approach also owns its drawbacks such as uncontrollable loading and limited metal atom variety. SACs have been studied as electrocatalysts for photocatalytic H_2 evolution, oxygen reduction reaction and CO_2 reduction owing to their high selectivity and superior activity.

Prior to the practical application and commercialization of SACs, there is a great challenge that how to achieve a feasible method for the controllable synthesis of SACs with appropriate mass loading of single atom. How to effectively prevent the single atom aggregation is the key problem. In this regard, the aim of this project is to develop the synthesis, characterization and application

of SACs. The overall objective is to achieve high loading and efficient catalyst for the catalysis application including carbon dioxide reduction reaction and lithium sulfur batteries.

1.2 Objectives and outline of the thesis

Based on the above-mentioned objectives, this thesis has 9 chapters. The first chapter gives an introduction of the background and the outline of this thesis. Chapter 2 focuses on the literature review of the state-of-the-art study in the field. Chapter 3 mainly introduces the materials characterization techniques involved in this thesis. The experiment results and discussion are presented in chapter 4-8. In Chapter 9, conclusions are made and the suggestions for future work are proposed.

Chapter 1: Introduction

The chapter briefly introduces the challenges of the efficient catalysis and SACs. Then the objectives and outlines of the thesis are presented.

Chapter 2: Literature Review

One comprehensive review of the state-of-the-art research progress of SACs is given, followed by the detailed analysis and discussion of the developments in the synthesis, characterization and application of SACs in different areas.

Chapter 3: Experimental

This chapter introduces the details of the experimental methods used in the thesis, including the materials, structural investigation techniques and the electrochemical methods.

Chapter 4: One-pot Pyrolysis Method to Fabricate Carbon Nanotube Supported Ni Single Atom Catalysts with Ultrahigh Loading

This chapter presents a novel approach to nickel SACs stabilized on a nitrogen-doped carbon nanotube structure (NiSA-N-CNT) with ultrahigh Ni atomic loading up to 20.3 wt% through one-pot pyrolysis method employing Ni acetylacetonate ($Ni(acac)_2$) and dicyandiamide (DCD) as precursors. This approach is different from the traditional CNT catalysis growth process. NiSA-

N-CNT structure most likely occurs via a solid-to-solid curling or rolling-up mechanism. The NiSA-N-CNT catalysts show an excellent activity and selectivity for the electrochemical reduction of CO_2.

Chapter 5: Unsaturated Edge-anchored Ni Single Atoms on Porous Microwave Exfoliated Graphene Oxide for Electrochemical CO2 Reduction

In this chapter, the new approach is continued to explore to achieve SACs through tailoring the edge structures of porous carbon. The porous structure with a high surface area (2649 m^2 g^{-1}) provided large number of anchor sites for single Ni atoms and the nanopores (<6 nm) also help prevent aggregation and stabilize the single atom Ni-N species during high temperature annealing.

Chapter 6: A universal seeding strategy to synthesis single atom catalysts on 2D materials

The controllable method to synthesize a series of single metal atom catalysts on two-dimensional materials was achieved. The seeding strategy is versatile and has been demonstrated on Ni, Co, Fe, Cu, Ag, Pd single atoms as well as binary NiCu atoms supported on 2D materials including GO, MoS_2 and BN nanosheets. The applicability of the synthesized SA-2D catalysts has been illustrated on the high activity and selectivity of SANi-GO for CO_2RR.

Chapter 7: Theoretical calculation guided design of single-atom catalysts towards fast kinetic and long-life Li-S batteries

Based on our seeding approach for SACs, the application of for Li-S batteries was achieved under the guidance of theoretical calculation. The dual between forward and reverse catalytic reaction were firstly taken into consideration to design the efficient catalyst, based on the guidance of experiments and DFT calculations. More importantly, the significantly improved battery performance has been obtained benefited from the great catalytic effects, consistent with the DFT theoretical calculations. The ability of single metal atoms to effectively trap the dissolved lithium polysulfides (LiPSs) and catalytically convert the LiPSs/Li_2S during cycling, significantly improved sulfur utilization, rate capability and cycling life.

Chapter 8: Facile methods to synthesize single nickel atoms embedded in carbon nanotube and graphene

In this chapter, two feasible closed associated approaches are reported to synthesize nickel single

and nitrogen atom doped carbon nanotube (NiSA-N-CNT) and graphene oxide (NiSA-N-G) to stabilize single nickel atom separately. The synthesis of NiSA-N-CNT and NiSA-N-G follows different mechanisms. One self-rolling up mechanism has been proposed to explain the formation of NiSA-N-CNT. The synthesis of NiSA-N-G is achieved by the addition of citric acid to interrupt the rolling-up mechanism. The CO_2 reduction reaction performance also have been compared for the two structures, which reveal that more exposed active sites owned in graphene structure achieves higher catalytic performance. The novel synthesis approaches and mechanism provides new understanding of single atom metal catalyst.

Chapter 9: Conclusions and recommendations for future work

The main achievements in my thesis were summarized and the recommendations for future work were also listed in this chapter.

1.3 References

[1] U. Heiz, A. Sanchez, S. Abbet, W.D. Schneider, Catalytic Oxidation of Carbon Monoxide on Monodispersed Platinum Clusters: Each Atom Counts, Journal of the American Chemical Society, 121 (1999) 3214-3217.

[2] E.F. Kukovitsky, S.G. L'Vov, N.A. Sainov, V.A. Shustov, L.A. Chernozatonskii, Correlation between metal catalyst particle size and carbon nanotube growth, Chemical Physics Letters, 355 (2002) 497-503.

[3] Z.D. Hu, Y.F. Hu, Q. Chen, X.F. Duan, L.M. Peng, Synthesis and Characterizations of Amorphous Carbon Nanotubes by Pyrolysis of Ferrocene Confined within AAM Templates, The Journal of Physical Chemistry B, 110 (2006) 8263-8267.

[4] Y.T. Kim, K. Ohshima, K. Higashimine, T. Uruga, M. Takata, H. Suematsu, T. Mitani, Fine size control of platinum on carbon nanotubes: From single atoms to clusters, Angew. Chem., Int. Ed., 118 (2006) 421.

[5] S.F. Hackett, R.M. Brydson, M.H. Gass, I. Harvey, A.D. Newman, K. Wilson, A.F. Lee, High-activity, single-site mesoporous Pd/Al2O3 catalysts for selective aerobic oxidation of allylic

alcohols, Angew. Chem., Int. Ed., 46 (2007) 8593.

[6] B. Qiao, A. Wang, X. Yang, L.F. Allard, Z. Jiang, Y. Cui, J. Liu, J. Li, T. Zhang, Single-atom catalysis of CO oxidation using Pt1/FeOx, Nature chemistry, 3 (2011) 634-641.

[7] J. Gao, Y. Zhou, Z. Li, S. Yan, N. Wang, Z. Zou, High-yield synthesis of millimetre-long, semiconducting carbon nitride nanotubes with intense photoluminescence emission and reproducible photoconductivity, Nanoscale, 4 (2012) 3687-3692.

[8] G. Kyriakou, M.B. Boucher, A.D. Jewell, E.A. Lewis, T.J. Lawton, A.E. Baber, H.L. Tierney, M. Flytzani-Stephanopoulos, E.C. Sykes, Isolated metal atom geometries as a strategy for selective heterogeneous hydrogenations, Science, 335 (2012) 1209.

[9] A. Wang, J. Li, T. Zhang, Heterogeneous single-atom catalysis, Nature Reviews Chemistry, 2 (2018) 65-81.

[10] X. Wang, Z. Chen, X. Zhao, T. Yao, W. Chen, R. You, C. Zhao, G. Wu, J. Wang, W. Huang, J. Yang, X. Hong, S. Wei, Y. Wu, Y. Li, Regulation of Coordination Number over Single Co Sites: Triggering the Efficient Electroreduction of CO2, Angewandte Chemie International Edition, 57 (2018) 1944-1948.

[11] S. Wei, A. Li, J.-C. Liu, Z. Li, W. Chen, Y. Gong, Q. Zhang, W.-C. Cheong, Y. Wang, L. Zheng, H. Xiao, C. Chen, D. Wang, Q. Peng, L. Gu, X. Han, J. Li, Y. Li, Direct observation of noble metal nanoparticles transforming to thermally stable single atoms, Nature Nanotechnology, 13 (2018) 856-861.

[12] S.H. Gage, D.A. Ruddy, S. Pylypenko, R.M. Richards, Deep eutectic solvent approach towards nickel/nickel nitride nanocomposites, Catalysis Today, (2016).

[13] Z. Chengzhou, F. Shaofang, S. Qiurong, D. Dan, L. Yuehe, Single-Atom Electrocatalysts, Angewandte Chemie International Edition, 56 (2017) 13944-13960.

[14] P.N. Duchesne, Z.Y. Li, C.P. Deming, V. Fung, X. Zhao, J. Yuan, T. Regier, A. Aldalbahi, Z. Almarhoon, S. Chen, D.-e. Jiang, N. Zheng, P. Zhang, Golden single-atomic-site platinum electrocatalysts, Nature Materials, (2018).

[15] R. Lang, W. Xi, J.-C. Liu, Y.-T. Cui, T. Li, A.F. Lee, F. Chen, Y. Chen, L. Li, L. Li, J. Lin,

S. Miao, X. Liu, A.-Q. Wang, X. Wang, J. Luo, B. Qiao, J. Li, T. Zhang, Non defect-stabilized thermally stable single-atom catalyst, Nature Communications, 10 (2019) 234.

Chapter 2: Literature Review

2.1 Introduction

Around 80% of industrial reactions make use of catalysts to improve the rate for the desired reaction and product [1][2] . The use of the catalysts will help to promote the main reaction and inhibit the side reactions, therefore, the superior selectivity is also necessary for the whole consideration[3-7]. Supported metal nanoparticles (NPs) are among the most significant catalysts that promote many heterogeneous catalysis reactions. In heterogeneous catalysis by NPs, enormous efforts have been conducted for advanced catalytic process, which closely related to contributions for triggering the related chemical reactions through the whole production chain with more main product, fewer unexpected byproduct and lower energy inputs [8-11].

The catalysis performance was adjusted through changing the catalyst size and was conducted like the following aspects: (1) surface confinement effects and the dramatic increase of unsaturated coordination bonds of a metal NP increases, which will enhance the strong bond between the metal and support surface[12-16]; (2) quantum size effects, where confinement of electrons results in the changing energy levels and the widening of the HOMO−LUMO gap [17-20]; (3) catalyst structural configurations, where the specific arrangement of metal atom positions and the amount of atoms in a cluster can vastly change their physicochemical activities[21-26]. Therefore, small metal NPs indicates a distinct and complicated size effects during the reaction process.

Since the size of the metal nanoparticles has a significant effect on the catalytic performance, it is expected that tuning the structure at an atomic level and minimizing the size of the metal nanocluster to single atoms could provide an appropriate approach to maximize the efficiency of atom utilization and enhance the electrocatalytic performance [4, 27-29]. Thus, the key to reduce cost is how to maximize the acquisition of surface atoms of noble metals. Currently, it has been becoming increasingly urgent to reduce the size of catalysts for maximizing the atom utilization. The minimum of the catalyst size is atomic level and cannot downsize anymore in the chemistry reaction [30-34]. SACs not only increase the atom efficiency but also supply an alternative method to adjust the activity and selectivity of a catalysis process [35-39]. Therefore, in this chapter, the recent development of synthesis and the applications focused on the SACs will be elaborated and

finally the most key issues, challenges for controllable synthesis and related specific applications will be discussed and summarized.

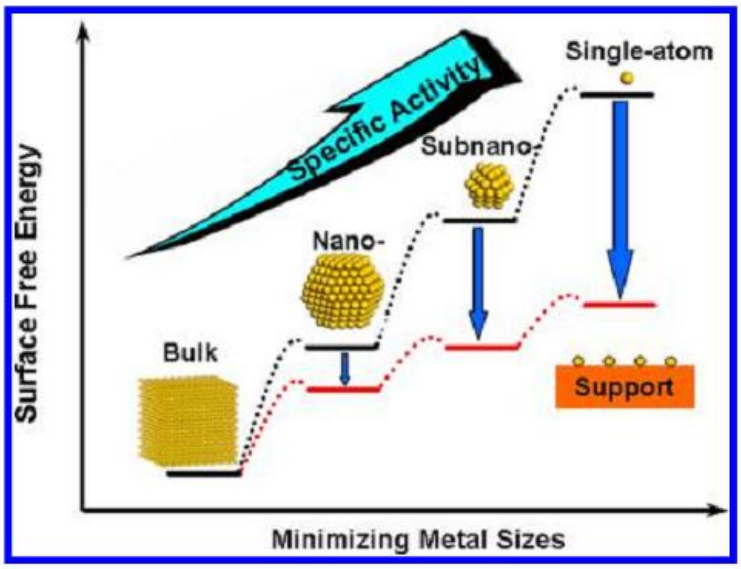

Figure 2.1 the relationship between the changes of surface free energy and specific activity. Reproduced with permission[40].Copyright Nature Publishing group.

Whilst the bulk materials are shrunk into nanoparticles, sub-nano clusters, and even single metal atoms, the surface free energy and specific activity will dramatically change as shown in Figure 2.1[40]. Through the size reduction, the amount of unsaturated coordination chemical environment will increase in the metal species. Therefore, the surface free energy of the metal also significantly increases, which will make metal sites to be more active during the chemical reaction process. The enhanced chemical interactions between the metal and the support relates to the size of metal nano catalysts. When the metal catalysts are reduced to extreme SACs, the quantum effects of electrons, the surface free energy will achieve the maximum due to the highly active valence electrons, which then results in the enhanced chemical activities of SACs for the catalysis process.

2.2. The approaches for the synthesis of SACs

Since SACs consist of only isolated single metal atoms dispersed onto the surfaces of a support material, the dispersion of a metal SAC, by definition, is almost 100%[41]. The key point to

achieve SACs is to hinder the aggregation of metal atoms into the cluster or nanoparticles. The general approaches can be divided into physical and chemical methods [42-46].

2.2.1 Definitions and Classifications

There is a long history for people to realize the development of SACs. The solution with solvable salts could be treated as the first SACs but in liquid states. The initial concept of single catalysis site can be traced back to the pioneering studies in 1960s[4], when scientists discussed the function of surface metals in the hydrocarbon reaction from molecular metal–olefin complexes[47]. The deep understanding of single site catalysis has been endowed especially from the advanced development of atomic chemical environmental technique[48-54], atomic-resolution characterization techniques[55-59] and theoretical modelling[60-62]. In 2000, Abbet et al. [63] reported the cyclotrimerization of acetylene on size-selected (Pd)n clusters ($1 \leq n \leq 30$) supported on MgO (100) film substrate and found that a single palladium atom was enough to produce benzene at 300 K, whereas for larger clusters ($7 \leq n \leq 30$) benzene was produced at the higher temperature of 430 K.

In 2005, Thomas et al.[32] briefly reported the efforts to the synthesis of SACs, which can be roughly divided into two approaches: the physical and chemical strategies. The former method has been proved to be feasible for synthesizing metal clusters and atoms including the laser evaporation, electron beam evaporation, atomic layer deposition, thermal transport, etc. The chemical methods are mainly related to the enzyme mimics, organometallic complexes and metal oxide surface absorption.

More and more advanced technology especially in recent years have given people a clear concept of single atom catalysis process. For better controllable synthesis of SACs, many efforts have been devoted to the dispersion of metal on different supports to achieve the single metal atoms.

2.2.2 The metal and metallic compound anchoring method

The metal surface is one of the candidates to disperse the single atom served as the support subtract due to the advantages of stability and rigidity. Kyriakou et al. [64] achieved isolated Pd atoms on the copper surface with low energy barrier for the hydrogen uptake on and desorption from the Cu foil. This facile hydrogen dissociation at Pd atom sites and weak binding to Cu allow for good selective hydrogenation of styrene and acetylene as compared with only Cu or Pd metal alone.

Besides the metal surface, the metal oxide also can be used as the support to disperse the SACs because of the effective oxygen defects and vacancies. Kwak et al. [39] utilized one series of approaches including ultrahigh magnetic field, solid-state magic-angle spinning nuclear magnetic resonance spectroscopy to achieve the platinum single atoms on Al_2O_3. The density functional theory and calculations indicated that the catalytically active phase of platinum on the surface of Al_2O_3 catalyst support material. The results reveal that coordinatively unsaturated pentacoordinate Al^{3+} centers occur on the (100) facets of Al_2O_3. This work verifies the feasibility of defective metal oxide can anchor the SACs. However, the limited active defective sites hinder the number of SACs loading and the practical application of SACs.

Hackett et al. [65] have obtained mesoporous catalysts that anchor atomically dispersed Pd atoms through a wet impregnation method. Furthermore, these materials indicate exceptional catalytic performance in the aerobic selox of allylic alcohols under mild condition. The dramatic dependence of cinnamaldehyde production on electron-deficient palladium highlighted the relationship between homogeneous and heterogeneous alcohol selox process and the significance of isolated Pd sites in the catalytic cycling process. The loading of Pd in this work was only 0.03 wt%, which indicates the limitation of wet impregnation method.

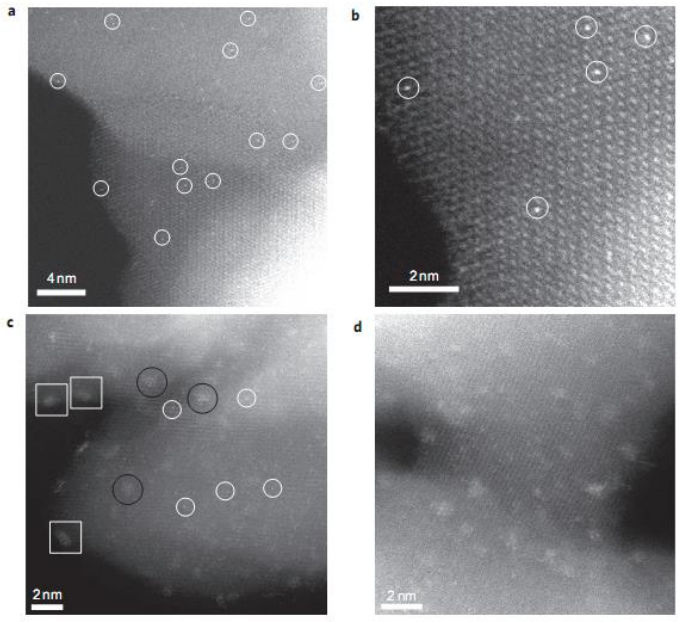

Figure 2.2 HAADF-STEM images of Pt single atoms and nanocluster uniformly dispersed on the FeOx support. Reproduced with permission[9]. Copyright Nature Publishing group.

Based on the previous study of nano clusters on catalysis, Qiao et al.[9] reported a new wet chemistry approach to synthesize isolated single Pt atoms with 0.17 wt% anchored to the surfaces of iron oxide nano-crystallites as shown in Figure 2.2. The extremely high atom efficiency has been achieved for both CO oxidation and preferential oxidation of CO in hydrogen environment. Furthermore, the authors also used the density functional theory approaches to confirm that the high catalytic activity attributes with the partially vacant 5d orbitals of the positively charged, high-valent Pt atoms, which contributes the decrease of the CO adsorption energy and the activation barriers for CO oxidation.

Besides the conventional wet approach, Liu et al.[66] synthesized the atomically dispersed palladium–titanium oxide catalyst ($Pd1/TiO_2$) through a photochemical method on ethylene glycolate (EG)–modified ultrathin TiO_2 nanosheets. The loading of Pd is up to 1.5wt.% and the catalyst revealed high catalytic activity in hydrogenation of C=C bonds. The activity of single atom Pd exhibited than commercial Pd catalysts by a factor of 9, which further demonstrated the high efficiency of SACs than the traditional catalyst.

2.2.3 The Metal–Organic Frameworks and their derived structure

Zhao et al.[67] reported metal−organic frameworks (MOFs) to assist the fabrication of single Ni sites with loading of 1.53 wt% for efficient CO2RR. The synthesis utilized ionic exchange between Zn nodes and adsorbed Ni ions inside the cavities of the MOF. This single-atom catalyst exhibited a turnover frequency for electro-reduction of CO_2 (5273 h−1), with a Faradaic efficiency for CO production up to 71.9% and with a current density of 10.48 mA cm^{-2} at an overpotential of 0.89 V. However, this approach will scarify the expensive MOF and is not fit for the large-scale application. Furthermore, the annealing process is difficult to prevent the appearance of the nanoparticle due to the aggregate of metal.

2.2.4 The carbon-based materials method

Carbon materials including graphene, carbon nanotubes and carbon porous structure have drawn significant attentions[68-71]. Furthermore, besides above well-known carbon materials, other carbon materials also have been studied for the SACs synthesis, such as carbon fiber, porous carbon spheres and so on.

2.2.4.1 Graphene based SACS by ALD

ALD was renowned because of the precise control of decomposition of metal on the targeted supports. Therefore, it is possible to achieve the synthesize of SACs on the surface of subtract. Sun et al.[72] showed the study of SACs on graphene by ALD in Figure 2.3, through comparing a series of catalysts including platinum sub-nanoclusters, and nanoparticles deposited on the surface of graphene supports. The ALD techniques can roughly control of morphology, particle size, and density as well as loading of Pt by controlling adjusting ALD cycle numbers. The SACs catalysts revealed a highly efficient activity for the methanol oxidation and great CO tolerance than the commercial Pt/C catalyst. The study confirmed that the low coordinated single Pt atoms from 5d orbitals contributed to the great electrochemical performance. However, besides the high requirements of costly instruments, ALD process will inevitably result in the SACs aggregation with the loading increase less than 0.5 wt% not fit for practical application.

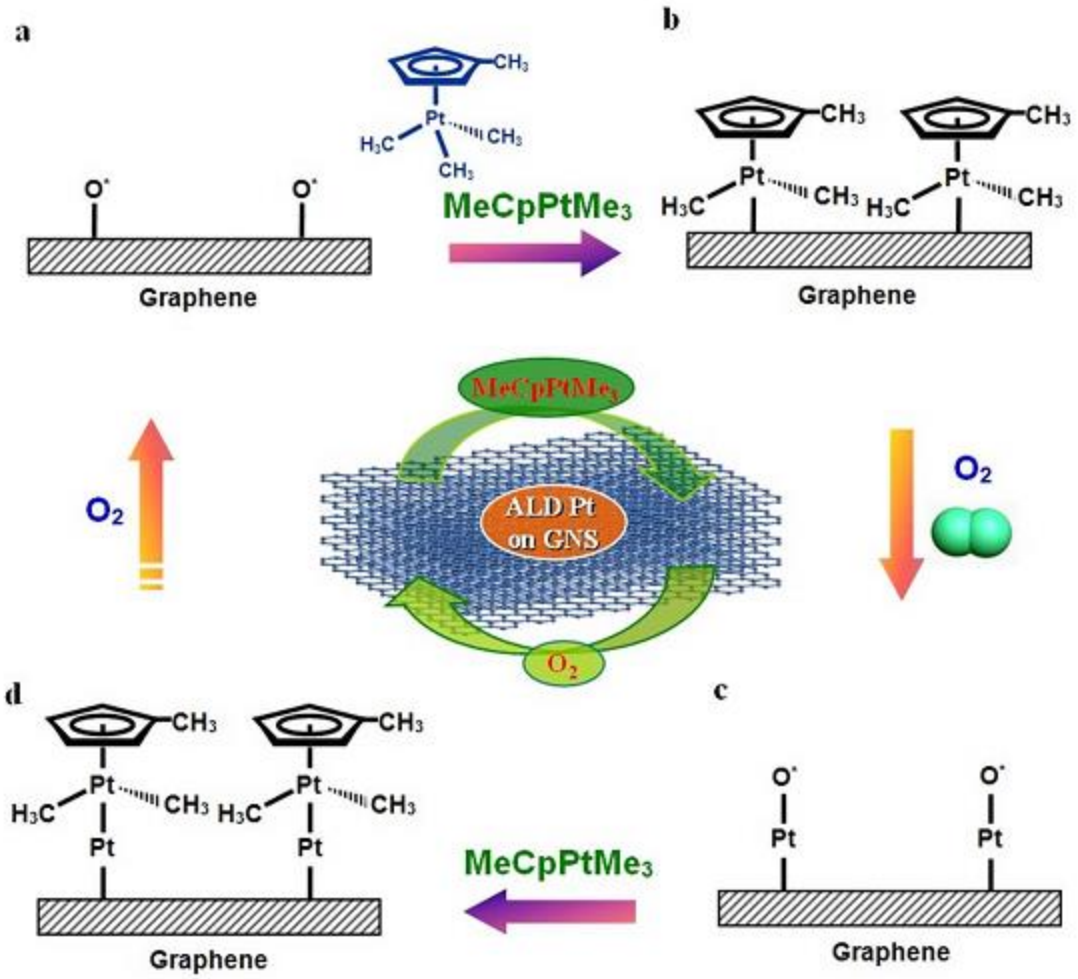

Figure 2.3 Schematic illustrations of Pt ALD mechanism on graphene nanosheets. Reproduced with permission[72]. Copyright 2013, Nature Publishing Group.

Furthermore, Yan et al.[73] also showed that uniformly dispersed Pd on atoms graphene can be synthesized through the ALD method. Then the durability against deactivation by either aggregation of metal atoms or carbonaceous deposits during a total 100 h of reaction time on stream was obtained. Pd SACs show good activity and durability in following selective hydrogenation reactions.

Based on this work, Yan et al.[74] confirmed that Pt_2 dimers can be achieved through a bottom–up method on graphene by ALD, by proper nucleation sites creation, Pt1 atom deposition and attaching a secondary Pt atom on the first one. The major reason of higher activity is considered as the lower adsorption energy of SAC and H_2 on the Pt2 dimers than that on Pt1 single atoms or Pt NPs. It is interesting that dimeric Pt_2/graphene catalyst exhibited a high stability under the inert

environment at below 300 °C, which bridged the inherent relationship between SAC and nanoparticles.

However, the ALD method requires highly advanced techniques and expensive instruments, which is not suitable for practical application. Besides the high requirements of costly instruments, ALD process inevitably results in the SACs aggregation and the catalyst loading is generally less than 0.5wt% not fit for practical application.

2.2.4.2 The porous nitrogen doping carbon materials

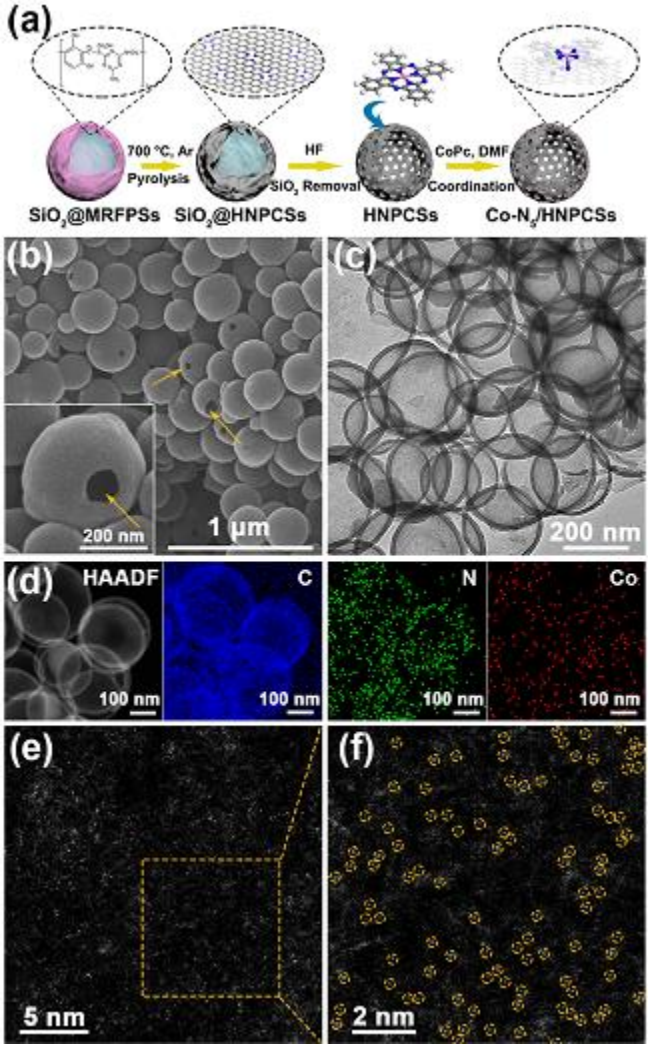

Figure 2.4 (a) Schematic illustration, (b) SEM, (c) TEM, (d) HAADF-STEM and EDS images, C (blue), N (green) and Co (red). (e, f) ACHAADF-STEM and magnified images. [70]Copyright 2018, American Chemical Society.

Among the transition metal, cobalt is very interesting one, which can achieve high catalysis but with low cost. Pan et al.[70] achieved one N-coordination strategy to obtain a robust CO2 reduction reaction (CO2RR) electrocatalyst with individually dispersed Co−N5 with loading of 3.54 wt% loaded on hollow N-doped porous carbon spheres as shown in Figure 2.4. The catalyst showed a good dispersion of Co active sites and indicates one high selectivity for CO2RR with CO Faradaic efficiency more than 90% with a wide potential range from −0.57 to −0.88 V. The 10 h test confirmed that CO current density and FECO remained nearly unchanged, which revealed the good stability. More importantly, the authors also carried out the density functional theory calculations shows that single-atom Co−N5 site is the main active sites mainly for CO_2 activation, consistent with the experimental results.

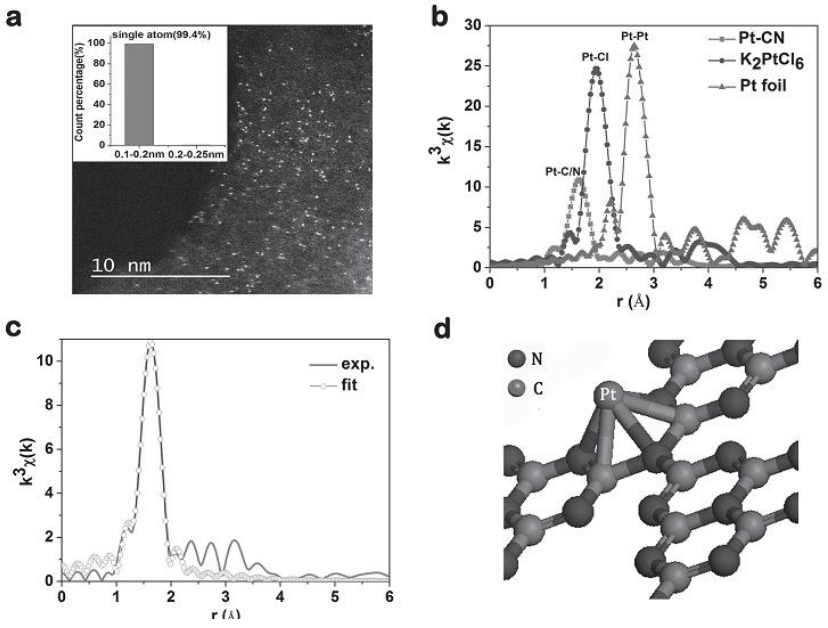

Figure 2.5 The structural investigation of Pt-CN. (a) HAADF-STEM image of Pt-CN. Inset is the size distribution of the bright spots. (b) Fourier transforms of the Pt L3-edge EXAFS oscillations of Pt-CN, K_2PtCl_6, and Pt foil. (c) Comparison of FT-EXAFS curves between the experimental

data and the fi t of the Pt-CN. (d) Schematic models of Pt-CN. Reproduced with permission [75]. Copyright 2016, American Chemical Society.

The graphited carbon nitride especially, g-C_3N_4 as one common photocatalyst is well renown by researchers. The g-C_3N_4 can provide sufficient active sites for the SACs as the supports. Li et al.[75] produced the isolated single Pt atoms as one co-catalyst with 0.16 wt% through embedding them in sub-nanoporosity on g-C_3N_4 indicated in Figure 2.5. The Pt atoms increased the atom efficiency of the noble metal and reveals one greatly efficient photocatalytic system for H_2 evolution. The combination of single-atom co-catalyst in g-C_3N_4 indicates one novel method to modulate the electronic structure, achieving one longer lifetime of the photogenerated electrons because of the isolated single Pt atoms induced, intrinsic change of the g-C_3N_4 surface trap states. More importantly, the SAC Pt atoms as co-catalyst finally produced greatly enhanced photocatalytic H_2 generation performance, almost 8.6 times higher than that of normal Pt nanoparticles based on Pt atoms. Besides the performance is nearly 50 times higher than the pure g-C_3N_4, which further confirmed that single-atom co-catalyst strategy provides one promising approach for the highly efficient catalysts. However, the impregnation approach is difficult to control the uniformity and loading of SACs. The loading of SACs anchored on the surface absorption is generally less than 1 wt%.

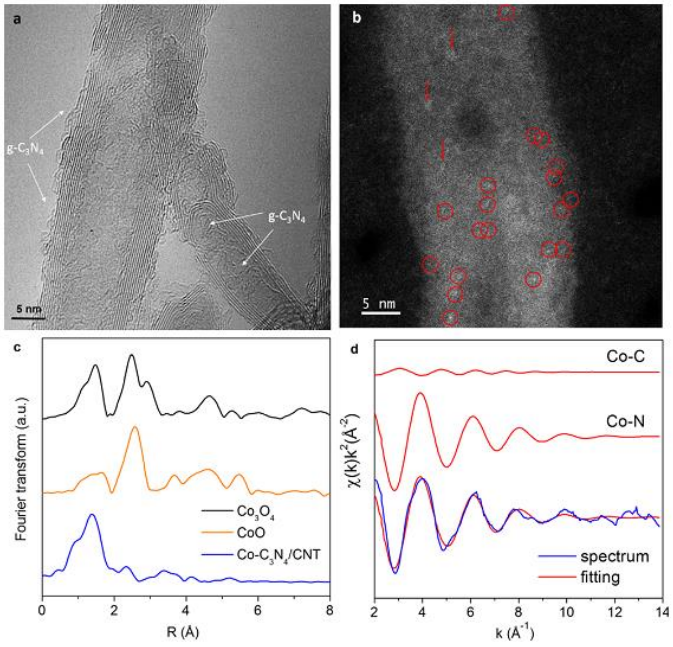

Figure 2.6 (a) High-resolution TEM and (b) HAADF-STEM images of Co−C_3N_4/CNT. Circles and arrows in panel b indicate single Co atoms and Co clusters, respectively. (c) Co K-edge Fourier transformed r-space EXAFS spectra. (d) Co K-edge k-space experimental EXAFS spectrum and fitting curves of Co−C_3N_4/CNT. Reproduced with permission[8].Copyright 2017, American Chemical Society.

In order to maximize the active sites dispersion, Zheng et al.[8] developed an approach to fix the transition metals on the surface of g−C_3N_4 as a new generation of Me−N/C catalysts for the application of oxygen electrode reactions, as shown in Figure2.6 . The electrocatalytic activity of Co-g-C_3N_4 with the loading of ~1wt% was comparable to that of noble metal references for the ORR and OER in alkaline media. The computational results indicate that the highly efficient activity sites are originated from the Co-N2 coordination in the g−C_3N_4 matrix.

Besides the g−C_3N_4, the carbon nanofiber was also chosen as support to disperse the SACs. Bulushev et al.[76] synthesized the Pt-group SACs with 1 wt% on carbon nanofiber through the N-doped coordination method. The Pt-group SACs can provide a high rate of formic acid decomposition. At the same time, the SACs also achieved good selectivity to H_2 and CO_2 and only using low loadings of Pt-group metals. Differently from the conventional nanoparticles and nanoclusters, the atomically dispersed metal atoms indicate quite low activity in ethylene hydrogenation. The SACs Pd shows poor chemical absorption of CO irreversibly room

temperature, therefore showing a strongly electron-deficient or ionic state of the metal atoms, which further confirmed the high selectivity for specific reaction.

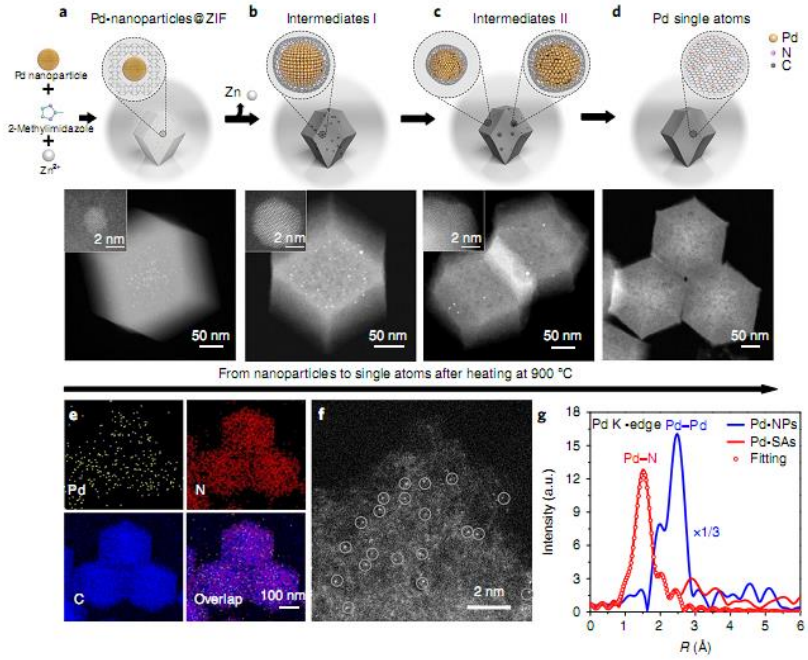

Figure 2.7 Scheme of the transformation of nanoparticles to single atoms and structural characterizations of Pd single atoms. a–d, HAADF-STEM images and high-resolution HAADF-STEM images (insets) of Pd-nanoparticles@ZIF-8 (a), intermediate I (b), intermediate II (c) and Pd single atoms (d). e, Energy dispersive X-ray spectroscopy elemental mapping images. f, High-resolution HAADF-STEM image. g, Fourier transforms of k3-weighted Pd K-edge EXAFS. Reproduced with permission[77]. Copyright 2013, Nature Publishing Group.

In order to better understand the SACs, some work was carried out to investigate the synthesis process of SACs. Wei et al.[77] shows the result that the noble metal nanoparticles (Pd, Pt, Au-NPs) could be transformed into stable single atoms through the thermal treatment at high temperature above 900 °C under the protection of inert atmosphere, see Figure 2.7. The aberration-corrected scanning transmission electron microscopy and X-ray absorption fine structures were used to confirm the atomically dispersed metal single atoms. The in situ environmental transmission electron microscopy revealed the competing sintering and atomization processes during the conversion from nano particles to single atoms. The DFT calculations confirmed that

the conversion from nanoparticles to single atom was achieved through the formation of Pd-N_4 structure at high temperature, which was more thermodynamically stable than the anno particles. Under the high temperature, the Pd atoms were anchored on the defects of nitrogen-doped carbon and formed into single atom structure.

2.3. The applications of SACs

2.3.1 Carbon Dioxide Reduction Reaction

Over the last several centuries, the rapid industrial development and booming population growth resulted in a dramatic increase of the excessive usage of fossil fuels including natural gas, petroleum, coal, which emitted massive carbon dioxide in the atmosphere[78]. It is urgent to find efficient solution to reduce the CO_2 emission[79-82]. There are many attractive solutions to cut the CO_2 emission such as restoring existing forests, carbon capture and storage and CO_2 reduction as energy source. Among of them, the reduction of CO_2 is one significant way to deal with the global warming, simultaneously producing fuels and building a low carbon emission economy. Nevertheless, one of the challenges for the CO_2 reduction reaction (CO2RR) is the lack of efficient catalyst. CO_2 is a linear molecule and needs high energy to break the bond because of the high energy barrier. Therefore, it is necessary to produce efficient and thermally stable catalyst for the catalysis process.

The CO2RR process[42, 81-83] consist of complicated process including proton coupled multi-electron transfer and involving two-, four-, six-, eight-, or twelve-electron reaction path. The following reaction equations (1–6) reveal the related typical process of CO_2 during different electron pathways. It is worth noting that reversible hydrogen electrode (RHE) especially in aqueous electrolyte with PH equal to 7.

$$CO_2 + 2(H^+ + e^-) \rightarrow HCOOH(aq)\ U = -0.20\ V_{RHE} \quad (1)$$

$$CO_2 + 2(H^+ + e^-) \rightarrow CO + H_2O\ U = -0.12\ V_{RHE} \quad (2)$$

$$CO_2 + 4(H^+ + e^-) \rightarrow CH_2O(aq) + H_2O\ U = -0.07\ V_{RHE} \quad (3)$$

$$CO_2 + 6(H^+ + e^-) \rightarrow CH_3OH(aq) + H_2O\ U = +0.03\ V_{RHE} \quad (4)$$

$$CO_2 + 8\,(H^+ + e^-) \rightarrow CH_4 + 2H_2O \quad U = +0.17\ V_{RHE} \quad (5)$$

$$CO_2 + 12(H^+ + e^-) \rightarrow C_2H_4 + H_2O \quad U = +0.08\ V_{RHE} \quad (6)$$

The final products from CO2RR rely on the utilization of electrocatalysts, the electrolyte types and related potential applied. The specific control of the products consists of various compounds, such as low carbon product CO, CO, HCOO− or HCOOH, CH_4, CH_3OH, and high value-added fuel like C_2H_4, C_2H_5OH, C_3H_7OH, $C_3H_7O_2$ etc. Recently, many studies have shown outstanding properties for the electro-chemical reduction of CO_2 to CO by Ag, Au and Ni-based catalysts [42, 79-85]. Even though, it is still highly difficult to produce high carbon hydrocarbon fuels with great activity and selectivity. Then, there are many problems left to obtain highly selective reduction of CO2 to high carbon hydrocarbon fuels through the optimization of the right support and the coordination elements[80-85].

2.3.2 Energy storage and application

Because of the advantages of atomically single-atom dispersion and well-defined configuration, SACs provide promising potentials for high selectivity and activity catalysis during the catalysis process. As for the energy storage application, there are various steps related to the catalysis and conversion like lithium sulfur battery, sodium sulfur battery, air battery and so on. Therefore, the SACs could be used in this area for the enhancement of the catalysis process.

As for the sodium sulfur battery application, Zhang et al. [86] used the atomic cobalt-decorated hollow carbon nanospheres as sulfur host, which is efficient to improve sulfur reactivity and utilization ratio. At the same time, it also achieved the polysulfide into the final product sodium sulfide with the good electrocatalytically reducing effects. The sulfur cathode with atomic catalyst could deliver an initial capacity of about 1081mA h g^{-1} with up to 64.7% sulfur utilization ratio. Finally, the constructed cell achieved a good reversible capacity around of 508mA h g^{-1} at 100mA g^{-1} even after 600 cycles.

The lithium-sulfur (Li-S) battery, one promising candidate for next higher energy storage technology, has attracted tremendous research interest because of its merits of high energy density, low cost, and environmental friendliness[87]. Nevertheless, the technological challenges arising from the low sulfur utilization, fast capacity decay and poor Coulombic efficiency have depressed Li-S battery extending to commercial application. The sluggish kinetics of this process results in

the accumulation of soluble LiPSs near the cathode area and further diffusing to anode which is renowned as shuttle effects in Li-S battery. To overcome the shuttle effects, tremendous strategies have been taken to accelerate the reversible conversion rates between soluble LiPSs and Li_2S through introducing active catalysis centers to enhance the S utilization such as metal and metal oxides [88], sulfide [89], nitride [90] and so on. However, there are still massive improvement space for the practical application of Li-S batteries. The dual catalysis process should be carefully considered to accelerate the sulfur utilization between LiPSs and Li_2S [91-95]. Only the dual conversion catalysis improved, the detrimental effects due to the sluggish kinetics may be dealt well. In order to achieve the catalysis efficiency between LiPSs and Li_2S, it has been required to push the further development of highly active and durable electrocatalysts, which possess a well-designed activation centers capable of facilitating desired the electrochemical reactions. The theoretical calculation is benefited to accelerate the lock of promising candidates [96-100]. Based on the above-mentioned discussion, it is promising to synthesize efficient appropriate SACs combined with theoretical principles, fit for Li-S batteries composed of good LiPSs absorption capacity, abundant LiPSs conversion catalysis centers, appropriate loading capacity and superior conductivity. The prerequisite for targeted synthesize SACs for certain application is to develop one versatile controllable synthesis method.

For better catalysis process in the Li-S battery, Du et al.[38] introduced the monodisperse cobalt atoms embedded in nitrogen-doped graphene (Co−N/G) as the sulfur host electrode to improve the transfer reaction of Li polysulfides. The utilization of SACs could trigger the fast dynamics of Li polysulfides from the S8 molecular. The characterization of Co SACs has been conducted by X-ray absorption spectroscopy. The first-principles calculation reveals that the Co−N−C coordination active center works as the bifunctional electrocatalyst to accelerate not only the formation but the decomposition of Li_2S during the process of discharge and charge separately. The composite electrode shows a gravimetric capacity of 1210 mAh g^{-1}, with a high S mass ratio up to 90 wt %, which also achieved the high areal capacity of 5.1 mAh cm^{-2}. Finally, the good electrochemical performance has been obtained, with capacity fading speed of 0.029% every cycle more than 100 cycles at 0.2 C with the sulfur loading of 6.0 mg cm^{-2}. The different SACs also need to be tested for higher performance Li-S battery.

Besides the Co single atoms, Wang et al.[101] synthesized the Fe SACs through the impregnation following the treatment at 700ºC for the Li-S batteries. The results showed that the single atom catalyst played a compelling role to boost the related electrochemical conversion kinetics, also achieving good performance at high rate cycling. The theoretical results confirmed that individual single iron atoms enhance the delithiation of relatively inert Li_2S cathode, which really improve the reversible conversion reactions during the charge and discharge process. The high rate test has been done up to 588 mAh g^{-1} at 12 C and with capacity fading rate low to 0.06% per cycle for 1000 cycles at 5 C. This Fe SACs also introduced one new possible approach for the high rate cycling Li-S batteries. The SACs can play vital role on the reverse catalysis process inside Li-S battery like other electrochemical reduction reaction. However, there is a capacity attenuation in this work. In order to achieve higher loading with better cycling performance, more feasible synthesis and different SACs are left to be finished. Therefore, it is worth to exploring the efficient SACs to enhance the performance of Li-S battery.

2.3.3 Oxygen reduction reaction

The oxygen reduction reaction (ORR) is one important step determining the performance of a variety of energy applications including the metal-air devices and fuel cells. Among all the promising catalysts, Pt-based catalysts have been considered the state-of-the-art efficient catalysts for ORR. However, the high cost, inferior long-time cycling stability, scarcity and poisoning effect have limited the large-scale applications. Therefore, it is urgently to find the Pt-free alternative electrocatalysts with high activity, low cost and excellent stability as well as feasible synthesis approaches[102-104].

ORR process involves multiple steps through either one four- electron pathway to one step transfer O_2 into H_2O as follows: $O_2+ 4H^++4e^-=2H_2O$. ORR can also proceed through a two-electron pathway to produce the intermediate H_2O_2 ($O_2+2H^++2e^-=H_2O_2$).

Some effects [103-106] have been made to verify the structure of the active SACs with non-noble metals like Fe-Nx , Co-N_x, Zn-N_x Cu-N_x pieces for the application as ORR electrocatalysts with low cost. Li et al.[107] synthesized the Fe SACs on the CNTs utilizing the modified CNTs with polypyrrole to absorb the iron ions . This method is called atomic isolation method, in which the metal isolation agents like Zn, Li were introduced to isolate Fe atoms and was then evaporated to produce abundant micropores. The abundant micropores are hosts for the Fe single atoms and

helps the electrolyte transport. The Fe loading in CNT@Fe-N-PC catalyst is around 0.3 at% and 1.70 wt%, which has exhibited good ORR performance with the half-wave potential of 0.82 V, closed to that of Pt/C in an acidic medium. This approach was also carried out on the CNT film and carbon cloth with Fe SACs doped showing ORR performance comparable to Pt/C catalyst. However, the loading of the SACs is still quite low less than 2 wt%.

Cheng et al.[108] synthesized the single Co atom with nitrogen doping modified carbon nanofibers (Co−N/CNFs) for ORR catalysis and showed that the Co SACs own high durability and desirable ORR efficiency not only in acidic and but alkaline environment. The electrode test revealed a good stability even after 10000 cycle durability tests. The structural stability of the atomically dispersed Co SACs on Co-N/CNFs is confirmed by the experimental characterization and density functional theory calculations. Different from the Pt-based catalyst, the Co SACs also owns good tolerance of methanol.

Till now, it is clear that the nitrogen coordination is very vital to stabilize the metal atoms on the surface of the supports. Besides the surface modification and solid nitrogen resource method, the nitrogen could be introduced into the supports by gas treatment techniques. Zhang et al. [109] prepared the Ru single atom on the surface of GO through annealing in the atmosphere of NH_3 and the as-synthesized Ru SACs exhibited a good four-electron ORR activity. The onset and half-wave potentials are 0.89 and 0.75 V, respectively, comparable to the Pt/C in the acidic medium. The DFT study of the ORR mechanism suggested that a Ru-Nx structure is responsible for the ORR catalytic activity in the acidic performance.

Besides the center metal atoms influenced the activity [106, 110-112], the research also finds that the chemical environment also will change the ORR performance dramatically. Xiao et al.[113] synthesized an interesting binuclear site structure to stabilize Co single atoms with the form Co_2N_5 and CoN_4, through a bimetal-organic-framework-self-adjusted approach with different chemical environment. The intrinsic activity followed consequence of $Co_2N_5 > > CoN_4 > > Co@C$, indicating that the different nitrogen coordination number influence the ORR activity. Co_2N_5 catalysts show almost more than 12 times higher activity than CoN_4.

In addition to the characteristics including high activity, long term stability, feasible synthesis, the scalable fabrication should also be considered for the catalyst design for the practical application [104, 114-117]. Zhang et al. [118] demonstrated a new strategy to utilize the biomass resource to

obtain the N-doped porous carbon materials as supports for the Fe SACs for ORR application. Fe-SACs revealed a good catalytic activity with the half wave potential of 0.87V due to the good dispersion of Fe. Based on the abovementioned examples, good performance in the alkline solution have been achieved, there are few good results in the acid solution due to the inactivation of active sites. Therefore, in the following research work, more dimetallic or even triple metal SACs should be tried to deal with this problem.

2.3.4 Oxygen Evolution reaction

The oxygen evolution reaction (OER) is one significant process, which plays a prime role in water splitting, rechargeable metal-air batteries[119, 120]. OER involves several steps of multiple proton-coupled electron and determines the reaction rate of water splitting. The OER is closely dependent on PH value. Under the condition of 1 atm and 25 °C, the equilibrium half-cell formula is as follows:

$$4OH^- \leftrightarrow 2H_2O(l)+O_2(g)+4\ e^-\quad E°=0.404\ V \text{ alkaline solution (1)}$$

$$2H_2O(l)\leftrightarrow 4H^+ +O_2(g)+4\ e^-\quad E°=1.23\ V \text{ acidic solution (2)}$$

The OER catalyst should equip the characteristics including low overpotential and high stability and low cost[121]. As for the successful OER application, it is urgent to explore highly efficient electrocatalysts.

Chen et al. [122] studied the Co-SAC for OER through DFT calculation, which involves two types of nitrogen on the substrates of graphene. The two types nitrogen includes graphitic nitrogen and pyridine-like nitrogen. The two nitrogen performs dramatically different and pyridine-like nitrogen is better than graphic nitrogen in OER performance. The pyridine-like nitrogen coordinated Co atom achieved high OER activity, which is consistent with experiments. Meng et al.[123] synthesized Co_4N structure through absorbing Co on the modified surface of carbon fiber clothing followed by high temperature annealing. The one integrated electrode shows one superior OER activity in terms of very low overpotential 310 mV at 10 mA cm^{-2}.

In addition to acting as efficient ORR catalysts [104, 110, 114], FeN_x supported on carbon material could be used for OER applications. Chen et al.[124] achieved Fe-Nx species on N and S co-decorated hierarchical carbon surface of CNTs as a bifunctional catalyst. The obtained Fe-N_x

electrocatalyst exhibited good electrocatalytic activity towards both ORR and OER under alkaline conditions. Through introducing different atoms like sulfur into the system, it may increase the activity of SACs as bifunctional catalyst.

2.3.5 Hydrogen Evolution Reaction

Hydrogen Evolution Reaction (HER) is an important process during electrochemical splitting of water to achieve the clean and renewable energy hydrogen. If we can achieve scalable synthesis of hydrogen by splitting water, thus, it will provide one efficient way of energy storage from clean energy like solar, wind, hydroelectric energy. The process of HER is as follows: $2H^{+}+2e^{-}=H_2$ Herein, the catalysts influenced the reaction speed thermodynamic value. H* is seen as the intermediate and plays a significant role in HER. It could be explained through two mechanism for the process. First, the Volmer–Heyrovsky process is like $H^{+}+e^{-}+*=H^{*}$; $H^{*}+H^{+}+e^{-}=H_2+*$. Then, according to the Volmer–Tafel process, it will carry on like $H^{+}+e^{-}+*=H^{*}$; $2H^{*}=H_2+2*$ [125]. The recent research confirms the free energy of H* is the dominant process of the HER, which could be controlled by the high performance catalysts [126-128].

Despite enormous efforts[129-132] have been done to explore cost-saving, highly efficient and long-term stable electrocatalyst, there are still challenges for the practical applications. The related research [133] revealed that Pt-based material is most efficient catalyst for fast reaction kinetics. However, the Pt-based catalyst suffers from the expensive cost and could not be used in large scale. Therefore, it is meaningful to study the earth-abundant catalysts to take place the Pt catalysts in order to reduce the cost, enhance the activity.

How to achieve automatically great dispersion of transition-metal atoms for HER is still one challenge. Wang et al.[134] revealed the Co-Nx with 0.22 at% bonded on the porous carbon structure. The electrode shows a good catalytic activity with low overpotential of 212 mV and current density 100 mA cm^{-2}, which is better than other traditional metals. Besides the experiments, the DFT results confirmed that C and N hybrid coordination around the Co improved the charge distribution and electron transfer during the HER process.

Fan et al. [135] obtained Ni-SACs through carbonization of metal-organic frameworks, with good HER performance with current density of 1.2 $mAcm^2$ and good durability. In addition to the Ni-SACs for HER, different metallic SACs also have been compared. Xue et al. [136] synthesized the

isolated nickel and iron atoms respectively, stabilized on the surface of graphdiyne. The Fe-SACs on gradiyne showed better performance than that of Ni-SACs different from the bulk metal results. The work shown abovementioned provide us new ideas to design and tune the properties of electrocatalysts through the single atom techniques, which is very important for the scalable water electrochemical splitting.

2.3.6 Photocatalytic H_2 production

Photocatalytic water splitting into H_2 fuel has been a research focus for its key role in solving the energy crisis and environment problem [137-140]. Photocatalysis, in which the inexhaustibly abundant, safe and clean energy from the sun can be used for nonhazardous, sustainable and economically viable technologies, is a major advance in this direction[141, 142]. SACs provide an effective way to enhance the atom efficiency. Li et al.[75] reported the Pt-SACs with 0.16 wt% dispersed on the surface of porous g-C_3N_4, which provided abundant space and sites for the Pt and increase the utilization of Pt atoms. The results further confirmed the Pt was in the form by bonding with the tri-s-triazine units in g-C_3N_4 even at low temperature. It is worth noting that this Pt-CN structure indicates high stability and excellent activity.

Furthermore, Liu et al.[143] introduced another noble metal palladium on the surface of g-C_3N_4 with loading mass of 0.1 wt%. The HER activity of Pd-g-C_3N_4 increased from 1.4 to 728 μmol g^{-1} h^{-1} under visible light irradiation, which was almost 10 times higher than that of Pd nanoparticles with 3 wt% mass loading. The dramatic performance enhancement was attributed to the electronic structure of graphitic carbon nitride due to the isolated palladium introducing. The combination contributed to the increase of photoinduced electrons fast charge separation and provided appropriate sites for the adsorption of hydrogen, which resulted in efficient charge separation, active sites for adsorption for hydrogen.

Based on the present SACs research on the photocatalytic reaction, the noble metal SACs show superior activity [144, 145]. It will be more interesting to obtain earth-abundant metal SACs like conventional transition metal for high performance photocatalytic reaction. There is still one big challenge before this target, including the proper tuning of transition metal electron structure, surrounding atomic environment and active sites density.

2.3.7 Other Reactions

Besides the above examples of the electrochemical applications, some other applications of SACs also have been proceeded [146-148].

Gu et al.[148] reported the single Pt1 and Au1 atoms stabilized by lattice oxygen on the surface of ZnO, which was used for high-performance methanol steam reforming. DFT calculations indicated that the catalysis of the Pt/Au atoms closed with coordinated lattice oxygen results in strong binding with the intermediates, and further lowering process barriers, optimizing the reaction pathway, sequentially enhancing the activity. The chemical environment confinement effects provide one new way when designing the new SACs.

Tao et al. [149] synthesized the Ru single atoms on the surface of ZrO_2 by hydrothermal treatment followed washing and annealing. They further revealed that Ru-SACs supported on nitrogen coordinated porous carbon owing high activity for electroreduction of aqueous N_2 to ammonia. The addition of ZrO_2 support could suppress HER, which is very easy occurring during N_2 reduction. The DFT calculation indicated Ru-SAC with O vacancies have high catalytic activity due to the good N_2 adsorption and selectivity.

Based on the above discussion, the SACs have been utilized for some applications and shown good catalysis performance. It can be concluded that the novel selectivity of SACs plays very significant role on specific catalysis process. Every catalysis process requires some certain active center to accelerate the reaction, which should be designed by scientific principles but not only repeated amount of experimental trials. In order to achieve versatile applications of SACs, it is also taken into consideration how to design different active sits in one system. Although the current researches have shown some good results of SACs application, there is still some problems unsettled for SACs, including the low loading, complex synthesis method, low uniformity and so on.

Methods	**Catalyst**	**Support**	**Stability**	**Scalable**	**Loading (wt%)**	**Application**	**Year**	**Reference**
Impregnation method	Pt	FeO_x	High	Y	0.17	CO oxidation	2011	9
	Pd	Al_2O_3	High	Y	0.03	Allylic alcohols oxidation	2007	65

	Ir	FeO_x	High	Y	0.01	Water gas shift	2013	41
	Pt	TiN	High	Y	0.35	Oxygen reduction	2016	111
	Pt	g-C_3N_4	High	Y	0.16	Photocatalytic H_2 Evolution	2016	75
Soft landing	Pt	MgO	Low	N	N/A	CO oxidation	1999	34
Laser evaporation	Pd	MgO	Low	N	N/A	Acetylene Cyclotrimerization	2000	63
Physical Evaporation	Pd	Cu foil	Low	N	1a.t.%	Heterogeneous Hydrogenations	2012	64
Photochemical	Pd	TiO_2	High	Y	1.5	Hydrogenation	2016	66
Atomic layer deposition	Pt	Graphene	High	N	~1.52	Methanol oxidation	2013	72
	Pt	Graphene	High	N	~2.1	HER	2016	11
MOF	Ni	MOF	Low	Y	N/A	CO2RR	2017	67
Impregnation &Annealing	Co	CNT	High	Y	~1	Oxygen Evolution	2017	8
freeze-dried &annealing	Co	Graphene	High	Y	0.57a.t.%	HER	2015	10

Table 2.1 the typical approaches to achieve the SACs. The HER stands for hydrogen evolution reaction.

Table 2.1 lists the typical approaches to obtain the SACs. As shown above, it can be concluded that there is still large space to further explore better methods in order to controllable synthesize the SACs. The most challenging problems left are how to simplify the fabrication, increase the SACs loading, maximize the application areas. Therefore, it is very meaningful to further carry out the related study focused on the controllable synthesis, characterization and application of SACs.

2.4. Conclusion and Perspective

SACs provide many possibilities for the new generation of low-cost, high efficiency, multifunctional catalysts, which are of tremendous interest and importance, due to the novel quantum size effect, maximum active sites utilization, excellent selectivity and high activity. The SACs provide a new approach for us to enhance the catalysis efficiency and reduce the catalyst cost, which is very promising to be used in the practical application. Prior to the real commercial application, there are still significant research efforts required to push forward the development of SACs. The possible points are left to be conducted as follows:

(a) How to achieve high bonding sites to obtain more coordinated isolated atom centers. Because the more active sites, the higher efficiency. (b) How to reduce the cost and simplify the synthesis process of SACs. Before any practical application, the price of an advanced technique is always the highest priority. Therefore, the more feasible approaches are left to explore to achieve the synthesis of SACs with lower cost and higher environmental friendliness. (c) How to achieve multifunctional SACs such as bifunctional or even tri-functional application. As for this application, we should combine different types SACs on one support to explore the possibilities of multifunctional applications. (d) How to carry out the new application based on the SACs. There are some unknow boundaries of SACs left to study. Therefore, it is worth paying great effort to carry on the new research areas for SACs.

2.5 References

[1] J. Liu, Catalysis by Supported Single Metal Atoms, ACS Catalysis, 7 (2017) 34-59.

[2] Z. Chengzhou, F. Shaofang, S. Qiurong, D. Dan, L. Yuehe, Single-Atom Electrocatalysts, Angewandte Chemie International Edition, 56 (2017) 13944-13960.

[3] R. Lang, W. Xi, J.-C. Liu, Y.-T. Cui, T. Li, A.F. Lee, F. Chen, Y. Chen, L. Li, L. Li, J. Lin, S. Miao, X. Liu, A.-Q. Wang, X. Wang, J. Luo, B. Qiao, J. Li, T. Zhang, Non defect-stabilized thermally stable single-atom catalyst, Nature Communications, 10 (2019) 234.

[4] A. Wang, J. Li, T. Zhang, Heterogeneous single-atom catalysis, Nature Reviews Chemistry, 2 (2018) 65-81.

[5] X. Li, X. Huang, S. Xi, S. Miao, J. Ding, W. Cai, S. Liu, X. Yang, H. Yang, J. Gao, J. Wang, Y. Huang, T. Zhang, B. Liu, Single Cobalt Atoms Anchored on Porous N-Doped Graphene with Dual Reaction Sites for Efficient Fenton-like Catalysis, Journal of the American Chemical Society, 140 (2018) 12469-12475.

[6] J. Li, G. Chen, Y. Zhu, Z. Liang, A. Pei, C.-L. Wu, H. Wang, H.R. Lee, K. Liu, S. Chu, Y. Cui, Efficient electrocatalytic CO2 reduction on a three-phase interface, Nature Catalysis, 1 (2018) 592-600.

[7] P.N. Duchesne, Z.Y. Li, C.P. Deming, V. Fung, X. Zhao, J. Yuan, T. Regier, A. Aldalbahi, Z. Almarhoon, S. Chen, D.-e. Jiang, N. Zheng, P. Zhang, Golden single-atomic-site platinum electrocatalysts, Nature Materials, (2018).

[8] Y. Zheng, Y. Jiao, Y.H. Zhu, Q.R. Cai, A. Vasileff, L.H. Li, Y. Han, Y. Chen, S.Z. Qiao, Molecule-Level g-C3N4 Coordinated Transition Metals as a New Class of Electrocatalysts for Oxygen Electrode Reactions, Journal of the American Chemical Society, 139 (2017) 3336-3339.

[9] B. Qiao, A. Wang, X. Yang, L.F. Allard, Z. Jiang, Y. Cui, J. Liu, J. Li, T. Zhang, Single-atom catalysis of CO oxidation using Pt1/FeOx, Nature chemistry, 3 (2011) 634-641.

[10] H. Fei, J. Dong, Y. Feng, C.S. Allen, C. Wan, B. Volosskiy, M. Li, Z. Zhao, Y. Wang, H. Sun, P. An, W. Chen, Z. Guo, C. Lee, D. Chen, I. Shakir, M. Liu, T. Hu, Y. Li, A.I. Kirkland, X. Duan, Y. Huang, General synthesis and definitive structural identification of MN4C4 single-atom catalysts with tunable electrocatalytic activities, Nature Catalysis, 1 (2018) 63-72.

[11] N.C. Cheng, S. Stambula, D. Wang, M.N. Banis, J. Liu, A. Riese, B.W. Xiao, R.Y. Li, T.K. Sham, L.M. Liu, G.A. Botton, X.L. Sun, Platinum single-atom and cluster catalysis of the hydrogen evolution reaction, Nature Communications, 7 (2016).

[12] H. Adler, M. Paszkiewicz, J. Uihlein, M. Polek, R. Ovsyannikov, T.V. Basova, T. Chassé, H. Peisert, Interface Properties of VOPc on Ni(111) and Graphene/Ni(111): Orientation-Dependent Charge Transfer, The Journal of Physical Chemistry C, 119 (2015) 8755-8762.

[13] Z. Chen, W. Wang, Z. Zhang, X. Fang, High-Efficiency Visible-Light-Driven Ag3PO4/AgI Photocatalysts: Z-Scheme Photocatalytic Mechanism for Their Enhanced Photocatalytic Activity, The Journal of Physical Chemistry C, 117 (2013) 19346-19352.

[14] Y. Wu, F. Ran, Vanadium nitride quantum dot/nitrogen-doped microporous carbon nanofibers electrode for high-performance supercapacitors, Journal of Power Sources, 344 (2017) 1-10.

[15] H. Wu, W. Chen, Copper Nitride Nanocubes: Size-Controlled Synthesis and Application as Cathode Catalyst in Alkaline Fuel Cells, Journal of the American Chemical Society, 133 (2011) 15236-15239.

[16] M.P. Karthikayini, T. Thirupathi, G. Wang, V.K. Ramani, R.K. Raman, Highly Active and Durable Non-Precious Metal Catalyst for the Oxygen Reduction Reaction in Acidic Medium, Journal of The Electrochemical Society, 163 (2016) F539-F547.

[17] J.C. Park, J. Kim, H. Kwon, H. Song, Gram-Scale Synthesis of Cu2O Nanocubes and Subsequent Oxidation to CuO Hollow Nanostructures for Lithium-Ion Battery Anode Materials, Advanced Materials, 21 (2009) 803-807.

[18] S. Yuan, X.l. Huang, D.l. Ma, H.g. Wang, F.z. Meng, X.b. Zhang, Engraving Copper Foil to Give Large-Scale Binder-Free Porous CuO Arrays for a High-Performance Sodium-Ion Battery Anode, Advanced Materials, 26 (2014) 2273-2279.

[19] Z. Xiang, Y. Xue, D. Cao, L. Huang, J.F. Chen, L. Dai, Highly Efficient Electrocatalysts for Oxygen Reduction Based on 2D Covalent Organic Polymers Complexed with Non-precious Metals, Angewandte Chemie International Edition, 53 (2014) 2433-2437.

[20] R. Arrigo, M. Havecker, R. Schlogl, D.S. Su, Dynamic surface rearrangement and thermal stability of nitrogen functional groups on carbon nanotubes, Chem Commun, (2008) 4891-4893.

[21] J.C. Crowhurst, A.F. Goncharov, B. Sadigh, C.L. Evans, P.G. Morrall, J.L. Ferreira, A.J. Nelson, Synthesis and Characterization of the Nitrides of Platinum and Iridium, Science, 311 (2006) 1275-1278.

[22] K. Huang, K. Bi, C. Liang, S. Lin, R. Zhang, W.J. Wang, H.L. Tang, M. Lei, Novel VN/C nanocomposites as methanol-tolerant oxygen reduction electrocatalyst in alkaline electrolyte, Scientific Reports, 5 (2015) 11351.

[23] Z. Li, Q. Gao, H. Zhang, W. Tian, Y. Tan, W. Qian, Z. Liu, Low content Pt nanoparticles anchored on N-doped reduced graphene oxide with high and stable electrocatalytic activity for oxygen reduction reaction, Scientific Reports, 7 (2017) 43352.

[24] H. Peng, Z. Mo, S. Liao, H. Liang, L. Yang, F. Luo, H. Song, Y. Zhong, B. Zhang, High Performance Fe- and N- Doped Carbon Catalyst with Graphene Structure for Oxygen Reduction, Scientific Reports, 3 (2013) 1765.

[25] Z.-R. Yang, S.-Q. Wang, J. Wang, A.-J. Zhou, C.-W. Xu, Pd supported on carbon containing nickel, nitrogen and sulfur for ethanol electrooxidation, Scientific Reports, 7 (2017) 15479.

[26] G. Silversmit, D. Depla, H. Poelman, G.B. Marin, R. De Gryse, An XPS study on the surface reduction of V2O5(001) induced by Ar+ ion bombardment, Surface Science, 600 (2006) 3512-3517.

[27] B. Zhang, J. Zhang, J. Shi, D. Tan, L. Liu, F. Zhang, C. Lu, Z. Su, X. Tan, X. Cheng, B. Han, L. Zheng, J. Zhang, Manganese acting as a high-performance heterogeneous electrocatalyst in carbon dioxide reduction, Nature Communications, 10 (2019) 2980.

[28] L. Zhao, Y. Zhang, L.-B. Huang, X.-Z. Liu, Q.-H. Zhang, C. He, Z.-Y. Wu, L.-J. Zhang, J. Wu, W. Yang, L. Gu, J.-S. Hu, L.-J. Wan, Cascade anchoring strategy for general mass production of high-loading single-atomic metal-nitrogen catalysts, Nature Communications, 10 (2019) 1278.

[29] Y. Zhu, W. Sun, J. Luo, W. Chen, T. Cao, L. Zheng, J. Dong, J. Zhang, M. Zhang, Y. Han, C. Chen, Q. Peng, D. Wang, Y. Li, A cocoon silk chemistry strategy to ultrathin N-doped carbon nanosheet with metal single-site catalysts, Nature Communications, 9 (2018) 3861.

[30] S.A. Krasnikov, A.B. Preobrajenski, N.N. Sergeeva, M.M. Brzhezinskaya, M.A. Nesterov, A.A. Cafolla, M.O. Senge, A.S. Vinogradov, Electronic structure of Ni(II) porphyrins and phthalocyanine studied by soft X-ray absorption spectroscopy, Chemical Physics, 332 (2007) 318-324.

[31] Y.T. Kim, K. Ohshima, K. Higashimine, T. Uruga, M. Takata, H. Suematsu, T. Mitani, Fine size control of platinum on carbon nanotubes: From single atoms to clusters, Angew. Chem., Int. Ed., 118 (2006) 421.

[32] J.M. Thomas, R. Raja, D.W. Lewis, Single-Site Heterogeneous Catalysts, Angewandte Chemie International Edition, 44 (2005) 6456-6482.

[33] G. Kresse, D. Joubert, From ultrasoft pseudopotentials to the projector augmented-wave method, Physical Review B, 59 (1999) 1758-1775.

[34] U. Heiz, A. Sanchez, S. Abbet, W.D. Schneider, Catalytic Oxidation of Carbon Monoxide on Monodispersed Platinum Clusters: Each Atom Counts, Journal of the American Chemical Society, 121 (1999) 3214-3217.

[35] S. Yang, J. Kim, Y.J. Tak, A. Soon, H. Lee, Single-Atom Catalyst of Platinum Supported on Titanium Nitride for Selective Electrochemical Reactions, Angew Chem Int Edit, 55 (2016) 2058-2062.

[36] T. Zheng, K. Jiang, N. Ta, Y. Hu, J. Zeng, J. Liu, H. Wang, Large-Scale and Highly Selective CO2 Electrocatalytic Reduction on Nickel Single-Atom Catalyst, Joule, (2018).

[37] K. Chi, Z. Chen, F. Xiao, W. Guo, W. Xi, J. Liu, H. Yan, Z. Zhang, J. Xiao, J. Liu, J. Luo, S. Wang, K.P. Loh, Maximizing the utility of single atom electrocatalysts on a 3D graphene nanomesh, Journal of Materials Chemistry A, (2019).

[38] Z. Du, X. Chen, W. Hu, C. Chuang, S. Xie, A. Hu, W. Yan, X. Kong, X. Wu, H. Ji, L.-J. Wan, Cobalt in Nitrogen-Doped Graphene as Single-Atom Catalyst for High-Sulfur Content Lithium–Sulfur Batteries, Journal of the American Chemical Society, 141 (2019) 3977-3985.

[39] J.H. Kwak, J. Hu, D. Mei, C.W. Yi, H. Kim do, C.H. Peden, L.F. Allard, J. Szanyi, Coordinatively unsaturated Al3+ centers as binding sites for active catalyst phases of platinum on γ-Al2O3, Science, 325 (2009) 1670.

[40] X.-F. Yang, A. Wang, B. Qiao, J. Li, J. Liu, T. Zhang, Single-Atom Catalysts: A New Frontier in Heterogeneous Catalysis, Accounts of Chemical Research, 46 (2013) 1740-1748.

[41] G. Vilé, D. Albani, M. Nachtegaal, Z. Chen, D. Dontsova, M. Antonietti, N. López, J. Pérez-Ramírez, A Stable Single-Site Palladium Catalyst for Hydrogenations, Angewandte Chemie International Edition, 54 (2015) 11265-11269.

[42] S. Back, J. Lim, N.Y. Kim, Y.H. Kim, Y. Jung, Single-atom catalysts for CO2 electroreduction with significant activity and selectivity improvements, Chem Sci, 8 (2017) 1090-1096.

[43] J. Lin, A. Wang, B. Qiao, X. Liu, X. Yang, X. Wang, J. Liang, J. Li, J. Liu, T. Zhang, Remarkable Performance of Ir1/FeOx Single-Atom Catalyst in Water Gas Shift Reaction, Journal of the American Chemical Society, 135 (2013) 15314-15317.

[44] M. Ranocchiari, C. Lothschütz, D. Grolimund, J.A. van Bokhoven, Single-atom active sites on metal-organic frameworks, Proceedings of the Royal Society A: Mathematical, Physical and Engineering Science, 468 (2012) 1985-1999.

[45] Z. Huang, X. Gu, Q. Cao, P. Hu, J. Hao, J. Li, X. Tang, Catalytically Active Single-Atom Sites Fabricated from Silver Particles, Angewandte Chemie International Edition, 51 (2012) 4198-4203.

[46] J. Gao, Y. Zhou, Z. Li, S. Yan, N. Wang, Z. Zou, High-yield synthesis of millimetre-long, semiconducting carbon nitride nanotubes with intense photoluminescence emission and reproducible photoconductivity, Nanoscale, 4 (2012) 3687-3692.

[47] J.J. Rooney, G. Webb, The importance of π-bonded intermediates in hydrocarbon reactions on transition metal catalysts, Journal of Catalysis, 3 (1964) 488-501.

[48] A.M. Shahin, F. Grandjean, G.J. Long, T.P. Schuman, Cerium LIII-Edge XAS Investigation of the Structure of Crystalline and Amorphous Cerium Oxides, Chemistry of Materials, 17 (2005) 315-321.

[49] M. Giorgetti, M. Berrettoni, S. Passerini, W.H. Smyrl, Absorption of polarized X-rays by V2O5-based cathodes for lithium batteries: an application, Electrochimica Acta, 47 (2002) 3163-3169.

[50] A. Zitolo, N. Ranjbar-Sahraie, T. Mineva, J. Li, Q. Jia, S. Stamatin, G.F. Harrington, S.M. Lyth, P. Krtil, S. Mukerjee, E. Fonda, F. Jaouen, Identification of catalytic sites in cobalt-nitrogen-carbon materials for the oxygen reduction reaction, Nature Communications, 8 (2017) 957.

[51] N. Jung, S. Bhattacharjee, S. Gautam, H.-Y. Park, J. Ryu, Y.-H. Chung, S.-Y. Lee, I. Jang, J.H. Jang, S.H. Park, D.Y. Chung, Y.-E. Sung, K.-H. Chae, U.V. Waghmare, S.-C. Lee, S.J. Yoo, Organic-inorganic hybrid PtCo nanoparticle with high electrocatalytic activity and durability for oxygen reduction, Npg Asia Materials, 8 (2016) e237.

[52] V. Martis, R. Oldman, R. Anderson, M. Fowles, T. Hyde, R. Smith, S. Nikitenko, W. Bras, G. Sankar, Structure and speciation of chromium ions in chromium doped Fe2O3 catalysts, Physical Chemistry Chemical Physics, 15 (2013) 168-175.

[53] P. Panda, R. Ramaseshan, M. Sahoo, N.G. Krishna, A.K. Yadav, S.N. Jha, D. Bhattacharyya, Local crystal structure in the vicinity of Cr in doped AlN thin films studied by X-ray absorption spectroscopy, Physical Chemistry Chemical Physics, 20 (2018) 13084-13091.

[54] A. Titov, X. Biquard, D. Halley, S. Kuroda, E. Bellet-Amalric, H. Mariette, J. Cibert, A.E. Merad, G. Merad, M.B. Kanoun, E. Kulatov, Y.A. Uspenskii, X-ray absorption near-edge structure and valence state of Mn in (Ga,Mn)N, Physical Review B, 72 (2005) 115209.

[55] H. Sawada, F. Hosokawa, T. Kaneyama, T. Ishizawa, M. Terao, M. Kawazoe, T. Sannomiya, T. Tomita, Y. Kondo, T. Tanaka, Y. Oshima, Y. Tanishiro, N. Yamamoto, K. Takayanagi, Achieving 63 pm Resolution in Scanning Transmission Electron Microscope with Spherical Aberration Corrector, Japanese Journal of Applied Physics, 46 (2007) L568-L570.

[56] C. Kisielowski, B. Freitag, M. Bischoff, H. van Lin, S. Lazar, G. Knippels, P. Tiemeijer, M. van der Stam, S. von Harrach, M. Stekelenburg, M. Haider, S. Uhlemann, H. Müller, P. Hartel, B. Kabius, D. Miller, I. Petrov, E.A. Olson, T. Donchev, E.A. Kenik, A.R. Lupini, J. Bentley, S.J. Pennycook, I.M. Anderson, A.M. Minor, A.K. Schmid, T. Duden, V. Radmilovic, Q.M. Ramasse, M. Watanabe, R. Erni, E.A. Stach, P. Denes, U. Dahmen, Detection of Single Atoms and Buried Defects in Three Dimensions by Aberration-Corrected Electron Microscope with 0.5-Å Information Limit, Microscopy and Microanalysis, 14 (2008) 469-477.

[57] D.J. Smith, Development of Aberration-Corrected Electron Microscopy, Microscopy and Microanalysis, 14 (2008) 2-15.

[58] E. Ruska, The development of the electron microscope and of electron microscopy, Reviews of Modern Physics, 59 (1987) 627-638.

[59] P.A. Midgley, M. Weyland, 3D electron microscopy in the physical sciences: the development of Z-contrast and EFTEM tomography, Ultramicroscopy, 96 (2003) 413-431.

[60] Y.L. Mao, X.H. Yan, Y. Xiao, First-principles study of transition-metal-doped single-walled carbon nanotubes, Nanotechnology, 16 (2005) 3092-3096.

[61] J.-C. Liu, Y. Tang, Y.-G. Wang, T. Zhang, J. Li, Theoretical understanding of the stability of single-atom catalysts, National Science Review, 5 (2018) 638-641.

[62] H. Xu, D. Cheng, D. Cao, X.C. Zeng, A universal principle for a rational design of single-atom electrocatalysts, Nature Catalysis, 1 (2018) 339-348.

[63] S. Abbet, A. Sanchez, U. Heiz, W.D. Schneider, A.M. Ferrari, G. Pacchioni, N. Rösch, Acetylene Cyclotrimerization on Supported Size-Selected Pdn Clusters ($1 \leq n \leq 30$): One Atom Is Enough!, Journal of the American Chemical Society, 122 (2000) 3453-3457.

[64] G. Kyriakou, M.B. Boucher, A.D. Jewell, E.A. Lewis, T.J. Lawton, A.E. Baber, H.L. Tierney, M. Flytzani-Stephanopoulos, E.C. Sykes, Isolated metal atom geometries as a strategy for selective heterogeneous hydrogenations, Science, 335 (2012) 1209.

[65] S.F. Hackett, R.M. Brydson, M.H. Gass, I. Harvey, A.D. Newman, K. Wilson, A.F. Lee, High-activity, single-site mesoporous Pd/Al2O3 catalysts for selective aerobic oxidation of allylic alcohols, Angew. Chem., Int. Ed., 46 (2007) 8593.

[66] P. Liu, Y. Zhao, R. Qin, S. Mo, G. Chen, L. Gu, D.M. Chevrier, P. Zhang, Q. Guo, D. Zang, B. Wu, G. Fu, N. Zheng, Photochemical route for synthesizing atomically dispersed palladium catalysts, Science, 352 (2016) 797-800.

[67] C. Zhao, X. Dai, T. Yao, W. Chen, X. Wang, J. Wang, J. Yang, S. Wei, Y. Wu, Y. Li, Ionic Exchange of Metal–Organic Frameworks to Access Single Nickel Sites for Efficient Electroreduction of CO2, Journal of the American Chemical Society, 139 (2017) 8078-8081.

[68] X. Wang, Z. Chen, X. Zhao, T. Yao, W. Chen, R. You, C. Zhao, G. Wu, J. Wang, W. Huang, J. Yang, X. Hong, S. Wei, Y. Wu, Y. Li, Regulation of Coordination Number over Single Co Sites: Triggering the Efficient Electroreduction of CO2, Angewandte Chemie International Edition, 57 (2018) 1944-1948.

[69] Z.D. Hu, Y.F. Hu, Q. Chen, X.F. Duan, L.M. Peng, Synthesis and Characterizations of Amorphous Carbon Nanotubes by Pyrolysis of Ferrocene Confined within AAM Templates, The Journal of Physical Chemistry B, 110 (2006) 8263-8267.

[70] Y. Pan, R. Lin, Y. Chen, S. Liu, W. Zhu, X. Cao, W. Chen, K. Wu, W.-C. Cheong, Y. Wang, L. Zheng, J. Luo, Y. Lin, Y. Liu, C. Liu, J. Li, Q. Lu, X. Chen, D. Wang, Q. Peng, C. Chen, Y. Li, Design of Single-Atom Co–N5 Catalytic Site: A Robust Electrocatalyst for CO2 Reduction with Nearly 100% CO Selectivity and Remarkable Stability, Journal of the American Chemical Society, 140 (2018) 4218-4221.

[71] S. Tian, Z. Wang, W. Gong, W. Chen, Q. Feng, Q. Xu, C. Chen, C. Chen, Q. Peng, L. Gu, H. Zhao, P. Hu, D. Wang, Y. Li, Temperature-Controlled Selectivity of Hydrogenation and Hydrodeoxygenation in the Conversion of Biomass Molecule by the Ru1/mpg-C3N4 Catalyst, Journal of the American Chemical Society, 140 (2018) 11161-11164.

[72] S. Sun, G. Zhang, N. Gauquelin, N. Chen, J. Zhou, S. Yang, W. Chen, X. Meng, D. Geng, M.N. Banis, R. Li, S. Ye, S. Knights, G.A. Botton, T.K. Sham, X. Sun, Single-atom catalysis using Pt/graphene achieved through atomic layer deposition, Sci. Rep., 3 (2013) 1775.

[73] H. Yan, H. Cheng, H. Yi, Y. Lin, T. Yao, C. Wang, J. Li, S. Wei, J. Lu, Single-Atom Pd1/Graphene Catalyst Achieved by Atomic Layer Deposition: Remarkable Performance in Selective Hydrogenation of 1,3-Butadiene, Journal of the American Chemical Society, 137 (2015) 10484-10487.

[74] H. Yan, Y. Lin, H. Wu, W. Zhang, Z. Sun, H. Cheng, W. Liu, C. Wang, J. Li, X. Huang, T. Yao, J. Yang, S. Wei, J. Lu, Bottom-up precise synthesis of stable platinum dimers on graphene, Nature Communications, 8 (2017) 1070.

[75] X. Li, W. Bi, L. Zhang, S. Tao, W. Chu, Q. Zhang, Y. Luo, C. Wu, Y. Xie, Single-Atom Pt as Co-Catalyst for Enhanced Photocatalytic H2 Evolution, Advanced Materials, 28 (2016) 2427-2431.

[76] D.A. Bulushev, M. Zacharska, A.S. Lisitsyn, O.Y. Podyacheva, F.S. Hage, Q.M. Ramasse, U. Bangert, L.G. Bulusheva, Single Atoms of Pt-Group Metals Stabilized by N-Doped Carbon Nanofibers for Efficient Hydrogen Production from Formic Acid, Acs Catalysis, 6 (2016) 3442-3451.

[77] S. Wei, A. Li, J.-C. Liu, Z. Li, W. Chen, Y. Gong, Q. Zhang, W.-C. Cheong, Y. Wang, L. Zheng, H. Xiao, C. Chen, D. Wang, Q. Peng, L. Gu, X. Han, J. Li, Y. Li, Direct observation of noble metal nanoparticles transforming to thermally stable single atoms, Nature Nanotechnology, 13 (2018) 856-861.

[78] Y. Cheng, S. Yang, S.P. Jiang, S. Wang, Supported Single Atoms as New Class of Catalysts for Electrochemical Reduction of Carbon Dioxide, 3 (2019) 1800440.

[79] J. Xie, R. Jin, A. Li, Y. Bi, Q. Ruan, Y. Deng, Y. Zhang, S. Yao, G. Sankar, D. Ma, J. Tang, Highly selective oxidation of methane to methanol at ambient conditions by titanium dioxide-supported iron species, Nature Catalysis, 1 (2018) 889-896.

[80] K. Tran, Z.W. Ulissi, Active learning across intermetallics to guide discovery of electrocatalysts for CO2 reduction and H2 evolution, Nature Catalysis, 1 (2018) 696-703.

[81] G. Neri, J.J. Walsh, G. Teobaldi, P.M. Donaldson, A.J. Cowan, Detection of catalytic intermediates at an electrode surface during carbon dioxide reduction by an earth-abundant catalyst, Nature Catalysis, (2018).

[82] C.G. Morales-Guio, E.R. Cave, S.A. Nitopi, J.T. Feaster, L. Wang, K.P. Kuhl, A. Jackson, N.C. Johnson, D.N. Abram, T. Hatsukade, C. Hahn, T.F. Jaramillo, Improved CO2 reduction activity towards C2+ alcohols on a tandem gold on copper electrocatalyst, Nature Catalysis, 1 (2018) 764-771.

[83] P. Hirunsit, W. Soodsawang, J. Limtrakul, CO2 Electrochemical Reduction to Methane and Methanol on Copper-Based Alloys: Theoretical Insight, The Journal of Physical Chemistry C, 119 (2015) 8238-8249.

[84] J. Wu, R.M. Yadav, M. Liu, P.P. Sharma, C.S. Tiwary, L. Ma, X. Zou, X.-D. Zhou, B.I. Yakobson, J. Lou, P.M. Ajayan, Achieving Highly Efficient, Selective, and Stable CO2 Reduction on Nitrogen-Doped Carbon Nanotubes, ACS Nano, 9 (2015) 5364-5371.

[85] Z. Sun, T. Ma, H. Tao, Q. Fan, B. Han, Fundamentals and Challenges of Electrochemical CO2 Reduction Using Two-Dimensional Materials, Chem, 3 (2017) 560-587.

[86] B.-W. Zhang, T. Sheng, Y.-D. Liu, Y.-X. Wang, L. Zhang, W.-H. Lai, L. Wang, J. Yang, Q.-F. Gu, S.-L. Chou, H.-K. Liu, S.-X. Dou, Atomic cobalt as an efficient electrocatalyst in sulfur cathodes for superior room-temperature sodium-sulfur batteries, Nature Communications, 9 (2018) 4082.

[87] G.M. Zhou, E. Paek, G.S. Hwang, A. Manthiram, Long-life Li/polysulphide batteries with high sulphur loading enabled by lightweight three-dimensional nitrogen/sulphur-codoped graphene sponge, Nature Communications, 6 (2015) 7760-7770.

[88] Q. Pang, D. Kundu, M. Cuisinier, L.F. Nazar, Surface-enhanced redox chemistry of polysulphides on a metallic and polar host for lithium-sulphur batteries, Nature Communications, 5 (2014) 4759.

[89] Z.A. Ghazi, X. He, A.M. Khattak, N.A. Khan, B. Liang, A. Iqbal, J. Wang, H. Sin, L. Li, Z. Tang, MoS2/Celgard Separator as Efficient Polysulfide Barrier for Long-Life Lithium–Sulfur Batteries, Advanced Materials, 29 (2017) 1606817-n/a.

[90] D.-R. Deng, F. Xue, Y.-J. Jia, J.-C. Ye, C.-D. Bai, M.-S. Zheng, Q.-F. Dong, Co4N Nanosheet Assembled Mesoporous Sphere as a Matrix for Ultrahigh Sulfur Content Lithium–Sulfur Batteries, ACS Nano, 11 (2017) 6031-6039.

[91] G. Hu, Z. Sun, C. Shi, R. Fang, J. Chen, P. Hou, C. Liu, H.-M. Cheng, F. Li, A Sulfur-Rich Copolymer@CNT Hybrid Cathode with Dual-Confinement of Polysulfides for High-Performance Lithium–Sulfur Batteries, Advanced Materials, 29 (2017) 1603835-n/a.

[92] G.J. Hu, C. Xu, Z.H. Sun, S.G. Wang, H.M. Cheng, F. Li, W.C. Ren, 3D Graphene-Foam-Reduced-Graphene-Oxide Hybrid Nested Hierarchical Networks for High-Performance Li-S Batteries, Advanced Materials, 28 (2016) 1603-1609.

[93] Z. Cui, C. Zu, W. Zhou, A. Manthiram, J.B. Goodenough, Mesoporous titanium nitride-enabled highly stable lithium-sulfur batteries, Adv. Mater., 28 (2016) 6926-6931.

[94] G.M. Zhou, S.F. Pei, L. Li, D.W. Wang, S.G. Wang, K. Huang, L.C. Yin, F. Li, H.M. Cheng, A graphene-pure-sulfur sandwich structure for ultrafast, long-life lithium-sulfur batteries, Adv. Mater., 26 (2014) 625-631.

[95] Y. Qiu, W. Li, W. Zhao, G. Li, Y. Hou, M. Liu, L. Zhou, F. Ye, H. Li, Z. Wei, S. Yang, W. Duan, Y. Ye, J. Guo, Y. Zhang, High-rate, ultralong cycle-life lithium/sulfur batteries enabled by nitrogen-doped graphene, Nano Lett., 14 (2014) 4821-4827.

[96] J. Chen, W.A. Henderson, H. Pan, B.R. Perdue, R. Cao, J.Z. Hu, C. Wan, K.S. Han, K.T. Mueller, J.-G. Zhang, Y. Shao, J. Liu, Improving Lithium–Sulfur Battery Performance under Lean Electrolyte through Nanoscale Confinement in Soft Swellable Gels, Nano Letters, 17 (2017) 3061-3067.

[97] C.-Y. Chen, H.-J. Peng, T.-Z. Hou, P.-Y. Zhai, B.-Q. Li, C. Tang, W. Zhu, J.-Q. Huang, Q. Zhang, A Quinonoid-Imine-Enriched Nanostructured Polymer Mediator for Lithium–Sulfur Batteries, Advanced Materials, 29 (2017) 1606802-n/a.

[98] M. Yu, J. Ma, H. Song, A. Wang, F. Tian, Y. Wang, H. Qiu, R. Wang, Atomic layer deposited TiO2 on a nitrogen-doped graphene/sulfur electrode for high performance lithium–sulfur batteries, Energy Environ. Sci., 9 (2016) 1495-1503.

[99] L.-C. Yin, J. Liang, G.-M. Zhou, F. Li, R. Saito, H.-M. Cheng, Understanding the interactions between lithium polysulfides and N-doped graphene using density functional theory calculations, Nano Energy, 25 (2016) 203-210.

[100] L. Sun, D. Wang, Y. Luo, K. Wang, W. Kong, Y. Wu, L. Zhang, K. Jiang, Q. Li, Y. Zhang, J. Wang, S. Fan, Sulfur embedded in a mesoporous carbon nanotube network as a binder-free electrode for high-performance lithium-sulfur batteries, ACS Nano, 10 (2016) 1300-1308.

[101] J. Wang, L. Jia, J. Zhong, Q. Xiao, C. Wang, K. Zang, H. Liu, H. Zheng, J. Luo, J. Yang, H. Fan, W. Duan, Y. Wu, H. Lin, Y. Zhang, Single-atom catalyst boosts electrochemical conversion reactions in batteries, Energy Storage Materials, 18 (2019) 246-252.

[102] Y. Liang, H. Wang, P. Diao, W. Chang, G. Hong, Y. Li, M. Gong, L. Xie, J. Zhou, J. Wang, T.Z. Regier, F. Wei, H. Dai, Oxygen Reduction Electrocatalyst Based on Strongly Coupled Cobalt Oxide Nanocrystals and Carbon Nanotubes, Journal of the American Chemical Society, 134 (2012) 15849-15857.

[103] X. Chen, L. Yu, S. Wang, D. Deng, X. Bao, Highly active and stable single iron site confined in graphene nanosheets for oxygen reduction reaction, Nano Energy, 32 (2017) 353.

[104] L. Jiao, G. Wan, R. Zhang, H. Zhou, S.-H. Yu, H.-L. Jiang, From Metal–Organic Frameworks to Single-Atom Fe Implanted N-doped Porous Carbons: Efficient Oxygen Reduction in Both Alkaline and Acidic Media, Angewandte Chemie International Edition, 57 (2018) 8525-8529.

[105] J. Kim, C.-W. Roh, S.K. Sahoo, S. Yang, J. Bae, J.W. Han, H. Lee, Highly Durable Platinum Single-Atom Alloy Catalyst for Electrochemical Reactions, Adv Energy Mater, 8 (2018) 1701476.

[106] P. Song, M. Luo, X. Liu, W. Xing, W. Xu, Z. Jiang, L. Gu, Zn Single Atom Catalyst for Highly Efficient Oxygen Reduction Reaction, Advanced Functional Materials, 27 (2017) 1700802.

[107] J.-C. Li, Z.-Q. Yang, D.-M. Tang, L. Zhang, P.-X. Hou, S.-Y. Zhao, C. Liu, M. Cheng, G.-X. Li, F. Zhang, H.-M. Cheng, N-doped carbon nanotubes containing a high concentration of single iron atoms for efficient oxygen reduction, Npg Asia Materials, 10 (2018) e461.

[108] Q. Cheng, L. Yang, L. Zou, Z. Zou, C. Chen, Z. Hu, H. Yang, Single Cobalt Atom and N Codoped Carbon Nanofibers as Highly Durable Electrocatalyst for Oxygen Reduction Reaction, ACS Catalysis, 7 (2017) 6864-6871.

[109] C. Zhang, J. Sha, H. Fei, M. Liu, S. Yazdi, J. Zhang, Q. Zhong, X. Zou, N. Zhao, H. Yu, Z. Jiang, E. Ringe, B.I. Yakobson, J. Dong, D. Chen, J.M. Tour, Single-Atomic Ruthenium Catalytic Sites on Nitrogen-Doped Graphene for Oxygen Reduction Reaction in Acidic Medium, ACS Nano, 11 (2017) 6930-6941.

[110] C. Zhu, S. Fu, J. Song, Q. Shi, D. Su, M.H. Engelhard, X. Li, D. Xiao, D. Li, L. Estevez, D. Du, Y. Lin, Self-Assembled Fe–N-Doped Carbon Nanotube Aerogels with Single-Atom Catalyst Feature as High-Efficiency Oxygen Reduction Electrocatalysts, Small, 13 (2017) 1603407.

[111] S. Yang, J. Kim, Y.J. Tak, A. Soon, H. Lee, Single-Atom Catalyst of Platinum Supported on Titanium Nitride for Selective Electrochemical Reactions, Angewandte Chemie International Edition, 55 (2016) 2058-2062.

[112] X. Zeng, J. Shui, X. Liu, Q. Liu, Y. Li, J. Shang, L. Zheng, R. Yu, Single-Atom to Single-Atom Grafting of Pt1 onto Fe N4 Center: Pt1@Fe N C Multifunctional Electrocatalyst with Significantly Enhanced Properties, Adv Energy Mater, 8 (2018) 1701345.

[113] M. Xiao, H. Zhang, Y. Chen, J. Zhu, L. Gao, Z. Jin, J. Ge, Z. Jiang, S. Chen, C. Liu, W. Xing, Identification of binuclear Co2N5 active sites for oxygen reduction reaction with more than one magnitude higher activity than single atom CoN4 site, Nano Energy, 46 (2018) 396-403.

[114] W. Yang, X. Liu, X. Yue, J. Jia, S. Guo, Bamboo-like Carbon Nanotube/Fe3C Nanoparticle Hybrids and Their Highly Efficient Catalysis for Oxygen Reduction, Journal of the American Chemical Society, 137 (2015) 1436-1439.

[115] Z. Zhang, J. Sun, F. Wang, L. Dai, Efficient Oxygen Reduction Reaction (ORR) Catalysts Based on Single Iron Atoms Dispersed on a Hierarchically Structured Porous Carbon Framework, Angewandte Chemie International Edition, 57 (2018) 9038-9043.

[116] G. Wan, P. Yu, H. Chen, J. Wen, C.-j. Sun, H. Zhou, N. Zhang, Q. Li, W. Zhao, B. Xie, T. Li, J. Shi, Engineering Single-Atom Cobalt Catalysts toward Improved Electrocatalysis, Small, 14 (2018) 1704319.

[117] Y. Cheng, J. Liang, J.-P. Veder, M. Li, S. Chen, J. Pan, L. Song, H.-M. Cheng, C. Liu, S.P. Jiang, Iron Oxide Nanoclusters Incorporated into Iron Phthalocyanine as Highly Active Electrocatalysts for the Oxygen Reduction Reaction, ChemCatChem, 10 (2018) 475-483.

[118] Z. Zhang, X. Gao, M. Dou, J. Ji, F. Wang, Biomass Derived N-Doped Porous Carbon Supported Single Fe Atoms as Superior Electrocatalysts for Oxygen Reduction, Small, 13 (2017) 1604290.

[119] N.-T. Suen, S.-F. Hung, Q. Quan, N. Zhang, Y.-J. Xu, H.M. Chen, Electrocatalysis for the oxygen evolution reaction: recent development and future perspectives, Chemical Society Reviews, 46 (2017) 337-365.

[120] M. Tahir, L. Pan, F. Idrees, X. Zhang, L. Wang, J.-J. Zou, Z.L. Wang, Electrocatalytic oxygen evolution reaction for energy conversion and storage: A comprehensive review, Nano Energy, 37 (2017) 136-157.

[121] Y. Xu, W. Zhang, Y. Li, P. Lu, Y. Wang, Z.-S. Wu, The Synergetic Effect of Ni and Fe Bi-metal Single Atom Catalysts on Graphene for Highly Efficient Oxygen Evolution Reaction, 6 (2019).

[122] C. Chen, G. Chen, X. Kong, Enhanced Oxygen Evolution Reaction for Single Atomic Co Catalyst via Support Modification: A Density Functional Theory Design Predication, Inorganic Chemistry, 57 (2018) 13020-13026.

[123] F. Meng, H. Zhong, D. Bao, J. Yan, X. Zhang, In Situ Coupling of Strung Co4N and Intertwined N–C Fibers toward Free-Standing Bifunctional Cathode for Robust, Efficient, and Flexible Zn–Air Batteries, Journal of the American Chemical Society, 138 (2016) 10226-10231.

[124] P. Chen, T. Zhou, L. Xing, K. Xu, Y. Tong, H. Xie, L. Zhang, W. Yan, W. Chu, C. Wu, Y. Xie, Atomically Dispersed Iron–Nitrogen Species as Electrocatalysts for Bifunctional Oxygen Evolution and Reduction Reactions, Angewandte Chemie International Edition, 56 (2017) 610-614.

[125] Z.W. Seh, J. Kibsgaard, C.F. Dickens, I. Chorkendorff, J.K. Nørskov, T.F. Jaramillo, Combining theory and experiment in electrocatalysis: Insights into materials design, Science, 355 (2017) eaad4998.

[126] W. Chen, J. Pei, C.-T. He, J. Wan, H. Ren, Y. Zhu, Y. Wang, J. Dong, S. Tian, W.-C. Cheong, S. Lu, L. Zheng, X. Zheng, W. Yan, Z. Zhuang, C. Chen, Q. Peng, D. Wang, Y. Li, Rational Design of Single Molybdenum Atoms Anchored on N-Doped Carbon for Effective Hydrogen Evolution Reaction, Angewandte Chemie International Edition, 56 (2017) 16086-16090.

[127] S. Cao, H. Li, T. Tong, H.-C. Chen, A. Yu, J. Yu, H.M. Chen, Single-Atom Engineering of Directional Charge Transfer Channels and Active Sites for Photocatalytic Hydrogen Evolution, Advanced Functional Materials, 28 (2018) 1802169.

[128] T. He, C. Zhang, A. Du, Single-atom supported on graphene grain boundary as an efficient electrocatalyst for hydrogen evolution reaction, Chemical Engineering Science, 194 (2019) 58-63.

[129] Y. Cao, S. Chen, Q. Luo, H. Yan, Y. Lin, W. Liu, L. Cao, J. Lu, J. Yang, T. Yao, S. Wei, Atomic-Level Insight into Optimizing the Hydrogen Evolution Pathway over a Co1-N4 Single-Site Photocatalyst, Angewandte Chemie International Edition, 56 (2017) 12191-12196.

[130] L. Cao, Q. Luo, W. Liu, Y. Lin, X. Liu, Y. Cao, W. Zhang, Y. Wu, J. Yang, T. Yao, S. Wei, Identification of single-atom active sites in carbon-based cobalt catalysts during electrocatalytic hydrogen evolution, Nature Catalysis, 2 (2019) 134-141.

[131] Y. Chen, S. Ji, Y. Wang, J. Dong, W. Chen, Z. Li, R. Shen, L. Zheng, Z. Zhuang, D. Wang, Y. Li, Isolated Single Iron Atoms Anchored on N-Doped Porous Carbon as an Efficient Electrocatalyst for the Oxygen Reduction Reaction, Angewandte Chemie International Edition, 56 (2017) 6937-6941.

[132] H.-J. Qiu, Y. Ito, W. Cong, Y. Tan, P. Liu, A. Hirata, T. Fujita, Z. Tang, M. Chen, Nanoporous Graphene with Single-Atom Nickel Dopants: An Efficient and Stable Catalyst for Electrochemical Hydrogen Production, Angewandte Chemie International Edition, 54 (2015) 14031-14035.

[133] N. Cheng, S. Stambula, D. Wang, M.N. Banis, J. Liu, A. Riese, B. Xiao, R. Li, T.-K. Sham, L.-M. Liu, G.A. Botton, X. Sun, Platinum single-atom and cluster catalysis of the hydrogen evolution reaction, Nature Communications, 7 (2016) 13638.

[134] Z.-L. Wang, X.-F. Hao, Z. Jiang, X.-P. Sun, D. Xu, J. Wang, H.-X. Zhong, F.-L. Meng, X.-B. Zhang, C and N Hybrid Coordination Derived Co–C–N Complex as a Highly Efficient Electrocatalyst for Hydrogen Evolution Reaction, Journal of the American Chemical Society, 137 (2015) 15070-15073.

[135] L. Fan, P.F. Liu, X. Yan, L. Gu, Z.Z. Yang, H.G. Yang, S. Qiu, X. Yao, Atomically isolated nickel species anchored on graphitized carbon for efficient hydrogen evolution electrocatalysis, Nature Communications, 7 (2016) 10667.

[136] Y. Xue, B. Huang, Y. Yi, Y. Guo, Z. Zuo, Y. Li, Z. Jia, H. Liu, Y. Li, Anchoring zero valence single atoms of nickel and iron on graphdiyne for hydrogen evolution, Nature Communications, 9 (2018) 1460.

[137] J.-J. Zou, H. He, L. Cui, H.-Y. Du, Highly efficient Pt/TiO2Pt/TiO2 photocatalyst for hydrogen generation prepared by a cold plasma method, International Journal of Hydrogen Energy, 32 (2007) 1762-1770.

[138] M.G. Walter, E.L. Warren, J.R. McKone, S.W. Boettcher, Q. Mi, E.A. Santori, N.S. Lewis, Solar Water Splitting Cells, Chemical Reviews, 110 (2010) 6446-6473.

[139] X.-J. Lv, W.-F. Fu, H.-X. Chang, H. Zhang, J.-S. Cheng, G.-J. Zhang, Y. Song, C.-Y. Hu, J.-H. Li, Hydrogen evolution from water using semiconductor nanoparticle/graphene composite photocatalysts without noble metals, Journal of Materials Chemistry, 22 (2012) 1539-1546.

[140] E.P. Melián, C.R. López, A.O. Méndez, O.G. Díaz, M.N. Suárez, J.M. Doña Rodríguez, J.A. Navío, D. Fernández Hevia, Hydrogen production using Pt-loaded TiO2 photocatalysts, International Journal of Hydrogen Energy, 38 (2013) 11737-11748.

[141] M. Kapilashrami, Y. Zhang, Y.-S. Liu, A. Hagfeldt, J. Guo, Probing the Optical Property and Electronic Structure of TiO2 Nanomaterials for Renewable Energy Applications, Chemical Reviews, 114 (2014) 9662-9707.

[142] J. Schneider, M. Matsuoka, M. Takeuchi, J. Zhang, Y. Horiuchi, M. Anpo, D.W. Bahnemann, Understanding TiO2 Photocatalysis: Mechanisms and Materials, Chemical Reviews, 114 (2014) 9919-9986.

[143] L. Liu, X. Wu, L. Wang, X. Xu, L. Gan, Z. Si, J. Li, Q. Zhang, Y. Liu, Y. Zhao, R. Ran, X. Wu, D. Weng, F. Kang, Atomic palladium on graphitic carbon nitride as a hydrogen evolution catalyst under visible light irradiation, Communications Chemistry, 2 (2019) 18.

[144] X. Zhang, X. Xie, H. Wang, J. Zhang, B. Pan, Y. Xie, Enhanced Photoresponsive Ultrathin Graphitic-Phase C3N4 Nanosheets for Bioimaging, Journal of the American Chemical Society, 135 (2013) 18-21.

[145] Á. Kmetykó, K. Mogyorósi, V. Gerse, Z. Kónya, P. Pusztai, A. Dombi, K. Hernádi, Photocatalytic H2 Production Using Pt-TiO2 in the Presence of Oxalic Acid: Influence of the Noble Metal Size and the Carrier Gas Flow Rate, Materials, 7 (2014) 7022.

[146] C. Ling, X. Bai, Y. Ouyang, A. Du, J. Wang, Single Molybdenum Atom Anchored on N-Doped Carbon as a Promising Electrocatalyst for Nitrogen Reduction into Ammonia at Ambient Conditions, The Journal of Physical Chemistry C, 122 (2018) 16842-16847.

[147] J. Zhao, J. Zhao, Q. Cai, Single transition metal atom embedded into a MoS2 nanosheet as a promising catalyst for electrochemical ammonia synthesis, Physical Chemistry Chemical Physics, 20 (2018) 9248-9255.

[148] X.-K. Gu, B. Qiao, C.-Q. Huang, W.-C. Ding, K. Sun, E. Zhan, T. Zhang, J. Liu, W.-X. Li, Supported Single Pt1/Au1 Atoms for Methanol Steam Reforming, ACS Catalysis, 4 (2014) 3886-3890.

[149] H. Tao, C. Choi, L.-X. Ding, Z. Jiang, Z. Han, M. Jia, Q. Fan, Y. Gao, H. Wang, A.W. Robertson, S. Hong, Y. Jung, S. Liu, Z. Sun, Nitrogen Fixation by Ru Single-Atom Electrocatalytic Reduction, Chem, 5 (2019) 204-214.

Chapter 3: Experimental

3.1 Materials and preparation

The chemicals used in this thesis were purchased from Sigma Aldrich unless other specified. They are listed as follows: nickel(II) acetylacetonate, cobalt (II) acetylacetonate, iron (III) acetylacetonate, silver acetylacetonate, copper (II) acetylacetonate and palladium (II) acetylacetonate, dicyandiamide ($C_2H_4N_4$, DCD), nickel phthalocyanine (NiPc), Ni foil, $Ni(OH)_2$, NiO , Pt/C (20 wt%), poly ethyleneimine (PEI) solution (50% (w/v) in H_2O,) and polyvinylpyrrolid (PVP, average mol 40000).

The annealing treatments in this project was done under argon or hydrogen atmosphere in the closed horizontal furnace.

3.2 Structure Characterization

In order to get one complete analysis of the materials in this thesis, the characterization was carried out including macro and micro morphology, chemical components, spectrum techniques.

The sample morphology was obtained by scanning the surface of the sample via focusing the electron beam and collecting the secondary electrons. Scanning electron microscopy (SEM, Zeiss Neon 40EsB) was used to observe the initial microstructure of the as-synthesized samples.

Transmission electron microscopy is a technique using an electron beam to pass through an ultrathin area and interact with the sample to get the microscopic morphology. High-resolution transmission electron microscopy (HRTEM, FEI Titan G2 80-200 TEM/STEM) was done to further analysis the microstructure. The TEM samples were made through dropping the sample ethanol solution on the surface of copper grid. Before observation the grids were dry in the 80^{o}C oven for 10h. High angle annular dark field scanning transmission electron microscopy (HAADF-STEM) together with imaging and elemental mapping were conducted with a ChemiSTEM Technology instrument operating at 200 kV. The elemental mapping test was done by energy dispersive X-ray spectroscopy using the Super-X detector on the Titan with a probe size ~1 nm and a current of ~0.4 nA. As for the higher resolution even to the atomic level, high-resolution aberration-corrected scanning transmission electron microscopy annular dark field images (AC-

STEM-ADF, Nion UltraSTEM100 microscope) was carried out by operating at 60 kV at a beam current of 60 pA. The recorded images were filtered using a Gaussian function with a full width half maximum of 0.12 nm to reduce the high frequency noise. The convergence half angle of the electron beam was set to 30 mrad and the inner collection half angle of the ADF images was 51 mrad. The samples were dried at 160 ^{o}C overnight before investigation by STEM.

Each crystal has a unique diffraction pattern because of its novel crystal lattice and structure, therefore by comparing the XRD spectrum of the synthesized sample with the standard XRD diffraction data to analyze the sample phase. X-ray Diffraction (XRD) data was collected with a Bruker D8 Advance diffractometer operated at 40 kV and 40 mA with Cu Kα (λ = 1.5406 Å) in the range of 10-80° with a scan rate of 3 ^{o}/min. X-ray photoelectron spectroscopy (XPS) was collected in Kratos AXIS Ultra DLD system to analyze the element valence state.

Raman spectroscopy measurements were carried using a Jobin Yvon Lab RAM HR800 instrument with a 632.8 nm He−Ne laser and the alpha300 RA Correlative Raman-AFM Microscope with a 532 nm He−Ne laser. FT-IR spectrum of the catalysts were conducted using a Perkin-Elmer Spectrum GX FT-IR/Raman spectrometer at a spectral resolution of 4 cm^{-1}, with an average of 10 scans utilized in the recording of spectra. Elemental loadings of Metal, C, N, O, and H were investigated by elemental analysis (Elementar, vario MICRO cube) at 950 ^{o}C. For a comprehensive component analysis, the loading of the metal was also investigated by Thermogravimetric Analysis (TGA). To specifically determine the mass content of metal, the inductively coupled plasma atomic emission spectroscopy (TJA RADIAL IRIS 1000, ICP-AES) was used. Nitrogen absorption and desorption experiment was conducted on an ASAP 2020 (Micromeritics) to analyze the specific surface area and pores size distribution.

Near edge x-ray absorption structure (NEXAFS) spectroscopy measurements were performed at the Soft X-Ray beamline of the Australian Synchrotron. All spectra were done in partial electron yield (TEY) mode. All NEXAFS spectra were processed and normalized through the QANT software program at the Australian Synchrotron. X-ray absorption spectroscopy (XAS) measurements were collected at the XAS Beamline (12ID) at the Australian Synchrotron in Melbourne. With the beamline optics employed (Si-coated collimating mirror and Rh-coated focusing mirror) the harmonic content of the incident X-ray beam was negligible. The powder samples were pressed into pellets following mechanical grinding with a cellulose binder. Both

fluorescence and transmission spectra were collected based on the concentration of vanadium and cobalt in each sample. As for the XAS measurements, the samples were fabricated as pellets through pressing samples that were mechanically ground in a mortar/pestle to get one uniform mixture. The validity of this approach was confirmed by comparing the fluorescence and transmission spectra of one sample in which both methods yielded a comparable signal-to-noise data.

3.3 Electrochemical performance tests

The electrochemical measurements including carbon dioxide reduction, oxygen reduction reaction and oxygen evolution were conducted in one three-electrode cell with a Luggin capillary, using a Gamery Reference 3000 Potentiostat. As for the Lithium sulfur batteries test, 2025-type coin cells were assembled inside one Ar-filled glove box to keep oxygen out. A LAND galvanostatic charge–discharge instrument was used to perform electrochemical measurements. Electrochemical impedance spectroscopy measurements were conducted with a Solartron Impedance Analyzer (Solartron 1260A) in the frequency range from 1MHz to 0.1Hz with one AC voltage amplitude of 5 mV at the open-circuit potential. For the parameter details, it can be seen in the specific chapter.

Chapter 4 One-pot Pyrolysis Method to Fabricate Carbon Nanotube Supported Ni Single Atom Catalysts with Ultrahigh Loading

Abstract

The practical application of single atom catalysts (SACs) is constrained by the low achievable loading of single metal atoms. Here, nickel SACs stabilized on a nitrogen-doped carbon nanotube structure (NiSA-N-CNT) with ultrahigh Ni atomic loading up to 20.3 wt% have been successfully synthesized using a new one-pot pyrolysis method employing Ni acetylacetonate ($Ni(acac)_2$) and dicyandiamide (DCD) as precursors. The yield and formation of NiSA-N-CNT depends strongly on the $Ni(acac)_2$/DCD ratio and annealing temperature. Pyrolysis at 350 and 650 ºC led to the formation of Ni single atom dispersed melem and graphitic carbon nitride (Ni-melem and Ni-*g*-C_3N_4). Transition from a stacked and layered Ni-*g*-C_3N_4 structure to a bamboo-shaped tubular NiSA-N-CNT structure most likely occurs via a solid-to-solid curling or rolling-up mechanism, thermally activated at temperatures of 700-900 ºC. Extended X-ray absorption fine structure (EXAFS) experiments and simulations show that Ni single atoms are stabilized in the N-CNT structure through nitrogen coordination, forming a structure with four nearest N coordination shell surrounded by two carbon shells, Ni-N_4. The NiSA-N-CNT catalysts show an excellent activity and selectivity for the electrochemical reduction of CO_2, achieving a turnover frequency (TOF) of 11.7 s^{-1} at -0.55 V (*vs*. RHE), but a low activity for the O_2 reduction and O_2 evolution reactions, as compared to Ni nanoparticles supported on N-CNTs.

4.1 Introduction

The supported single atom catalysts (SACs) contain isolated atoms dispersed on and/or coordinated with the surface atoms of an appropriate support[1, 2]. Characterized by high catalytic activity, selectivity and high atomic efficiency, SACs have been attracting increasing attention in recent years[3][4] . Because the single atoms are highly active and tend to form aggregates to reduce the Gibbs free energy, the atomic loading of SACs is generally very low, less than 3 wt%[3, 5-8] .

Various techniques have been employed and developed to synthesize SACs. Atomic layer

deposition (ALD) has been adapted to fabricate SACs through controlling the ALD cycle number to deposit the targeted metal on the support[7, 9, 10] . Sun et al. [7] synthesized a Pt single atom catalyst supported on graphene using ALD method and the Pt single atoms showed significantly improved activity for methanol oxidation reaction as compared to that of commercial Pt/C catalysts. The Pt single atoms are stabilized on the graphene support through the oxygen or nitrogen ligands, making it difficult to increase the Pt loading due to the high tendency of aggregation. Metal-organic frameworks (MOFs), compounds consisting of metal ions or clusters coordinated to organic ligands to form one-, two-, or three-dimensional structures, have been used as templates for the single atom synthesis. Li et al. synthesized Ni SACs for the electrochemical reduction of CO_2 through annealing MOFs-Ni precursor and reported a turnover frequency of 5273/h with a Faradaic efficiency for CO production of 71.9%, achieving a current density of 10.48 mA cm^{-2} at an overpotential of 0.89 V[11]. The Ni loading anchored within MOFs by ionic exchange was 1.53 wt%.

Chemical wet techniques such as impregnation, deposition-precipitation and co-precipitation method have been used to directly immobilize metallic ions onto the surface of metal oxide or nitride (e.g., FeO_x[3], Al_2O_3[2, 12], ZnO[13] , CuO[14] , TiO_2[15], TiN[16].) via the surface charging effects. This method highly depends on the distribution and number of defects such as oxygen or nitrogen vacancies to anchor single atoms. To avoid the agglomeration, highly diluted metal salt solution is generally used. Zhang et al.[4] synthesized Pt SACs anchored on the surface defects of iron oxide nanocrystals by co-precipitation method and reported high atomic efficiency, good stability and activity for CO oxidation reaction. However, when the loading of Pt atoms increased from 0.17 wt% to 2.5 wt%, significant agglomeration and cluster formation were observed. The low loading of single Pt atoms is due to the limited oxygen vacancies on the surface of FeO_x nanocrystals. Carbon-based materials have been explored as effective supports for the synthesis of SACs due to the high surface area and abundant defects to trap single atoms, including porous carbon[10], CNTs[17, 18], graphene[19-22], graphitic carbon nitride (g-C_3N_4) [17, 23-25], and carbon nanofiber.[26] Qiao et al.[17] designed a class of g-C_3N_4 coordinated transition metals (Fe, Co, Ni) supported on the surface of CNTs and observed good performance of Co-C_3N_4/CNT with Co loading ~1 wt% for the oxygen reduction reaction (ORR) and oxygen evolution reaction (OER) in alkaline media, comparable with Pt(111) surfaces. The single atom loading on carbon materials is low due to the limited defects on the outmost surface of carbon to stabilize the single

atoms. Thus, in general, the fundamental reason for the very low loading of SACs synthesized by the substrate support or the template-based synthesis methods is the limited number of defects or trapping sites for SACs, as shown in Table 1. Despite the significant advantage and benefit of SAC in terms of high activity and selectivity, the practical application of SACs is hindered by the very low atomic loading.

Thus, in general, the fundamental reason for the very low loading of SACs synthesized by the substrate support or the template-based synthesis methods is that they possess a limited number of defects or trapping sites for SACs, as shown in Table 4.1.

Table 4.1 List of selected synthesis methods for single atom catalysts reported in the literature.

SACs	**Synhtesis method**	**Loading**	**Application**	**Ref**
Pt	Co-precipitation on FeO_x support	0.17wt%	CO oxidation	[4]
Ir	Co-precipitation on FeO_x support	0.01wt%	Water gas shift reaction	[3]
Pt	ALD on graphene support	<1.52wt%	Methanol oxidation	[7]
Co	Pyrolysis on graphene support	0.57 at%	Hydrogen generation	[22]
Pd	Impregnation on g-C_3N_4 support	0.5 wt%	Hydrogenations	[24]
Pd	ALD on graphene support	0.25wt%	Hydrogenation of 1,3-butadiene	[21]
Pt	Impregnation on TiN nanoparticles support	0.35 wt %	Oxygen reduction, formic acid oxidation, and methanol oxidation	[16]
Pd	Impregnation on N-doped carbon nanofibers	1 wt %	Hydrogen production from formic acid decomposition	[26]

Pt	Impregnation on *g*-C_3N_4 support	0.16 wt%	Photocatalytic H_2 Evolution	[25]
Pt	Impregnation on phosphomolybdic acid-modified active carbon	1 wt %	Hydrogenation of nitrobenzene and cyclohexanone	[10]
Ni	Metal-organic frameworks	1.53wt%	CO_2 oxidation	[11]
Pt	Impregnation on *g*-C_3N_4 support	0.5 wt%	Semihydrogenation of 1-hexyne	[27]
Co	Template approach on C_3N_4/CNT	<1wt%	Oxygen reduction and oxygen evolution reaction	[17]
Ni	One pot pyrolysis	20.3 wt%	CO_2 reduction	[28]

This work presents a detailed study of the mechanism of formation of Ni SACs on nitrogen-doped CNT structure. XANES simulations and EXAFS fitting indicate that Ni single atoms are confined within the carbon lattice in the form of Ni-N_4, which contributes to the very high Ni single atom loading of 20.3 wt%. A new rolling-up mechanism is proposed to explain the transition from Ni single atoms dispersed *g*-C_3N_4 layered structures to tubular structured Ni SACs, NiSA-N-CNT at annealing temperatures of 700-900 ºC.

4.2. Experimental section

4.2.1 Materials and synthesis

Nickel(II) acetylacetonate ($Ni(acac)_2$, Sigma Aldrich), dicyandiamide ($C_2H_4N_4$, DCD, Sigma Aldrich), nickel phthalocyanine (NiPc, SigmaAldrich), Ni foil (SigmaAldrich), $Ni(OH)_2$ (Sigma Aldrich), NiO (Sigma Aldrich), Pt/C (20 wt%, from Sigma-Aldrich) were purchased and used without further treatment. DCD with 66.67 wt% nitrogen and 28.6 wt% carbon was used as the nitrogen and carbon sources and was also the dispersant agent for the $Ni(acac)_2$. $Ni(acac)_2$ is a coordination complex and can be dispersed atomically in DCD due to weak Van der Waals' force.

$Ni(acac)_2$ and DCD with different ratios from 1:50 to 1:800 were prepared, stirred for 10 h and dried for 24 h followed by uniformly grinding. Subsequently, the mixture was heated at 350 ^oC for 3 h and then at 650 ^oC for 3 h under Ar with a flow rate of 50 mL min^{-1}. The as-prepared powder was subsequently annealed in a selected temperature in the range of 700-900 ^oC. The final samples were denoted as NiSA-N-CNT-T (T=700, 800 and 900 ^oC). Figure 4.1 shows the procedure of one-pot pyrolysis synthesis method.

In order to study the formation mechanism, the intermediate products of the mixture with $Ni(acac)_2$:DCD ratio of 1:200 and treated at 350 ^oC and 650 ^oC under Ar, denoted as $Ni(acac)_2$-DCD-350^oC and $Ni(acac)_2$-DCD-650^oC, respectively, were obtained and examined. For the purpose of comparison, nitrogen-doped CNTs (N-CNTs), Ni nanoparticles (NPs) supported on N-CNTs (Ni-N-CNTs) were prepared. In the case of N-CNTs, CNTs (30 mg, Nanostructured@Amorphous Materials, Inc., USA) was oxidized by treatment in a concentrated H_2SO_4 and HNO_3 solution with volume ratio of 3:1[29]. The treated CNTs were then placed into a tubular furnace and heated to 800 ^oC at a heating rate of 5 ^oC min^{-1} and maintained for 1 h under NH_3 (10 vol % NH_3 in He) at a flow rate of 100 mL min^{-1}[30]. For Ni-CNTs and Ni-N-CNTs, treated CNTs or N-CNTs (30 mg) were dispersed in ethanol glycol and with addition of 23 mg $Ni(acac)_2$, then the dispersion was stirred at room temperature for 3 h before being placed in the microwave oven and heated for 3 min. The dispersion was then filtered and dried at 71 ^oC. The as-prepared solid was placed in a furnace and heated to 400 ^oC at a heating rate of 5 ^oC min^{-1} for 1 h under H_2 flow (50 mL min^{-1}) to reduce NiO_x NPs to Ni.

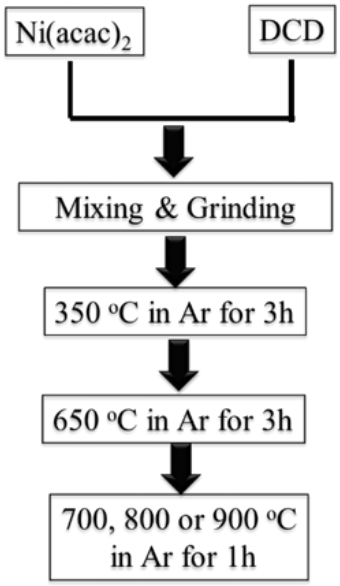

Figure 4.1 Synthesis steps of NiSA-N-CNT electrocatalysts via a one-pot pyrolysis method.

4.2.2 Microstructure and phase characterization

The mass change during the one-pot pyrolysis process was monitored by thermogravimetric analysis (TGA, Q5000, TA Instruments). $Ni(acac)_2$:DCD mixture with weight ratio of 1:200 was put into an alumina crucible and heated to 350 °C for 3 h in N_2 with the temperature ramped up to 650 °C and held at this temperature for 3 h in a N_2 flow at a rate of 20 mL min^{-1}. The yellowish powder was subsequently heated to 800 °C for 1 h in a N_2 atmosphere to obtain the final product. Microstructural and morphological features of as-synthesized powder samples were observed using scanning electron microscopy (SEM, Zeiss Neon 40EsB) and high-resolution transmission electron microscopy (HRTEM, FEI Titan G2 80-200 TEM/STEM). High angle annular dark field scanning transmission electron microscopy (HAADF-STEM) together with imaging and elemental mapping were carried out using a ChemiSTEM Technology instrument operating at 200 kV. The elemental mapping was obtained by energy dispersive X-ray spectroscopy using the Super-X detector on the Titan with a probe size ~1 nm and a probe current of ~0.4 nA. The powdered sample was dispersed using an ethanol solution onto TEM sample grids. High resolution aberration-corrected scanning transmission electron microscopy annular dark field images (AC-STEM-ADF) and annular bright field images (AC-STEM-ABF) were collected using a Nion

UltraSTEM100 microscope operating at an acceleration voltage of 60 kV and a beam current of 60 pA. The recorded images were filtered using a Gaussian function (full width half maximum = 0.12 nm) to remove the high frequency noise. The convergence half angle of the electron beam was set to 30 mrad and the inner collection half angle of the ADF images was 51 mrad. The samples were baked at 160 ^{o}C overnight before examination by STEM. X-ray Diffraction (XRD) data was collected with a Bruker D8 Advance diffractometer operated at 40 kV and 40 mA with Cu Kα (λ = 1.5406 Å) in the range of 10-80°. The loading of the metal was also investigated by TGA.

Elemental loadings of Ni, C, N, O, and H were probed by elemental analysis (Elementar, vario MICRO cube) at 950 ^{o}C. Raman spectroscopy measurements were performed using a Jobin Yvon Lab RAM HR800 instrument with a 632.8 nm He−Ne laser. FT-IR spectra of the catalysts were measured using a Perkin-Elmer Spectrum GX FT-IR/Raman spectrometer at a spectral resolution of 4 cm^{-1}, with an average of 10 scans utilized in the recording of spectra.

X-ray absorption spectroscopy (XAS) measurements were performed at the wiggler XAS Beamline (12ID) at the Australian Synchrotron in Melbourne, Australia using a set of liquid nitrogen cooled Si(111) monochromator crystals. With the associated beamline optics (Si-coated collimating mirror and Rh-coated focussing mirror), the harmonic content of the incident X-ray beam was negligible. XAS measurements were performed at the Ni K-edge (8.3 keV) at < 10 K to minimize thermal disorder and to ensure that the samples were not subjected to radiation damage as confirmed via quick scans of the absorption edge for 2 h comprising 12 repetitive scans. Note that a single XAS scan took ~1 hour. With the XAS measurements, the samples were prepared as pellets after pressing samples that were mechanically ground in a mortar/pestle using a cellulose binder. The measurement of fluorescence and transmission spectra were dependent on the concentration of Ni in each sample. The validity of this approach was confirmed by comparing the fluorescence and transmission spectra of one sample in which both methods yielded a comparable signal-to-noise data.

Data processing and analysis were performed following standard methods.[31] The extended X-ray absorption fine structure (EXAFS) data was isolated using the Athena software.[32] The normalised EXAFS was then Fourier transformed over a photoelectron momentum (*k*) range of 2.0-12.5 $Å^{-1}$. The coordination shell(s) to be analysed were isolated by inverse transforming over a non-phase-corrected radial distance (R) range of 0.7-2.7Å. Structural parameters were

determined by nonlinear least squares fitting using IFEFFIT,[33] with phases and backscattering amplitudes calculated *ab initio* with the FEFF8.1 code[34]. The amplitude reduction factor (S_0^2) was determined from a bulk metallic Ni standard and held constant for the analysis of the samples.

X-ray absorption near edge structure spectroscopy (XANES) measurements below photon energies of 2,500 eV were conducted at the Soft X-Ray beamline of the Australian Synchrotron[35]. These measurements were carried out at room temperature under ultra-high vacuum (UHV) conditions with a base pressure of 5 x 10^{-10} mbar or better. All spectra were obtained in total electron yield (TEY) mode. The XANES spectra were recorded at the Ni L-edge (850-875 eV), C K-edges (280-320 eV) and N K-edges (395-420 eV). All XANES spectra were processed and normalized using the QANT software program developed at the Australian Synchrotron[36]. X-ray energy calibrations were achieved by applying the offset required to shift the simultaneously measured reference spectra of nickel foil and boronnitride powder to its known energy. Intensities have been normalized with respect to impinging photon flux. Standard chemicals including nickel phthalocyanine (NiPc, Sigma Aldrich), NiO (99.8%, Sigma Aldrich) and $Ni(OH)_2$ (99.8% Sigma Aldrich) were used as reference materials.

4.2.3. Simulation of XANES

The structures containing different Ni-N configurations were first relaxed using projected augmented wave method (PAW) [37, 38], as implemented in Vienna ab-initio simulation package (VASP) [39, 40]. For the structural relaxation and electronic structure calculations generalized gradient approximation (GGA) method was used with Perdew-Burke-Ernzerhof (PBE) exchange-correlation function[41]. The electron wave function was expanded in a plane-wave basis set with an energy cutoff of 520 eV. The molecule structure was placed in a cube box with dimension of 20 Å. A single K point at (0,0,0) was chosen. The convergence criteria for structural optimization and energy on each atom were set to 0.01 eV/Å and 10^{-4} eV. X-ray near edge spectra were then simulated using the FDMNES package. Ni K edge spectra were simulated through multiple scattering on a muffin-tin potential with a cluster radius of 4 Å.

4.2.4 Electrochemical characterization

Electrocatalytic activity of the as-synthesized catalysts was evaluated via the electrochemical CO_2 reduction reaction (CO2RR) in N_2 and CO_2 saturated 0.5 M $KHCO_3$ solution using linear scan

voltammetry (LSV). The electrochemical cell comprised the electrocatalyst as the working electrode, a saturated calomel electrode (SCE) as the reference electrode, and Pt as the counter electrode. The electrolyte was purged initially by N_2 for 5 min and subsequently by CO_2 for 15 min before the conduct of the CO2RR experiments. A catalyst loading of 0.2 mg cm^{-2} was used in the LSV experiments. The electrodes used in the CO_2 electrolysis experiments were prepared by casting a slurry of the catalyst in an ethanol-Nafion solution (6 mg mL catalysts, 1% Nafion) onto carbon paper (1 cm^{-2}) at a catalyst loading of 1 mg cm^{-2}. The CO2RR was conducted in a gas-tight electrochemical cell at different applied potentials over a period of 2 h at each potential. The outlet gas was collected using a gas bag for analysis by double channel gas chromatography (Shimadzu 2014) analysis. The amount of CO was calibrated using standard gas (BOC) at CO concentration of 0.059%, 0.0738%, 0.0983%, 0.1475% and 0.295%, and the H_2 was calibrated using standard gas (BOC) at H_2 concentration of 0.0534%, 0.06675%, 0.089%, 0.1335% and 0.267%. The chromatographic peak areas were determined using the EZChrom SI software. The collected solutions after CO_2 electrolysis (0.200 g) were mixed with 0.100 g of 2 M HCl, so as to eliminate the $KHCO_3$ and convert the possible existing format to formic acid. The formic acid content was determined using tetrahydrofuran as the solvent and methanol was analysed using the dimethylformamide as the solvent, using gas chromatography-mass spectrometry (Agilent GC-MS, 6890 series GC with a 5973 MS detector). The rate of product yield was based on the average rate over the 2 h electrolysis period. The Faradaic efficiency (FE) of CO production and turn over frequency (TOF, mol CO mol^{-1} Ni h^{-1}) were deduced from the cyclic voltammetry (CV) curves using the transition of Ni^{2+} to Ni^{3+}. The electrochemical activity of NiSA-N-CNT catalysts for oxygen reduction and evolution reactions (ORR and OER) was also measured in 0.1 M KOH solution using LSV with a catalyst loading of 0.2 mg cm^{-2}.

4.3. Results and discussion

4.4.1 Effect of precursor ratios and annealing temperatures

Figure 4.2 shows the optical and TEM images of as-synthesized powder samples as function of $Ni(acac)_2$:DCD ratios that have been annealed at 800 °C. The yield of final products of precursors with $Ni(acac)_2$:DCD ratios of 1:50, 1:100, 1:200, 1:400 and 1:800 was 35, 18, 11, 4 and 1.5 mg, respectively (see Figure4.2A). This indicates that the yield of the powder depends strongly on the

Ni content in the $Ni(acac)_2$ and DCD mixture. The morphology of the products also varies significantly with the $Ni(acac)_2$:DCD ratio (Figure 4.2B). For samples synthesized with a $Ni(acac)_2$:DCD ratio of 1:50, a large proportion of NPs were observed with particle sizes in the range of 2 to 150 nm. As the $Ni(acac)_2$:DCD ratio increased to 1:200, the number of NPs decreased significantly, coinciding with a clear formation of CNTs. However, with a further increase in the ratio to 1:400 and 1:800, there is a resurgence in the proportion of NPs. However, with the increase of DCD, Ni content was reduced in the precursor. During the annealing process, more ammonia would be produced, which could etch the carbon or CNTs (DCD contains more N as compared to C). This could result in the instability of the Ni single atoms, leading to the aggregation and formation of Ni NPs. On the other hand, as Ni is a catalyst for CNT formation, the lower the $Ni(acac)_2$:DCD ratio would have a higher Ni content, thus produce a higher carbon yield (Figure 4.2A). Thus, there is an optimum ratio of $Ni(acac)_2$:DCD for the formation of CNT structures possessing a low number of NPs as shown in Figure 4.2B. The optimum ratio of the $Ni(acac)_2$:DCD precursors is around 1:200 under the conditions of this study.

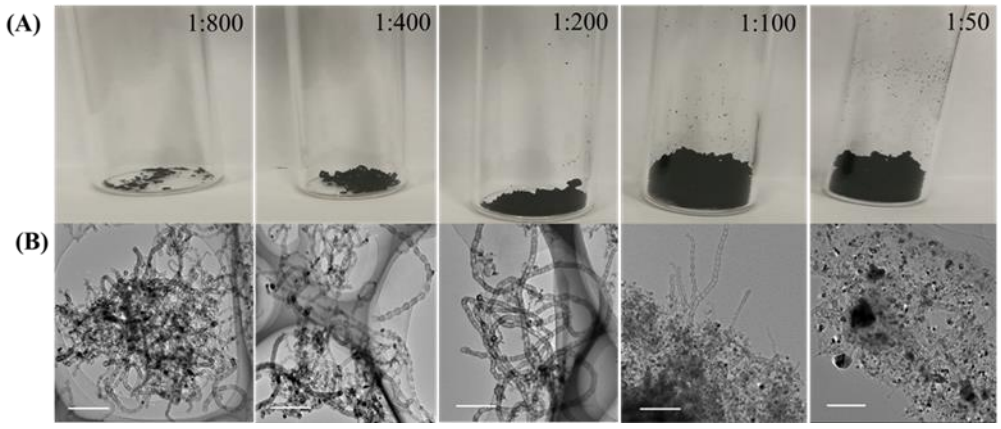

Figure 4.2 (A) Optical and (B) TEM micrographs showing the yield of catalyst produced after the pyrolysis of 2 g precursors with different $Ni(acac)_2$:DCD ratios. The final annealing temperature was 800°C. The scale bar in (B) is 200 nm.

Figure 4.3 presents TEM micrographs, XRD diffraction patterns and Raman spectra for catalysts synthesized using a $Ni(acac)_2$:DCD ratio of 1:200 following annealing at different temperatures. At an annealing temperature of 700°C, a CNT structure was prevalent with a preponderance of amorphous carbon (see Figure 4.3A). The corresponding XRD diffraction pattern shows a broad

and weak peak at ~26º, indicating a poor crystallinity of the catalyst (see Figure 4.3D). Similarly, Raman spectra (Figure 4.3E) also possess poorly resolved peaks. When the annealing temperature is increased to 800 ºC, the microstructure of the synthesized powder is characterized by well-formed CNTs with a substantially reduced amorphous content (see Figure 4.3B). The intensity of the XRD peak at ~26º also increases, indicating an enhancement in the crystallinity of carbon (Figure 4.3D) [45]. Similar CNT formation was also observed with catalysts annealed at 900 ºC (Figure 4.3C). Raman spectra for the samples annealed at 800 ºC and 900 ºC also revealed an intensity enhancement in the peak at 1580 cm^{-1}, which again confirms an increase in the degree of crystallinity. For catalysts annealed at 900 ºC, a weak peak at 44.8º was observed, can be attributed to the formation of Ni NPs[42]. However, compared to the XRD patterns observed on Ni-N-CNTs, the intensity of the XRD peak at 44.8º is very low, indicating that the majority of Ni in the catalyst samples does not exist as Ni NPs.

Based on this preliminary analysis, the best microstructure was obtained with samples comprising a $Ni(acac)_2$:DCD ratio of 1:200 at an annealing temperature of 800ºC. As such, the microstructure and phase analyses will be performed on catalyst samples annealed at 800 ºC, *i.e.*, NiSA-N-CNT-800.

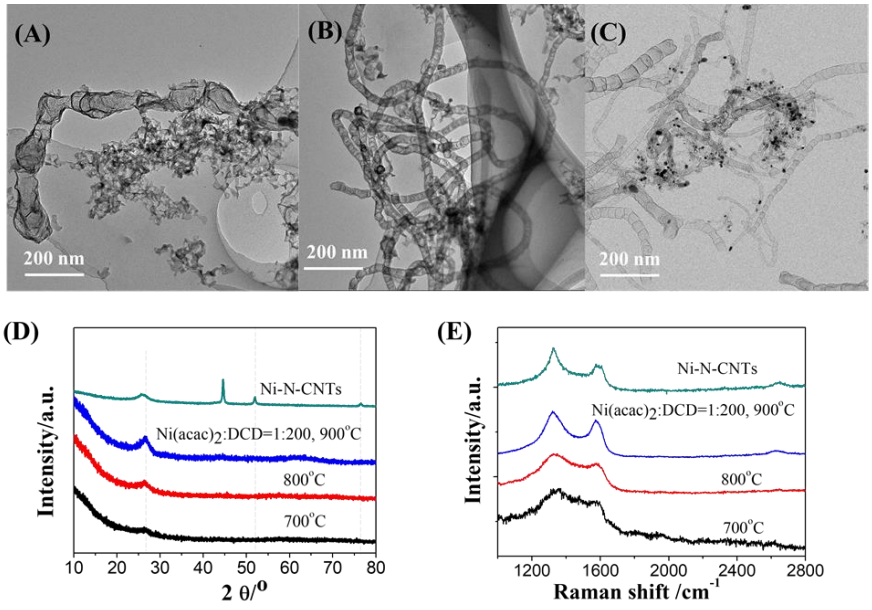

Figure 4.3 TEM micrographs of as-synthesized catalysts at different annealing temperatures of (A) 700 ºC, (B) 800 ºC and (C) 900 ºC, with the corresponding XRD patterns and Raman spectral data

presented in (D) and (E), respectively. The $Ni(acac)_2$:DCD ratio of the precursor was 1:200, with XRD and Raman curves of Ni-N-CNTs presented for comparison.

4.4.2 Characterization of NiSA-N-CNT-800

Figure 4.4 presents the structural characterization of NiSA-N-CNT-800 samples. Here, bamboo-like CNTs with lengths of up to 5 μm and average tubular diameters of 20-50 nm were observed, with no obvious NPs observed in this catalyst sample (see Figures 4.4A, B and C). Elemental mapping of a typical tubal structure revealed a uniform distribution of N and Ni across the tubes (see Figure 4.4D). Bamboo-like CNTs are multi-walled, possessing an average of ~11 layers (Figure 4.4E). Here, the individual Ni atoms were incorporated within the carbon layers, but not confined between carbon layers (see Figure 4.4F). White dots represent Ni atoms distributed on CNTs with an average diameter of 0.15±0.01 nm, close to the diameter of Ni atom, which is 0.144 nm (see Figure 4.4F, G and H). There is a formation of defective non-C_6 carbon rings such as C_5 and C_7 with incorporation of nitrogen atoms (indicated by red dots in Figure4G, and characterized by electron energy loss spectroscopy, EELS).

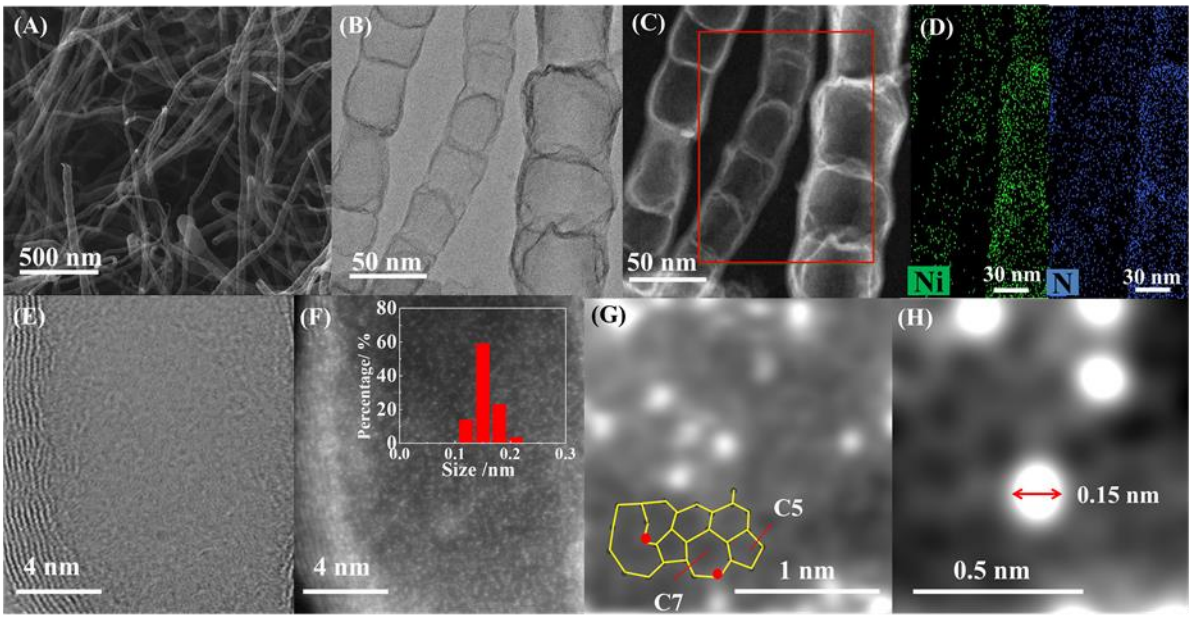

Figure 4.4 (A) SEM, (B) TEM, (C) STEM, (D) STEM-EDS mapping (Ni and N elements), (E) AC-STEM-ABF and (F) AC-STEM-ADF micrographs showing the atomic dispersion of Ni in NiSA-N-CNT-800. AC-STEM-ADF micrographs (G,H) show the non-C6 carbon environmental in NiSA-N-CNT, with the red and white dots depicting N and Ni atoms, respectively.

The chemical environment of nickel, nitrogen and carbon in NiSA-N-CNT-800 was investigated by NEXAFS spectroscopy and the results are shown in Figure 4.5. The typical sp2 carbon from the C 1s peak at 285.2 eV for pure CNTs and N-CNTs was not observed in the C K-edge NEXAFS spectra of NiSA-N-CNT-800 (see Figure 4.5A). Instead, the spectra shifted positively, forming a predominant peak at 286.9 eV. This indicates that majority of carbons in NiSA-N-CNT-800 may not be present as C=C. The N K-edge spectrum possesses a number of peaks in the range of 397 to 403 eV, which can be assigned to Ni-N (399.5 eV), pyridinic N (398.4 eV) and graphitic N (401.5 eV) (see Figure 4.5B). Analysis of the Ni L-edge NEXAFS spectra of NiSA-N-CNT-800 reveals that the Ni L_3 and L_2-edeges are located at 854.2 and 871.1 eV, similar to those of NiPc which possesses a Ni-N_4 center [43], as depicted in Figure5C. In the case of $Ni(OH)_2$ and Ni foil, the Ni L_3 and L_2-edeges are located at 853 eV and 871 eV as well as 852.5 eV and 869 eV, respectively, corresponding to Ni-O, Ni-Ni bond[20]. This demonstrates that Ni in NiSA-N-CNT-800 is most likely bonded to N. The Fourier transform of the extended X-ray absorption fine structure (EXAFS) Ni K-edge spectra shows that the NiSA-N-CNT-800 is similar with NiPc, but very different from the Ni metal (Figure 4.5D). Furthermore, the linear combination analysis (LCA) of NiSA-N-CNT-800 using NiPc, $Ni(OH)_2$ and Ni foil as standards, indicates that the material has similar bonding characteristics to a material consisting of 88±2% Ni-N, 5.8±0.7% $Ni(OH)_2$ and 6.3±1.8% Ni^0 [44, 45]. The high nitrogen content of NiSA-N-CNT-800 also favored the formation of defective non-C_6 rings including C_5 and C_7, consistent with the AC-STEM-ADF analysis (see Figure 4.4G).

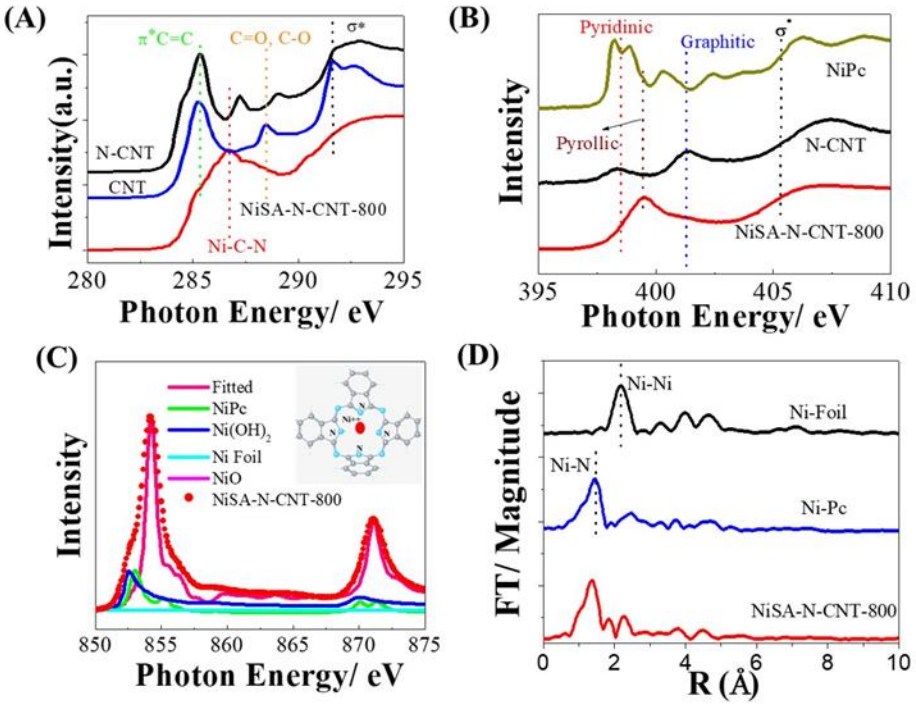

Figure 4.5 Chemical environment of NiSA-N-CNT as probed by X-ray absorption spectroscopy (XAS). (A) C K-edge. (B) N K-edge. (C) Linear combination analysis of the Ni L-edge spectra fitted using standards of NiPc, $Ni(OH)_2$, NiO and Ni foil, with the embedded structure representing the molecular model for NiPc. (D) Fourier transforms of the EXAFS spectra for Ni foil, NiPc, and NiSA-N-CNT-800.

Figures 4.6A-E present a comparison of experimental and simulated X-ray absorption near edge spectroscopy (XANES) spectra of the inserted Ni-core structures with varying Ni-N-C configurations associated with a possible molecular structure model. The structural parameters are carried out by nonlinear least squares fitting using IFEFFIT. The molecular structures were relaxed to the lowest energy configuration using DFT simulations. The molecular structures were relaxed to the lowest energy configuration using density functional theory simulations. The *x* values of 1, 2, 3 and 4 for Ni-N_x complex embedded in perfect graphene layer were tested. Ni-N_4 was found to be the best configuration. To get better agreement between experimental spectra, different configurations were conceived for Ni-N_4 complex. Those configurations lead to pronounced different at the pre-edge. Perfect C_6 rings surrounding the Ni-N complex (Figs. 4.6A,B) do not agree with experimental results. The Ni-N_4 structures with defective non-C_6 carbon rings were

found to have better resemblance with experimental results. Two typical configurations (Fig. 4.6C,D) show similarities to the experimental XANES spectra. It should be noted that the experimental spectrum is the average signal of different possible configurations. The high nitrogen content in the NiSA-N-CNTs also favors the formation of defective non-C_6 rings, which are further confirmed by atomic resolution STEM images. Here, Ni-N_4 was found to be the best Ni-N_x complex associated with a perfect graphene layer configuration. To achieve a closer convergence between the experimental and fitted data, a variety of configurations were conceived for the Ni-N_4 complex, which led to pronounced differences at the pre-edge of Ni. The most suitable fitting result for the EXAFS data was obtained for a structure with four nearest N neighbors in a coordination shell followed by two carbon shells (1^{st} carbon shell in red, 2^{nd} carbon shell in green, as shown in Figure 4.6E). This structural model simulates satisfactorily the EXAFS data despite the presence of different defect structures in the carbon rings (see Figure 4.4G).

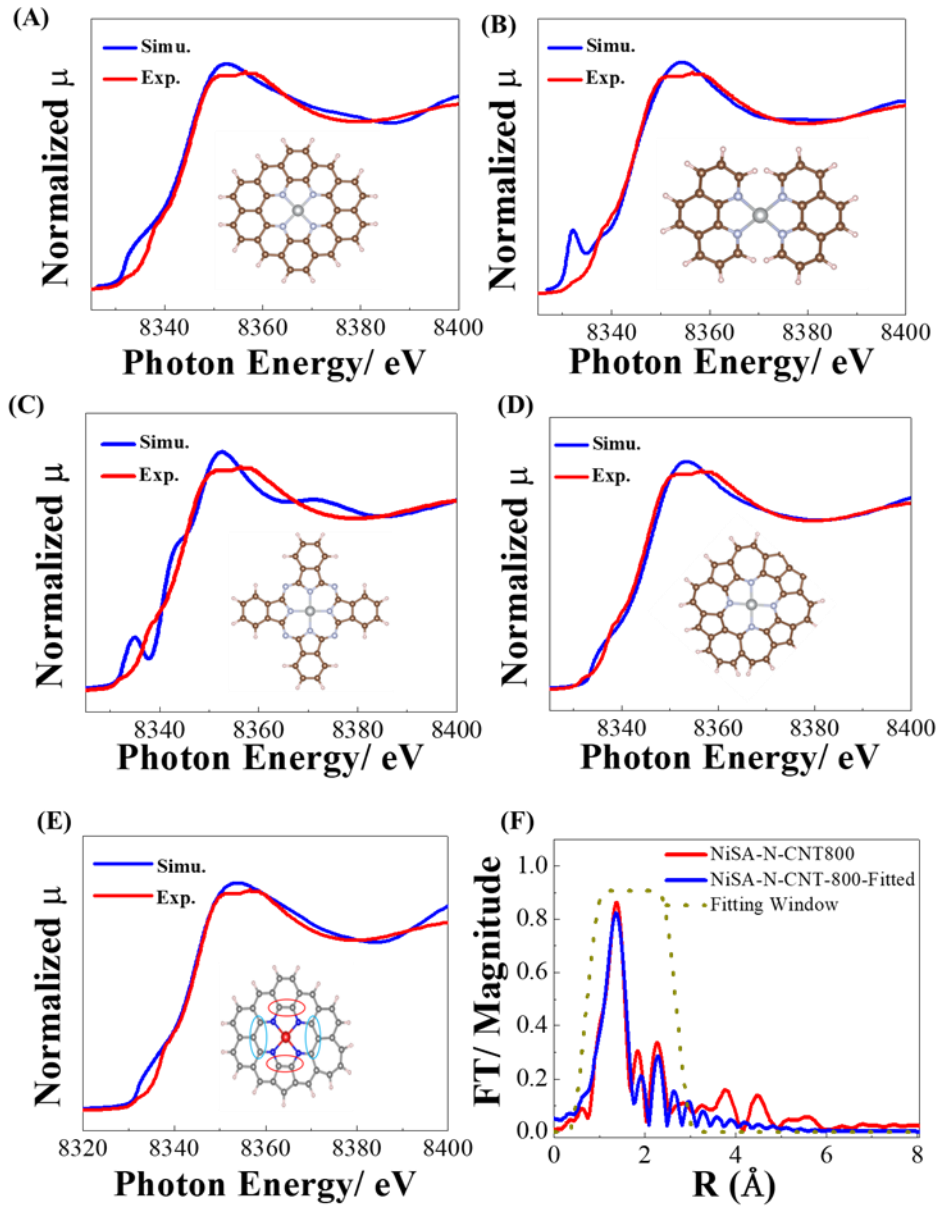

Figure 4.6 (A-E) Comparison of a simulated XANES spectra of the inserted Ni-core structures with experimental results, and (F) fitted Fourier transforms of the EXAFS spectra with NiSA-N-CNT-800.

The loading of Ni single atoms was calculated using TGA and XANES data. Here, the NiSA-N-CNT-800 material begins to decompose at 381 ^{o}C in air (Figure 4.7), while the decomposition of multiwalled CNTs (MWCNTs) starts at 422 ^{o}C. The NiSA-N-CNT-800 material is fully decomposed at around 480 ^{o}C, significantly lower than that of 640 ^{o}C for MWCNTs. This may be

attributed to a highly efficient self-catalysis of thermal decomposition resulting from the nickel single atoms.

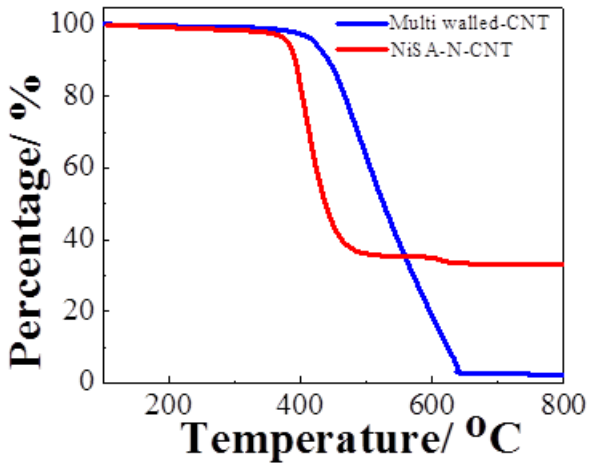

Figure 4.7 The thermogravimetric analysis of NiSA-N-CNT as compared with pure carbon nanotubes.

The final decomposition product of NiSA-N-CNT-800 in air is NiO, which accounts for 29.4% of the total mass from TGA, validating that the Ni species in the sample is 24.1%. The LCA of the Ni L-edge XANES spectra (see Figure 4.5C) shows that 87.9% of the Ni signals coincide with a Ni-N chemical environment. Based on the aforementioned analyses, the total content of Ni single atom in NiSA-N-CNT-800 was found to be 20.3%.

Thus, Ni-N-C bonding and confinement effects within the carbon nanotubes are responsible for the high Ni single atom loading in the present study. While at a temperature of 700 ^{o}C, amorphous carbons mixed with CNTs were formed. With an increase in temperature from 800 ^{o}C to 900 ^{o}C, there is a significant loss in nitrogen from 18.7 wt% to 11.3 wt%(Table 4.1).

Sample	C/wt% EA	N/wt% EA	Ni (wt%) EA	Ni (wt%) TGA	*O(wt%) EA	H(wt%) EA
NiSA-N-CNT ($Ni(acac)_2$:DCD=1:50,800°C)	43.2±4.3	11.3±4	42±3.5	41±1.2	2.4±0.5	1.1±0.2
NiSA-N-CNT ($Ni(acac)_2$:DCD=1:100,800°C)	50.3±3.9	16.3±3.7	30.8±3.6	33±2.3	1.8±0.6	0.8±0.2
NiSA-N-CNT ($Ni(acac)_2$:DCD=1:200,800°C)	56.5±5.1	18.7±3.8	22.7±3.5	23±4	1.6±0.9	0.5±0.2
NiSA-N-CNT ($Ni(acac)_2$:DCD=1:400,800°C)	53.2±5.2	14.7±3.1	29.2±3.6	31.2±3	3.6±0.9	0.7±0.2
NiSA-N-CNT ($Ni(acac)_2$:DCD=1:800,800°C)	51.2±4.9	11.7±2.2	33.3±3.5	33.5±4	3.1±0.5	0.7±0.3
NiSA-N-CNT ($Ni(acac)_2$:DCD=1:200,700°C)	59.3±3.8	17.3±3.6	21.1±3.6	23±2.1	1.5±0.5	0.8±0.2
NiSA-N-CNT ($Ni(acac)_2$:DCD=1:200,900°C)	52.3±3.9	11.3±3.7	33.8±3.6	35.2±2.5	1.7±0.6	0.9±0.2

Table 4.1 The nickel content is calculated based on the elemental analyser(EA) data by subtraction of the content of C, N, O and H. And the metal content also calculated by the TGA curve. *the O content could be affected by the metal elements existed in the sample.

4.3.3 Microstructure of intermediate products, $Ni(acac)_2$-DCD-350 and $Ni(acac)_2$-DCD-650

Figure 4.8A presents the TGA decomposition and carbonization results for the precursor mixture with $Ni(acac)_2$: DCD=1:200. After the first heat treatment at 350°C for 3 h in Ar, the original white powder changed to yellow proceeding to dark yellow after a second heat treatment at 650 °C in Ar. Final annealing at 800°C led to the formation of a black powder. TGA analysis shows a dramatic weight loss of about 40 wt% at 350 °C and 75 wt% at 650 °C, while the final weight of the residual after annealing at 800°C for 1 h is 1.7 wt%.

In the case of $Ni(acac)_2$-DCD heat treated at 350°C, $Ni(acac)_2$-DCD-350, XRD peaks centered at 12.5, 14.6, 16.9, 18.4, 19.4, 19.8, 25.4, 26.1, 27.2, 28.7, 30.7 and 31.2° were observed, which is in good agreement with a melem structure (2,5,8-Triamino-tri-*s*-triazine, $C_6N_7(NH_2)_3$), as reported in the literature[46]. After the second heat treatment at 650 °C in Ar (i.e., $Ni(acac)_2$-DCD-650), two main XRD peaks at 13.0° and 27.4° were observed and ascribable to the (100) and (002) planes of graphitic carbon nitride, *g*-C_3N_4(shown as in Figure 4.8B)[47].This indicates that DCD was condensed into a melem phase at 350 °C, with further heating to 650 °C resulting in the formation of polymeric *g*-C_3N_4 via rearrangement of the melem units. The characteristic Ni XRD peaks at 44.8° and 51.7 ° were not observed in both of these intermediate samples. This suggests strongly that Ni is most probably present as single atoms dispersed within the melem and *g*-C_3N_4 structures.

The incorporation of Ni single atoms in melem and *g*-C_3N_4 intermediates, *i.e.*, Ni-melem and Ni-*g*-C_3N_4, was further confirmed by FTIR analysis (see Figure 4.8C). In the case of Ni(acac)$_2$-DCD-350, there are three characteristic bands at 801, 1443 and 1601 cm^{-1}, corresponding to the bending vibrations of C–N in the C_6N_7 ring of the melem structural units, which are similar to those for DCD heat-treated at 350°C[48]. This provides evidence for the incorporation of Ni single atoms into the melem structure. The presence of broad bands at 2600–3400 cm^{-1}, which are typical of N–H vibrational stretching modes with Ni(acac)$_2$-DCD-650 and DCD heat-treated at 650°C (DCD-650°C) are indicative of the retention of amino functional groups in Ni(acac)$_2$-DCD-650°C, which might provide bridges for Ni-N bonding, again suggesting Ni single atom incorporation in *g*-C_3N_4. Several strong bands in the 1200-1650 cm^{-1} region were found in Ni(acac)$_2$-DCD-650 and DCD-650°C, which are ascribable to the typical stretching modes of CNT heterocycles[49].

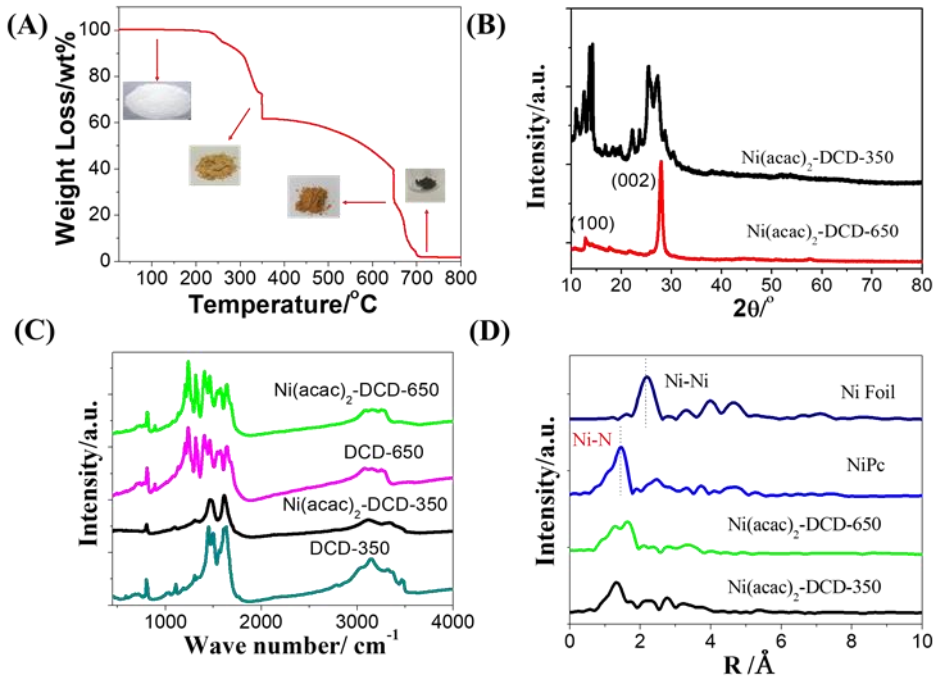

Figure 4.8 (A) TGA of annealing process in a nitrogen atmosphere of Ni(acac)$_2$:DCD at a weight ratio of 1:200, (B) XRD of the Ni(acac)$_2$:DCD mixture annealed at 350 °C and 650 °C, (C) FTIR of the Ni(acac)$_2$-DCD and DCD materials that had been heat-treated at 350°C and 650°C, and (D) Fourier transforms of the EXAFS spectra of Ni(acac)$_2$-DCD-350, Ni(acac)$_2$-DCD-650, NiPc and Ni foil.

EXAFS spectroscopy indicates that the Ni K-edge of Ni in Ni-melem and Ni-*g*-C_3N_4 is very close

to that of Ni in NiPc, but very different from Ni in Ni foil (see Figure 4.8D). This suggests that Ni is likely to be in the form of Ni(II) similar to Ni in NiPc rather than Ni in metallic Ni foil (*i.e.*, Ni-Ni). The EXAFS spectra reveal that the Ni in Ni(acac)$_2$-DCD-350 ^{o}C is coordinated with 4.8 O with a bond length of 1.88 Å, which is consistent with the Ni L-edge spectrum (Figure 4.5C). In the case of Ni-*g*-C_3N_4, the first shell shows a broad peak at 1.88 Å and a shoulder at 1.45 Å, which are indicative of a complex coordination environment that results from interaction of Ni in the voids of *g*-C_3N_4 that bonds to O and also coordinated with the pyridinic-N from the separate triazine units[43].

Figure 4.9 presents TEM micrographs for Ni(acac)$_2$-DCD-350 and Ni(acac)$_2$-DCD-650. In both cases, there was no evidence of Ni NPs (see Figures 4.9B and D). AC-ADF analysis shows a uniform distribution and high density of bright dots, represented of Ni single atoms in the melem and *g*-C_3N_4 structures. The uniform distribution of Ni single atoms is indicative of Ni single atoms within these structures, also showing that the incorporated Ni single atoms have induced a structural transformation from melem to *g*-C_3N_4.

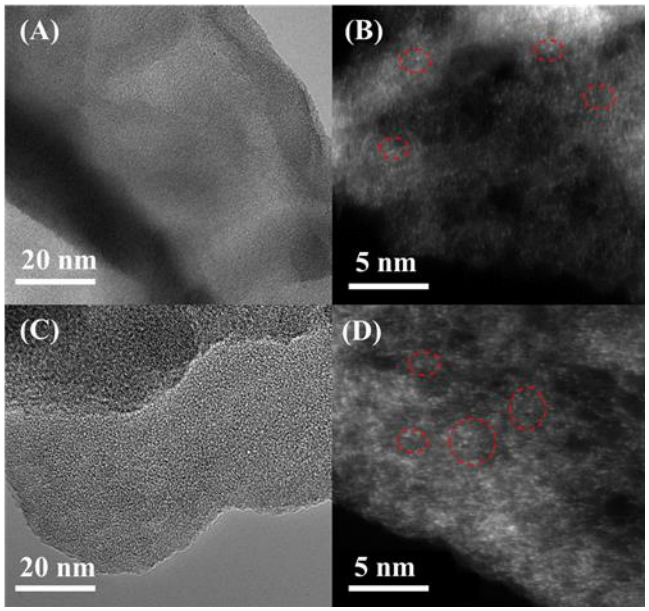

Figure 4.9 HRTEM and AC-STEM-ADF micrographs of (A,B) Ni(acac)$_2$:DCD-350 and (C,D) Ni(acac)$_2$:DCD-650. The presence of Ni single atoms is indicated by circles.

4.4.4. Formation mechanism of NiSA-N-CNT tubular structure

We have already shown that the formation of bamboo-shaped tubular structure supported Ni single atom catalysts, NiSA-N-CNT, occurs during the annealing of $Ni(acac)_2$-DCD-650 (i.e., Ni-*g*-C_3N_4 intermediates) at temperatures of 700-900 ºC. We also found that there was no residual carbon in DCD-650ºC that was heat treated at a temperature of 700 ºC for 1 h. This is consistent with a report by Cui et al.[50] showing that pure *g*-C_3N_4 decomposes into nitrogen and cyano fragments at temperatures above 650 ºC. The observation of the formation of CNTs from $Ni(acac)_2$-DCD-650 after annealing at temperatures of 700-900 ºC (Figures 4.2 and 4.3) effectively demonstrates that the presence of Ni single atoms enhances the thermal stability of the *g*-C_3N_4 structure. Accordingly, the carbonization and transformation of the Ni-*g*-C_3N_4 layered structures into a NiSA-N-CNT tubular structure are clearly due to the catalytic effects of Ni single atoms during annealing at high temperatures of 700-900 ºC. However, the mechanism of the formation of CNT stabilized Ni SAC is likely to be very different from conventional CNTs formation based on Ni NPs as the catalyst cap[51]. Although there is still considerable debate around the exact mechanism of CNT growth, the most generally-accepted mechanism may be outlined as follows: hydrocarbon decomposes into carbon and hydrogen species at the outer surface of metal nanoparticles at elevated temperatures; hydrogen is evolved; and carbon diffuses/dissolves into the metal[52, 53]. After achieving saturation of carbon in the metal, the dissolved carbon precipitates out and crystalizes in the form of a seamless graphitic cylinders having no dangling bonds and hence are energetically stable.

In the case of the transformation of Ni-*g*-C_3N_4 to NiSA-N-CNT, there is no hydrocarbon vapor phase, so the diffusion and dissolution carbon species was not possible under these conditions. The precursor for the CNT formation, *g*-C_3N_4, is a layered carbon nitride compound with a structure similar to graphite, which is composed of two tectonic units: *s*-triazine unites and tri-*s*-triazine units. As shown above, the presence of Ni single atoms increases the thermal stability of the *g*-C_3N_4 structure. During annealing at high temperatures of 700-900 ºC, Ni single atoms within the g-C_3N_4 structure are thermally activated, resulting in the accelerated mobility of Ni single atoms. The thermal movement of Ni single atoms is expected to create internal stresses, which can cause a curling of the layered Ni-*g*-C_3N_4, thereby forming a seamless graphitic cylindrical network. This rolling-up phenomenon will occur if the internal stresses are high enough, which in turn would depend on the density of Ni single atoms in the *g*-C_3N_4 material. This is also supported by the fact that the morphology of NiSA-N-CNT depends strongly on the content of Ni (i.e., $Ni(acac)_2$) rather

than the carbon and nitrogen contents of the source materials, i.e., DCD) (see Figures 4.2 and 4.3). Accordingly, the transformation of the stacked Ni-*g*-C_3N_4 layered configuration into the tubular NiSA-N-CNT structure takes place through a solid-to-solid rolling-up mechanism. The driving force behind this rolling or curling behavior is attributable to a minimization of the surface free energy. Figure 4.10 presents a scheme for the formation of Ni single atoms supported on a carbon nanotube structure via a one-step pyrolysis and rolling-up process from the layered Ni-*g*-C_3N_4 structures. The observed bamboo-shaped CNTs may be related to the fact that the NiSA-N-CNTs were rolled from the layered Ni-*g*-C_3N_4 structure, which has limited dimension and length. Thus conventional formation and continuous growth of CNTs based on Ni NPs as the catalyst cap would not be possible in the solid-to-solid rolling-up process. Nevertheless, more extensive studies are needed to understand the fundamentals of such rolling-up mechanisms.

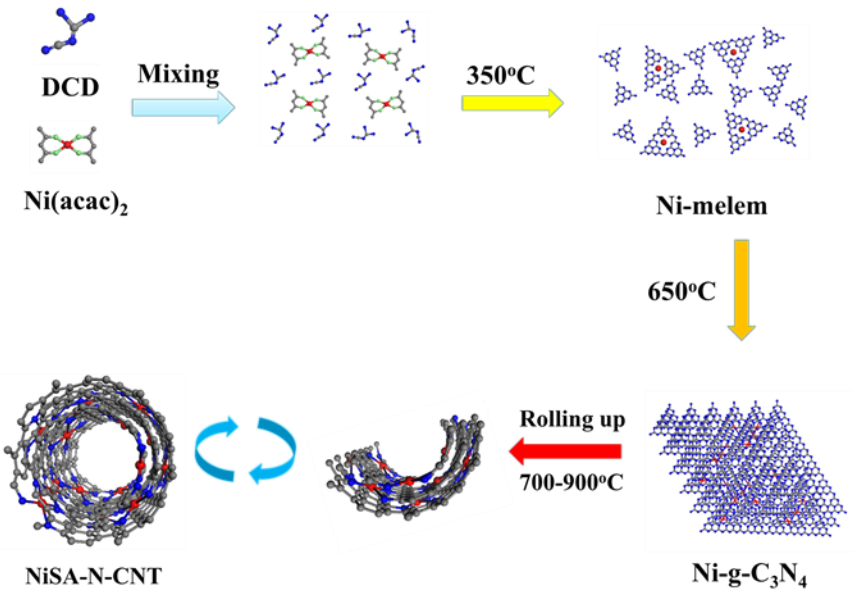

Figure 4.10 Scheme for the formation of tubular structured Ni single atom catalysts, NiSA-N-CNT. The red and blue dots are Ni and N atoms, respectively.

The mobility of CNT supported Ni single atoms was also investigated by *in situ* TEM measurements (see Figure 4.11). Here, the experiments were performed on NiSA-N-CNT at room temperature with continuous beam scanning. During these TEM observations, the Ni single atoms were shown to migrate out of the outer layer first, with the single Ni atoms from the inner layer hopping to the adjacent outer layer as a consequence of continuous thermal and electron beam irradiation. This implies that Ni single atoms are capable of jumping across the inner and outer

layers under thermal and electron radiation effects without agglomeration of the Ni single atoms. Furthermore, there is a clearly observable movement in Ni atoms from P1 to P1' (see Figure 4.11A and B); along with a previous vacancy at P2, a new atom appearing (P2' position, Figure 4.11B), and the disappearance of the Ni atom at P3 (see Figure 4.11A) and formation of a vacancy at P3' (Figure 4.11B) following thermal electron beam irradiation treatment. The structural change before and after heat treatment at 900 ^{o}C was also recorded. The structures of the cylindrical tubes were observed to change significantly after the 1 hour *in situ* treatment, which is indicative of electron beam irradiation damage. Compared with that before *in-situ* heat treatment at 900 ^{o}C, the number of bright dots, which reflect the presence of single Ni atoms, was dramatically reduced (cf., Figures 4.11C and 4.11D). This indicates that nitrogen atoms in the Ni-N-C tubular structure are removed due to the thermal and/or electron beam irradiation effects, resulting in the instability of the Ni-N-C complex structure. Here, Ni atoms without nitrogen coordination are expected to be released from the structure. This is confirmed by the reduced density of Ni single atoms as shown in Figure 4.11D. The *in situ* TEM results reveal the importance of nitrogen in the stabilization of Ni SACs in the NiSA-N-CNT structure. This also explains why, when the annealing temperature increased to 900 ^{o}C, there was a presence of Ni NPs with NiSA-N-CNT structures due to agglomeration of some of the Ni single atoms (see Figure 4.3). By contrast, at 700 ^{o}C, amorphous carbons were formed together with CNTs, as amorphous carbon is commonly obtained at low carbonization temperatures [52, 53].

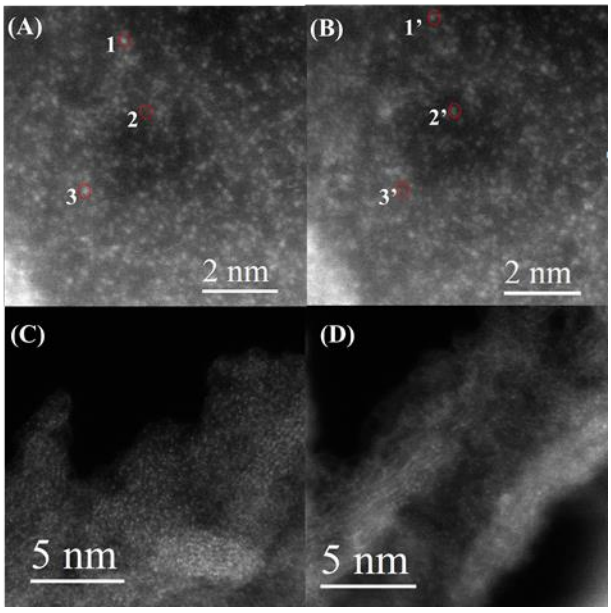

Figure 4.11 *In situ* AC-STEM-ADF micrographs of (A,B) revealing a dynamic movement of atoms during the recording images of NiSA-N-CNT-800 and (C,D) before and after *in situ* 900 ^{o}C treatment for 1h on NiSA-N-CNT-800.

4.4.5 Electrochemical activity

Figure 4.12 presents the electrocatalytic activity data for NiSA-N-CNT on the electrochemical reduction reaction of CO_2 (CO2RR), the oxygen reduction reaction (ORR) and the oxygen evolution reaction (OER). The NiSA-N-CNT shows a much higher activity in CO_2-saturated $KHCO_3$ solution with a low onset potential of -0.275 V vs RHE. Carbon monoxide was confirmed as the only detectable product from the CO2RR on NiSA-N-CNT catalysts, demonstrating a much higher activity and selectivity for the CO2RR, as compared to Ni NPs supported on N-CNT, Ni-N-CNTs (see Figure 4.12A). The CO2RR activity was gauged using the current density for CO production (j_{CO}), with j_{CO} showing a significant elevation in magnitude with increases in the cathodic potential with NiSA-N-CNT, as compared to a much smaller increase with Ni-N-CNT. For example, at -0.7 V (vs RHE), j_{CO} values of NiSA-N-CNT-700, NiSA-N-CNT-800 and NiSA-N-CNT-900 are 20.4, 24.5 and 20.2 mA cm^{-2}, respectively, which are approximately 3-to-4-fold higher than those with Ni-N-CNTs (see Figure 4.12A). The NiSA-N-CNT-800 shows a higher activity for the CO2RR, which is most ascribable to an increased crystallinity of the CNTs and the lower amount of amorphous carbons as compared to NiSA-N-CNT-700. In the case of NiSA-N-CNT-900, the increased number of Ni NPs is likely to be the root cause of a slight decrease in the catalytic activity. The activity of the NiSA-N-CNT-800 is significantly higher than that of noble-metal-free catalysts such as Zn dendrite[54] in a $KHCO_3$ electrolyte, and better and/or comparable to most noble-metal-based catalysts reported to date [55] .It is also comparable to or even higher than the latest reported results on Ni single atoms catalysts, such as the metal-organic frameworks derived Ni single atom catalysts (10.48 mA cm^{-2} at -1.0 V)[13] and Ni single atoms in a graphene shell (4 mA cm^{-2} at -0.81 V vs RHE, or a mass loading 0.2 mg cm^{-2})[20].The advantages of Ni single atom catalysts are further exemplified by the high Faraday efficiency (FE) of the CO2RR as compared with a Ni NP benchmark system. The FE increases significantly with the polarization potential, noting that at -0.55 and -0.7 V, the FE is as high as 86.7-89.1% and 90.3-91.3%, respectively, which is significantly higher than that of Ni NPs supported on N doped CNTs (see

Figure 4.12B). At -0.55 V, the turnover frequency of the NiSA-N-CNT-800 was calculated to be 11.7±0.2 s^{-1}, which is almost 3 higher than that of Ni-N-CNTs, demonstrating the high intrinsic activity of the Ni SAC system. It is also comparable and better than the TOF values reported recently for the CO2RR on Ni SACs, such as 1.46 s^{-1},[13] and 4.11 s^{-1} [43] .

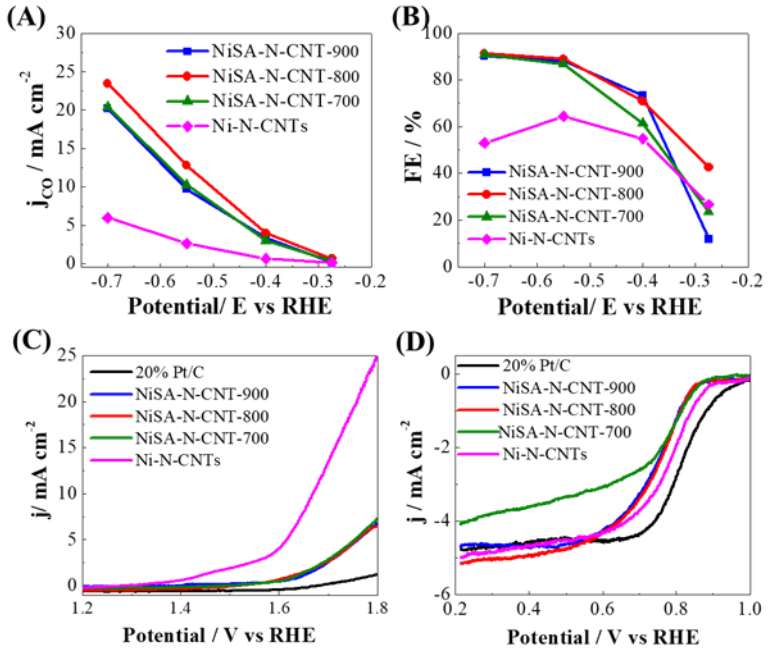

Figure 4.12 (A) jco and (B) Faradaic efficiency of the electrochemical reduction of CO_2 to CO on NiSA-N-CNT-T and Ni-N-CNTs electrocatalysts at different applied potentials, measured in CO_2 saturated 0.5 M $KHCO_3$ solution. The catalyst loadings were 1 mg cm^{-2} and the potentials were IR corrected. Linear scan voltammetry (LSV) curves of (C) the oxygen evolution reaction (OER) and (D) the oxygen reduction reaction (ORR) on NiSA-N-CNT-T and Ni-N-CNTs electrocatalysts, measured in O_2-saturated 0.1 M KOH solution. The catalyst loading was 0.2 mg cm^{-2}.

The NiSA-N-CNT-700, NiSA-N-CNT-800, NiSA-N-CNT-900 were also evaluated for their selectivity against the OER and ORR in 0.1 M KOH solution. The NiSA-N-CNT materials displayed a poor activity for OER with an onset potential of 1.6 V and a current density of 5 mA cm^{-2} at 1.75 V, which is significantly lower than that for the reaction on Ni-N-CNTs (Figure 4.12C). The NiSA-N-CNT materials exhibited an onset potential of 0.88 V (*vs*. RHE) with a half-wave potential of 0.75V, which is 30 and 25 mV lower than that of Ni-N-CNTs and 60 and 100 mV lower than those for Pt/C (Figure 4.12D). The poor activity of the NiSA-N-CNT for the ORR and

OER is probably due to the significant change in the electron and chemical environments of Ni single atoms in NiSA-N-CNT as compared to that of Ni NPs.

4.4. Conclusion

Carbon nanotube supported Ni single atom catalysts, NiSA-N-CNT, with Ni single atom loadings as high as 20.3 wt% have been successfully synthesized using a new one-pot pyrolysis approach. During the initial pyrolysis processes at relatively low temperatures of 350 and 650ºC, Ni single atoms were confined and atomically dispersed in melem and graphitic carbon nitride (*g*-C_3N_4) structures. The presence of Ni atoms was shown to stabilize the *g*-C_3N_4 structure. At high annealing temperatures in the range of 700-900 ºC, the stacked and layered Ni-*g*-C_3N_4 sheets transformed into nanotube supported Ni single atom catalysts, NiSA-N-CNT, proposed to occur via a rolling-up mechanism. This solid-to-solid rolling-up of stacked and layered Ni-*g*-C_3N_4 sheets to NiSA-N-CNT bamboo-shaped tubular structure is most likely activated by the high kinetic energy of confined Ni single atoms, which is supported by the high mobility of Ni single atoms under high temperature and electron beam irradiation conditions via *in situ* TEM observations. The Ni single atoms were stabilized within the tubular structure via nitrogen coordination, forming a structure with four nearest N coordination shell followed by two carbon shells, viz., Ni-N_4. The synthesized NiSA-N-CNT catalysts displayed an improved electrochemical efficiency for the CO2RR, but a diminished activity for ORR and OER, as compared to carbon nanotube supported Ni NPs. The CNT stabilized Ni SACs formed by the rolling-up of layered Ni-g-C_3N_4 sheets represent an attractive path to realize the SACs with high catalysts loadings for a wide range of practical applications.

4.5 References

[1] J. Liu, Catalysis by Supported Single Metal Atoms, ACS Catalysis, 7 (2017) 34-59.

[2] J.H. Kwak, J. Hu, D. Mei, C.W. Yi, H. Kim do, C.H. Peden, L.F. Allard, J. Szanyi, Coordinatively unsaturated Al3+ centers as binding sites for active catalyst phases of platinum on γ-Al2O3, Science, 325 (2009) 1670.

[3] J. Lin, A. Wang, B. Qiao, X. Liu, X. Yang, X. Wang, J. Liang, J. Li, J. Liu, T. Zhang, Remarkable Performance of Ir1/FeOx Single-Atom Catalyst in Water Gas Shift Reaction, Journal of the American Chemical Society, 135 (2013) 15314-15317.

[4] B. Qiao, A. Wang, X. Yang, L.F. Allard, Z. Jiang, Y. Cui, J. Liu, J. Li, T. Zhang, Single-atom catalysis of CO oxidation using Pt1/FeOx, Nature chemistry, 3 (2011) 634-641.

[5] J.S. Jirkovsky, I. Panas, E. Ahlberg, M. Halasa, S. Romani, D.J. Schiffrin, Single atom hot-spots at Au-Pd nanoalloys for electrocatalytic H_2O_2 production, J. Am. Chem. Soc., 133 (2011) 19432.

[6] G. Kyriakou, M.B. Boucher, A.D. Jewell, E.A. Lewis, T.J. Lawton, A.E. Baber, H.L. Tierney, M. Flytzani-Stephanopoulos, E.C. Sykes, Isolated metal atom geometries as a strategy for selective heterogeneous hydrogenations, Science, 335 (2012) 1209.

[7] S. Sun, G. Zhang, N. Gauquelin, N. Chen, J. Zhou, S. Yang, W. Chen, X. Meng, D. Geng, M.N. Banis, R. Li, S. Ye, S. Knights, G.A. Botton, T.K. Sham, X. Sun, Single-atom catalysis using Pt/graphene achieved through atomic layer deposition, Sci. Rep., 3 (2013) 1775.

[8] X.-F. Yang, A. Wang, B. Qiao, J. Li, J. Liu, T. Zhang, Single-Atom Catalysts: A New Frontier in Heterogeneous Catalysis, Accounts of Chemical Research, 46 (2013) 1740-1748.

[9] H. Yan, Y. Lin, H. Wu, W. Zhang, Z. Sun, H. Cheng, W. Liu, C. Wang, J. Li, X. Huang, T. Yao, J. Yang, S. Wei, J. Lu, Bottom-up precise synthesis of stable platinum dimers on graphene, Nature Communications, 8 (2017) 1070.

[10] B. Zhang, H. Asakura, J. Zhang, J. Zhang, S. De, N. Yan, Stabilizing a Platinum1 Single-Atom Catalyst on Supported Phosphomolybdic Acid without Compromising Hydrogenation Activity, Angewandte Chemie International Edition, 55 (2016) 8319-8323.

[11] C. Zhao, X. Dai, T. Yao, W. Chen, X. Wang, J. Wang, J. Yang, S. Wei, Y. Wu, Y. Li, Ionic Exchange of Metal–Organic Frameworks to Access Single Nickel Sites for Efficient Electroreduction of CO2, Journal of the American Chemical Society, 139 (2017) 8078-8081.

[12] S.F. Hackett, R.M. Brydson, M.H. Gass, I. Harvey, A.D. Newman, K. Wilson, A.F. Lee, High-activity, single-site mesoporous Pd/Al2O3 catalysts for selective aerobic oxidation of allylic alcohols, Angew. Chem., Int. Ed., 46 (2007) 8593.

[13] X.K. Gu, B.T. Qiao, C.Q. Huang, W.C. Ding, K.J. Sun, E.S. Zhan, T. Zhang, J.Y. Liu, W.X. Li, Supported Single Pt-1/Au-1 Atoms for Methanol Steam Reforming, Acs Catalysis, 4 (2014) 3886-3890.

[14] X. Zhou, W. Yang, Q. Chen, Z. Geng, X. Shao, J. Li, Y. Wang, D. Dai, W. Chen, G. Xu, X. Yang, K. Wu, Stable Pt Single Atoms and Nanoclusters on Ultrathin CuO Film and Their Performances in CO Oxidation, The Journal of Physical Chemistry C, 120 (2016) 1709-1715.

[15] P. Liu, Y. Zhao, R. Qin, S. Mo, G. Chen, L. Gu, D.M. Chevrier, P. Zhang, Q. Guo, D. Zang, B. Wu, G. Fu, N. Zheng, Photochemical route for synthesizing atomically dispersed palladium catalysts, Science, 352 (2016) 797-800.

[16] S. Yang, J. Kim, Y.J. Tak, A. Soon, H. Lee, Single-Atom Catalyst of Platinum Supported on Titanium Nitride for Selective Electrochemical Reactions, Angew Chem Int Edit, 55 (2016) 2058-2062.

[17] Y. Zheng, Y. Jiao, Y.H. Zhu, Q.R. Cai, A. Vasileff, L.H. Li, Y. Han, Y. Chen, S.Z. Qiao, Molecule-Level g-C3N4 Coordinated Transition Metals as a New Class of Electrocatalysts for Oxygen Electrode Reactions, Journal of the American Chemical Society, 139 (2017) 3336-3339.

[18] J. Xu, F. Xu, M. Qian, F. Xu, Z. Hong, F. Huang, Conductive Carbon Nitride for Excellent Energy Storage, Advanced Materials, 29 (2017) n/a-n/a.

[19] H.J. Qiu, Y. Ito, W.T. Cong, Y.W. Tan, P. Liu, A. Hirata, T. Fujita, Z. Tang, M.W. Chen, Nanoporous Graphene with Single-Atom Nickel Dopants: An Efficient and Stable Catalyst for Electrochemical Hydrogen Production, Angew Chem Int Edit, 54 (2015) 14031-14035.

[20] K. Jiang, S. Siahrostami, A.J. Akey, Y. Li, Z. Lu, J. Lattimer, Y. Hu, C. Stokes, M. Gangishetty, G. Chen, Y. Zhou, W. Hill, W.-B. Cai, D. Bell, K. Chan, J.K. Nørskov, Y. Cui, H. Wang, Transition-Metal Single Atoms in a Graphene Shell as Active Centers for Highly Efficient Artificial Photosynthesis, Chem, 3 (2017) 950-960.

[21] H. Yan, H. Cheng, H. Yi, Y. Lin, T. Yao, C. Wang, J. Li, S. Wei, J. Lu, Single-Atom Pd1/Graphene Catalyst Achieved by Atomic Layer Deposition: Remarkable Performance in Selective Hydrogenation of 1,3-Butadiene, Journal of the American Chemical Society, 137 (2015) 10484-10487.

[22] H. Fei, J. Dong, M.J. Arellano-Jimenez, G. Ye, N. Dong Kim, E.L. Samuel, Z. Peng, Z. Zhu, F. Qin, J. Bao, M.J. Yacaman, P.M. Ajayan, D. Chen, J.M. Tour, Atomic cobalt on nitrogen-doped graphene for hydrogen generation, Nature communications, 6 (2015) 8668.

[23] Z. Chen, S. Mitchell, E. Vorobyeva, R.K. Leary, R. Hauert, T. Furnival, Q.M. Ramasse, J.M. Thomas, P.A. Midgley, D. Dontsova, M. Antonietti, S. Pogodin, N. López, J. Pérez-Ramírez, Stabilization of Single Metal Atoms on Graphitic Carbon Nitride, Advanced Functional Materials, 27 (2017) n/a-n/a.

[24] G. Vilé, D. Albani, M. Nachtegaal, Z. Chen, D. Dontsova, M. Antonietti, N. López, J. Pérez-Ramírez, A Stable Single-Site Palladium Catalyst for Hydrogenations, Angewandte Chemie International Edition, 54 (2015) 11265-11269.

[25] X. Li, W. Bi, L. Zhang, S. Tao, W. Chu, Q. Zhang, Y. Luo, C. Wu, Y. Xie, Single-Atom Pt as Co-Catalyst for Enhanced Photocatalytic H2 Evolution, Advanced Materials, (2016).

[26] D.A. Bulushev, M. Zacharska, A.S. Lisitsyn, O.Y. Podyacheva, F.S. Hage, Q.M. Ramasse, U. Bangert, L.G. Bulusheva, Single Atoms of Pt-Group Metals Stabilized by N-Doped Carbon Nanofibers for Efficient Hydrogen Production from Formic Acid, Acs Catalysis, 6 (2016) 3442-3451.

[27] Z. Chen, S. Mitchell, E. Vorobyeva, R.K. Leary, R. Hauert, T. Furnival, Q.M. Ramasse, J.M. Thomas, P.A. Midgley, D. Dontsova, M. Antonietti, S. Pogodin, N. López, J. Pérez-Ramírez, Stabilization of Single Metal Atoms on Graphitic Carbon Nitride, Advanced Functional Materials, 27 (2017) 1605785.

[28] Y. Cheng, S. Zhao, B. Johannessen, J.-P. Veder, M. Saunders, M.R. Rowles, M. Cheng, C. Liu, M.F. Chisholm, R. De Marco, H.-M. Cheng, S.-Z. Yang, S.P. Jiang, Atomically Dispersed Transition Metals on Carbon Nanotubes with UltraHigh Loading for Selective Electrochemical Carbon Dioxide Reduction, Advanced Materials, (2018) 1706287-n/a.

[29] Y. Liang, H. Wang, P. Diao, W. Chang, G. Hong, Y. Li, M. Gong, L. Xie, J. Zhou, J. Wang, T.Z. Regier, F. Wei, H. Dai, Oxygen Reduction Electrocatalyst Based on Strongly Coupled Cobalt Oxide Nanocrystals and Carbon Nanotubes, Journal of the American Chemical Society, 134 (2012) 15849-15857.

[30] Y. Liu, Y. Shen, L. Sun, J. Li, C. Liu, W. Ren, F. Li, L. Gao, J. Chen, F. Liu, Y. Sun, N. Tang, H.-M. Cheng, Y. Du, Elemental superdoping of graphene and carbon nanotubes, 7 (2016) 10921.

[31] H. Baumgartel, EXAFS, SEXAFS, XANES: X-Ray Absorption - Principles, Applications, Techniques of EXAFS, SEXAFS and XANES. Von D. Koningsberger und R. Prins. John Wiley & Sons Ltd., Chichester 1988. 673 S., Abb., Tab., Formeln. ISBN 0-471-87547-3, Nachrichten aus Chemie, Technik und Laboratorium, 36 (1988) 650-650.

[32] B. Ravel, M. Newville, ATHENA, ARTEMIS, HEPHAESTUS: data analysis for X-ray absorption spectroscopy using IFEFFIT, Journal of Synchrotron Radiation, 12 (2005) 537-541.

[33] M. Newville, IFEFFIT: interactive XAFS analysis and FEFF fitting, Journal of Synchrotron Radiation, 8 (2001) 322-324.

[34] J.J. Rehr, R.C. Albers, Theoretical approaches to x-ray absorption fine structure, Reviews of Modern Physics, 72 (2000) 621-654.

[35] B.C.C. Cowie, A. Tadich, L. Thomsen, The Current Performance of the Wide Range (90–2500 eV) Soft X-ray Beamline at the Australian Synchrotron, AIP Conference Proceedings, 1234 (2010) 307-310.

[36] E. Gann, C.R. McNeill, A. Tadich, B.C.C. Cowie, L. Thomsen, Quick AS NEXAFS Tool (QANT): a program for NEXAFS loading and analysis developed at the Australian Synchrotron, Journal of Synchrotron Radiation, 23 (2016) 374-380.

[37] P.E. Blöchl, Projector augmented-wave method, Physical Review B, 50 (1994) 17953-17979.

[38] G. Kresse, D. Joubert, From ultrasoft pseudopotentials to the projector augmented-wave method, Physical Review B, 59 (1999) 1758-1775.

[39] G. Kresse, J. Furthmüller, Efficiency of ab-initio total energy calculations for metals and semiconductors using a plane-wave basis set, Computational Materials Science, 6 (1996) 15-50.

[40] G. Kresse, J. Furthmüller, Efficient iterative schemes for ab initio total-energy calculations using a plane-wave basis set, Physical Review B, 54 (1996) 11169-11186.

[41] J.P. Perdew, K. Burke, M. Ernzerhof, Generalized Gradient Approximation Made Simple, Physical Review Letters, 77 (1996) 3865-3868.

[42] R.D. Tilley, D.A. Jefferson, The preparation of chromium, nickel and chromium-nickel alloy nanoparticles on supports, Journal of Materials Chemistry, 12 (2002) 3809-3813.

[43] H.B. Yang, S.-F. Hung, S. Liu, K. Yuan, S. Miao, L. Zhang, X. Huang, H.-Y. Wang, W. Cai, R. Chen, J. Gao, X. Yang, W. Chen, Y. Huang, H.M. Chen, C.M. Li, T. Zhang, B. Liu, Atomically dispersed Ni(i) as the active site for electrochemical CO2 reduction, Nature Energy, 3 (2018) 140-147.

[44] Y. Cheng, S. Zhao, B. Johannessen, J.-P. Veder, M. Saunders, M.R. Rowles, M. Cheng, C. Liu, M.F. Chisholm, R. Marco, H.-M. Cheng, S.-Z. Yang, S.P. Jiang, Atomically Dispersed Transition Metals on Carbon Nanotubes with Ultrahigh Loading for Selective Electrochemical Carbon Dioxide Reduction, Advanced Materials, 30 (2018) 1706287.

[45] C. Yi, S. Zhao, H. Li, S. He, J.-P. Veder, B. Johannessen, J. Xiao, S. Lu, J. Pan, M.F. Chisholm, S.-Z. Yang, C. Liu, J.G. Chen, S.P. Jiang, Unsaturated Edge-anchored Ni Single Atoms on Porous Microwave Exfoliated Graphene Oxide for Electrochemical CO2, Applied Catalysis B: Environmental, (2018).

[46] B. Jürgens, E. Irran, J. Senker, P. Kroll, H. Müller, W. Schnick, Melem (2,5,8-Triamino-tri-s-triazine), an Important Intermediate during Condensation of Melamine Rings to Graphitic Carbon Nitride: Synthesis, Structure Determination by X-ray Powder Diffractometry, Solid-State NMR, and Theoretical Studies, Journal of the American Chemical Society, 125 (2003) 10288-10300.

[47] X. Wang, K. Maeda, A. Thomas, K. Takanabe, G. Xin, J.M. Carlsson, K. Domen, M. Antonietti, A metal-free polymeric photocatalyst for hydrogen production from water under visible light, Nature materials, 8 (2009) 76.

[48] H.B. Zheng, W. Chen, H. Gao, Y.Y. Wang, H.Y. Guo, S.Q. Guo, Z.L. Tang, J.Y. Zhang, Melem: an efficient metal-free luminescent material, Journal of Materials Chemistry C, 5 (2017) 10746-10753.

[49] S.C. Yan, Z.S. Li, Z.G. Zou, Photodegradation Performance of g-C3N4 Fabricated by Directly Heating Melamine, Langmuir, 25 (2009) 10397-10401.

[50] Y. Cui, J. Zhang, G. Zhang, J. Huang, P. Liu, M. Antonietti, X. Wang, Synthesis of bulk and nanoporous carbon nitride polymers from ammonium thiocyanate for photocatalytic hydrogen

evolution, Journal of Materials Chemistry, 21 (2011) 13032-13039.

[51] E.F. Kukovitsky, S.G. L'Vov, N.A. Sainov, V.A. Shustov, L.A. Chernozatonskii, Correlation between metal catalyst particle size and carbon nanotube growth, Chemical Physics Letters, 355 (2002) 497-503.

[52] W. Yang, X. Liu, X. Yue, J. Jia, S. Guo, Bamboo-like Carbon Nanotube/Fe3C Nanoparticle Hybrids and Their Highly Efficient Catalysis for Oxygen Reduction, Journal of the American Chemical Society, 137 (2015) 1436-1439.

[53] Z.D. Hu, Y.F. Hu, Q. Chen, X.F. Duan, L.M. Peng, Synthesis and Characterizations of Amorphous Carbon Nanotubes by Pyrolysis of Ferrocene Confined within AAM Templates, The Journal of Physical Chemistry B, 110 (2006) 8263-8267.

[54] J. Rosen, G.S. Hutchings, Q. Lu, R.V. Forest, A. Moore, F. Jiao, Electrodeposited Zn Dendrites with Enhanced CO Selectivity for Electrocatalytic CO2 Reduction, ACS Catalysis, 5 (2015) 4586-4591.

[55] W. Zhu, R. Michalsky, Ö. Metin, H. Lv, S. Guo, C.J. Wright, X. Sun, A.A. Peterson, S. Sun, Monodisperse Au Nanoparticles for Selective Electrocatalytic Reduction of CO2 to CO, Journal of the American Chemical Society, 135 (2013) 16833-16836.

Chapter 5: Unsaturated Edge-anchored Ni Single Atoms on Porous Microwave Exfoliated Graphene Oxide for Electrochemical CO_2 Reduction

Abstract

Supported single atom catalysts (SACs), emerging as a new class of catalytic materials, have been attracting increasing interests. Here we developed a Ni SAC on microwave exfoliated graphene oxide (Ni-N-MEGO) to achieve single atom loading of ~6.9 wt%. The atomically dispersed Ni atoms, stabilized by coordination with nitrogen, were found to be predominantly anchored along the edges of nanopores (<6 nm) using a combination of X-ray absorption spectroscopy (XAS) and aberration-corrected scanning transmission electron microscopy (AC-STEM). The Ni-N-MEGO exhibits an onset overpotential of 0.18 V, and a current density of 53.6 mA mg^{-1} at overpotential of 0.59 V for CO_2 reduction reaction (CO2RR), representing one of the best non-precious metal SACs reported so far in the literature. Density functional theory (DFT) calculations suggest that the electrochemical CO_2-to-CO conversion occurs more readily on the edge-anchored unsaturated nitrogen coordinated Ni single atoms that lead to enhanced activity toward CO2RR.

5.1. Introduction

Electrochemical reduction of CO_2 (CO2RR) to C1 or C2 chemicals (e.g., CO, HCOOH, CH_4, CH_3OH, C_2H_4, etc) coupled with renewable energy is the most attractive technology in both CO_2 utilization and renewable energy storage[1]. However, directly reducing CO_2 to liquid fuels is hampered by the limited number of electrocatalysts available to selectively produce hydrocarbons, as well as difficulties in the separation and purification of liquid fuels. An alternative strategy is to reduce CO_2 to CO because CO production is kinetically favorable compared with other C1 and C2 products, and CO is a key feedstock for the production of liquid fuels via the well-established Fischer-Tropsch process[2]. Precious metal catalysts such as Au[3, 4], Ag[5, 6], and Pd[7, 8] have been extensively investigated for electrochemical CO production from CO_2 due to their high activities and low overpotentials, unfortunately their applications are constrained by high cost. Non-precious metal catalysts such as Zn[9, 10], Bi[11] and Sn[12] and their alloys[13] also show

activities for electrochemical CO_2-to-CO conversion, while they suffer from high overpotential (η) and slow kinetics.

Single-atom catalysts (SACs) are an emerging class of electrocatalysts that possess electronic structures different from their bulk counterparts. They have demonstrated outstanding activities and selectivities for catalytic reactions such as CO oxidation[14, 15], oxygen reduction[16, 17], hydrogen evolution[18, 19] and organic synthesis[20-22]. Density functional theory (DFT) calculations showed that single transition metal atoms would be highly selective for the CO2RR due to its favorable adsorption of carboxyl (*COOH) or formate (*OCHO) over hydrogen (*H)[23, 24]. Most recently, Jiang et al. reported that single Ni atomic sites in graphene vacancies can dramatically lower the CO_2 activation barrier, weakening the binding with CO for facile product release[25]. Zhao et al. reported that metal-organic framework (MOF)-derived Ni SAC exhibits a current density of 10.5 mA cm^{-2} at an overpotential of 0.89 V for CO2RR with a Faradaic efficiency of 71.9 %[26].

The challenge in the development of efficient SAC-based electrocatalyst is the very low atomic loading (normally less than 2 wt%) due to the limited number of anchoring sites based on conventional physical or chemical synthesis methods[27, 28]. The defects created not only provide the anchoring sites for isolated atoms, but also benefit the catalytic activity[29-31]. Dispersion of single-metal atoms on carbon materials with high surface area provides a high volume of anchoring sites, as well as a highly conductive matrix that facilitates the electrochemical catalytic processes[32-35]. Typically, these SACs are prepared through top-down methods that involve annealing metal precursors with carbon materials or precursors to form a metal-carbon composite followed by a subsequent dealloying[17, 33, 34]. The process generates not only atomically dispersed single atoms, but also a significant amount of metal nanoparticles (NPs) [33, 36]. Thus, the fraction of active atomically dispersed metal atoms is still very low because of the inherent tendency of aggregation of metal atoms during the high temperature annealing process[17, 33, 34]. Li et al. used topo-chemical transformation by carbon layer coating to preserve the Ni-N_4 structures and to avoid agglomeration of Ni atoms, but the Ni single atom loading obtained is only 1.41 wt %[37]. Recently, our group developed a new one-pot pyrolysis soft-template method to synthesize SACs based on atomically-dispersed transition-metals on nitrogen-doped carbon nanotubes (MSA-N-CNTs, where M = Ni, Co, NiCo, CoFe, NiPt) with outstanding metal loading, e.g., 20 wt % in the case of NiSA-N-CNTs[38]. The high Ni single atom loading is attributed to the high

concentration of N dopants, which create defects to anchor the atomically dispersed Ni atoms. Nevertheless, due to the formation of multi-walled carbon nanotubes, significant amounts of metal single atoms are trapped in the inner tubes and only a fraction of single atoms anchored at the outmost walls would be active for CO2RR, which could limit the overall activity[38].

Herein, we employed a highly porous and high surface defect-rich microwave exfoliated graphene oxide, MEGO, as supports to atomically dispersed Ni single atoms with high activity and efficiency for CO2RR. The results indicate that MEGO provides large surface area and abundant defects on the pore edge as anchoring sites for single atoms, achieving Ni single atom loading as high as 6.9% for electrochemical CO2RR. The Ni SACs exhibit a mass activity of 53.6 mA mg^{-1} and a high selectivity of 92.1% at an overpotential (η) of 0.59 V for CO2RR. DFT calculations suggested that the experimental growth conditions cause the formation of edge-anchored coordinative unsaturated Ni-N active structures, which exhibit higher catalytic activity for CO2RR compared with the in-plane Ni-N species.

5.2 Experimental Methods

5.2.1 Preparation of Ni-N-MEGO

Nitric acid (65%) was purchased from Fluka. Potassium hydroxide, ethanol, nickel(II) nitrite ($Ni(NO_3)_2$), nickel oxide (NiO), nickel hydroxide ($Ni(OH)_2$), anhydrous propylene carbonate (PC, 99.7%), Nafion solution (5% in isopropanol and water), potassium hydroxide and potassium bicarbonate were all purchased from Sigma-Aldrich and used without further purification.

The porous three dimensional microwave exfoliated graphene oxide (3D-MEGO) structure was synthesized following a previously reported procedure[39]. Briefly, graphene oxide (GO) powders prepared by the modified Hummers method was dispersed in anhydrous propylene carbonate with the aid of sonication for 30 mins in a corn-horn sonicator (900 W, with 20% power output and a tip radius of 6 mm, SCIENTZ-II D). The GO dispersion was then treated with microwave irradiation at 750 W power setting for 8 seconds, yielding MEGO. The as-prepared MEGO powder was further treated with KOH to form MEGO/KOH mixtures for chemical activation. The MEGO/KOH mixture was put in a tube furnace under a 200 sccm Ar flow at normal atmosphere and heated at 800 ºC for 1 hour to create pores[40]. Finally, the samples were annealed at 1100 ºC in Ar of 300 sccm to improve the conductivity of the MEGO.

The Ni-N-MEGO were prepared by mixing 3 ml 0.1 mol L^{-1} nickel nitrate ethanol solution with 100 mg MEGO powder through grinding before being dried at 80 ºC. The resulting black powder was ground with 2g urea to obtain a homogenous grey powder. The as-prepared mixture was put into a tube furnace under an NH_3 (100sccm) atmosphere at 800 ºC for 30 min, yielding a black powder, Ni-N-MEGO. Then the Ni-N-MEGO was further treated with 2 M HNO_3 to eliminate nickel nanoparticles, yielding Ni-N-MEGO. The Ni-MEGO is prepared following the same procedure of that of Ni-N-MEGO without grinding with urea and annealed under a Ar flow (100sccm) instead of NH_3. And the N-MEGO is prepared following the same procedure of that of Ni-N-MEGO under a NH_3 flow (100sccm) without nickel nitrate.

For comparison, nickel phthalocynine (NiPc) supported on was prepared as follow: Graphene (50 mg) was sonicated in 100 mL ethanol in the presence of 100 mg NiPc for 2 h, then the dispersion was stirred for 8 h, filtered and then dried in a vacuum oven at 71 ºC. The product was denoted as NiPc-G.

5.2.2 Catalyst Characterization

The morphology of Ni-N-MEGO was studied by transmission electron microscopy (TEM) and high angle annular dark field (HAADF) scanning TEM (STEM) with elemental mapping on a Titan G2 60-300 at 80 kV. The synthesized materials were dispersed using ethanol solution onto TEM grids. The annular dark field images (ADF) were collected using a Nion UltraSTEM100 microscope operated at 60 kV at a beam current of 60 pA. The recorded images were filtered using a Gaussian function (full width half maximum = 0.12 nm) to remove high frequency noise. The convergence half angle of the electron beam was set to be 30 mrad and the inner collection half angle of the ADF images was 51 mrad. The samples were baked at 160 ºC overnight before STEM observation. Diffraction data was collected with a Bruker D8 Advance diffractometer operated at 40 kV and 40 mA with Cu Kα (2Θ = 1.5406 Å) in the range of 20-90°[41].

X-ray absorption spectroscopy (XAS) measurements were performed at the wiggler XAS Beamline (12ID) at the Australian Synchrotron in Melbourne, Australia using a set of liquid nitrogen cooled Si(111) monochromator crystals. With the beamline optics employed (Si-coated collimating mirror and Rh-coated focusing mirror) the harmonic content of the incident X-ray beam was negligible. XAS measurements were performed at the Ni K-edge (8.3 keV) at < 10 K to minimize thermal disorder and to ensure that the samples were not radiation-damaged This was

confirmed via repetitive quick scanning of the absorption edge for up to 2 hours (12 scans, note that a single complete XAS scan took ~1 hour). For these measurements, samples were prepared as pellets via mechanical grinding in a cellulose binder using a mortar/pestle. Both fluorescence and transmission spectra were recorded depending on the concentration of Ni in each sample (the validity of this approach was confirmed by comparing the fluorescence and transmission spectrum for one of the samples for which both methods yielded comparable signal-to-noise data).

5.2.3 Electrochemical performance

The electrocatalytic activity of Ni-N-MEGO catalysts was evaluated for electrochemical CO_2RR in N_2 and CO_2 saturated 0.5 M $KHCO_3$ solution using linear scan voltammetry (LSV). Electrolyte was first bubbled with N_2 for 5 min and then bubbled with CO_2 for 15 min before experiments. The catalysts loading for LSV was 0.2 mg cm^{-2}. The electrodes for CO_2 electrolysis were prepared by casting the catalysts-ethanol-Nafion solution (6 mg mL catalysts, 1% Nafion) on carbon paper (1 cm^{-2}) with a gas diffusion layer and a catalyst loading of 0.5 mg cm^{-2}. Ir black on carbon paper (1 cm^{-2}) with a loading of 1 mg cm^{-2} was used as the counter electrode (The aim of using Ir black as the counter electrode is because Pt will be oxidized, dissolved and precipitated on the working electrode under the electrolysis condition, which may affect the property and performance of the working electrode). The CO_2 electrolysis was conducted in a gas tight electrochemical cell at different potentials for 2 h. The outlet gas was collected with a gas bag for double channel gas chromatography (Shimadzu, GC-2014 Series) analysis. The electrocatalytic activity of Ni-N-MEGO catalysts was evaluated for electrochemical CO_2 reduction reaction (CO_2RR) in N_2 and CO_2 saturated 0.5 M $KHCO_3$ solution using linear scan voltammetry (LSV). Electrolyte was first bubbled with N_2 for 5 min and then bubbled with CO_2 for 15 min before experiments. The catalysts loading for LSV was 0.2 mg cm^{-2}. The electrodes for CO_2 electrolysis were prepared by casting the catalysts-ethanol-nafion solution (6 mg mL catalysts, 1% Nafion) on carbon paper (1 cm^{-2}) with a gas diffusion layer and a catalyst loading of 0.5 mg cm^{-2}. Ir black on carbon paper (1 cm^{-2}) with a loading of 1 mg cm^{-2} was used as the counter electrode (The aim of using Ir black as the counter electrode is because Pt will be oxidized, dissolved and precipitated on the working electrode under the electrolysis condition, which will affect the study of the working electrode). The CO_2 electrolysis was conducted in a gas tight electrochemical cell at different potentials for 2 h. The outlet gas was collected with a gas bag for double channel gas chromatography (Shimadzu,

GC-2014 Series) analysis. The amount of CO is calibrated using standard gas (BOC) with CO concentration of 0.059%, 0.0738%, 0.0983%, 0.1475% and 0.295%, and the H_2 is calibrated using standard gas (BOC) with H_2 concentration of 0.0534%, 0.06675%, 0.089%, 0.1335% and 0.267%. And the peak area is obtained using the EZChrom SI software. The solutions after CO_2 electrolysis were collected, 0.200 g of the solution were mixed with 0.100 g 2 M HCl to eliminate the $KHCO_3$ with the aim to convert the possible existed formate to formic acid. The formic acid was analyzed using tetrahydrofuran as a solvent, and methanol was analyzed using dimethylformamide as a solvent using Agilent gas chromatography-mass spectrometry (GC-MS, 6890 series GC with a 5973 MS detector).

The rate of product yield is based on the average rate in 2 h. The Faradaic efficiency of CO production is calculated based on [42]:

$$FE\% = \frac{Qco}{Qtot} \text{x} 100 \quad (1)$$

And the j_{CO} is calculated by

$$j_{tot} = \frac{Qtot}{At} \text{x} 1000 \quad (2)$$

$$j_{CO} = FE\% \text{ x } j_{tot} \quad (3)$$

where Q_{CO} is the total number of electrons for CO production in the range of 2 hours, Q_{tot} the total number of electrons pass the electrode in 2 hours. j_{tot} (mA cm^{-2}) is the total average current density pass the electrode in 2 hours, A is the area of the electrode (1 cm^{-2}), and j_{CO} (mA cm^{-2}) is the current density contribute to the CO_2-to-CO reduction, and t (s) is sampling time.

The turn over frequency (TOF, mol CO mol^{-1} Ni h^{-1}) was calculated based on:[26]

$$TOF = \frac{Mjco}{NFm\omega} \quad (4)$$

j_{CO} is partial current for CO,

N: the number of electron transferred for product formation, which is 2 for CO,

F: Faradaic constant, 96485 C mol^{-1},

m: catalyst mass in the electrode, g,

ω: Ni single atom loading in the catalyst, g,

M: atomic mass of Ni, 58.69 g mol^{-1}.

5.2.3 Computational details

DFT calculations were performed using Vienna *ab* initio simulation packages (VASP)[43] with the projector-augmented wave (PAW) pseudopotentials[44]. All calculations were based on the same generalized gradient approximation method with the Perdew-Burke- Ernzerhof (PBE)[45] functional for the exchange-correlation term. The plane wave cutoff was set to 400 eV. The convergence of energy and forces were set to 1×10^{-4} eV and 0.05 eV·Å^{-1}, respectively.

The model of graphene sheet edge was simulated with a periodically repeated graphene nanoribbon in rectangular supercells, with the carbon atoms on the edge saturated with hydrogen atoms. The vacuum thickness in the direction perpendicular and parallel to the ribbon plane was ~12 and ~20 Å, respectively. The Brillouin zone was sampled by a 2×1×1 *k*-point grid with the Monkhorst-Pack[46] scheme. The model of graphene plane was simulated with a periodically repeated graphene layer with a vacuum slab height of 17 Å using a 2×2×1 Monkhorst-Pack *k*-point sampling. The model of NiPc was based on a cubic cell of 18 Å with gamma point calculations.

The formation energy for Ni-N was calculated as: $E_{tot} - n_C\mu_C - n_N\mu_N - n_H\mu_H - n_{Ni}\mu_{Ni}$, where E_{tot} is the total energy of the graphene nanoribbon embedded with Ni-N structures, n_C, n_N, n_H and n_{Ni} represent the total number of C, N, H, Ni atoms, and μ_C, μ_N, μ_H and μ_{Ni} represent their chemical potentials, respectively. μ_C is reference to pristine graphene nanoribbon, μ_H is reference to H_2: $\mu_H = 1/2\ \mu(H_2)$, μ_{Ni} is reference to a Ni atom. The vertical dashed line for μ_N in reference to NH_3 was calculated by: $\mu_N = \mu(NH_3) - 1/2\ \mu(N_2) - 3/2\ \mu(H_2)$.

The adsorption energy of *CO is calculated as: $E_{tot} - E_{surface} - \mu_{CO}$, where E_{tot} is the total energy of the surface with adsorption species, $E_{surface}$ is the energy of bare surface, μ_{CO} is the chemical potential of CO molecule. The free energy of each species is calculated by: $G = E_{DFT} + ZPE + \int CvdT - T\Delta S$, where E_{DFT} is the DFT-optimized total energy, ZPE is the zero-point vibrational energy, $\int CvdT$ is the heat capacity, T is the temperature (298 K) and ΔS is the entropy change. The simplified solvent stabilization has been applied as: 0.25 eV for *COOH and 0.1 eV for *CO. The reaction energy is defined as the free energy difference between different reaction steps.

5.3. Results and Discussions

5.3.1 Synthesis and characterization of Ni SAC

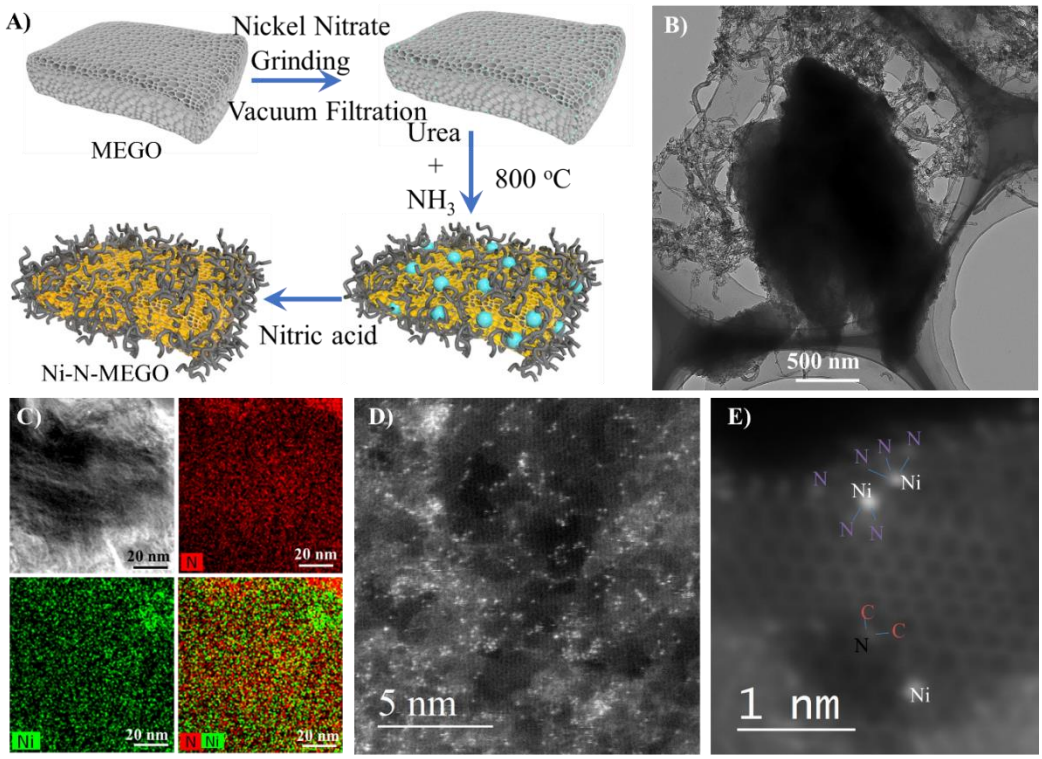

Figure 5.1 (A) Scheme showing the synthesis of Ni-N-MEGO; (B) TEM images of Ni-N-MEGO; (C) STEM-EDS mapping of the Ni-N-MEGO; (D) AC-STEM image of Ni-N-MEGO showing the porous structure; (E) local defects of N dopants and Ni-N_x single atom sites were identified by the atomic column intensity.

The highly porous MEGO support was prepared using microwave treated graphene oxide with a subsequent pore creation (Figure 5.1A, supporting information)[39]. The as prepared MEGO possesses a very high surface area of 2649 m^2 g^{-1} and a pore volume of 1.79 cm^{-3} g^{-1} with an average pore size of 2.7 nm (Figure 5.2). Raman spectrum shows a high I_D/I_G (2.57) ratio, revealing the large number of defects formed during the pore creation process (Figure 5.2D) [47]. The Ni single atom catalyst was prepared by mixing 3 mL 0.1 mol L^{-1} nickel nitrate in ethanol solution with 100 mg MEGO powder (~18 wt% Ni in MEGO) through vacuum filtration to allow Ni^{2+} infiltrating into the pores. The material was then processed by mixing and grinding with urea before being heated in a tube furnace under an NH_3 atmosphere at 800 °C. The resultant powder was thoroughly treated with acid to remove the Ni NPs, forming Ni-N-MEGO.

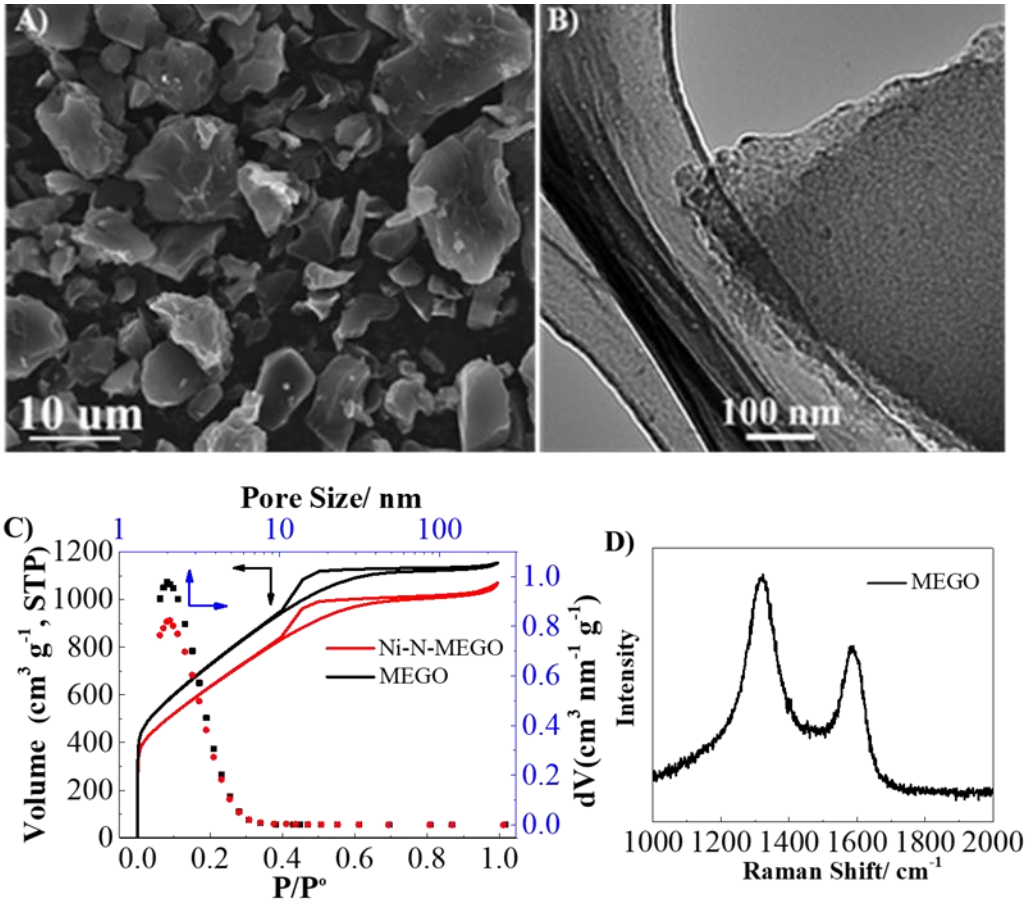

Figure 5.2 (A) SEM image, (B) TEM image of MEGO and (C) nitrogen isothermal adsorption curves and pore-size distribution of Ni-N-MEGO and MEGO. (D) Raman spectrum of MEGO.

Ni-N-MEGO exhibits a surface area of 2380 m^2 g^{-1} and a pore volume of 1.68 m^3 with a mean size of 2.6 nm, which is slightly lower than that of MEGO (Figure 5.2C). Transmission electron microscope (TEM) images reveal that Ni-N-MEGO exhibits a typical 3D structure connected with bamboo like carbon nanotubes (CNTs) with an outer diameter of ~30 nm (Figure 5.1B). The formation of CNTs may be due to catalytic effect of Ni NPs formed on the MEGO surface, which is confirmed by the TEM image of the catalysts before acid treatment (Figure 5.3). Scanning TEM with energy-dispersive X-ray spectroscopy (STEM-EDS) of Ni-N-MEGO shows homogeneously dispersed Ni and N species (Figure 5.1C). Ni NPs are not observed, revealing that the Ni NPs have been removed by acid treatment.

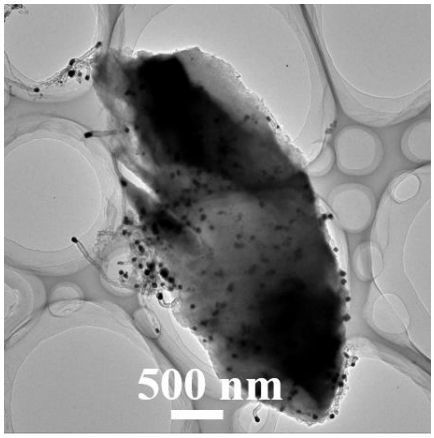

Figure 5.3 TEM image of a typical Ni-N-MEGO structure before acid treatment.

The atomic dispersion of Ni single atoms was confirmed by aberration-corrected scanning TEM (AC-STEM). The bright dots (Ni atoms) are evenly distributed across the MEGO structure (Figure 5.1D and Figure 5.4). The imperfect stacking of graphene layers creates high volume micropores with sizes less than 6 nm, consistent with the cryo-nitrogen adsorption measurements. AC-STEM images show imperfect stacking structure with clear Morrie patterns, i.e., the surface atomic layers have a different crystal structure than that in the bulk (Figure 5.4A). Those imperfectly stacked graphene layers should produce more grain boundary edges with anchor sites for single atoms. The AC-STEM images clearly show Ni single atoms are predominately anchored on the edge of the pores, exposed basal-plane edges and the steps of graphene sheets (Figure 5.1E and Figure 5.4B). Two elements with intensities higher than carbon were observed, which could be assigned to Ni and N by considering the synthesis environment and the following XAS results. Most N dopants adjacent to the Ni single atoms were found near the edges of pores, revealing that the unsaturated Ni at the edge coordinated with N species.

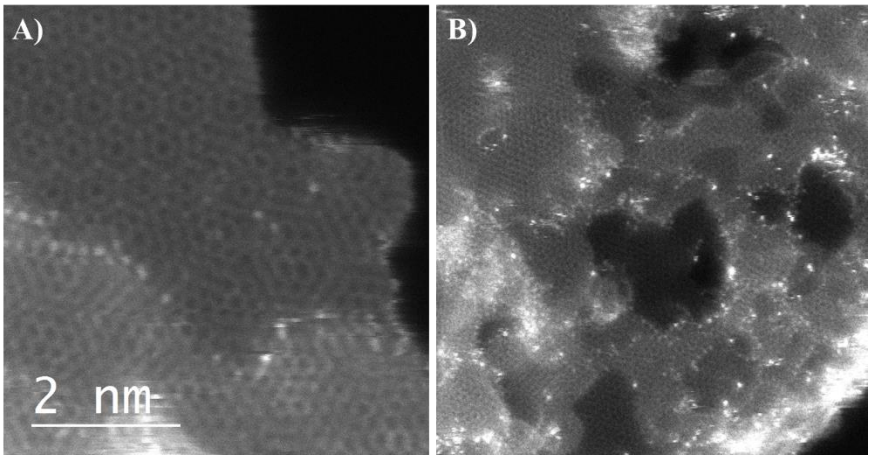

Figure 5.4 AC-STEM image shows (A) distorted stacking of graphene sheets, (B) the unsaturated Ni single atoms anchored on the edge of the pores in Ni-N-MEGO.

Cross-sections of the Ni-N-MEGO structure were obtained using a focused ion beam and scanning electron microscope (FIB-SEM, Figure 5.5). Before acid treatment, Ni NPs with sizes in the range of 15-80 nm were formed on the surface and in the bulk of MEGO structure (Figure 5.3 and Figure 5.5B). Apart from the large Ni NPs, the cross section of MEGO shows a highly patterned flake-like structure. The flakes with sizes less than 15 nm are typically rich in Ni and N in contrast to the bright NPs, which are simply rich in Ni (Figure 5.5B, white circle). The formation of large Ni NPs is related to the high concentration of Ni^{2+} precursor absorbed in large pores (>50 nm) in the MEGO, which result in preferential formation of Ni NPs. Ni^{2+} is encapsulated in the small sized nanopores (less than 6 nm) that lead to a preferential formation of Ni-N single atom on the edge of pores. The cross section of Ni-N-MEGO further confirms that all surface NPs and the majority of the larger NPs inside the MEGO are removed by an acid treatment (Figure 5.5C), as indicated by the disappearance of the flake structures and large NPs. The C, N and Ni elements are uniformly distributed across the structure, revealing the atomically dispersed Ni species both inside and on the surface. The AC-STEM images clearly show that the Ni single sites are predominately anchored on the edge of the pores, exposed basal-plane edges and steps of graphene sheets inside the MEGO (Figure 5.5D).

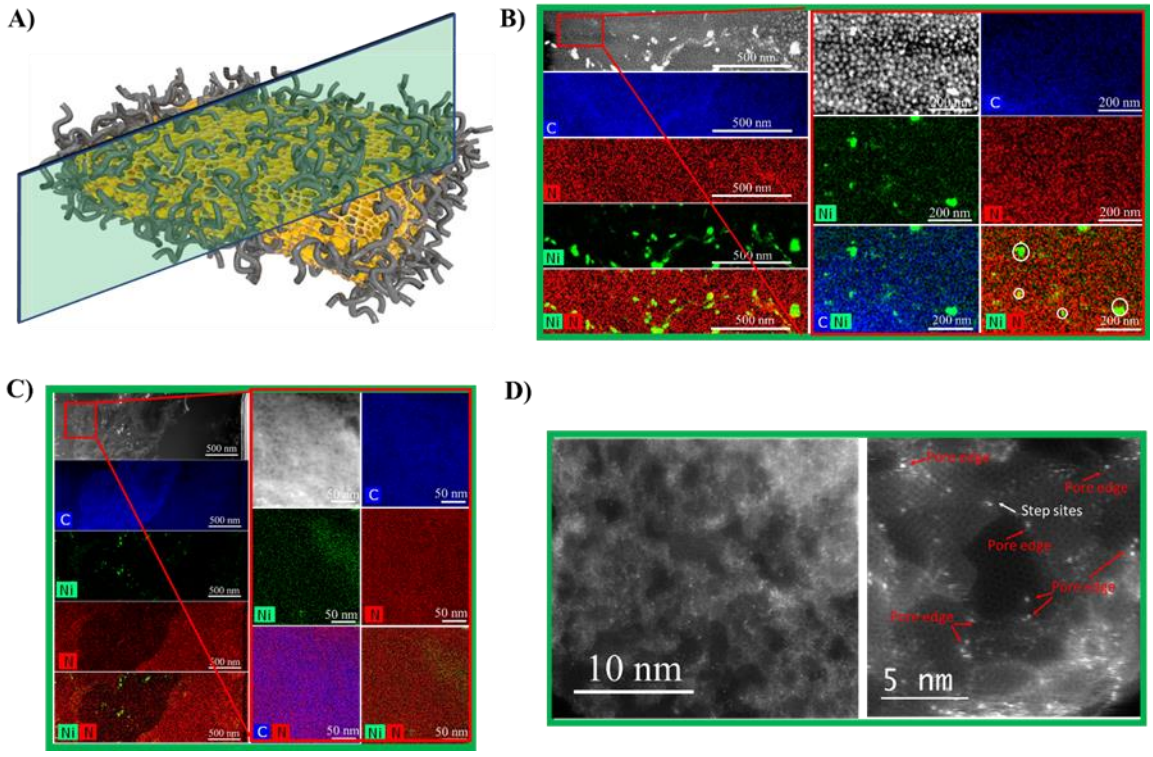

Figure 5.5 (A) A scheme showing the cross-sections of Ni-N-MEGO structure obtained using a focused ion beam scanning electron microscope (FIB-SEM). STEM-EDS mapping of the cross section of (B) Ni-N-MEGO before acid treatment and (C) Ni-N-MEGO, (D) AC-STEM images showing the single atom Ni sites are predominately anchored on the edges of nanopores inside Ni-N-MEGO.

The chemical environments of Ni-N-MEGO were examined by X-ray absorption spectroscopy (X-ray absorption near edge structure, XANES, and X-ray absorption fine structure, XAFS, Figure 5.6). The Ni L-edge shows typically two groups of peaks around 850-860 eV (L_3-edge) and 868-876 eV (L_2-edge) due to the splitting of the Ni 2p orbitals (Figure 5.6A). The Ni L_3-edge of the Ni-N-MEGO shows a major peak at 855.4 eV and a small shoulder at 852.9 eV. The intense peak at ~855.4 eV for Ni-N-MEGO is very close to that of nickel phthalocyanine (NiPc, ~854.2 eV), but very different from Ni in Ni foil (Ni^0, 852.8 eV), NiO (852.9 eV) or $Ni(OH)_2$ (853.1 eV). This evidently indicates that the Ni in N-MEGO is mainly coordinated with N rather than Ni-Ni, Ni-O or Ni-OH. The Ni-N-MEGO exhibits a broad peak (Figure 5.6A and Figure 5.7A), indicating that the Ni single atoms exhibit a more complex coordination environment compared to NiPc which is purely $Ni-N_4$. The N K-edge of Ni-N-MEGO (Figure 5.6B) shows two peaks at 398.6 eV and 401.5 eV, assigned to pyridinic and graphitic N, respectively, consistent with that of N-MEGO[48].

Different from that of N-MEGO, the new feature of Ni-N-MEGO centered at 399.4 eV can be assigned to Ni-N-C species,[38] and the new peak at 403.7 eV is likely attributed to N-O[49]. Compared to a Ni foil (Ni^0), the rising-edge of Ni K-edge XANES spectra shift to higher energies and indicate an increase in the oxidation state of Ni in the case of Ni-N-MEGO (Figure 5.7B). The Fourier-transformed extended X-ray absorption fine structure reveals that NiPc shows a sharp peak centering at 1.43 Å (Figure 5.6C), consistent with the well-difiened Ni-N_4 species.[50] However, in the case of Ni-N-MEGO, a broader peak around 1.42 Å is observed, which is consistent with Ni-N coordination[26]. However, the intensity of the peak at 1.42 Å is lower than that of NiPc, likely due to the formation of unsaturated Ni-N_2, Ni-N_3 and well-defined Ni-N_4 species. Further, the broad peaks at 2.30 Å is likely contributed by the presence trace amount of Ni NPs (Ni-Ni at 2.15 Å).

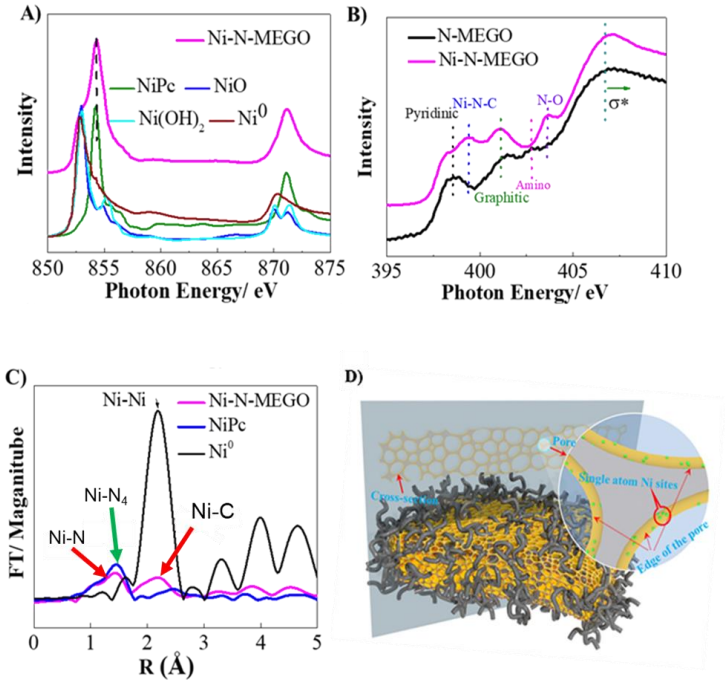

Figure 5.6 Chemical environment of Ni-N-MEGO as probed via X-ray absorption spectroscopy. (A) Ni L-edge spectra of Ni-N-MEGO compared with NiPc, $Ni(OH)_2$, NiO and Ni foil (Ni^0); (B) N K-edge spectra of EXAFS spectra of Ni-N-MEGO compared with N-MEGO; (C) Fourier transform of the EXAFS spectra of Ni-N-MEGO and nickel foil (Ni^0); and (D) The scheme shows the distribution of the Ni single atoms on the edges of the pores in Ni-N-MEGO.

The content of the atomically dispersed Ni atoms was estimated by the combination of inductively

coupled plasma (ICP) and linear combination analysis (LCA) of the Ni L-edge. The ICP results reveal that the Ni species in the Ni-N-MEGO are estimated to be ~8.3 wt %. LCA of the Ni L-edge reveals that Ni-N-MEGO is mainly composed of Ni-N (83.8 %) species with a small contribution of Ni^0 (8.6 %) and $Ni(OH)_2$ (7.7 %) (Table 5.1). Thus, the total Ni single atoms in the Ni-N-MEGO is estimated be to ~6.9 wt %, significantly higher than the metal-organic framework (MOF) derived SACs (1.53 wt %),[26] Ni(I)-NSG (5.6 wt %)[51] (Table 5.2).

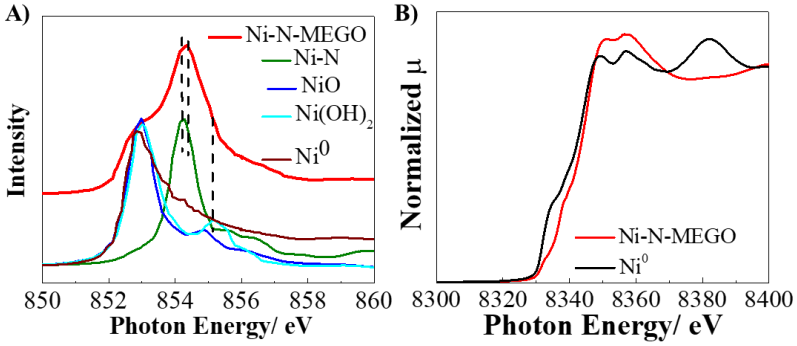

Figure 5.7 (A) Comparison of Ni L_3-edge spectra of Ni-N-MEGO with NiPc, NiO, $Ni(OH)_2$, and Ni fiol (Ni^0). (B) comparison of XANES spectrum of Ni K-edge for Ni-N-MEGO and Ni foil (Ni^0).

Samples	Ni-N	Ni Foil	$Ni(OH)_2$	NiO
Ni-N-MEGO before acid treatment	55.1±1.2	26.4±0.6	18.2±1.3	0.3±3.8
Ni-N-MEGO	83.8±1.6	8.6±0.9	7.7±1.2	0±1.3

Table 5.1 Summarized Ni species in Ni-N-MEGO based on the LCA of Ni L-edge spectra.

Materials	Preparation method	Loading and comments	Application	References
Pt on θ-Alumina	Sol-gel	0.18 wt% Pt	CO oxidation	[52]
Pd on γ-alumina	Impregnation-calcination	<0.5 wt%	CO oxidation	[53]
Pd/meso-Al_2O_3	surfactant-templated route	0.03 wt %	Selective aerobic oxidation of allylic alcohols	[54]
Pd/N-Doped Carbon	incipient wetness impregnation	1 wt %	Hydrogen production from formic acid decomposition	[55]
Rh_1/TiO_2	deposition precipitation method	0.37 wt %	Water-gas shift reaction	[56]
Pt on g-C_3N_4	impregnation	0.16 wt%	Photocatalytic H_2 Evolution	[57]
Pt/TiN	incipient wetness impregnation	0.35 wt %	Oxygen reduction, formic acid oxidation, and methanol oxidation	[16]
Fe-N*x*-C	Pyrolysis-leaching	0.8 at% (XPS)	Oxygen reduction, oxygen evolution	[17]
Co nitrogen-doped porous carbon	Pyrolysis of metal-organic frameworks	4 wt %	Oxygen reduction reaction	[58]
Co-N-C	temperate-sacrificial approach	3.6 wt%	Chemoselective hydrogenation of nitroarenes to produce azo compounds	[59]
Co-NG	Pyrolysis	0.57 at% Co	Hydrogen generation	[60]
Pt-g-C_3N_4	impregnation	0.5 wt%	Semihydrogenation of 1-hexyne	[61]
Ir-g-C_3N_4	impregnation	0.5 wt%	Semihydrogenation of 1-hexyne	[61]

Pd-g-C_3N_4	impregnation	0.5 wt%	Semihydrogenation of 1-hexyne	[61]
Ag-g-C_3N_4	impregnation	0.5 wt%	Semihydrogenation of 1-hexyne	[61]
Fe-N/C	temperate-sacrificial approach	2.9 wt%	Oxygen reduction reaction	[33]
Co-C_3N_4/CNT	temperate approach	0.2 wt%	Oxygen reduction reaction and oxygen evolution reaction	[32]
Fe-N/graphene	Ball milling	1.5 wt%	Catalytic oxidation of benzene to phenol	[34]
Ni SAs/N-C	Metal-organic frameworks derived	1.5 wt%	Electro-reduction of CO_2	[26]
NiN-GS	Electrospinning	~1.6 wt%	Electro-reduction of CO_2	[25]
Ni-N4-C	Topo-chemical transformation	~1.41 wt%	Electro-reduction of CO_2	[37]
A-Ni-NG	Soft-template Pyrolysis	~5.6 wt%	Electro-reduction of CO_2	[51]
NiSA-N-CNT	Soft-template Pyrolysis	20.3%	Electro-reduction of CO_2	[62]
Ni-N-MEGO	Bottom-up approach	6.9 wt%	CO_2 reduction	This study

Table 5.2. A summary of loading content of single atom catalysts from literature.

5.3.2 Electrochemical CO_2 reduction

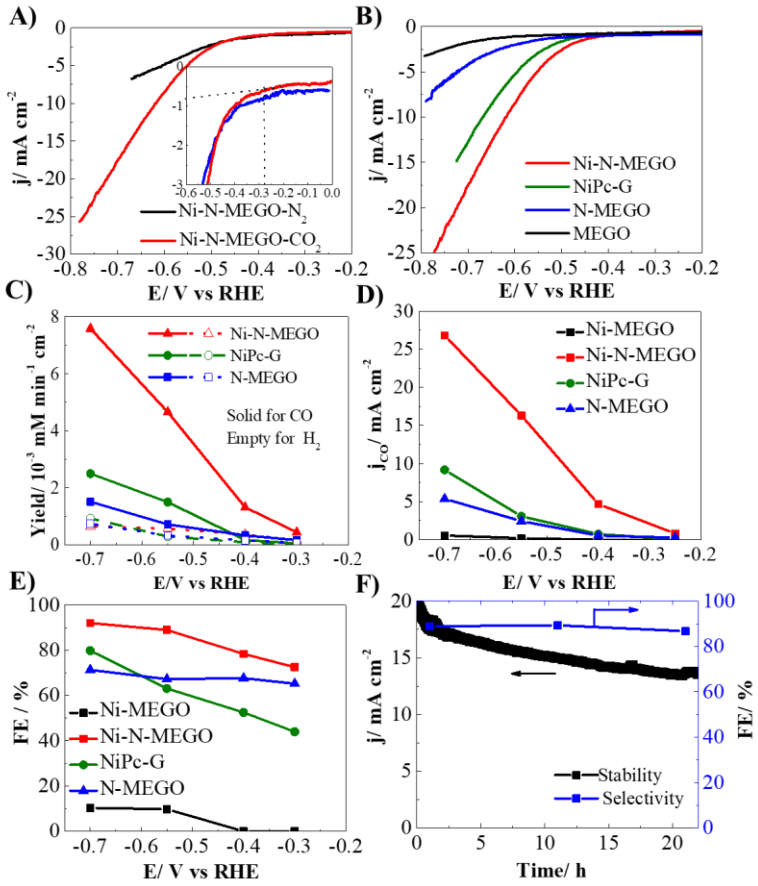

Figure 5.8 CO_2 reduction performance. Linear scan voltammetry (LSV) curves of A) Ni-N-MEGO in N_2 and CO_2 saturated 0.5 M $KHCO_3$ solution, and B) Ni-N-MEGO, NiPc, N-MEGO and MEGO in CO_2 saturated 0.5 M $KHCO_3$ solution. Plots of C) product yields and D) j_{co} and E) Faradaic efficiency of CO at -0.30, -0.40, -0.55 and -0.7 V on Ni-N-MEG, NiPc, N-MEGO and/or Ni-MEGO electrodes. F) Preliminary stability of Ni-N-MEGO electrodes. The CO2RR was conducted in CO_2 saturated 0.5 M $KHCO_3$ solution with catalysts loading of 0.5 mg cm^{-2}. The potential is IR corrected.

The electrochemical activity of Ni-N-MEGO for CO2RR was investigated in N_2- and CO_2-saturated 0.5 M $KHCO_3$ solution (Figure 5.8A). A significantly higher current density was obtained in CO_2-saturated solution as compared to that in N_2-saturated solution for Ni-N-MEGO with an onset potential of -0.29 V vs RHE (reversible hydrogen electrode), i.e., $\eta = 0.18$ V. Ni-N-MEGO exhibits a better activity for CO2RR with suppressed H_2 evolution as compared to NiPc supported on graphene, NiPc-G, and N-MEGO (Figure 5.8B-D). The CO yield increases with the increase of

cathodic potentials (Figure 5.8C). On Ni-N-MEGO catalysts, the CO yield is as high as 5.66×10^{-3} mmol cm^{-2} min^{-1} at potenital of -0.55 V (η = 0.44 V) with suppresed H_2 yield (5.6×10^{-4} mmol cm^{-2} min^{-1}). The CO yield of Ni-N-MEGO is 4 and 2 times higher than that of N-MEGO and NiPc-G, respecitvely. The corresponding current density, $j_{CO,}$ for CO2RR on Ni-N-MEGO is 5.6, 16.3 and 26.8 mA cm^{-2} (9.2, 32.6 and 53.6 mA mg^{-1}) at η = 0.29, 0.44 and 0.59 V, respectively (Figure 5.8D). This is significantly higher than non-precious metal catalysts such as Zn (4 mA cm^{-2} at η = 0.69 V)[10] measured under similar test conditions, and also comparable or even better than noble metal catalysts such as Au,[3, 63, 64] and Ag [5, 6] (Table S3). For example, Zhu et al. reported that gold NPs achieves a j_{CO} value of 3.1 mA mg^{-1} at η=0.44 V[4]. Our Ni-N-MEGO outperforms the single Ni atom counterparts due to its high loading of Ni single atoms (Table 5.3). For example, the MOF-derived Ni SACs with a Ni single atom loading of 1.53 wt% show a current density of 2.94 mA mg^{-1} (7.35 mA cm^{-2}) at η=0.89 V,[26] the Ni and N doped nanofiber produced by electrospinning with a Ni single atom loading of 1.6 wt% shows a j_{CO} of 20 mA mg^{-1} at η=0.7 V,[25] and Ni single atoms cooridnated with four N on carbon with a single atom loading of 1.41 wt % exhibts a current density of 28.6 mA cm^{-2} at η=0.771 V[37] . The turnover frequency (TOF) of Ni-N-MEGO was calculated to be 0.04, 0.14 and 0.24 s^{-1} at η=0.29, 0.44 and 0.59 V, respectively. The TOF of Ni-N-MEGO is comparable to the best noble metal based catalysts for electrochemical CO_2-to-CO conversion such as nanoporous Ag (0.002 s^{-1} @η=0.39 V), ultrathin Au NWs (0.02 s^{-1} @η=0.24 V) and other protoporphyrin-based homogeneous catalysts (<0.1 s^{-1})[65, 66] and similar to that of 0.22 s^{-1} at η=0.59 V of MOF derived Ni SAC [26] (Table 5.4). The Faraday efficiency (FE, Figure 5.8E) of Ni-N-MEGO is 72.5%, 78.4%, 89.0% and 92.1% at -0.3, -0.4, -0.55 and -0.7 V, repectively, significantly higher than those of NiPc-G and N-MEGO with a FE only around 40-71%, further revealing the outstanding performance of Ni-N-MEGO. The preliminary stability of Ni-N-MEGO for CO2RR was tested at -0.55 V (Figure 5.8F). The initial current density was ~19.3 mA cm^{-2}, and decreased by 29.1% to ~13.7 mA cm^{-2} after polarization for 21 h. Nevertheless, the FE of elctrochemical CO_2-to-CO conversion remains at ~89%, showing that the Ni-N-MEGO is reasonably stable for the electrochemical reduction CO_2 to CO.

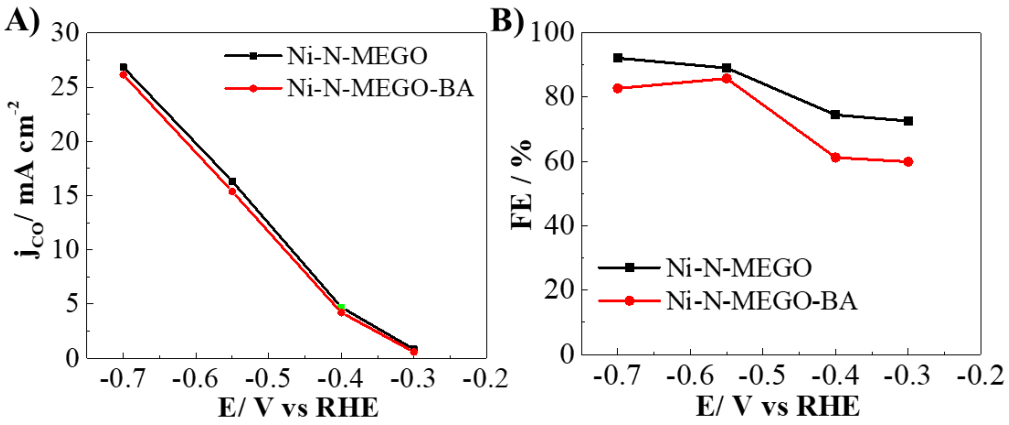

Figure 5.9 Plots of A) jco and B) Faradaic efficiency of CO at -0.30, -0.40, -0.55 and -0.7 V on Ni-N-MEG, Ni-N-MEGO-BA (Ni-N-MEGO before acid treatment) electrodes.

In the Ni-N-MEGO, there are four types of species could be the active sites for electrochemical CO_2 reduction, Ni single atoms cordinated with nitrigen (Ni-N), nitrogen doped carbon (N-C, eg, pyridinic and graphitic N), Ni nanoparticles, Ni single atoms cordinated with carbon (Ni-C). N-C exhibits activity for CO_2 to CO convension, but the current density is very low (Figure 4B-D), which is consistent with the reported results[67, 68]. A comparison of the Ni-N-MEGO and Ni-N-MEGO before acid treatment has been revealed with similar j_{CO}, but the FE for Ni-N-MEGO before acid treatment is only 60-83%, which is lower than that of 72-92% for Ni-N-MEGO (Figure 5.9). The results indicate the Ni nanoparticles are not contributed to CO2RR but hydrogen evolution, consitent with the reported results[69, 70].

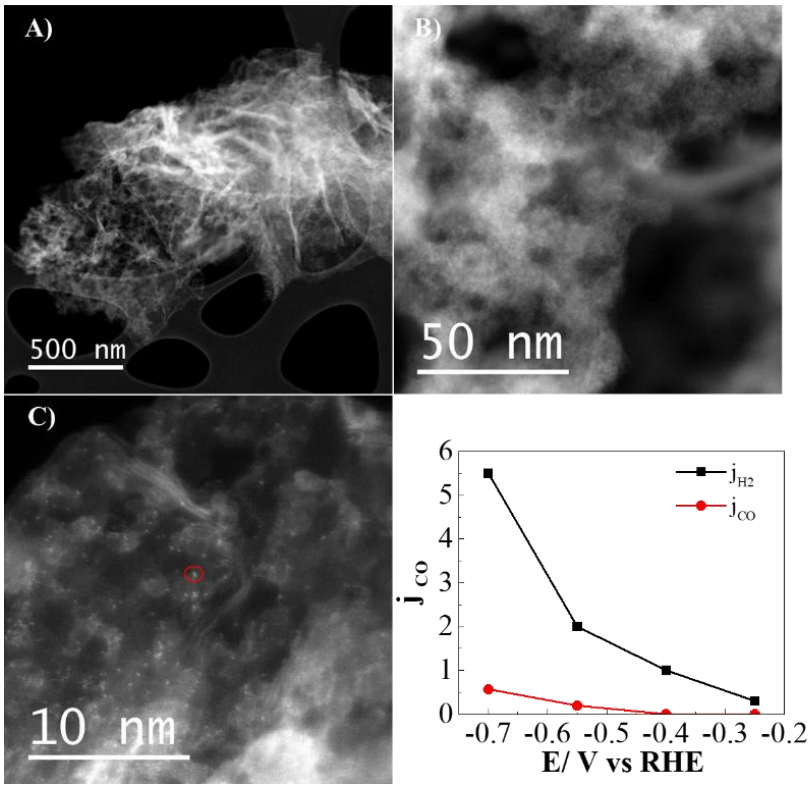

Figure 5.10 A) STEM images of a whole Ni-MEGO structure, and B) an enlarged part of Ni-MEGO showing the porous structure; C) AC-STEM image of Ni-MEGO showing the single Ni atoms; and D) the current density for CO production and H_2 production in CO_2 saturated 0.5 M $KHCO_3$ solution.

In order to investigate the activity of Ni-C, a Ni-MEGO has been prepare with a similar procedure of preparation of Ni-N-MEGO without nitrogen source, and the Ni single atoms with mass loading less than 2% coordinated with the defects of the carbon matrix has been obtained on the edge of the pores (Figure 5.10A-C), while the electrochemical study show that the Ni-C species are not active for electrochemical CO_2 reduction but with preferntially activity for hydrogen evolution reaction (Figure 5.8D and E and Figure 5.10D). These results all confirm that the Ni-N species are the major active species that contributed to CO_2 electrochemical reduction.

5.3.3 Density functional theory simulation

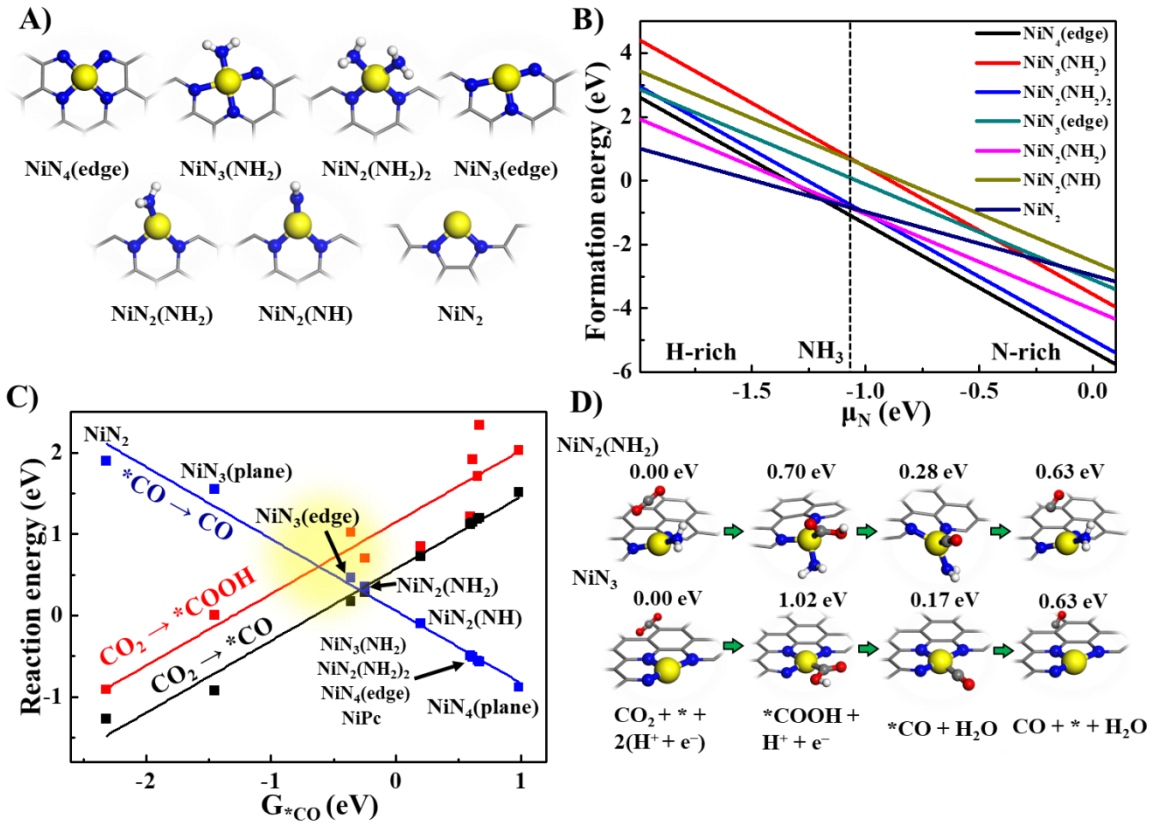

Figure 5.11 DFT calculation results. A) different Ni-N active site structures on the edges of graphene sheets, B) formation energies as function of chemical potential for nitrogen (μN) for different Ni-N active site structures. A lower formation energy indicates better stability. The vertical dashed line locates where the N source is referenced to NH_3. C) The reaction energy is in linear relationship with the adsorption free energy of *CO (G*CO) on the active sites. A lower reaction energy indicates higher reactivity. Different Ni-N structures were located in the lines. A lower G*CO indicates weaker adsorption. The region around the insection point of the higher adsorption and desorption steps (shown in yellow) indicates the optimal reactivity. D) Reaction pathway on the $NiN_2(NH_2)$ and NiN_3 site, with the free energy shown on top. (C: grey; N: blue; Ni: yellow; O: red; H: white).

DFT calculations were performed in order to understand the structure of Ni-N active sites. A model of graphene nanoribbon with the edge substituted with N atoms and embedded with Ni atoms has been built to simulate the single Ni atoms anchored on graphene edge, while a graphene plane embedded with Ni-N structures was used to simulate the in-plane Ni-N sites for comparison.

Considering that various adsorption structures on the single Ni atoms is possible under the reaction environment of catalyst synthesis, several different structures with Ni-N coordination number of 2-4 have been considered and their formation energies were calculated to evaluate the stability (Figure 5.11A, we define Ni coordinated with 4 nitrogen is saturated Ni-N_4, and the coordination number less than 4 is unsaturated Ni-N species). As shown in Figure 5.11B, under N-rich (e.g. N_2) conditions (right side) the edge-anchored 4-coordinate structures (NiN_4, $NiN_2(NH_2)_2$) are more stable, while the Ni-N structures with lower coordination numbers (NiN_2, $NiN_2(NH_2)$) become more stable as the chemical potential of N (μ_N) decreases under H-rich conditions (left side). In our case, the materials were synthesized in NH_3 reducing atmosphere (vertical dashed line), the edge-anchored Ni-N_4 edge species and the coordinatively edge-anchored unsaturated Ni-N species such as NiN_2, $NiN_2(NH_2)$, $NiN_2(NH_2)_2$ and NiN_3 should be preferentially generated in NH_3 conditions. These calculations are consistent with our AC-STEM image, Ni L-edge and Ni K-edge results, which indicate that the unsaturated Ni-N are generated at the edge of the pores of MEGO structure.

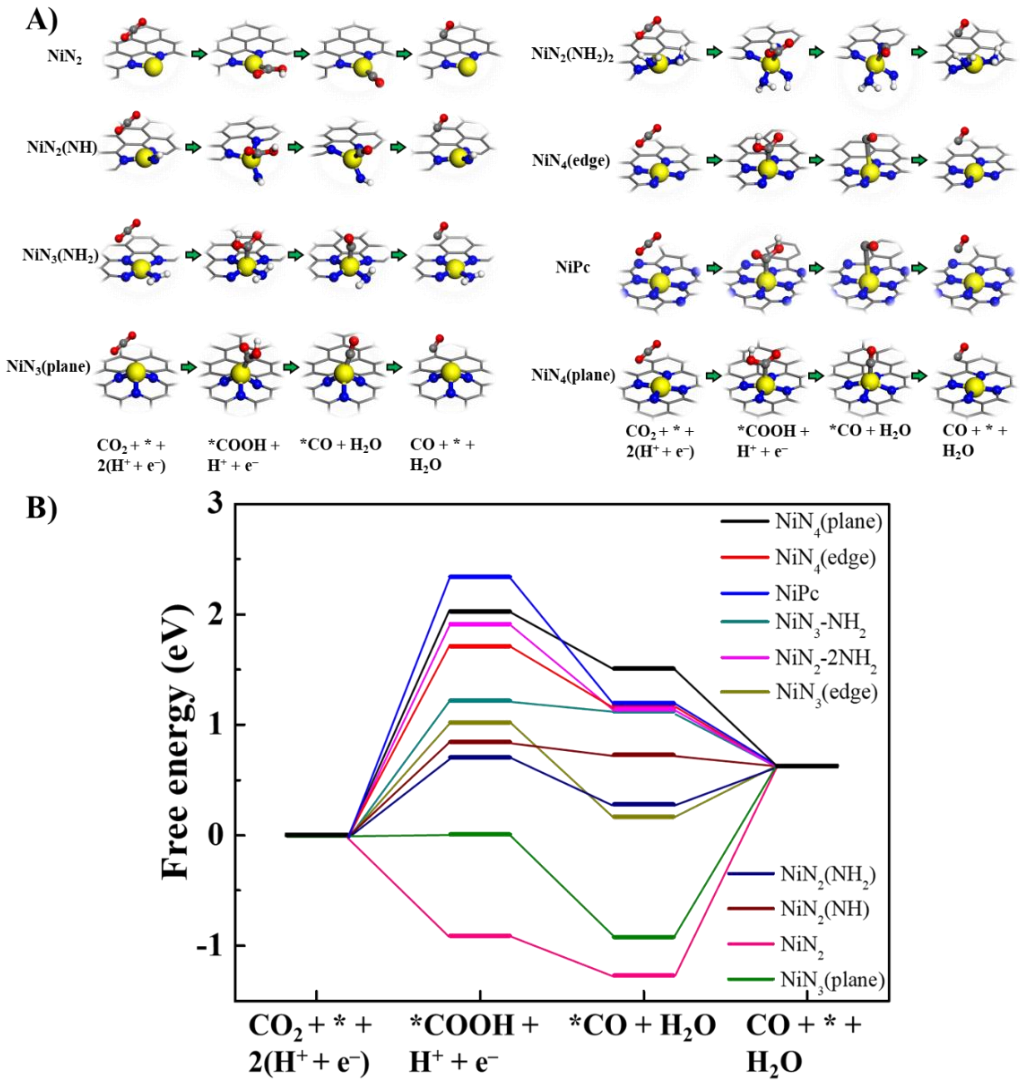

Figure 5.12 (A) Reaction pathway on different Ni-N sites corresponding to the points in Figure 4c, with the reaction free energy shown on top (C: grey; N: blue; Ni: yellow; O: red; H: white). (B) Reaction energy profile of different pathways.

The mechanism for CO2RR to CO has been considered with three steps: an adsorption step (CO_2→*COOH), a conversion step on the surface (*COOH→*CO) and a desorption step (*CO→CO). The binding free energy of CO (G_{*CO}) is a good descriptor for the reactivity on metal sites [34]. As shown in Figure 5.11C, the reaction energy shows a linear correlation with G_{*CO}, exhibiting straight lines for both the adsorption and desorption steps. According to the Sabatier principle [35], the optimal activity is achieved at an intermediate adsorption strength, that is, the

intersection points of the steps (shown in yellow). Among the different Ni-N active sites studied, 4-coordinate structures (NiN_4 plane and NiN_4 edge) are unfavorable for the adsorption step (red) and 2-coordinate structures (NiN_2) is unfavorable for the desorption step (blue), 3-corrdinate edge-anchored structures (NiN_3 and $NiN_2(NH_2)$) exhibit highest reactivity due to the favorable energy for both the adsorption of CO_2 and the desorption of CO (Figure 5.12), while the in-plane NiN_3 is unfavorable for desorption of CO. Note that $NiN_2(NH_2)$ and NiN_3 are also quite stable under experimental conditions (Figure 5.11B), suggesting that they are the major active sites in the Ni-N-MEGO for electrochemical CO2RR. The reaction pathway with free energy on edge-anchored unsaturated NiN_3 and $NiN_2(NH_2)$ was then shown in Figure 5.11D, which show the intermediate energy of 0.7 and 1.02 eV for CO_2 activation ($CO_2 \rightarrow$*COOH), and 0.63 and 0.63 eV for CO desorption (*CO→CO), respectively.

Single atom catalysts are strongly constrained by the loading mainly due to the low surface area and limited number of defects that can stabilize the single atoms. Our method creates a high surface area (2649 $m^2 g^{-1}$) MEGO structure with high volume of pores with an average size of 2.7 nm. The defect-rich small sized pores provide multi-function roles: a) Since only limited amount of Ni precursors are absorbed in the small sized pores through vacuum filtration, the precursors could efficiently contact with the nitrogen sources such as NH_3 and urea during the high temperature annealing process resulting in a preferential formation of the Ni-N species[33] , which is evidenced by the high density of Ni and N elements in the small pores and the formation of Ni particles in the large pores (Figure 5.5B). b) The small size pores provide a confinement effect that prevents the aggregation of Ni atoms during the high temperature annealing process[26, 71]. c) The pores expose graphene edges with abundant defects that could anchor single Ni atoms. Due to these reasons the single atom Ni is distributed in the entire MEGO structure with loading estimated to be ~6.9 wt %. The loading is significantly higher than the metal-organic framework (MOF) derived SACs (1.53 wt %),[26] Ni(I)-NSG (5.6 wt %),[51] and also higher than the atomically dispersed Fe-N (2.9 wt %) supported on carbon materials prepared by template-induced methods[33]. The loading achieved in the current work is among the highest single atom loading reported to date in the area of non-precious metal-based SACs (Table 5.2). Our DFT calculations reveal that the edge-sites of NiN_4, $NiN_2(NH_2)$, $NiN_2(NH_2)_2$ and NiN_2 are energetically favorable to form under the NH_3 atmosphere (formation energy lower than 0 eV), then followed by NiN_3 (Figure 5.11B). This is consistent with the EXAFS fitting with the Ni-N coordination number of 3.3±0.6, which suggests

the formation of unsaturated NiN_3 species or probably a combination of unsaturated NiN_2, NiN_3 and NiN_4. These results are consistent with previous observations that edge-anchored Fe-N structures show lower formation energies and increased stability than in-plane FeN_4 structures.[72, 73] Thus, the high loading of single Ni atoms in the high surface area MEGO results from a large number of edges and defects around the pores that could stabilize Ni single atoms.

Ni single atoms anchored with nitrogen have attracted enormous attention recently[37, 51],[25, 74]. Normally, the in-plane NiN_4 is considered as the active center for CO2RR[37, 51, 74]. However, Zhao et al. proposed that the in-plane NiN_3 could be responsible for CO2RR.[26] Our DFT results reveal that the in-plane NiN_4 exhibits significantly higher energy for CO_2 activation (2.03 eV, CO_2→*COOH) compared with edge NiN_4, while in-plane NiN_3 is quite unfavorabale for CO desorption (1.52 eV, *CO→CO) (Figure 5.11 and Figure 5.12), disclosing that these in-plane Ni-N structures should be less active for CO2RR compared with edge-anchored structures. The edge-anchored saturated NiN_4 is better than the corresponding in-plane NiN_4, but still exhits high enegey for CO_2 activation (1.71 eV, CO_2→*COOH). In contrast, the edge-anchored unsaturated NiN_2 center turns out not favorable for CO desorption due to the high binding energy (1.82 eV) of the CO on NiN_2, even though it shows favorable energy for CO_2→*COOH and *COOH→*CO. The edge-anchored NiN_3, $NiN_2(NH_2)$ structures with moderate degree of unsaturation exhibits optimized energies for CO_2 activation and CO desorption, as the intermediates binding to these edge-anchored unsaturated moistures are neither too strong nor too week. Bear in mind that NiN_4, $NiN_2(NH_2)$, $NiN_2(NH_2)_2$, NiN_2 and NiN_3 are preferentially formed under the NH_3 atmosphere, we could propose that the edge-anchored unsaturated $NiN_2(NH_2)$ and NiN_3 sites could be the best active sites for CO_2 reduction to CO, followed by the edged $NiN_2(NH_2)_2$ and NiN_4, while NiN_2 should be less active due to the strong binding energy of CO.

Materials	Test condition		CO_2RR		References
	Electrolyte	Loading	E_{onset} (V vs RHE)	j_{CO}	
Ni-N-MEGO	0.5 M $KHCO_3$	6.7 wt%	-0.29	26.8 mA cm^{-2} @ -0.70 V	This work
Ni-N-Gr	0.1 M $KHCO_3$	2.2 wt%	-0.50	3 mA cm^{-2} @ -0.80 V	[75]
NiSAs/N-C	0.5 M $KHCO_3$	1.53%	-0.57	10.48 mA cm^{-2} @ -1.00 V	[26]
NiN-GS	0.1 M $KHCO_3$	-	-0.35	4 mA cm^{-2} @ -0.80 V	[25]
Ni-NG	0.5 M $KHCO_3$	0.44 at%	-0.31	11 mA cm^{-2} @ -0.73 V	[76]
Ni-N_4-C	0.5 M $KHCO_3$	1.41 wt%	-0.40	36.2 mA cm^{-2} @ -0.91 V	[37]

C-Zn_xNi_y ZIF-8	1 M $KHCO_3$	5.44 wt%	-0.40	71.5 mA cm^{-2} @ -1.03 V	[77]
A-Ni-NG	0.5 M $KHCO_3$	4.0 wt%	-0.20		[51]
A-Ni-NSG	0.5 M $KHCO_3$	2.5 wt%	-0.15	22.5 mA cm^{-2} @ -0.72 V	
NiSA-N-CNT	0.5 M $KHCO_3$	20.7 wt%	-0.27	4.0 mA/cm^{-2} @ -0.4 V	[74]

Table 5.3 Summarized CO2RR electrochemical activity of NiSA reported so far with the results in this work.

Materials	Test condition		CO_2RR		References
	Electrolyte	Loading and comments	E_{onset} (V vs RHE)	j_{CO}	
Oxide-derived Au	0.5 M $NaHCO_3$	thick amorphous Au oxide layers (>1 μm)	-0.2	2-4 mA/cm^2 @-0.35 V	[63]
Gold nanoparticles	0.5 M $KHCO_3$	-	-0.37	3.1 A/g @ -0.55 V	[4]
Ultrathin (2 nm wide) Au NWs	0.5 M $KHCO_3$	-	-0.2	1.84 A/g@-0.35 V, TOF: 0.02 s^{-1} @-0.35 V	[64]
Au nanoneedles on porous carbon fibers	0.5 M $KHCO_3$	-	-0.25	38 mA/cm^{-2} @ -0.4 V	[78]
Au needles	0.5 M KHCO3	-	-0.25	15 mA cm^{-2} @ −0.35 V	[79]
Oxide-derived nanostructured Ag catalysts	0.5 M $KHCO_3$	0.25 mm thick silver foil	-	1.02 mA cm^{-2}@-0.8 V	[5]
Nanoporous silver	0.5 M $KHCO_3$	thin plates with dimensions of 15 × 5 × 0.20 mm^3	-	19.5 mAcm^{-2} @-0.6 V, TOF: 0.002 s^{-1} @-0.5 V	[6]
Ag nanocoral	0.1 M $KHCO_3$	1.2 mg cm^{-2}	-	2 mAcm^{-2} @-0.37 V; TOF: 0.4 s^{-1} @-0.49 V	[80]

Zn dendrite	0.5 M $NaHCO_3$	-	-	4 mA cm^{-2} @-0.9 V	[10]
Bismuth	MeCN containing 20 mM $[EMIM]BF_4$	-	-	3.77 ± 0.7 mA cm^{-2} @-1.95 V vs SCE;	[81]
Electropolymerized cobalt protoporphyrin	0.1 M K_2SO_4	-	-0.33	TOF: 0.05 s^{-1} @-0.6 V	[65]
FeTDHPP	DMF + 0.1 M n-Bu_4NPF_6	1 mM	-	TOF: $10^{-5.6}$ s^{-1} @-0.73 V	[66]
Fe-Porphyrin-Based Metal–Organic Framework	1 M $TBAPF_6$ in DMF	-	-	TOF: 0.05 s^{-1} @-0.78 V	[82]
CoPc on carbon	0.5 M $NaHCO_3$	-	-0.50	1.85 mA cm^{-2} @-0.6 V	[83]
CoPc-P4VP	0.1 M NaH_2PO_4 (pH 5.7)	-	-0.23	2.4 mA cm^{-2} @-0.73 V	[84]
CoPc-CNT	0.1 M $KHCO_3$	0.4 mg cm^{-2}	-0.30	5.6 mA cm^{-2} @-0.59 V	[85]
Re(R-2,2′-bipyridine)$(CO)_3Cl$	acetonitrile solution and 0.1 M $TBAPF_6$	1 mM	-	13.3 s^{-1} @-2.8 V	[86]
NiN-GS	0.1 M $KHCO_3$	0.2 mg cm^{-2}	-0.35	4.0 mA/cm^{-2} @ -0.81 V	[25]
NiSAs/N-C	0.5 M $KHCO_3$	0.22 mg cm^{-2}	-0.57	7.37 mA cm^{-2} @-1.0 V TOF: 1.46 s^{-1} @ -1.0 V; 0.22 s^{-1} @ -0.7 V	[26]
Ni-N-MEGO	0.5 M $KHCO_3$	0.5 mg cm^{-2}	-0.27	26.8 mA/cm^{-2} @ -0.7 V; 5.3 mA/cm^{-2} @ -0.4 V; TOF: 0.23 s^{-1} @-0.7 V, 0.139 s^{-1} @-0.55 V, 0.04 s^{-1} @-0.4 V，0.02 s^{-1} @-0.29 V	This study

* E_{onset} is obtained based on the linear scan voltammetry results from literature. The potential is

based on SHE except specified.

Table 5.4 Summarized CO_2RR electrochemical activity of typical catalysts.

5.4 Conclusion

Here we successfully tailored the edge structures of porous carbon with Ni single atoms. The porous structure with a high surface area (2649 m^2 g^{-1}) provided large number of anchor sites for single Ni atoms and the nanopores (<6 nm) also help prevent aggregation and stabilize the single atom Ni-N species during high temperature annealing. The unsaturated edge anchored Ni single sites with loading as high as 6.9 % show a mass activity of 53.6 mA mg^{-1} and a high selectivity of 92.1% at an overpotential of 0.59 V for CO2RR. The DFT results identify that the edge-anchored unsataured three nitrogen coordinated Ni single atoms exibit better activity for CO2RR compared with in-plane structures, and the high CO2RR activity originates from the high loading of unsaturated Ni single atoms on edges. Our results provide a new avenue to develop highly efficient noble-metal-free SACs with high loading for electrocatalysis.

5.5 References

[1] B. Kumar, J.P. Brian, V. Atla, S. Kumari, K.A. Bertram, R.T. White, J.M. Spurgeon, New trends in the development of heterogeneous catalysts for electrochemical CO2 reduction, Catal. Today, 270 (2016) 19-30.

[2] D.J. Wilhelm, D.R. Simbeck, A.D. Karp, R.L. Dickenson, Syngas production for gas-to-liquids applications: technologies, issues and outlook, Fuel Processing Technology, 71 (2001) 139-148.

[3] H. Mistry, R. Reske, Z. Zeng, Z.-J. Zhao, J. Greeley, P. Strasser, B.R. Cuenya, Exceptional Size-Dependent Activity Enhancement in the Electroreduction of CO2 over Au Nanoparticles, Journal of the American Chemical Society, 136 (2014) 16473-16476.

[4] W. Zhu, R. Michalsky, Ö. Metin, H. Lv, S. Guo, C.J. Wright, X. Sun, A.A. Peterson, S. Sun, Monodisperse Au Nanoparticles for Selective Electrocatalytic Reduction of CO2 to CO, Journal of the American Chemical Society, 135 (2013) 16833-16836.

[5] M. Ma, B.J. Trześniewski, J. Xie, W.A. Smith, Selective and Efficient Reduction of Carbon Dioxide to Carbon Monoxide on Oxide-Derived Nanostructured Silver Electrocatalysts,

Angewandte Chemie International Edition, 55 (2016) 9748-9752.

[6] Q. Lu, J. Rosen, Y. Zhou, G.S. Hutchings, Y.C. Kimmel, J.G. Chen, F. Jiao, A selective and efficient electrocatalyst for carbon dioxide reduction, Nature Communications, 5 (2014) 3242.

[7] D. Gao, H. Zhou, J. Wang, S. Miao, F. Yang, G. Wang, J. Wang, X. Bao, Size-Dependent Electrocatalytic Reduction of CO2 over Pd Nanoparticles, Journal of the American Chemical Society, 137 (2015) 4288-4291.

[8] W. Sheng, S. Kattel, S. Yao, B. Yan, Z. Liang, C.J. Hawxhurst, Q. Wu, J.G. Chen, Electrochemical reduction of CO2 to synthesis gas with controlled CO/H2 ratios, Energy & Environmental Science, 10 (2017) 1180-1185.

[9] D.H. Won, H. Shin, J. Koh, J. Chung, H.S. Lee, H. Kim, S.I. Woo, Highly Efficient, Selective, and Stable CO2 Electroreduction on a Hexagonal Zn Catalyst, Angewandte Chemie International Edition, 55 (2016) 9297-9300.

[10] J. Rosen, G.S. Hutchings, Q. Lu, R.V. Forest, A. Moore, F. Jiao, Electrodeposited Zn Dendrites with Enhanced CO Selectivity for Electrocatalytic CO2 Reduction, ACS Catalysis, 5 (2015) 4586-4591.

[11] Z. Zhang, M. Chi, G.M. Veith, P. Zhang, D.A. Lutterman, J. Rosenthal, S.H. Overbury, S. Dai, H. Zhu, Rational Design of Bi Nanoparticles for Efficient Electrochemical CO2 Reduction: The Elucidation of Size and Surface Condition Effects, ACS Catalysis, 6 (2016) 6255-6264.

[12] J. Medina-Ramos, R.C. Pupillo, T.P. Keane, J.L. DiMeglio, J. Rosenthal, Efficient Conversion of CO2 to CO Using Tin and Other Inexpensive and Easily Prepared Post-Transition Metal Catalysts, Journal of the American Chemical Society, 137 (2015) 5021-5027.

[13] Z. Yin, D. Gao, S. Yao, B. Zhao, F. Cai, L. Lin, P. Tang, P. Zhai, G. Wang, D. Ma, X. Bao, Highly selective palladium-copper bimetallic electrocatalysts for the electrochemical reduction of CO2 to CO, Nano Energy, 27 (2016) 35-43.

[14] B. Qiao, A. Wang, X. Yang, L.F. Allard, Z. Jiang, Y. Cui, J. Liu, J. Li, T. Zhang, Single-atom catalysis of CO oxidation using Pt1/FeOx, Nat Chem, 3 (2011) 634-641.

[15] J. Liu, F.R. Lucci, M. Yang, S. Lee, M.D. Marcinkowski, A.J. Therrien, C.T. Williams, E.C.H.

Sykes, M. Flytzani-Stephanopoulos, Tackling CO Poisoning with Single-Atom Alloy Catalysts, Journal of the American Chemical Society, 138 (2016) 6396-6399.

[16] S. Yang, J. Kim, Y.J. Tak, A. Soon, H. Lee, Single-Atom Catalyst of Platinum Supported on Titanium Nitride for Selective Electrochemical Reactions, Angewandte Chemie International Edition, 55 (2016) 2058-2062.

[17] P. Chen, T. Zhou, L. Xing, K. Xu, Y. Tong, H. Xie, L. Zhang, W. Yan, W. Chu, C. Wu, Y. Xie, Atomically Dispersed Iron–Nitrogen Species as Electrocatalysts for Bifunctional Oxygen Evolution and Reduction Reactions, Angewandte Chemie International Edition, 56 (2017) 610-614.

[18] H.J. Qiu, Y. Ito, W. Cong, Y. Tan, P. Liu, A. Hirata, T. Fujita, Z. Tang, M. Chen, Nanoporous Graphene with Single-Atom Nickel Dopants: An Efficient and Stable Catalyst for Electrochemical Hydrogen Production, Angewandte Chemie, 127 (2015) 14237-14241.

[19] N. Cheng, S. Stambula, D. Wang, M.N. Banis, J. Liu, A. Riese, B. Xiao, R. Li, T.-K. Sham, L.-M. Liu, G.A. Botton, X. Sun, Platinum single-atom and cluster catalysis of the hydrogen evolution reaction, Nature Communications, 7 (2016) 13638.

[20] B. Zhang, H. Asakura, J. Zhang, J. Zhang, S. De, N. Yan, Stabilizing a Platinum1 Single-Atom Catalyst on Supported Phosphomolybdic Acid without Compromising Hydrogenation Activity, Angewandte Chemie International Edition, 55 (2016) 8319-8323.

[21] L. Wang, W. Zhang, S. Wang, Z. Gao, Z. Luo, X. Wang, R. Zeng, A. Li, H. Li, M. Wang, X. Zheng, J. Zhu, W. Zhang, C. Ma, R. Si, J. Zeng, Atomic-level insights in optimizing reaction paths for hydroformylation reaction over Rh/CoO single-atom catalyst, Nature Communications, 7 (2016) 14036.

[22] R. Lang, T. Li, D. Matsumura, S. Miao, Y. Ren, Y.-T. Cui, Y. Tan, B. Qiao, L. Li, A. Wang, X. Wang, T. Zhang, Hydroformylation of Olefins by a Rhodium Single-Atom Catalyst with Activity Comparable to RhCl(PPh3)3, Angewandte Chemie International Edition, 55 (2016) 16054-16058.

[23] S. Back, J. Lim, N.Y. Kim, Y.H. Kim, Y. Jung, Single-atom catalysts for CO2 electroreduction with significant activity and selectivity improvements, Chem Sci, 8 (2017) 1090-1096.

[24] H. He, Y. Jagvaral, Electrochemical reduction of CO2 on graphene supported transition metals

- towards single atom catalysts, Physical Chemistry Chemical Physics, 19 (2017) 11436-11446.

[25] K. Jiang, S. Siahrostami, A.J. Akey, Y.B. Li, Z.Y. Lu, J. Lattimer, Y.F. Hu, C. Stokes, M. Gangishetty, G.X. Chen, Y.W. Zhou, W. Hill, W.B. Cai, D. Bell, K.R. Chan, J.K. Norskov, Y. Cui, H.T. Wang, Transition-Metal Single Atoms in a Graphene Shell as Active Centers for Highly Efficient Artificial Photosynthesis, Chem, 3 (2017) 950-960.

[26] C. Zhao, X. Dai, T. Yao, W. Chen, X. Wang, J. Wang, J. Yang, S. Wei, Y. Wu, Y. Li, Ionic Exchange of Metal–Organic Frameworks to Access Single Nickel Sites for Efficient Electroreduction of CO2, Journal of the American Chemical Society, 139 (2017) 8078-8081.

[27] J. Liu, Catalysis by Supported Single Metal Atoms, ACS Catalysis, 7 (2017) 34-59.

[28] X.-F. Yang, A. Wang, B. Qiao, J. Li, J. Liu, T. Zhang, Single-Atom Catalysts: A New Frontier in Heterogeneous Catalysis, Accounts of Chemical Research, 46 (2013) 1740-1748.

[29] Y. Wang, M. Qiao, Y. Li, S. Wang, Tuning Surface Electronic Configuration of NiFe LDHs Nanosheets by Introducing Cation Vacancies (Fe or Ni) as Highly Efficient Electrocatalysts for Oxygen Evolution Reaction, Small, 14 (2018) 1800136.

[30] S. Dou, L. Tao, R. Wang, S. El Hankari, R. Chen, S. Wang, Plasma-Assisted Synthesis and Surface Modification of Electrode Materials for Renewable Energy, Advanced Materials, 30 (2018) 1705850.

[31] L. Zhang, Y. Jia, G. Gao, X. Yan, N. Chen, J. Chen, M.T. Soo, B. Wood, D. Yang, A. Du, X. Yao, Graphene Defects Trap Atomic Ni Species for Hydrogen and Oxygen Evolution Reactions, Chem, 4 (2018) 285-297.

[32] Y. Zheng, Y. Jiao, Y. Zhu, Q. Cai, A. Vasileff, L.H. Li, Y. Han, Y. Chen, S.-Z. Qiao, Molecule-Level g-C3N4 Coordinated Transition Metals as a New Class of Electrocatalysts for Oxygen Electrode Reactions, Journal of the American Chemical Society, 139 (2017) 3336-3339.

[33] Y.J. Sa, D.-J. Seo, J. Woo, J.T. Lim, J.Y. Cheon, S.Y. Yang, J.M. Lee, D. Kang, T.J. Shin, H.S. Shin, H.Y. Jeong, C.S. Kim, M.G. Kim, T.-Y. Kim, S.H. Joo, A General Approach to Preferential Formation of Active Fe–Nx Sites in Fe–N/C Electrocatalysts for Efficient Oxygen Reduction Reaction, Journal of the American Chemical Society, 138 (2016) 15046-15056.

[34] D. Deng, X. Chen, L. Yu, X. Wu, Q. Liu, Y. Liu, H. Yang, H. Tian, Y. Hu, P. Du, R. Si, J. Wang, X. Cui, H. Li, J. Xiao, T. Xu, J. Deng, F. Yang, P.N. Duchesne, P. Zhang, J. Zhou, L. Sun, J. Li, X. Pan, X. Bao, A single iron site confined in a graphene matrix for the catalytic oxidation of benzene at room temperature, Sci Adv, 1 (2015) e1500462.

[35] H. Yan, H. Cheng, H. Yi, Y. Lin, T. Yao, C. Wang, J. Li, S. Wei, J. Lu, Single-Atom Pd1/Graphene Catalyst Achieved by Atomic Layer Deposition: Remarkable Performance in Selective Hydrogenation of 1,3-Butadiene, Journal of the American Chemical Society, 137 (2015) 10484-10487.

[36] W.-J. Jiang, L. Gu, L. Li, Y. Zhang, X. Zhang, L.-J. Zhang, J.-Q. Wang, J.-S. Hu, Z. Wei, L.-J. Wan, Understanding the High Activity of Fe–N–C Electrocatalysts in Oxygen Reduction: Fe/Fe3C Nanoparticles Boost the Activity of Fe–Nx, Journal of the American Chemical Society, 138 (2016) 3570-3578.

[37] X. Li, W. Bi, M. Chen, Y. Sun, H. Ju, W. Yan, J. Zhu, X. Wu, W. Chu, C. Wu, Y. Xie, Exclusive Ni–N4 Sites Realize Near-Unity CO Selectivity for Electrochemical CO2 Reduction, Journal of the American Chemical Society, 139 (2017) 14889-14892.

[38] Y. Cheng, S. Zhao, B. Johannessen, J.P. Veder, M. Saunders, M.R. Rowles, M. Cheng, C. Liu, M.F. Chisholm, R. De Marco, H.M. Cheng, S.Z. Yang, S.P. Jiang, Atomically Dispersed Transition Metals on Carbon Nanotubes with Ultrahigh Loading for Selective Electrochemical Carbon Dioxide Reduction, Adv Mater, 30 (2018) e1706287.

[39] Y. Zhu, S. Murali, M.D. Stoller, K.J. Ganesh, W. Cai, P.J. Ferreira, A. Pirkle, R.M. Wallace, K.A. Cychosz, M. Thommes, D. Su, E.A. Stach, R.S. Ruoff, Carbon-Based Supercapacitors Produced by Activation of Graphene, Science, 332 (2011) 1537-1541.

[40] M.A. Lillo-Ródenas, D. Cazorla-Amorós, A. Linares-Solano, Understanding chemical reactions between carbons and NaOH and KOH: An insight into the chemical activation mechanism, Carbon, 41 (2003) 267-275.

[41] S. Zhao, Y. Cheng, J.-P. Veder, B. Johannessen, M. Saunders, L. Zhang, C. Liu, M.F. Chisholm, R. De Marco, J. Liu, S.-Z. Yang, S.P. Jiang, One-Pot Pyrolysis Method to Fabricate Carbon Nanotube Supported Ni Single-Atom Catalysts with Ultrahigh Loading, ACS Applied Energy

Materials, (2018).

[42] C.S. Chen, A.D. Handoko, J.H. Wan, L. Ma, D. Ren, B.S. Yeo, Stable and selective electrochemical reduction of carbon dioxide to ethylene on copper mesocrystals, Catalysis Science & Technology, 5 (2015) 161-168.

[43] G. Kresse, J. Furthmüller, Efficient iterative schemes for ab initio total-energy calculations using a plane-wave basis set, Physical Review B, 54 (1996) 11169-11186.

[44] P.E. Blöchl, Projector augmented-wave method, Physical Review B, 50 (1994) 17953-17979.

[45] J.P. Perdew, K. Burke, M. Ernzerhof, Generalized Gradient Approximation Made Simple, Physical Review Letters, 77 (1996) 3865-3868.

[46] H.J. Monkhorst, J.D. Pack, Special points for Brillouin-zone integrations, Physical Review B, 13 (1976) 5188-5192.

[47] L.M. Malard, M.A. Pimenta, G. Dresselhaus, M.S. Dresselhaus, Raman spectroscopy in graphene, Physics Reports, 473 (2009) 51-87.

[48] H.B. Yang, J. Miao, S.F. Hung, J. Chen, H.B. Tao, X. Wang, L. Zhang, R. Chen, J. Gao, H.M. Chen, L. Dai, B. Liu, Identification of catalytic sites for oxygen reduction and oxygen evolution in N-doped graphene materials: Development of highly efficient metal-free bifunctional electrocatalyst, Sci Adv, 2 (2016) e1501122.

[49] J. Zhong, J.-J. Deng, B.-H. Mao, T. Xie, X.-H. Sun, Z.-G. Mou, C.-H. Hong, P. Yang, S.-D. Wang, Probing solid state N-doping in graphene by X-ray absorption near-edge structure spectroscopy, Carbon, 50 (2012) 335-338.

[50] L.A. Avakyan, A.S. Manukyan, A.A. Mirzakhanyan, E.G. Sharoyan, Y.V. Zubavichus, A.L. Trigub, N.A. Kolpacheva, L.A. Bugaev, Atomic structure of nickel phthalocyanine probed by X-ray absorption spectroscopy and density functional simulations, Optics and Spectroscopy, 114 (2013) 347-352.

[51] W. Liu, Y. Chen, H. Qi, L. Zhang, W. Yan, X. Liu, X. Yang, S. Miao, W. Wang, C. Liu, A. Wang, J. Li, T. Zhang, A Durable Nickel Single-Atom Catalyst for Hydrogenation Reactions and Cellulose Valorization under Harsh Conditions, Angewandte Chemie International Edition, 57

(2018) 7071-7075.

[52] M. Moses-DeBusk, M. Yoon, L.F. Allard, D.R. Mullins, Z. Wu, X. Yang, G. Veith, G.M. Stocks, C.K. Narula, CO Oxidation on Supported Single Pt Atoms: Experimental and ab Initio Density Functional Studies of CO Interaction with Pt Atom on θ-Al2O3(010) Surface, Journal of the American Chemical Society, 135 (2013) 12634-12645.

[53] E.J. Peterson, A.T. DeLaRiva, S. Lin, R.S. Johnson, H. Guo, J.T. Miller, J. Hun Kwak, C.H.F. Peden, B. Kiefer, L.F. Allard, F.H. Ribeiro, A.K. Datye, Low-temperature carbon monoxide oxidation catalysed by regenerable atomically dispersed palladium on alumina, 5 (2014) 4885.

[54] S.F.J. Hackett, R.M. Brydson, M.H. Gass, I. Harvey, A.D. Newman, K. Wilson, A.F. Lee, High-Activity, Single-Site Mesoporous Pd/Al2O3 Catalysts for Selective Aerobic Oxidation of Allylic Alcohols, Angewandte Chemie International Edition, 46 (2007) 8593-8596.

[55] D.A. Bulushev, M. Zacharska, E.V. Shlyakhova, A.L. Chuvilin, Y. Guo, S. Beloshapkin, A.V. Okotrub, L.G. Bulusheva, Single Isolated Pd2+ Cations Supported on N-Doped Carbon as Active Sites for Hydrogen Production from Formic Acid Decomposition, ACS Catalysis, 6 (2016) 681-691.

[56] H. Guan, J. Lin, B. Qiao, S. Miao, A.-Q. Wang, X. Wang, T. Zhang, Enhanced performance of Rh1/TiO2 catalyst without methanation in water-gas shift reaction, AIChE Journal, 63 (2017) 2081-2088.

[57] X. Li, W. Bi, L. Zhang, S. Tao, W. Chu, Q. Zhang, Y. Luo, C. Wu, Y. Xie, Single-Atom Pt as Co-Catalyst for Enhanced Photocatalytic H2 Evolution, Advanced Materials, 28 (2016) 2427-2431.

[58] P. Yin, T. Yao, Y. Wu, L. Zheng, Y. Lin, W. Liu, H. Ju, J. Zhu, X. Hong, Z. Deng, G. Zhou, S. Wei, Y. Li, Single Cobalt Atoms with Precise N-Coordination as Superior Oxygen Reduction Reaction Catalysts, Angewandte Chemie International Edition, 55 (2016) 10800-10805.

[59] W. Liu, L. Zhang, W. Yan, X. Liu, X. Yang, S. Miao, W. Wang, A. Wang, T. Zhang, Single-atom dispersed Co-N-C catalyst: structure identification and performance for hydrogenative coupling of nitroarenes, Chemical Science, 7 (2016) 5758-5764.

[60] H. Fei, J. Dong, M.J. Arellano-Jiménez, G. Ye, N. Dong Kim, E.L.G. Samuel, Z. Peng, Z. Zhu, F. Qin, J. Bao, M.J. Yacaman, P.M. Ajayan, D. Chen, J.M. Tour, Atomic cobalt on nitrogen-

doped graphene for hydrogen generation, 6 (2015) 8668.

[61] Z. Chen, S. Mitchell, E. Vorobyeva, R.K. Leary, R. Hauert, T. Furnival, Q.M. Ramasse, J.M. Thomas, P.A. Midgley, D. Dontsova, M. Antonietti, S. Pogodin, N. López, J. Pérez-Ramírez, Stabilization of Single Metal Atoms on Graphitic Carbon Nitride, Advanced Functional Materials, (2017) 1605785-n/a.

[62] Y. Cheng, S. Zhao, B. Johannessen, J.P. Veder, M. Saunders, M.R. Rowles, M. Cheng, C. Liu, M.F. Chisholm, R. De Marco, H.M. Cheng, S.Z. Yang, S.P. Jiang, Atomically Dispersed Transition Metals on Carbon Nanotubes with Ultrahigh Loading for Selective Electrochemical Carbon Dioxide Reduction, Advanced Materials, 30 (2018).

[63] Y. Chen, C.W. Li, M.W. Kanan, Aqueous CO2 Reduction at Very Low Overpotential on Oxide-Derived Au Nanoparticles, Journal of the American Chemical Society, 134 (2012) 19969-19972.

[64] W. Zhu, Y.-J. Zhang, H. Zhang, H. Lv, Q. Li, R. Michalsky, A.A. Peterson, S. Sun, Active and Selective Conversion of CO2 to CO on Ultrathin Au Nanowires, Journal of the American Chemical Society, 136 (2014) 16132-16135.

[65] J.E. Pander, A. Fogg, A.B. Bocarsly, Utilization of Electropolymerized Films of Cobalt Porphyrin for the Reduction of Carbon Dioxide in Aqueous Media, ChemCatChem, 8 (2016) 3536-3545.

[66] C. Costentin, S. Drouet, M. Robert, J.-M. Savéant, A Local Proton Source Enhances CO₂ Electroreduction to CO by a Molecular Fe Catalyst, Science, 338 (2012) 90-94.

[67] J. Wu, R.M. Yadav, M. Liu, P.P. Sharma, C.S. Tiwary, L. Ma, X. Zou, X.-D. Zhou, B.I. Yakobson, J. Lou, P.M. Ajayan, Achieving Highly Efficient, Selective, and Stable CO2 Reduction on Nitrogen-Doped Carbon Nanotubes, ACS Nano, 9 (2015) 5364-5371.

[68] S. Liu, H. Yang, X. Huang, L. Liu, W. Cai, J. Gao, X. Li, T. Zhang, Y. Huang, B. Liu, Identifying Active Sites of Nitrogen-Doped Carbon Materials for the CO2 Reduction Reaction, Advanced Functional Materials, (2018).

[69] D.S. Hall, C. Bock, B.R. MacDougall, The Electrochemistry of Metallic Nickel: Oxides, Hydroxides, Hydrides and Alkaline Hydrogen Evolution, Journal of The Electrochemical Society,

160 (2013) F235-F243.

[70] M. Gong, W. Zhou, M.-C. Tsai, J. Zhou, M. Guan, M.-C. Lin, B. Zhang, Y. Hu, D.-Y. Wang, J. Yang, S.J. Pennycook, B.-J. Hwang, H. Dai, Nanoscale nickel oxide/nickel heterostructures for active hydrogen evolution electrocatalysis, Nature Communications, 5 (2014) 4695.

[71] S. Wang, Q. Zhao, H. Wei, J.-Q. Wang, M. Cho, H.S. Cho, O. Terasaki, Y. Wan, Aggregation-Free Gold Nanoparticles in Ordered Mesoporous Carbons: Toward Highly Active and Stable Heterogeneous Catalysts, Journal of the American Chemical Society, 135 (2013) 11849-11860.

[72] E.F. Holby, G. Wu, P. Zelenay, C.D. Taylor, Structure of Fe–Nx–C Defects in Oxygen Reduction Reaction Catalysts from First-Principles Modeling, The Journal of Physical Chemistry C, 118 (2014) 14388-14393.

[73] E.F. Holby, P. Zelenay, Linking structure to function: The search for active sites in non-platinum group metal oxygen reduction reaction catalysts, Nano Energy, 29 (2016) 54-64.

[74] Y. Cheng, S. Zhao, B. Johannessen, J.P. Veder, M. Saunders, M.R. Rowles, M. Cheng, C. Liu, M.F. Chisholm, R. De Marco, H.M. Cheng, S.Z. Yang, S.P. Jiang, Atomically Dispersed Transition Metals on Carbon Nanotubes with UltraHigh Loading for Selective Electrochemical Carbon Dioxide Reduction, Adv Mater, (2018) 1706287-n/a.

[75] P. Su, K. Iwase, S. Nakanishi, K. Hashimoto, K. Kamiya, Nickel-Nitrogen-Modified Graphene: An Efficient Electrocatalyst for the Reduction of Carbon Dioxide to Carbon Monoxide, Small, 12 (2016) 6083-6089.

[76] K. Jiang, S. Siahrostami, T. Zheng, Y. Hu, S. Hwang, E. Stavitski, Y. Peng, J. Dynes, M. Gangisetty, D. Su, K. Attenkofer, H. Wang, Isolated Ni single atoms in graphene nanosheets for high-performance CO2 reduction, Energy & Environmental Science, (2018).

[77] C. Yan, H. Li, Y. Ye, H. Wu, F. Cai, R. Si, J. Xiao, S. Miao, S. Xie, F. Yang, Y. Li, G. Wang, X. Bao, Coordinatively unsaturated nickel–nitrogen sites towards selective and high-rate CO2 electroreduction, Energy & Environmental Science, 11 (2018) 1204-1210.

[78] T. Saberi Safaei, A. Mepham, X. Zheng, Y. Pang, C.-T. Dinh, M. Liu, D. Sinton, S.O. Kelley, E.H. Sargent, High-Density Nanosharp Microstructures Enable Efficient CO2 Electroreduction, Nano Letters, 16 (2016) 7224-7228.

[79] M. Liu, Y. Pang, B. Zhang, P. De Luna, O. Voznyy, J. Xu, X. Zheng, C.T. Dinh, F. Fan, C. Cao, F.P.G. de Arquer, T.S. Safaei, A. Mepham, A. Klinkova, E. Kumacheva, T. Filleter, D. Sinton, S.O. Kelley, E.H. Sargent, Enhanced electrocatalytic CO2 reduction via field-induced reagent concentration, Nature, 537 (2016) 382-386.

[80] Y.-C. Hsieh, S.D. Senanayake, Y. Zhang, W. Xu, D.E. Polyansky, Effect of Chloride Anions on the Synthesis and Enhanced Catalytic Activity of Silver Nanocoral Electrodes for CO2 Electroreduction, ACS Catalysis, 5 (2015) 5349-5356.

[81] J.L. DiMeglio, J. Rosenthal, Selective Conversion of CO2 to CO with High Efficiency Using an Inexpensive Bismuth-Based Electrocatalyst, Journal of the American Chemical Society, 135 (2013) 8798-8801.

[82] I. Hod, M.D. Sampson, P. Deria, C.P. Kubiak, O.K. Farha, J.T. Hupp, Fe-Porphyrin-Based Metal–Organic Framework Films as High-Surface Concentration, Heterogeneous Catalysts for Electrochemical Reduction of CO2, ACS Catalysis, 5 (2015) 6302-6309.

[83] N. Morlanés, K. Takanabe, V. Rodionov, Simultaneous Reduction of CO2 and Splitting of H2O by a Single Immobilized Cobalt Phthalocyanine Electrocatalyst, ACS Catalysis, 6 (2016) 3092-3095.

[84] W.W. Kramer, C.C.L. McCrory, Polymer coordination promotes selective CO2 reduction by cobalt phthalocyanine, Chemical Science, 7 (2016) 2506-2515.

[85] X. Zhang, Z. Wu, X. Zhang, L. Li, Y. Li, H. Xu, X. Li, X. Yu, Z. Zhang, Y. Liang, H. Wang, Highly selective and active CO2 reduction electrocatalysts based on cobalt phthalocyanine/carbon nanotube hybrid structures, Nature Communications, 8 (2017) 14675.

[86] M.L. Clark, B. Rudshteyn, A. Ge, S.A. Chabolla, C.W. Machan, B.T. Psciuk, J. Song, G. Canzi, T. Lian, V.S. Batista, C.P. Kubiak, Orientation of Cyano-Substituted Bipyridine Re(I) fac-Tricarbonyl Electrocatalysts Bound to Conducting Au Surfaces, The Journal of Physical Chemistry C, 120 (2016) 1657-1665.

Chapter6: A universal seeding strategy to synthesis single atom catalysts on 2D materials

Abstract

Single-atom catalysts (SACs) are attracting significant attention due to their exceptional catalytic performance and stability. However, the controllable, scalable and efficient synthesis of SACs remains a significant challenge for practical application of SACs. Herein, we report a novel and versatile seeding approach to synthesize SACs with kinds of single metal atoms on two-dimensional (2D) materials such as graphene, boron nitride (BN) and Molybdenum Disulfide (MoS_2). This method has been demonstrated on the synthesis of Ni, Co, Fe, Cu, Ag, Pd single atoms as well as binary atoms of Ni and Cu co-doped on 2D support materials with the mass loading of single atom in the range of 2.8-7.9 wt%. In particular, we demonstrate that nickel-based SACs on graphene oxide (SANi-GO) exhibits excellent catalytic performance for electrochemical CO_2 reduction reaction, with a low overpotential of 0.63V and high selectivity of 96.5% for CO production. The facile, controllable and scalable nature of this approach in the synthesis of SACs is expected to open new research avenues for the applications of SACs.

6.1 Introduction

Single-atom catalysts (SACs), comprised of monodispersed metal atoms on various supports with large surface area, have been demonstrated to exhibit high efficiency and excellent selectivity in energy-related or environmental catalysis, far exceeding those of metal nanoparticles catalysts[1-3]. The high catalytic efficiency of SACs originates from the maximized atom utilization and unique coordination environments of metal atoms. However, the great challenge in the practical application and commercialization of SACs is how to develop a facile method for the synthesis of SACs with high mass loading of single atom and to prevent the aggregation of the single atoms on the supports[4, 5]. Therefore, much effort has been devoted to the synthesis of SACs, ranging from noble metals to non-noble metals[6-8]. Owing to the relative ease of preparation by the impregnation method, metal surface[7-9], metal oxides[10] and metal nitrides[11] have been studied as the potential supports to anchor SACs. However, the large mass ratio and limited surface

area of the supports give rise to a restrained mass loading of SACs in the range of 0.5-3 wt.% [3, 4]. Physical deposition methods such as atomic layer deposition(ALD) [12-14] have also been applied to synthesize SACs, but the catalyst loading is generally less than 1wt% and agglomeration of the single atom to nanoclusters and particles is inevitable after a certain number of deposition cycles. Carbon materials possessing high levels of nitrogen doping with a suitable chemical coordination environment have also been utilized for the support of SACs, including carbon nanotubes(CNTs) [15-18], graphene[19-24], carbon nanosheet[25-27], g-C_3N_4 [28, 29], porous carbon and so on. However, the widespread applicability of the reported methods is also restricted by the limited catalyst loading. Recently, a facile one-pot pyrolysis method has been reported to possesses advantages in achieving high loadings for SACs[20, 22, 30]. Despite the ease of use, the one-pot pyrolysis approach has hitherto been limited to some of transition metals (i.e., Fe, Co and Ni). Moreover, the loading cannot be controllably adjusted, due to multiple high-temperature annealing processes involving in the complex chemical reaction pathway. The mass-selected soft-landing method, a physical deposition method well-known for synthesizing metal clusters with precisely controlled number of atoms, has also been utilized to prepare SACs[31]. But the general conditions required for a soft landing are difficult to achieve in view of the precise control of single atom on the material, as well as the substrate properties including surface energy, hardness, polarizability and temperature, which are difficult to control for the practical applications[32]. Therefore, it is highly desirable to develop a synthetic approach that is easy, controllable, and generally applicable while achieving high mass loading of single metal atoms. Such an approach is highly attractive and would open up possibilities to selectively design on-demand active sites for targeted applications[5, 33].

In this work, we have developed a general strategy, referred to as a seeding approach, to synthesize wide range of SAs on various 2D materials (including Graphene, MoS_2, and BN) by utilizing single metal atom dispersed carbon nitride (CNx) as the seed. The synergistic combination of 2D materials and single metal atom seeds makes it possible to achieve SACs with tunable mass loading and superior catalytic performance that cannot be otherwise achieved by using conventional synthesis method. In contrast to previously reported methods, the seeding strategy reported herein exhibits distinct advantages with respect to the compatibility of different metal elements and different substrates. To some extent, the loading can also be adjusted to satisfy the needs of various applications by simply controlling the seed concentration and content. The

synthesized SACs exhibit high dispersion and uniformity, void of any aggregation, opening up prospects for further studies into their electrochemical, photochemical and thermal properties. For example, nickel-based SACs-GO exhibits excellent catalytic performance for electrochemical CO_2 reduction reaction, with a low overpotential of 0.63V and high selectivity of 96.5% for CO production.

6.2 Experimental

6.2.1 Materials synthesis

Synthesis of single atom seed on CNx (SA-Seed). All chemicals were purchased from Sigma-Aldrich unless otherwise specified. All the annealing process is done at Ar atmosphere. Dicyandiamide ($C_2H_4N_4$, DCD) was heated at a ramping rate of 7 ^oC per min and held at 350 ^oC for 1 h, noted as DCD-350. Metal acetylacetonate($Me(acac)_x$) encompassed nickel(II) acetylacetonate, cobalt (II) acetylacetonate, iron (III) acetylacetonate, copper (II) acetylacetonate, silver acetylacetonate and palladium (II) acetylacetonate. The $Me(acac)_x$ ethanol solution (50% distilled water with 10 mg/ml citric acid) was added dropwise to DCD-350(with Metal content of 1wt% vs DCD-350) whilst grinding. The mixture was subsequently annealed at 650-700 ^oC for 2 h, noted as SA-Seed (Me = Ni, Co, Fe, Cu, Ag, Pd). SA-Seed with two different metal atoms was also prepared in similar way.

Synthesis of single atom on 2D material (SA-2D material). The 2D material was dispersed with poly ethyleneimine (PEI) solution (50% (w/v) in H_2O,) and polyvinylpyrrolid (PVP, average mol 40000) (with mass ratio=1:1; 50 wt % in total) in ethanol and sonicated for 20 mins. SA-Seed was subsequently added to the above-mentioned solution and sonicated by tip sonication for 1 h. Afterwards, the mixture was stirred for 5 h, dried and grounded to fine powder. The as-prepared powder was subsequently heated in a horizontal furnace at 800 ^oC and held for 1h. During the heating stage, the temperature was held constant for 2 h at 650-700 ^oC prior to final ramping to 800 ^oC. Finally, the SA-2D material was obtained. All other single or binary metal atoms were prepared using the same procedure as described above.

Thermally reduced graphene oxide (GO) was synthesized based on one method reported previously[47]. Here, g-C_3N_4 was synthesized via an annealing of DCD at 650 ^oC for 1 h. Nitrogen-

doped graphene was synthesized by mixing DCD-350 with graphene oxide and annealing at 800 ^{o}C for 1 h. Ni-GO was synthesized through our previously reported microwave method[48]. MoS_2 nanosheets (ACS Materials, USA) were used as received, without further purification. BN nanosheets were synthesized based on the approach of a previous study[34].

6.2.2 Structural characterizations

X-Ray Diffraction (XRD) data were collected with a Bruker D8 Advance diffractometer operated at 40 kV and 40 mA with Cu Kα (λ = 1.5406 Å) in the range of 10-80°. The specific surface area was calculated by the Brunauer–Emmett–Teller (BET) method. The inductively coupled plasma atomic emission spectroscopy (TJA RADIAL IRIS 1000, ICP-AES) was used to determine the mass content of each metal. Nitrogen adsorption/desorption characteristics were determined using a Micromeritics ASAP 2020 instrument at 77 K. The Microstructure and morphology of SA-2D material samples were obtained using scanning electron microscopy (SEM, Zeiss Neon 40 EsB) and high-resolution transmission electron microscopy (HRTEM, FEI Titan G2 80-200 TEM/STEM). High angle annular dark field scanning transmission electron microscopy (HAADF-STEM) imaging and element mapping were performed through ChemiSTEM Technology operating at 200 kV. The elemental mapping was obtained via energy dispersive X-ray spectroscopy using the Super-X detector on the Titan instrument with a probe size ~1 nm and a probe current of ~0.4 nA. The SA-2D material samples were dispersed and deposited onto TEM sample grids using a high purity anhydrous ethanol solution. High-resolution aberration-corrected scanning transmission electron microscopy annular dark field images (AC-STEM-ADF) and annular bright field images (AC-STEM-ABF) were carried out by a Nion UltraSTEM100 microscope operating at 60 kV at a beam current of 60 pA. The recorded images were filtered through a Gaussian function (full width half maximum = 0.12 nm) to reduce high frequency noise. The convergence half angle of the electron beam was set to 30 mrad and the inner collection half angle of the ADF images was 51 mrad. The samples were dried at 160 ^{o}C overnight prior performing STEM. XPS measurements were carried out using a Kratos AXIS Ultra DLD system with monochromated Al Kα X-rays (1486.7 eV) operating at 225 W. The vacuum pressure of 1 x 10^{-9} mbar or better was kept throughout the duration of the experiment. The high-resolution spectra were collected with a pass energy of 160 eV for survey and 40 eV. The spectra were analyzed using CasaXPS software and further calibrated by shifting the main peak in the C 1s spectrum to 284.5 eV associated with SP2 carbon. Element loading of C, N, O, H was obtained by the elemental

analyzer (Elementar, vario MICRO cube) at 950 ºC. Raman patterns tests were performed using one alpha300 RA Correlative Raman-AFM Microscope with a 532 nm He−Ne laser. The spectrum represents the average of 20 scans. Near edge x-ray absorption structure (NEXAFS) spectroscopy measurements were performed at the Soft X-Ray beamline of the Australian Synchrotron[35]. These measurements were carried out under ultra-high vacuum (UHV) conditions with a base pressure of 5 x 10^{-10} mbar or better. All spectra were obtained in partial electron yield (TEY) mode. All NEXAFS spectra were processed and normalized using the QANT software program developed at the Australian Synchrotron[36]. X-ray absorption spectroscopy (XAS) measurements were carried out at the XAS Beamline (12ID) at the Australian Synchrotron in Melbourne. With the beamline optics employed (Si-coated collimating mirror and Rh-coated focusing mirror) the harmonic content of the incident X-ray beam was negligible. The powder samples were made into pellets via mechanical grinding with cellulose binder using a mortar/pestle for at least 30 mins. Both fluorescence and transmission spectra were recorded based on the concentration of Ni in each sample (the validity of this method was confirmed through comparing the fluorescence and transmission spectra for one of the samples for which both methods yielded comparable signal-to-noise data). All XAS data were processed on Athena software.

6.2.3 Computational methods.

In this work, the density functional theory (DFT) calculations were performed by using the Vienna Ab-initio Simulation Package[37] with the projector augmented wave method[38] to describe the electron-ion interaction. The Perdew-Burke-Ernzerhof functional was used for the exchange-correlation term[39]. The plane-wave cutoff was set to be 400 eV. A 2×2×1 g-C_3N_4 and a 6×6×1 graphene supercell with the vacuum thickness of 15 Å were used to calculate the binding energy of metal atom in the g-C_3N_4 and N-doped graphene, respectively. The Monkhorst-Pack (3×3×1) k-point was used to sample the Brillouin zone. For 3d metal atoms, we have considered the V, Cr, Mn, Fe, Co, Ni, and Cu atoms. For 4d metal atoms, we only considered the Pd, Ag, and Cd atoms in this work.

6.2.4 Electrochemical measurements

Electrochemical CO_2 reduction reaction (CO_2RR) experiments were performed using a BioLogic VMP3 workstation with a customized gastight H-type glass cell that was separated thorough Nafion cation-exchange membrane (Nafion-117, Fuel Cell Store). Before assembling the device,

all of the glass components of the H-type cell were immersed in 1M nitric acid solution overnight to remove the trace amount of contaminated metals, with subsequent rinsing with deionized water and complete drying in an oven. The tests were performed in a typical three-electrode test system with a saturated calomel electrode (SCE) and a platinum foil as the reference and counter electrodes, respectively. To prepare the working electrode, the catalyst ink was prepared by ultrasonically mixing 10 mg of catalysts with 1.85 ml of anhydrous ethanol and 0.15 ml of 5 weight % (wt %) Nafion solution for 1 hour. The suspension of 10 µl was deposited on glassy carbon electrode (GCE) (5 mm in diameter) and dried naturally under ambient condition. Catalyst loading was controlled about 0.52 mg/cm^2. The electrolyte was 0.5 M $KHCO_3$, which was purified by electrolysis between two graphite rods at -0.15 mA for 24 h under CO_2 flow to remove any trace amount of metal ions. Furthermore, the electrolyte was obtained after filtering through a polyethersulfone membrane (0.22 micron). Before testing, the average flow rate of CO_2 was controlled at 20.0 standard cubic centimetres per minute (sccm), monitored by Alicat Scientific mass flow controller, for 30 minutes to make the electrolyte saturated with CO_2. During electrolysis, CO_2 gas was also kept delivering into the electrolyte (stirring at 400 r.p.m.) in the working area with a rate of 20.0 sccm and the outlet gas containing gas products was introduced into an on-line gas chromatography (GC, SRI 8610). All electrochemical measurements were tested versus the SCE reference electrode and converted into the reversible hydrogen electrode (RHE) from the following equations: E (vs RHE) = E (vs SCE) + 0.244V + 0.0591 × pH, where pH values of electrolytes were obtained through one pH Meter (Thermo Scientific). The prereduction of the catalyst was performed by holding the working potential at −0.23 V versus RHE in CO_2-saturated electrolyte until the current reached a stable value. The stability test was done on the carbon fiber paper (Toray) electrode through drop-painting catalyst ink(1mg/ml). The area of the electrode was fixed as 1 cm^{-2} and loading of 0.5 mg/cm^2.

The gas products were quantified by a gas chromatograph (GC), which was equipped with three columns (MS 13X, Hayesep D and MS 5A) and thermal conductivity detector (TCD) and two detectors (flame ionization detector, FID). The TCD detector was mainly used for the H_2 quantification, while FID combined with a methanizer was used for the analysis of carbon monoxide (CO) and hydrocarbons. All the detectors were calibrated using standard gas mixtures with different concentrations. The liquid products were analyzed by NMR spectroscopy (Varian Inova 600 MHz) with one water suppression technique. In a typical case, 0.5 ml electrolyte was

uniformly mixed with 0.1 ml deuterated water (D_2O, Sigma-Aldrich, 99.9 atom % deuterium) as well as 0.05 µl dimethyl sulfoxide (DMSO, Sigma, 99.99%) as an internal standard reference. The NMR spectroscopy was also calibrated using standard liquid products with different concentrations before tests.

6.3 Result and discussion

6.3.1 SACs preparation and characterization

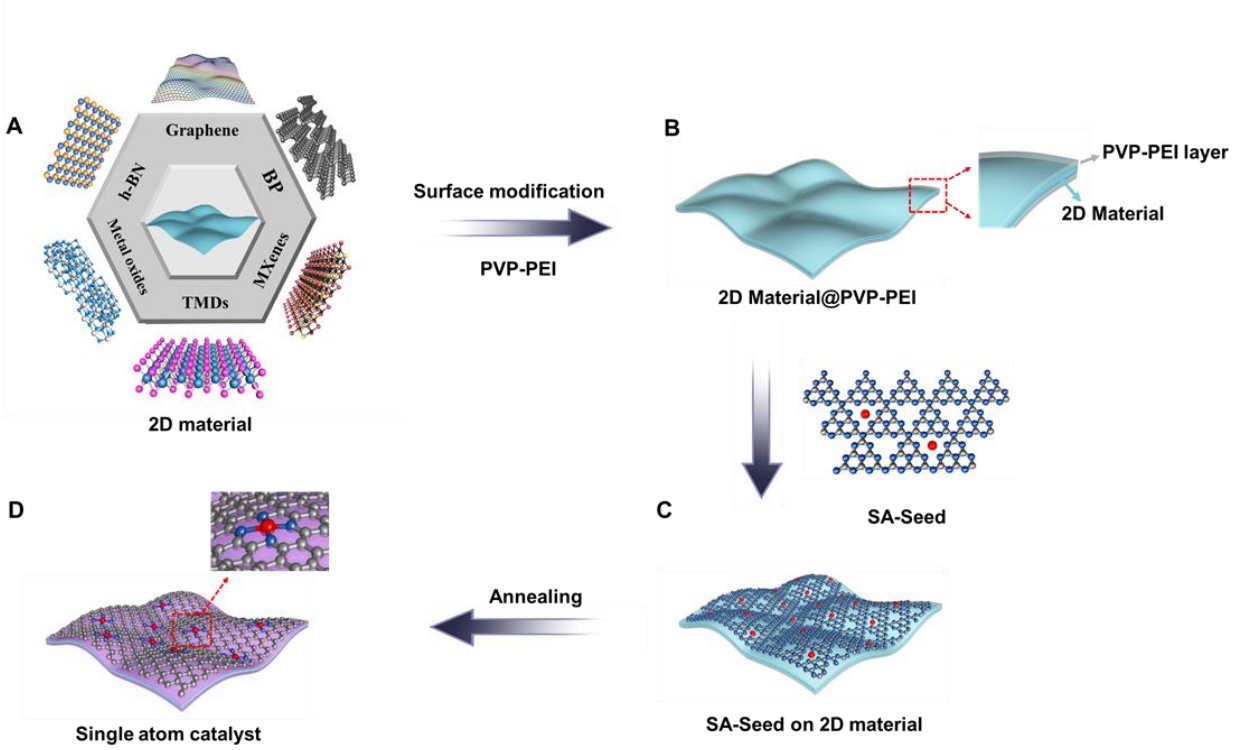

Figure 6.1 The schematic of synthesis of SA-2D material through hard loading process. (A) 2D material. (B) the modified 2D material, where the red inserted area shows the PVP/PEI layer on the 2D material. (C) the uniform mixing between SA-Seed and 2D material. (D) the SA-2D material obtained through hard landing approach.

To load the SAs onto the 2D materials with large surface area, we have developed a seeding approach which mainly included three steps of the SA-seed preparation, surface modification of the 2D materials and final high temperature annealing (Figure 6.1). The preparation of SA-Seed involves a two-step process, including metal absorption followed by annealing process (Figure

6.2).

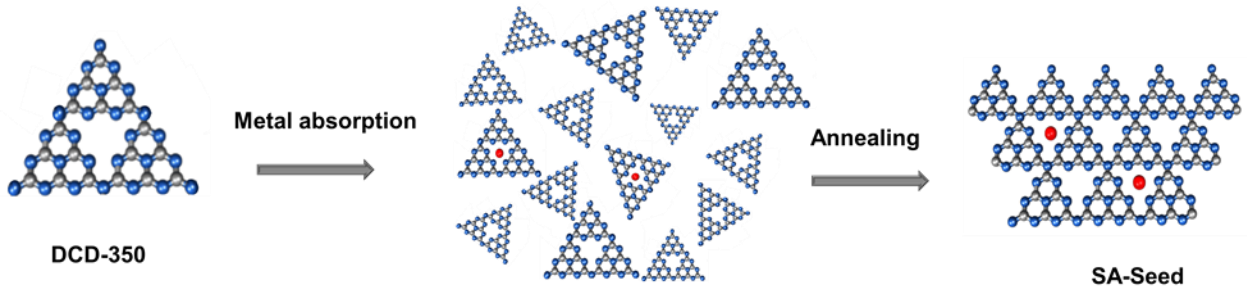

Figure 6.2 the synthesis mechanism schematic of SA-Seed.

The strategy was illustrated by making the nickel single atom catalysts by using graphene oxide as the support. SANi-Seed posseses a nanosheet-type structure after annealing at 660 ºC for 2h (Figure 6.3). The abberration-corrected high-angle annular dark-field (AC-HAADF) image (Figure 6.3h) confirms that single Ni atoms are trapped within the g-C_3N_4 layer structure, being anchored in the six-fold interstices between tri-s-triazine units[40].

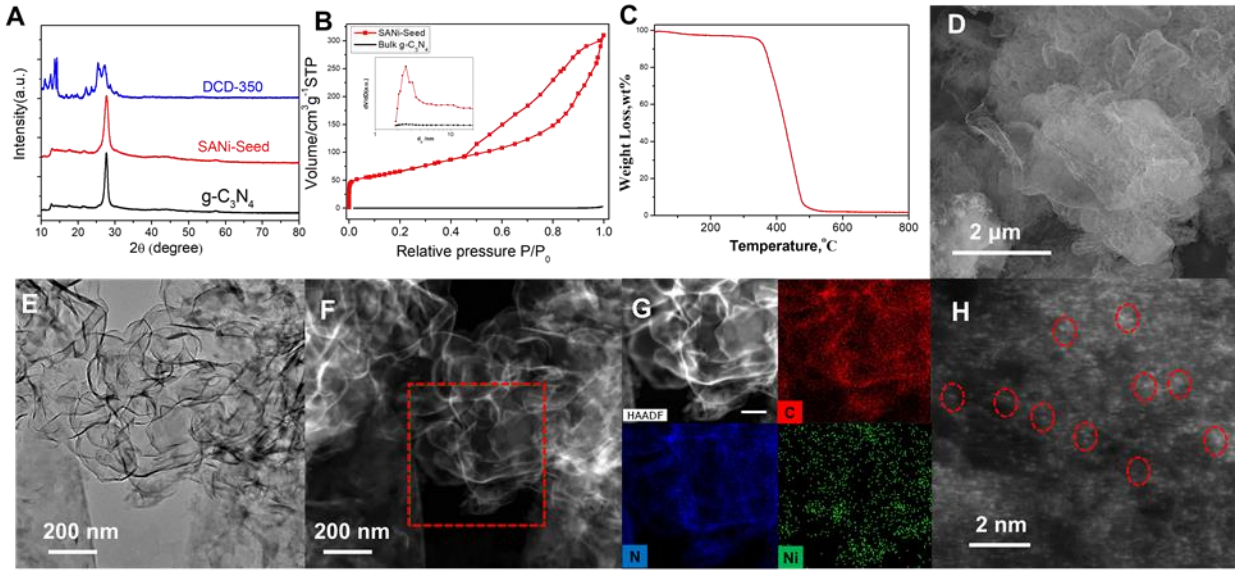

Figure 6.3 Structural investigation of SANi-Seed. (A)XRD patterns of DCD-350, bulk g-C_3N_4 and SANi-Seed. (B)Nitrogen isotherms and corresponding Barrett-Joyner-Halenda mesopore size distributions (inset) of SANi-Seed and bulk C_3N_4. (C) the TGA of SA-Seed. (D)SEM image of SANi-Seed. (E)TEM image of SANi-Seed. (F) STEM image of SANi-Seed. (G) EDS patterns of elements Carbon, nitrogen, and nickel, the scale bars are 100 nm. (H) AC-HAADF image, the red cycled stands for Ni atoms.

To increase the dispersibility and absorption capacity, GO was first modified or functionalized with PVP and PEI, which serves as an essential step to anchor the single atoms. SANi-Seed is similar to that g-C_3N_4 without peaks associated with Ni nanopartilces. The XRD pattern for SANi-Seed is close to g-C_3N_4, different from the DCD-350 which is consistent with melem structure (Figure 6.3A). The SANi-Seed shows a much higher surface area of 235 m^2/g than the C_3N_4 bulk of only 8 m^2/g(Figure 6.3B). TGA analysis indicates that the content of Ni in the SANi-Seed is about 1.3 wt%, consistent with the ICP test (Figure 6.3C). The EDS reveals the N and Ni elements uniformly dispersed on the surface of nanosheet structure(Figure 6.3G). The STEM resluts in Figure 6.3H confirm the good dispersion of Ni atoms.

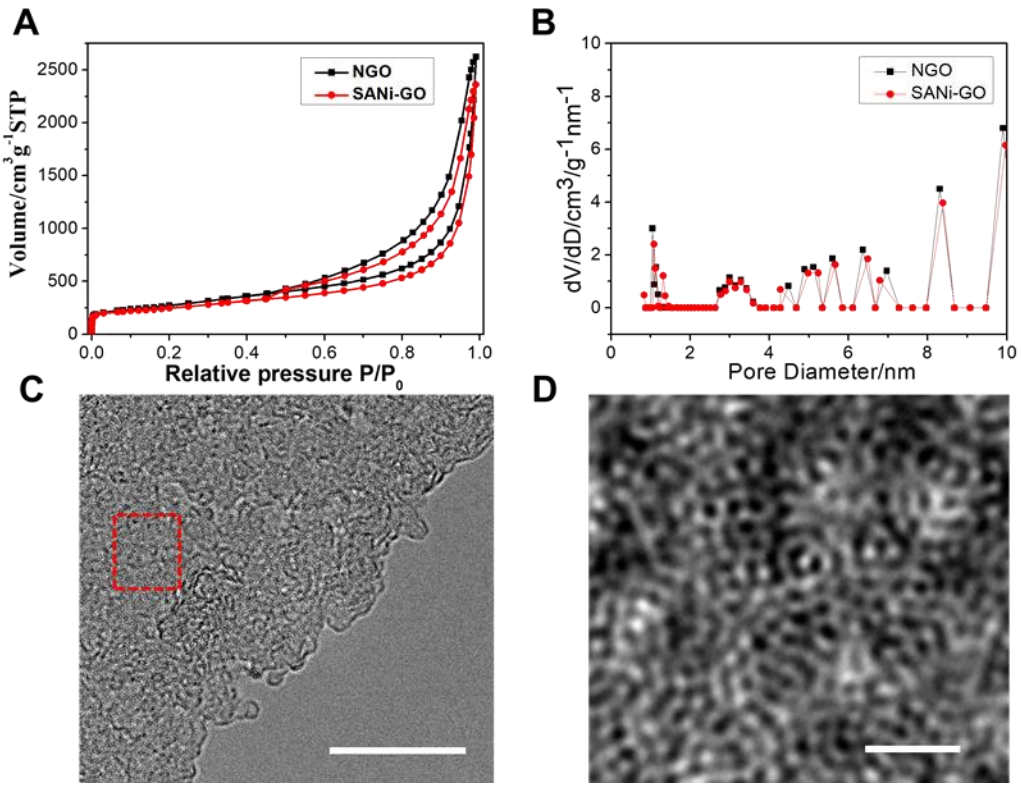

Figure 6.4 (A) Nitrogen adsorption–desorption isotherms of NGO and SANi-GO. (B) the DFT pore distribution. (C) TEM image of SANi-GO, scale bar: 10 nm. (D) HRTEM image in the selected area in c, scale bar: 1 nm.

The surface area of SANi-GO is 816 m^2g^{-1} with a pore volume of 3.4 cm^3 g^{-1}, close to that of N-doped GO (3.8 cm cm^3 g^{-1}) (Figures 6.4A, B). There is a clear formation of abundant defects, which provides abundant coordination positions for Ni. The micro pore increases in SANi-GO around 1 nm, which is consistent with abundant defects (Figures 6.4CD).

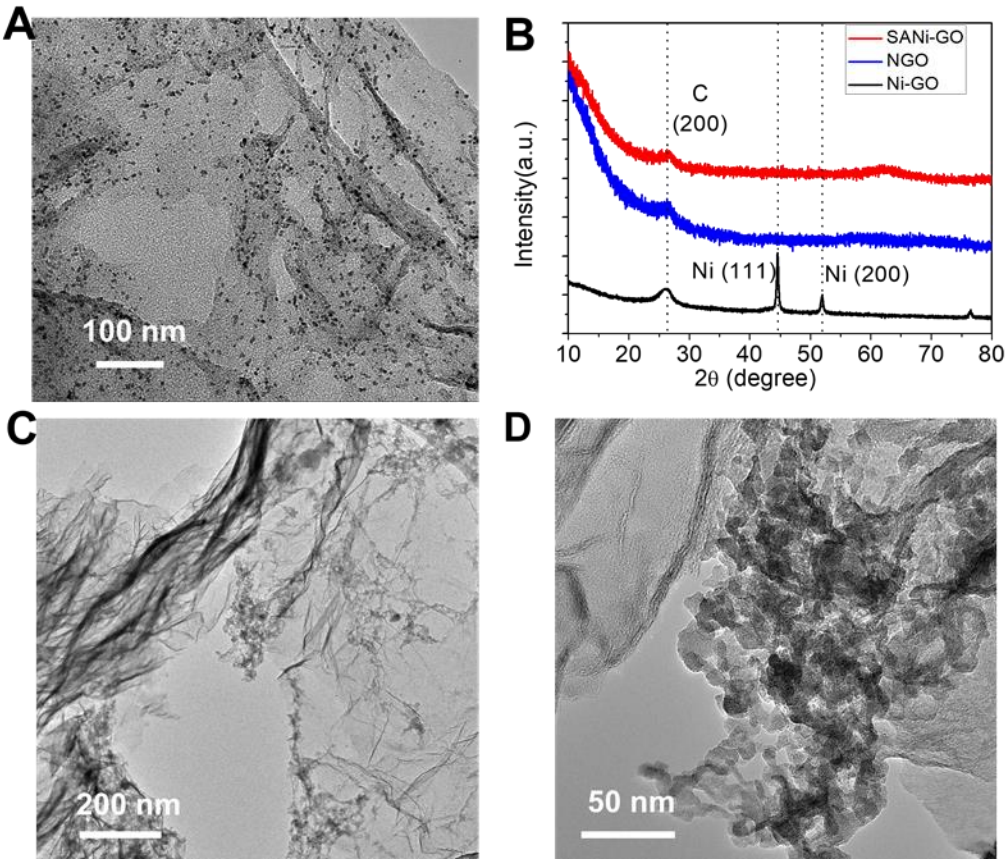

Figure 6.5 (A) the TEM images of Ni-GO, the average particle size of Ni is about 8 nm, with the loading around 6 wt%. (B)XRD patterns of Ni-GO, NGO and SANi-GO. the TEM images of GO-Ni without PEI and PVP modification. (C) low magnification. (D) higher magnification. Only the characteristic carbon peak (200) at 26.2° was observed for SANi-GO. It confirms that without PVP and PEI, metal carbide aggregation occurs on the surface of graphene. The PVP and PEI modification plays one vital role for the synthesis of SACs.

If without surface modification, the metal carbide aggregation occurs on the support (Figures 6.5C and D). The uniform deposition of SANi-Seed on GO is most likely through the non-covalent interaction between PVP/PEI functionalized GO and SANi-Seed, similar to the self-assembly process[42]. The slow annealing process caused the gradual decomposition of SANi-Seed, leading to the formation of single atoms anchored uniformly onto GO, namely SANi-GO.

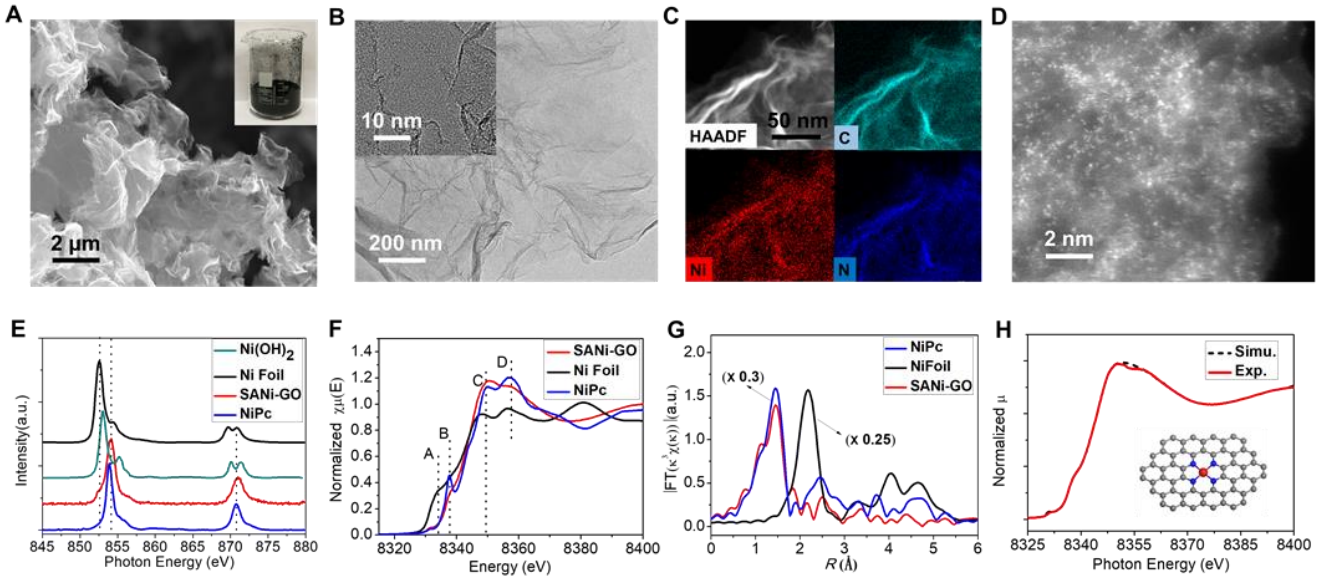

Figure 6.6 Structural Characterization of SANi-GO(A) SEM image of SANi-GO, scale bar: 2 μm, the inserted optical image is 0.63g SANi-GO. (B) typical TEM image of SANi-GO, scale bar: 200 nm, insert shows the HRTEM image, scale bar: 10 nm. (C) the element maps showing the distribution of carbon(green), nickel(red) and nitrogen(blue)scale bar: 30 nm. (D) the AC-STEM image, the scale bar is 4 nm. (E) NEXAFS spectrum of Ni. (F) Ni K-edge XANES spectra of NiPc, Ni foil, and SA-GO-Ni. (G) Fourier transformation of the EXAFS spectra, in which the NiPc and Ni foil spectrum has been reduced in size. (H) comparison of a simulated XANES spectrum of the inserted Ni-core structure with experimental results, the grey, blue and red spheres represent the C, N, Ni, respectively.

The SANi-GO exhibits smooth 2D structure and inserted optical image indicates the fluffy black product with a mass of 630 mg, indicating this method is scalable (Figure 6.6A). The SANi-GO was then characterized by high-resolution transmission electron microscopy and no nanoparticles were observed (Figure 6.6B). The XRD patterns confirm that the SANi-GO is alike to that of the GO without any signals of metallic nickel or Ni nanoparticles detectable (Figure 6.7B), consistent with the TEM results.

Importantly, the energy dispersive spectrum (EDS) elemental mapping images indicated that the C, Ni, N elements are uniformly distributed throughout the entire structure (Figure 6.6C). Isolated single atoms were atomically dispersed on the substrate as shown by the AC-STEM image (Figure 6.6D). XPS pattern of Ni 2p confirm the Ni is Ni^{2+} (Figure 6.7A), and the N 1s is also dominated

by pyrrolic nitrogen which is consistent with Ni-N structure[23,43].

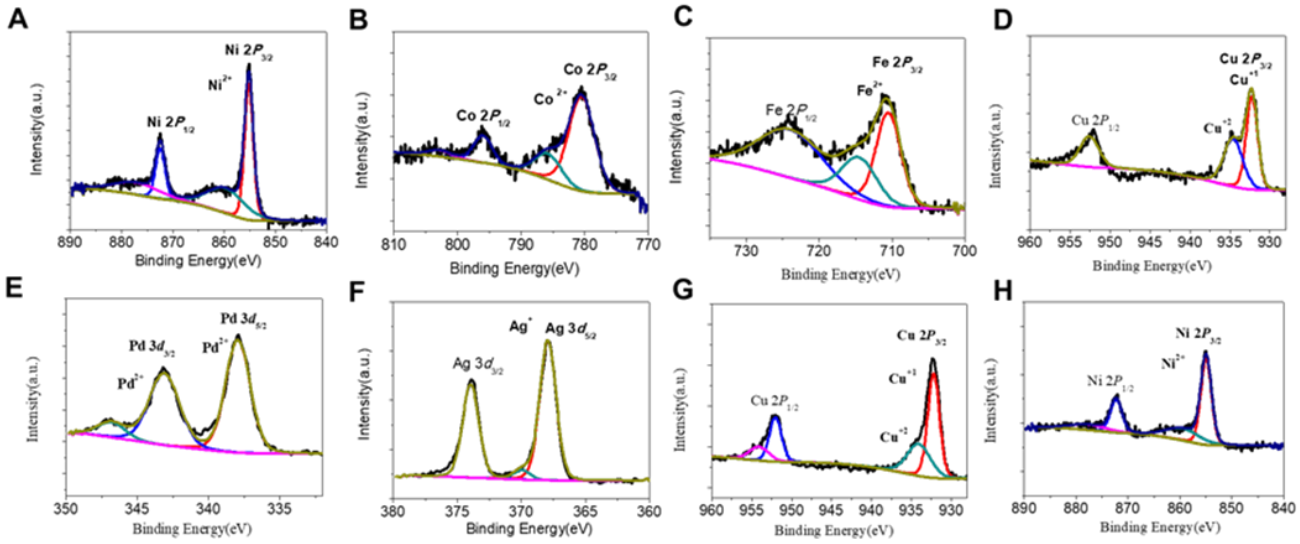

Figure 6.7 XPS patterns of SA-GO. (A) Ni 2p of SANi-GO. (B)Co 2p of SACo-GO. (C) Fe 2p of SAFe-GO. (D)Cu 2p of SACu-GO.(E) Pd 3d of SAPd-GO. (F) Ag 3d of SAAg-GO. (G)and (H) Ni, Cu 2p of SACuNi-GO. The XPS results confirm the metal atoms are in the form of ion not particles.

X-ray absorption spectroscopy (XAS) measurements were performed to further characterize the local coordination environment of Ni. As shown in Figure 6.6E, the Ni K-edge NEXAFS spectra for the SANi-GO exhibit strong similarities to that of nickel phthalocyanine (NiPc), suggestive of the existence of Ni-N bonds in SANi-GO. By contrast, the spectra are dissimilar to Ni metal, which compliments XPS observations that pointed to a lack of Ni (0). The Ni K-edge is shown in Figure6.7b, where the pre-edge at around 8333 eV in position A is attributed to the dipole-forbidden but quadrupole-allowed transition (1s→3d), which is corresponding to 3d and 4p orbital hybridization of the Ni center atom. The integrated pre-edge peak intensity of NiPc is inconspicuous, which can be explained by its high D4h centrosymmetry[22]. The increase in the pre-edge peak intensity in SANi-GO is attributed to increased dipole-allowed transitions (1s→4p), which occur through mixing of the 3d and 4p orbitals because of the distorted D4h symmetry. In contrast with that found from NiPc, the intensities of the 1s→4pz transition (peak B) in SANi-GO are reduced. These transitions act as an evidence for square-planar M-N4 moieties, and this result further confirms the distorted D4h symmetry of the Ni atoms from SANi-GO, contrary to that

observed in NiPc. The Fourier-transform of the extended X-ray absorption fine structure (EXAFS) spectra is presented in Figure 6.6G. A dominant peak at 1.34 Å consistent with NiPc and assigned to the Ni-N coordination is evident, which demonstrates the bonding environment of Ni in SANi-GO. The simulated near edge curve (Figure 6.7H) matches well with the experimental result, which confirms the existence of Ni-N4 structure in SANi-GO[41, 42].

In order to obtain a more comprehensive understanding of the synthesis process of Me-N4 atomistic structure, DFT calculations were performed to explore the thermodynamic stability of different metal atoms in g-C_3N_4 and Me-N4 (Figure 6.8A). After a full relaxation, the metal atoms preferred to locate in the six-fold interstices between tri-s-triazine units of g-C_3N_4[43]. The Ni was stabilized by the surrounding carbon and nitrogen, which prevented the Ni from aggregation. Pure DCD-350 completely decomposed at 660 ºC after 2 h, which further confirms the critical role of metal atoms in stabilizing the g-C_3N_4 structure. Nevertheless, binding energy calculations show that it is energetically unstable for the single metal atoms in the g-C_3N_4 environment, due to weak interactions between metal atoms and g-C_3N_4. When the temperature increases up to 800 ºC, the six-fold interstices structure transforms into a strong Me-N4 stable structure anchored on the surface of substrate. Among the series of single atom metals explored in this study, the Me-N4 structure on graphene is considered to be energetically stable (Table 6.1).

Structure	E_{total} (eV)	E_{atom} (eV)	$E_{binding1}$ (eV)
g-C_3N_4	-471.443		
V-g-C_3N_4	-480.398	-8.959	-0.004
Cr-g-C_3N_4	-480.231	-9.515	-0.727
Mn-g-C_3N_4	-480.033	-8.917	-0.327
Fe-g-C_3N_4	-478.281	-8.260	-1.422
Co-g-C_3N_4	-476.512	-7.034	-1.965
Ni-g-C_3N_4	-475.496	-5.496	-1.443
Cu-g-C_3N_4	-473.889	-3.760	-1.314
Pd-g-C_3N_4	-474.424	-5.206	-2.225
Ag-g-C_3N_4	-472.945	-2.701	-1.199
Cd-g-C_3N_4	-471.390	-0.735	-0.788
Structure	E_{total} (eV)	E_{atom} (eV)	$E_{binding2}$ (eV)
4N-Gr	-638.802		
V-4N-Gr	-649.933	-8.959	2.173
Cr-4N-Gr	-650.980	-9.515	2.664
Mn-4N-Gr	-650.551	-8.917	2.832
Fe-4N-Gr	-649.374	-8.260	2.313
Co-4N-Gr	-648.330	-7.034	2.494
Ni-4N-Gr	-647.218	-5.496	2.920
Cu-4N-Gr	-644.270	-3.760	1.708
Pd-4N-Gr	-646.052	-5.206	2.044
Ag-4N-Gr	-641.013	-2.701	-0.49
Cd-4N-Gr	-639.179	-0.735	-0.358

Table 6.1 Summary of the binding energy based on DFT calculations for metal atom in g-C_3N_4 and metal atom in 4 Nitrogen graphene(Me-4N-Gr), $E_{binding1} = E_{total}$ (g-C_3N_4) + $E_{atom} - E_{total}$ (metal-g-C_3N_4) $E_{binding2} = E_{total}$ (4N-Gr) + $E_{atom} - E_{total}$ (Me-4N-Gr). E_{atom} is the energy of metal atom in the corresponding bulk metal. According to the definition of binding energy, negative value of the $E_{binding1}$ and/or $E_{binding2}$ means an energetically unstable structure.

Consequently, it is reasonable to speculate that, at high temperatures, metal atoms prefer to take the Me-N4 structure in graphene rather than the Me-g-C_3N_4 structures. It should be noted that, among the metal atoms studied in this work, the Ni-N4 structure on graphene possesses the highest positive binding energy, indicative of its high stability, which is also consistent with our experimental results[22]. The methods to achieve SAMe-Seed are significantly versatile, which

establishes the premise of dispersing wide range of metal single atoms (Figures 6.8).

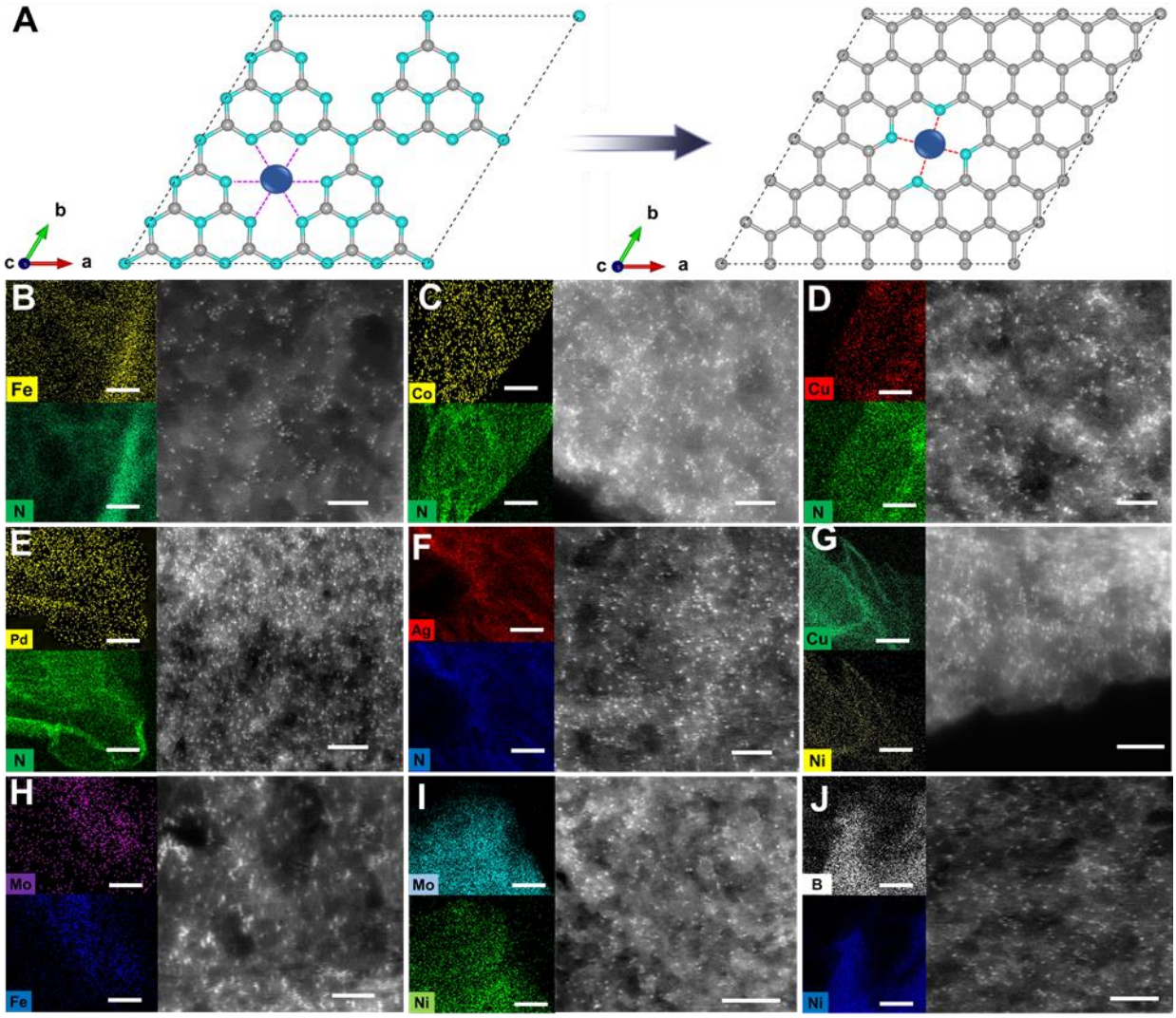

Figure 6.8 DFT calculation of SA synthesis and structural investigations of various SAMe-2D materials. (A)Schematic structures of g-C_3N_4-Me and Graphene-N4, the grey, green, blue balls denote the C, N, and metal atoms, respectively. High-angle annular dark field (HAADF)-STEM-EDS mapping and AC-STEM images. (B) SAFe-GO. (C) SACo-GO. (D) SACu-GO. (E)SAPd-GO. (F) SAAg-GO. (G) SACuNi-GO. (H) SAFe-MoSx. (I)SANi-MoSx. (J) SANi-BN.

Through seeding approach, the synthesis of SACs is not only applicable to transition metal (Fe, Co, Ni, Cu), but also can be easily extended to noble metals like Ag and Pd (Figures 6.8B-F). Besides single metal elements, binary metal SACs can also be achieved through careful preparation of the SAMe-Seed using two metal sources together, such as but not limited to Cu and

Ni, dispersed within CNx (Figure 6.8F). After the seeding process, the Cu and Ni atoms were separately loaded on the surface of graphene (Figure 6.8G). Furthermore, the structure of SAMe-GO has been investigated by Raman and XRD, which indicates the basic graphene sheet structure with typical carbon peaks (Figures 6.9 A,B).

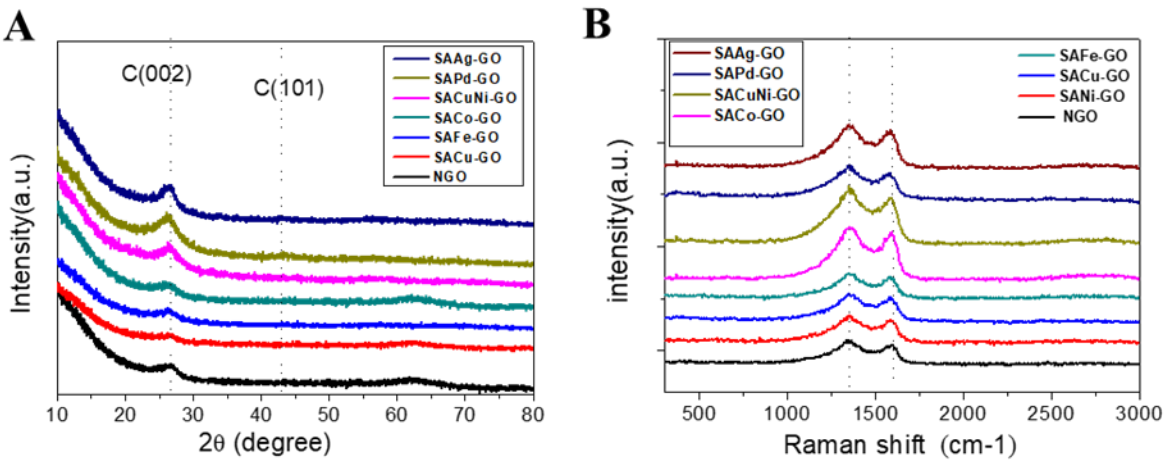

Figure 6.9 Investigation of SA-GO. (A) XRD. (B) Raman patterns.

XPS initially shows a high nitrogen content in SAMe-GO of more than 9.5 at. % (Table 6.2) and Me-N elemental environment, where sufficient nitrogen could confine the metal single atom. The electronic structure of SAFe-GO were also characterized by XAS measurements (Figure 6.10), where the Me-N4 structure is consistent with recent reports[22, 42].

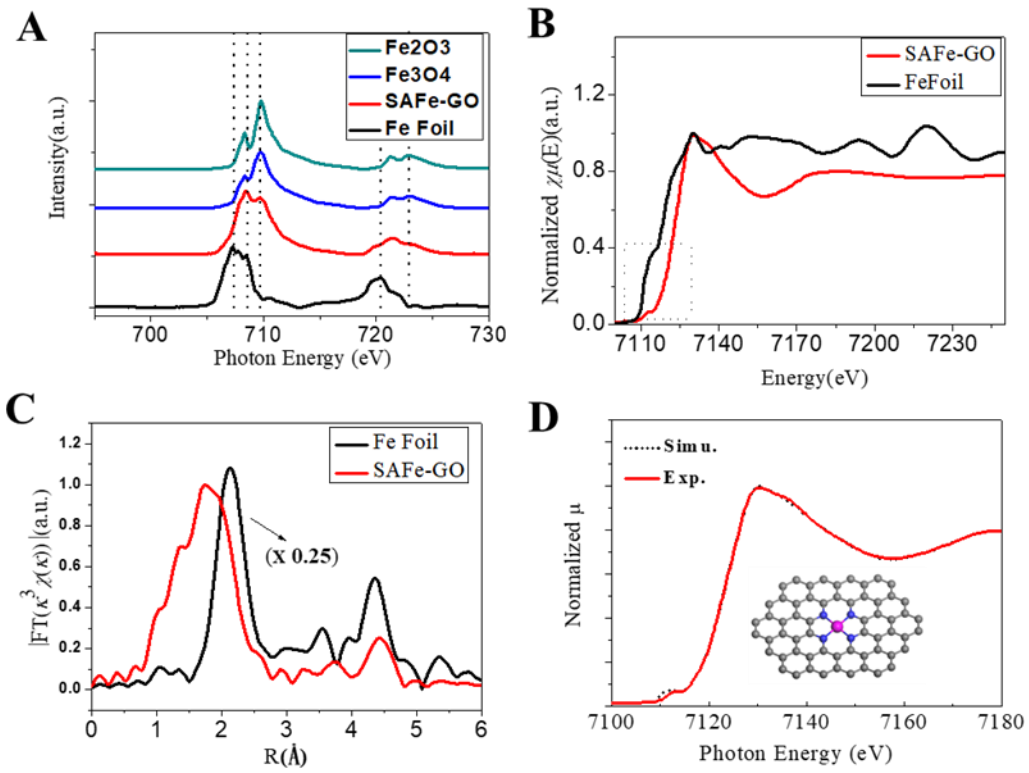

Figure 6.0 The Electronic state of Fe in SAFe-GO. (A) NEXAFS spectrum of Fe. (B) Fe K-edge XANES spectra of Fe foil and SAFe-GO. (C)Fourier transformation of the EXAFS spectra, in which the Fe foil spectrum has been reduced in size. (D) comparison of a simulated XANES spectrum of the inserted Fe-core structure with experimental results, the grey, blue and purple spheres represent the C, N, Fe, respectively.

Sample	C (at. %)	N (at. %)	O (at. %)	Me (wt. %)
SANi-GO1	82.3	14.7	2.6	5.1
SANi-GO2	84.1	12.3	3.4	2.5
SANi-GO3	81.3	16.1	2.1	7.9
SACo-GO	85.8	10.5	2.9	3.6
SAFe-Go	85.3	9.5	5.8	3.2
SACu-GO	85.3	11.2	2.9	2.7
SAPd-GO	84.9	10.8	3.8	3.8
SAAg-GO	83.2	14.5	1.6	2.8
SACuNi-GO	84.4	11.9	2.3	5.6(Cu),5.2(Ni)

Table 6.2 Summary of the compositions in SA-GO. The C, N and O contents are determined by XPS and Element Analysis while the Me content was determined by ICP-AES.

The single atom loading achieved was in the range of 2.8 wt% for SAAg-GO to 7.9wt% in the case of SANi-GO (Table 6.2). Most importantly, the loading of single metals could be controllable through adjusting the content of SA-Seed. In addition to GO substrates, other 2D materials such as MoS_2, BN were also used in the synthesis of SACs. To demonstrate the feasibility of this approach, Ni and Fe atoms were successfully loaded on the surface of MoS_2 nanosheet using the abovementioned seeding approach (Figures 6.8 H,I).

The PVP/PEI functionalization immobilizes the SAMe-Seed on MoS_2 and BN, similar to that on GO. The SAMe-Seed nanosheets landed uniformly on the surface, which is crucial for the formation of the final SACs on the 2D materials. The gradual integration of the single atom dispersed g-C_3N_4 structure on the 2D substrates during the final pyrolysis steps may effectively stabilize single atoms on 2D materials, preventing them from forming metal clusters or nanoparticles. The seeding strategy presented in this study is essentially different from the conventional approaches which mainly relies on the anchoring the SACs by defects on the

substrate surface. The SACs catalyst we made with controllable structure would exhibit good performance for electrochemical catalysis.

6.3.2 Electrochemical CO_2 reduction performance

For example, the electrochemical activity of SANi-GO catalysts was studied for the electrochemical reduction of CO_2 (CO_2RR) in CO_2-saturated 0.5 M $KHCO_3$ solution and the results are given in Figure 6.11. Linear sweep voltammetry (LSV) was firstly performed over SANi-GO catalysts under CO_2 atmosphere and N_2 curves showed one cathodic peak at approximately -0.7 V (versus RHE) observed in the CV curve, compared with no obvious peak present in N_2 (Figure 6.11A). The gaseous products were analyzed by on-line gas chromatography and only carbon monoxide (CO) and hydrogen (H_2) products were identified. The Faradaic efficiency (FE) of CO formation was tested at several applied potentials. Among them, the electrode exhibits FE (CO) of 91%, 94.7% and 96.6% at -0.83, -0.73 and -0.63 V (versus RHE) respectively.

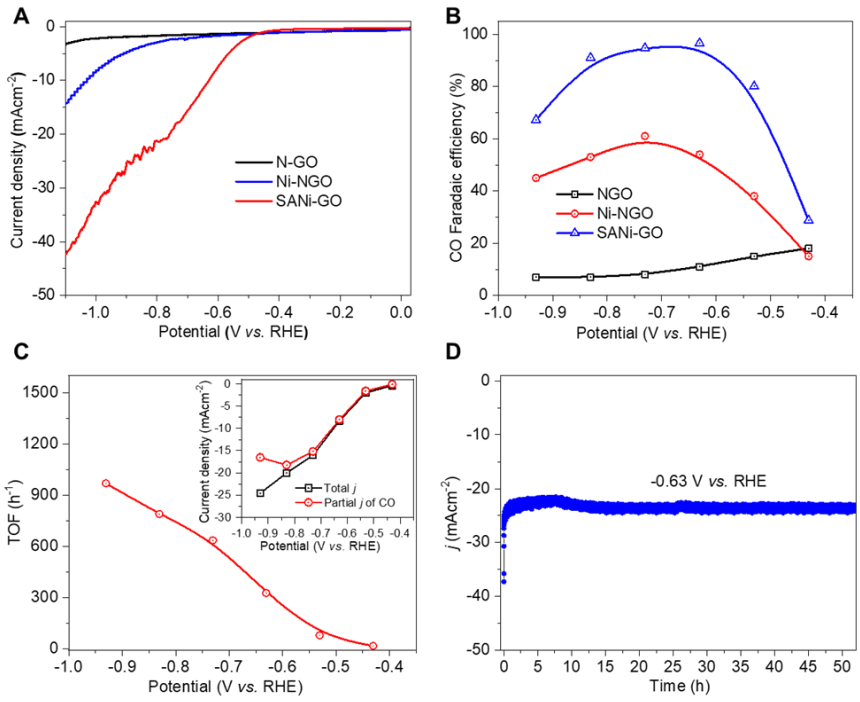

Figure 6.11 Electrochemical CO_2RR performance (A) LSV curves acquired in CO_2-saturated 0.5 M $KHCO_3$ solution. (B) CO Faradaic efficiency at various applied potentials. (C) TOF of SANi-GO at different over potential, the insert image shows the total and partial current density. (D)

Current–time response of for CO_2 reduction on carbon paper at an overpotential of -0.63 V.

Further reduction of CO to methane or other liquid products was not found, which was confirmed by mass spectrometry. The much higher selectivity of CO_2 by SANi-GO was achieved, compared with Ni-GO and NGO (Figure 6.11B). The high current density 8.3 $mAcm^{-2}$ for CO production was achieved at -0.63 V. The turnover frequency (TOF) of CO in Figure 6.11C increased with the overpotential and 325.9 h^{-1} at -0.63 V. (Figure 11C). The excellent selectivity and activity of SANi-GO were further investigated by *in situ* monitoring of the products formed at different potentials collected over 2 h of electrolysis using gas chromatographic analysis of gas products and gas chromatographic-mass spectroscopic analysis of liquid products. CO and H_2 were confirmed as the only products for the CO_2RR on SANi-GO. The cycling stability of the CO_2RR was investigated at -0.63 V, which exhibited high CO_2 selectivity even after 50 h at a 91% FE(Figure 6.11D). The performance of SANi-GO is comparable with reported results, which is due to the single atom structure[19, 44-46].

6.4 Conclusion

In summary, we have developed a highly controllable method to synthesize a series of single metal atom catalysts supported on two-dimensional materials via a new seeding strategy. Th seeding strategy is versatile and has been demonstrated on Ni, Co, Fe, Cu, Ag, Pd single atoms as well as binary NiCu atoms supported on 2D materials including GO, MoS_2 and BN nanosheets. The applicability of the synthesized SA-2D catalysts has been illustrated on the high activity and selectivity of SANi-GO for CO_2RR. The seeding approach described in this paper serves as an enabling technology for multiple applications including heterogeneous catalysis, electrode materials for energy storage and conversion, etc. The method represents a generic strategy for the fabrication of SACs sites on 2D support. This paper is expected to prompt further research on surface modification of 2D materials in a search for reliable materials for multiple applications.

6.5 References

[1] X.-F. Yang, A. Wang, B. Qiao, J. Li, J. Liu, T. Zhang, Single-Atom Catalysts: A New Frontier in Heterogeneous Catalysis, Accounts of Chemical Research, 46 (2013) 1740-1748.

[2] C. Zhu, S. Fu, Q. Shi, D. Du, Y. Lin, Single-Atom Electrocatalysts, Angewandte Chemie International Edition, 56 (2017) 13944-13960.

[3] A. Wang, J. Li, T. Zhang, Heterogeneous single-atom catalysis, Nature Reviews Chemistry, 2 (2018) 65-81.

[4] J. Liu, Catalysis by Supported Single Metal Atoms, ACS Catalysis, 7 (2017) 34-59.

[5] J. Wang, Z. Li, Y. Wu, Y. Li, Fabrication of Single-Atom Catalysts with Precise Structure and High Metal Loading, Advanced Materials, 30 (2018) 1801649.

[6] B. Qiao, A. Wang, X. Yang, L.F. Allard, Z. Jiang, Y. Cui, J. Liu, J. Li, T. Zhang, Single-atom catalysis of CO oxidation using Pt1/FeOx, Nat Chem, 3 (2011) 634.

[7] G. Kyriakou, M.B. Boucher, A.D. Jewell, E.A. Lewis, T.J. Lawton, A.E. Baber, H.L. Tierney, M. Flytzani-Stephanopoulos, E.C.H. Sykes, Isolated Metal Atom Geometries as a Strategy for Selective Heterogeneous Hydrogenations, Science, 335 (2012) 1209-1212.

[8] P.N. Duchesne, Z.Y. Li, C.P. Deming, V. Fung, X. Zhao, J. Yuan, T. Regier, A. Aldalbahi, Z. Almarhoon, S. Chen, D.-e. Jiang, N. Zheng, P. Zhang, Golden single-atomic-site platinum electrocatalysts, Nature Materials, 17 (2018) 1033-1039.

[9] J. Mao, C.-T. He, J. Pei, W. Chen, D. He, Y. He, Z. Zhuang, C. Chen, Q. Peng, D. Wang, Y. Li, Accelerating water dissociation kinetics by isolating cobalt atoms into ruthenium lattice, Nature Communications, 9 (2018) 4958.

[10] B. Qiao, A. Wang, X. Yang, L.F. Allard, Z. Jiang, Y. Cui, J. Liu, J. Li, T. Zhang, Single-atom catalysis of CO oxidation using Pt1/FeOx, Nature chemistry, 3 (2011) 634-641.

[11] S. Yang, J. Kim, Y.J. Tak, A. Soon, H. Lee, Single-Atom Catalyst of Platinum Supported on Titanium Nitride for Selective Electrochemical Reactions, Angewandte Chemie International Edition, 55 (2016) 2058-2062.

[12] S. Sun, G. Zhang, N. Gauquelin, N. Chen, J. Zhou, S. Yang, W. Chen, X. Meng, D. Geng, M.N. Banis, R. Li, S. Ye, S. Knights, G.A. Botton, T.-K. Sham, X. Sun, Single-atom Catalysis Using Pt/Graphene Achieved through Atomic Layer Deposition, Scientific Reports, 3 (2013) 1775.

[13] H. Yan, H. Cheng, H. Yi, Y. Lin, T. Yao, C. Wang, J. Li, S. Wei, J. Lu, Single-Atom

Pd1/Graphene Catalyst Achieved by Atomic Layer Deposition: Remarkable Performance in Selective Hydrogenation of 1,3-Butadiene, Journal of the American Chemical Society, 137 (2015) 10484-10487.

[14] H. Yan, Y. Lin, H. Wu, W. Zhang, Z. Sun, H. Cheng, W. Liu, C. Wang, J. Li, X. Huang, T. Yao, J. Yang, S. Wei, J. Lu, Bottom-up precise synthesis of stable platinum dimers on graphene, Nature Communications, 8 (2017) 1070.

[15] Y.-T. Kim, K. Ohshima, K. Higashimine, T. Uruga, M. Takata, H. Suematsu, T. Mitani, Fine Size Control of Platinum on Carbon Nanotubes: From Single Atoms to Clusters, Angewandte Chemie International Edition, 45 (2006) 407-411.

[16] P. Chen, T. Zhou, L. Xing, K. Xu, Y. Tong, H. Xie, L. Zhang, W. Yan, W. Chu, C. Wu, Y. Xie, Atomically Dispersed Iron–Nitrogen Species as Electrocatalysts for Bifunctional Oxygen Evolution and Reduction Reactions, Angewandte Chemie International Edition, 56 (2017) 610-614.

[17] Y. Zheng, Y. Jiao, Y. Zhu, Q. Cai, A. Vasileff, L.H. Li, Y. Han, Y. Chen, S.-Z. Qiao, Molecule-Level g-C3N4 Coordinated Transition Metals as a New Class of Electrocatalysts for Oxygen Electrode Reactions, Journal of the American Chemical Society, 139 (2017) 3336-3339.

[18] J.-C. Li, Z.-Q. Yang, D.-M. Tang, L. Zhang, P.-X. Hou, S.-Y. Zhao, C. Liu, M. Cheng, G.-X. Li, F. Zhang, H.-M. Cheng, N-doped carbon nanotubes containing a high concentration of single iron atoms for efficient oxygen reduction, Npg Asia Materials, 10 (2018) e461.

[19] K. Jiang, S. Siahrostami, A.J. Akey, Y. Li, Z. Lu, J. Lattimer, Y. Hu, C. Stokes, M. Gangishetty, G. Chen, Y. Zhou, W. Hill, W.-B. Cai, D. Bell, K. Chan, J.K. Nørskov, Y. Cui, H. Wang, Transition-Metal Single Atoms in a Graphene Shell as Active Centers for Highly Efficient Artificial Photosynthesis, Chem, 3 (2017) 950-960.

[20] F. Li, G.-F. Han, H.-J. Noh, S.-J. Kim, Y. Lu, H.Y. Jeong, Z. Fu, J.-B. Baek, Boosting oxygen reduction catalysis with abundant copper single atom active sites, Energy & Environmental Science, 11 (2018) 2263-2269.

[21] X. Li, X. Huang, S. Xi, S. Miao, J. Ding, W. Cai, S. Liu, X. Yang, H. Yang, J. Gao, J. Wang, Y. Huang, T. Zhang, B. Liu, Single Cobalt Atoms Anchored on Porous N-Doped Graphene with

Dual Reaction Sites for Efficient Fenton-like Catalysis, Journal of the American Chemical Society, 140 (2018) 12469-12475.

[22] H.B. Yang, S.-F. Hung, S. Liu, K. Yuan, S. Miao, L. Zhang, X. Huang, H.-Y. Wang, W. Cai, R. Chen, J. Gao, X. Yang, W. Chen, Y. Huang, H.M. Chen, C.M. Li, T. Zhang, B. Liu, Atomically dispersed Ni(i) as the active site for electrochemical CO2 reduction, Nature Energy, 3 (2018) 140-147.

[23] Y. Cheng, S. Zhao, H. Li, S. He, J.-P. Veder, B. Johannessen, J. Xiao, S. Lu, J. Pan, M.F. Chisholm, S.-Z. Yang, C. Liu, J.G. Chen, S.P. Jiang, Unsaturated edge-anchored Ni single atoms on porous microwave exfoliated graphene oxide for electrochemical CO2, Applied Catalysis B: Environmental, 243 (2019) 294-303.

[24] S. Zhou, L. Shang, Y. Zhao, R. Shi, G.I.N. Waterhouse, Y.-C. Huang, L. Zheng, T. Zhang, Pd Single-Atom Catalysts on Nitrogen-Doped Graphene for the Highly Selective Photothermal Hydrogenation of Acetylene to Ethylene, Advanced Materials, 31 (2019) 1900509.

[25] Y. Zhu, W. Sun, W. Chen, T. Cao, Y. Xiong, J. Luo, J. Dong, L. Zheng, J. Zhang, X. Wang, C. Chen, Q. Peng, D. Wang, Y. Li, Scale-Up Biomass Pathway to Cobalt Single-Site Catalysts Anchored on N-Doped Porous Carbon Nanobelt with Ultrahigh Surface Area, Advanced Functional Materials, 28 (2018) 1802167.

[26] Y. Zhu, W. Sun, J. Luo, W. Chen, T. Cao, L. Zheng, J. Dong, J. Zhang, M. Zhang, Y. Han, C. Chen, Q. Peng, D. Wang, Y. Li, A cocoon silk chemistry strategy to ultrathin N-doped carbon nanosheet with metal single-site catalysts, Nature Communications, 9 (2018) 3861.

[27] G. Zhang, Y. Jia, C. Zhang, X. Xiong, K. Sun, R. Chen, W. Chen, Y. Kuang, L. Zheng, H. Tang, W. Liu, J. Liu, X. Sun, W.-F. Lin, H. Dai, A general route via formamide condensation to prepare atomically dispersed metal–nitrogen–carbon electrocatalysts for energy technologies, Energy & Environmental Science, (2019).

[28] X. Li, W. Bi, L. Zhang, S. Tao, W. Chu, Q. Zhang, Y. Luo, C. Wu, Y. Xie, Single-Atom Pt as Co-Catalyst for Enhanced Photocatalytic H2 Evolution, Advanced Materials, 28 (2016) 2427-2431.

[29] S. Tian, Z. Wang, W. Gong, W. Chen, Q. Feng, Q. Xu, C. Chen, C. Chen, Q. Peng, L. Gu, H. Zhao, P. Hu, D. Wang, Y. Li, Temperature-Controlled Selectivity of Hydrogenation and

Hydrodeoxygenation in the Conversion of Biomass Molecule by the Ru1/mpg-C3N4 Catalyst, Journal of the American Chemical Society, 140 (2018) 11161-11164.

[30] Y. Cheng, S. Zhao, B. Johannessen, J.-P. Veder, M. Saunders, M.R. Rowles, M. Cheng, C. Liu, M.F. Chisholm, R. De Marco, H.-M. Cheng, S.-Z. Yang, S.P. Jiang, Atomically Dispersed Transition Metals on Carbon Nanotubes with Ultrahigh Loading for Selective Electrochemical Carbon Dioxide Reduction, Advanced Materials, 30 (2018) 1706287.

[31] V.N. Popok, I. Barke, E.E.B. Campbell, K.-H. Meiwes-Broer, Cluster–surface interaction: From soft landing to implantation, Surface Science Reports, 66 (2011) 347-377.

[32] S. Vajda, M.G. White, Catalysis Applications of Size-Selected Cluster Deposition, ACS Catalysis, 5 (2015) 7152-7176.

[33] H. Xu, D. Cheng, D. Cao, X.C. Zeng, A universal principle for a rational design of single-atom electrocatalysts, Nature Catalysis, 1 (2018) 339-348.

[34] A. Nag, K. Raidongia, K.P.S.S. Hembram, R. Datta, U.V. Waghmare, C.N.R. Rao, Graphene Analogues of BN: Novel Synthesis and Properties, ACS Nano, 4 (2010) 1539-1544.

[35] B.C.C. Cowie, A. Tadich, L. Thomsen, The Current Performance of the Wide Range (90–2500 eV) Soft X-ray Beamline at the Australian Synchrotron, AIP Conference Proceedings, 1234 (2010) 307-310.

[36] E. Gann, C.R. McNeill, A. Tadich, B.C.C. Cowie, L. Thomsen, Quick AS NEXAFS Tool (QANT): a program for NEXAFS loading and analysis developed at the Australian Synchrotron, Journal of Synchrotron Radiation, 23 (2016) 374-380.

[37] G. Kresse, J. Furthmüller, Efficient iterative schemes for ab initio total-energy calculations using a plane-wave basis set, Physical Review B, 54 (1996) 11169-11186.

[38] G. Kresse, D. Joubert, From ultrasoft pseudopotentials to the projector augmented-wave method, Physical Review B, 59 (1999) 1758-1775.

[39] J.P. Perdew, K. Burke, M. Ernzerhof, Generalized Gradient Approximation Made Simple, Physical Review Letters, 77 (1996) 3865-3868.

[40] Z. Chen, S. Mitchell, E. Vorobyeva, R.K. Leary, R. Hauert, T. Furnival, Q.M. Ramasse, J.M.

Thomas, P.A. Midgley, D. Dontsova, M. Antonietti, S. Pogodin, N. López, J. Pérez-Ramírez, Stabilization of Single Metal Atoms on Graphitic Carbon Nitride, Advanced Functional Materials, 27 (2017) 1605785.

[41] Y. Cheng, S. Zhao, B. Johannessen, J.-P. Veder, M. Saunders, M.R. Rowles, M. Cheng, C. Liu, M.F. Chisholm, R. Marco, H.-M. Cheng, S.-Z. Yang, S.P. Jiang, Atomically Dispersed Transition Metals on Carbon Nanotubes with Ultrahigh Loading for Selective Electrochemical Carbon Dioxide Reduction, Advanced Materials, 30 (2018) 1706287.

[42] H. Fei, J. Dong, Y. Feng, C.S. Allen, C. Wan, B. Volosskiy, M. Li, Z. Zhao, Y. Wang, H. Sun, P. An, W. Chen, Z. Guo, C. Lee, D. Chen, I. Shakir, M. Liu, T. Hu, Y. Li, A.I. Kirkland, X. Duan, Y. Huang, General synthesis and definitive structural identification of MN4C4 single-atom catalysts with tunable electrocatalytic activities, Nature Catalysis, 1 (2018) 63-72.

[43] Z. Chen, S. Mitchell, E. Vorobyeva, R.K. Leary, R. Hauert, T. Furnival, Q.M. Ramasse, J.M. Thomas, P.A. Midgley, D. Dontsova, M. Antonietti, S. Pogodin, N. López, J. Pérez-Ramírez, Catalysts: Stabilization of Single Metal Atoms on Graphitic Carbon Nitride (Adv. Funct. Mater. 8/2017), Advanced Functional Materials, 27 (2017).

[44] N. Kornienko, Y. Zhao, C.S. Kley, C. Zhu, D. Kim, S. Lin, C.J. Chang, O.M. Yaghi, P. Yang, Metal–Organic Frameworks for Electrocatalytic Reduction of Carbon Dioxide, Journal of the American Chemical Society, 137 (2015) 14129-14135.

[45] Z. Cao, D. Kim, D. Hong, Y. Yu, J. Xu, S. Lin, X. Wen, E.M. Nichols, K. Jeong, J.A. Reimer, P. Yang, C.J. Chang, A Molecular Surface Functionalization Approach to Tuning Nanoparticle Electrocatalysts for Carbon Dioxide Reduction, Journal of the American Chemical Society, 138 (2016) 8120-8125.

[46] M. Liu, Y. Pang, B. Zhang, P. De Luna, O. Voznyy, J. Xu, X. Zheng, C.T. Dinh, F. Fan, C. Cao, F.P.G. de Arquer, T.S. Safaei, A. Mepham, A. Klinkova, E. Kumacheva, T. Filleter, D. Sinton, S.O. Kelley, E.H. Sargent, Enhanced electrocatalytic CO2 reduction via field-induced reagent concentration, Nature, 537 (2016) 382.

Chapter 7: Theoretical calculation guided design of single-atom catalysts towards fast kinetic and long-life Li-S batteries

Abstract

Lithium-sulfur (Li-S) batteries are promising next-generation energy storage technologies due to their high theoretical energy density, environmental friendliness and low cost. However, low conductivity of sulfur species, dissolution of polysulfides, poor conversion from sulfur reduction and lithium sulfide (Li_2S) oxidation reactions during discharge-charge processes hinder their practical applications. Herein, under the guidance of density functional theory calculations, we have successfully synthesized large-scale single atom vanadium catalysts seeded on graphene to achieve high sulfur content (80 wt% sulfur), fast kinetic (a capacity of 645 mAh g^{-1} at 3 C rate) and long-life Li-S batteries. Both forward (sulfur reduction) and reverse reactions (Li_2S oxidation) are significantly improved by the single atom catalysts. This finding is confirmed by experimental results and consistent with theoretical calculations. The ability of single metal atoms to effectively trap the dissolved lithium polysulfides (LiPSs) and catalytically convert the LiPSs/Li_2S during cycling, significantly improved sulfur utilization, rate capability and cycling life. Our work demonstrates an efficient design pathway for single atom catalysts and provides solutions for the development of high energy/power density Li-S batteries.

7.1 Introduction

Lithium-sulfur (Li-S) battery is regarded as a promising candidate for energy storage due to its high energy density, low cost, and environmental friendliness[1-3] . Nevertheless, technological challenges arising from the low electronic/ionic conductivity of sulfur species, the sluggish reaction kinetics with accumulated sulfur species and dissolved polysulfides, lead to large internal resistance, low sulfur utilization, and fast capacity decay[4-6] . These challenges have prevented the commercialization of Li-S batteries. To overcome these drawbacks, introducing active adsorption and catalysis centers is required for cathode to enhance the sulfur utilization and accelerate the reversible conversion between lithium polysulfides (LiPSs) and Li_2S. Therefore, much effort has been devoted to developing highly active and durable catalysts, which possess

well-designed activation centers capable of adsorbing active species and facilitating desired redox reactions[7-10] . Our previous work identified metal sulfides as effective catalysts in lowering the overpotential and the Li_2S decomposition energy barrier compared with the more commonly used carbon materials in Li-S batteries[11] . Several other bulk and nanosized catalysts including TiO_{2-x} nanosheets[10], MnO_2 nanosheets[12], Fe_2O_3 nanoparticles[13], mesoporous TiN[14], amorphous CoS_3 film,[15] VN nanoribbon[16] , and phosphorene[17] have also been synthesized to promote the transformation of sulfur, LiPSs, and Li_2S, resulting in a significant increase in utilization of active materials and enhancing the reaction kinetics of Li-S batteries[8] . However, attention should be paid to control the weight percentages of these inactive additives without sacrificing the overall energy density of Li-S batteries.

Since catalytic performance is correlated to catalytic particle size, it is natural to hypothesize that maximum catalytic efficiency is achieved at the single atomic level[18-20]. Single-atom catalysts (SACs), comprised of monodispersed single atoms supported on various substrates, have recently been demonstrated to exhibit high efficiency and distinctive selectivity in various energy, environment, and chemical related devices, far exceeding conventional metal nanoparticle catalysts[21-23]. SACs not only maximize the atomic efficiency, making every atom contribute, but also supply an alternative strategy to adjust the activity and selectivity of a catalytic process by introducing lowest amount of catalyst[19, 21, 24] . Most recently, SACs have been studied and applied as electrocatalysts for Li-S batteries with significantly improved electrochemical performance[25-28] . However, in those studies, SACs were randomly selected, and fabricated *via* an impregnation method (relying on absorption sites of the substrates), which inherently limits variety and yield. To efficiently meet the requirements of Li-S batteries, both enhanced selection and synthesis sophistication are required.

Theoretical modelling represents a powerful tool to accelerate the search for promising catalyst candidates, which can significantly reduce the number of unsuccessful trials[29, 30]. Taking the above discussion into consideration, herein we first screen SAC materials for the catalytic decomposition of Li_2S using theoretical simulation. Considering the cost issue and the diversity of metal atoms, ten materials comprised of graphene, N-doped graphene (NG), single atom Fe, Mn, Ru, Zn, Co, Cu, V and Ag on NG were chosen. Among all the materials screened, we discover that vanadium single atoms on NG (SAV@NG) show the smallest decomposition barrier (1.10 eV). To

apply SAV@NG as effective and practical cathodes for Li-S batteries, we develop one universal strategy, referred to as one seeding approach, to synthesize single atoms coated on graphene with scalable quantities, controllable loading, and adjustable components. The results demonstrate a dramatic enhancement of capacity, kinetics, and cycling performance for SAV@NG based electrodes in Li-S batteries, which is consistent with the simulation results.

7.2 Experimental section

7.2.1 Preparation of Seed-SACo and Seed-SAV

All chemicals purchased from Sigma-Aldrich were used without further purifying unless otherwise specified in this study. All the annealing treatments are processed at Ar of 50 sccm. Dicyandiamide ($C_2H_4N_4$, DCD) was annealed at 350 ºC for 1 h, noted as DCD-350 after finely grinded. Cobalt (II) acetylacetonate, vanadyl acetylacetonate were chosen as the metal resource. The metal salts were resolved into ethanol solution (50% acetone, with 10 mg mL^{-1} citric acid) and sonicated for 1 h. The above solution was dropped dropwise to DCD-350 powder (with metal content of 1wt% *vs.* DCD-350) when grinding. The powder was annealed at 665 ºC for 2 h and then grinded for 30 min. The brown product was noted as Seed-SAMe (Me = Co, V), prior to leaching in the HCl (2 mol L^{-1}) for 2 h following dry at 80 ºC for 5 h.

7.2.2 Preparation of SACo@NG and SAV@NG

The graphene was mixed with poly ethyleneimine (PEI) solution (50% (w/v) in H_2O,) and polyvinylpyrrolid (PVP, average mol 40000) (with mass ratio=1:1; 50 wt% in total) in ethanol and sonicated for 20 min into uniform solution. Seed-SACo or Seed-SAV was subsequently added to the above PEI and PVP solution and sonicated by tip sonication for 1 h. Furthermore, the mixture was stirred for 5 h, dried and grounded to fine powder. The as-prepared sample was then heated at 800 ºC and held for 1h. During the heating stage, the temperature was held constant for another 2 h at 680 ºC before final ramping to 800 ºC. Herein, the PVP and PEI adhering to the surface of graphene oxide (GO) and seeds will enhance the uniformity and dispersion of seeds on GO. During the following annealing process, the PVP and PEI will be pyrolyzed into amorphous carbon, which enables the good contact between GO and single metal atoms. Finally, the samples were denoted as SACo@NG and SAV@NG.

The reference g-C_3N_4 was synthesized through an annealing of DCD at 665 ºC for 1 h. Nitrogen-

doped graphene (NG) was synthesized by mixing DCD-350 with GO and annealing at 800 ºC for 1 h. GO was reduced into graphene (G) at 800 ºC for 1 h under Ar flow.

7.2.3 Structural characterizations

The microstructure and morphology of SACo@NG and SAV@NG samples were obtained using scanning electron microscopy (SEM, Zeiss Neon 40 EsB) and high-resolution transmission electron microscopy (HRTEM, FEI Titan G2 80-200 TEM/STEM). High-resolution aberration-corrected scanning transmission electron microscopy annular dark field images (AC-STEM-ADF, Nion UltraSTEM100 microscope) was carried out by operating at 60 kV at a beam current of 60 pA. The inductively coupled plasma atomic emission spectroscopy (TJA RADIAL IRIS 1000, ICP-AES) was used to determine the mass content of vanadium and cobalt. X-ray diffraction (XRD, Bruker D8 Advance diffractometer) was operated at 40 kV and 40 mA with Cu Kα (λ = 1.5406 Å). X-ray photoelectron spectroscopy (XPS) was collected in Kratos AXIS Ultra DLD system. Nitrogen absorption and desorption experiment was conducted on an ASAP 2020 (Micromeritics) to analyze the specific surface area and pores size distribution. Raman patterns were performed using one alpha300 RA Correlative Raman-AFM Microscope with a 532 nm He−Ne laser. Near edge x-ray absorption structure (NEXAFS) spectroscopy measurements were performed at the Soft X-Ray beamline of the Australian Synchrotron. All spectra were obtained in partial electron yield (TEY) mode. All NEXAFS spectra were processed and normalized using the QANT software program developed at the Australian Synchrotron. X-ray absorption spectroscopy (XAS) measurements were collected at the XAS Beamline (12ID) at the Australian Synchrotron in Melbourne. With the beamline optics employed (Si-coated collimating mirror and Rh-coated focusing mirror) the harmonic content of the incident X-ray beam was negligible. The powder samples were pressed into pellets following mechanical grinding with a cellulose binder. Both fluorescence and transmission spectra were collected based on the concentration of vanadium and cobalt in each sample (the validity of this method was confirmed *via* comparing the fluorescence and transmission spectra intensity for one of the samples based on which both methods yielded comparable quantitative data). All XAS data were processed and analyzed usingDemeter software[31].

7.2.4 Electrochemical measurements

The blank electrolyte was prepared by dissolving an appropriate amount of lithium tri-

fluoromethanesulfonate ($LiCF_3SO_3$, 98%, Acros Organics, 1M) and $LiNO_3$ (99.9%, Acros Organics, 0.1M) in DME (99%, Acros Organics) and DOL (99.5%, Acros Organics) (1:1 by volume). The Li_2S_6 catholyte was mixing stoichiometric amounts of sublimed sulfur (99.5%, Fisher Scientific) and an appropriate amount of Li_2S (99.9%, Acros Organics) in the blank electrolyte to form Li_2S_6 in the solution. $LiNO_3$ was added to passivate the Li metal surface and suppress its reaction with polysulfide.[32] The solution was then magnetic stirred vigorously at 60 ^oC in an Ar-filled glove box overnight to produce a brownish-red Li_2S_6 catholyte solution.

As-prepared graphen (G), NG, SACo@NG , SAV@NG and sulfur powder (99.5%, Alfa Aesar) in a mass ratio of 1:4 were ground together for 30 minutes. The mixture was then transfered to a sealed stainless steel vessel and heated to 155 °C for 15 h to obtain the S-G, S-NG, S-SACo@NG and S-SAV@NG. A well-mixed slurry (85 wt% S-G, S-NG, S-SACo@NG and S-SAV@NG, 5wt% Super P as conductive additive and 10 wt% polyvinylidene fluoride as binder in N-methyl-2-pyrolidone) was coated onto the Al foil current collector followed by drying under vacuum at 60℃ for 24 h. The S-G, S-NG, S-SACo@NG and S-SAV@NG electrodes were shaped into a circular pellet with areal sulfur mass loading of around 2 mg cm^{-2}. 20 μL electrolyte was added to wet the sulfur cathode. The Celgard 2400 separator was then placed on top of the electrodes. Finally, the lithium-metal foil anode was placed on the separator as the anode. Galvanostatic charge-discharge cycles were performed on a CT2001A cell test instrument (LAND Electronic Co.) The sulfur cathode-based cells were measured with the potential range of 1.5-2.8 V (*vs.* Li/Li^+). The C-rate for tests was referred to the mass of sulfur in the cathode and was varied from 0.2 C to 3 C rate.

7.2.5 Theoretical calculations

The projector augmented wave (PAW) formalism of density functional theory as implemented in the Vienna Ab-initio Simulation Package (VASP) was used in the system energy and electronic structure calculations.[33] The Gaussian smearing method[34] was used and the width of smearing was chosen as 0.05 eV. The energy cutoff for plane-wave expansion of the PAWs is 500 eV. In the vertical direction, a vacuum layer of about 20 Å in thickness was introduced for all the surfaces. For the binding energy and adsorption conformation simulations, we used the vdW-DF2 functional to include the physical van der Waals interaction, which was demonstrated to be very important in the simulation of Li_2S adsorption[35]. The Brillouin zone was sampled using Monkhorst-Pack scheme with a k-point mesh of 3×3×1 in the Gamma-centered grids for the structural relaxation.[36] The structure relaxation was continued until the forces on all the atoms were converged to less

than 0.02 eV/Å. The decomposition barrier for Li_2S was determined by climbing image-nudged elastic band (CI-NEB)[37].

7.3 Results and discussion

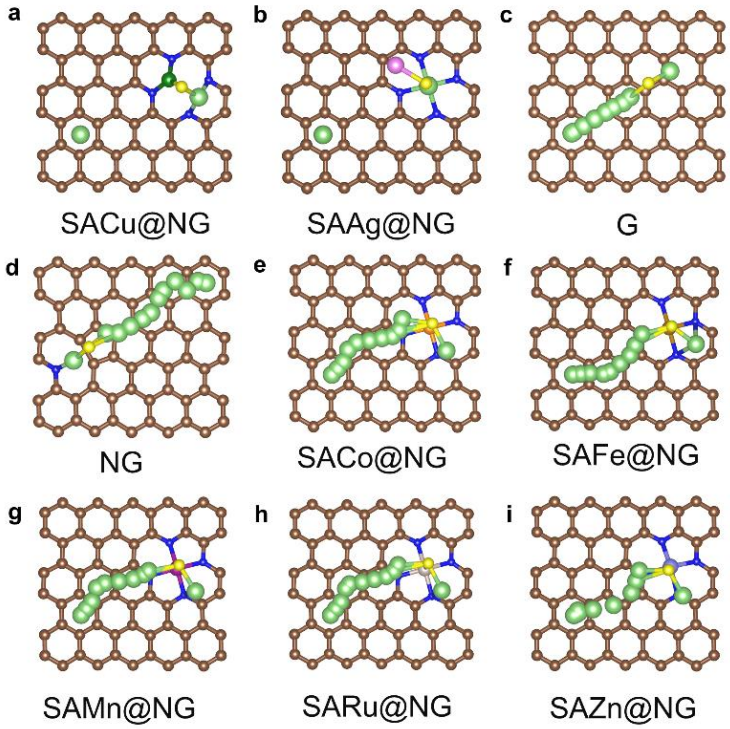

Figure 7.1 Optimized atomic configuration of LiS cluster adsorption on the (a) SACu@NG and (b) SAAg@NG. (c-i) Detailed decomposition path for Li_2S cluster on graphene, NG, SACo@NG, SAFe@NG, SAMn@NG, SARu@NG and SAZn@NG, respectively.

Firstly, the stability of these ten materials (graphene, NG, SAFe@NG, SAMn@NG, SARu@NG, SAZn@NG, SACo@NG, SAV@NG, SACu@NG and SAAg@NG) were considered. According to the optimized structure results, graphene, NG and single atom substrates (Fe, Mn, Ru, Zn, Co and V) can maintain pristine atomic configuration after the Li_2S and LiS adsorption, while the pristine substrates show a deformed atomic lattice after LiS cluster adsorption for the SACu@NG and SAAg@NG materials, *i.e.* the pristine bonds between the Cu atom and adjacent coordinated N atoms break and Ag is replaced by the Li atom of LiS cluster (Figure 7.1a-b). The implication of this finding is that the single atom substrates (Fe, Mn, Ru, Zn, Co and V) materials can maintain the structure stability during repeated charge-discharge cycles while the SACu@NG and

SAAg@NG are unstable. We also calculate out that the decomposition energy barrier of Li_2S on these stable substrates was highly related to the kinetic property of Li_2S oxidation during the charging process. Reducing the decomposition barrier of Li_2S can greatly increase the utilization of active materials, decrease the formation of dead Li_2S and achieve a long cycling life.

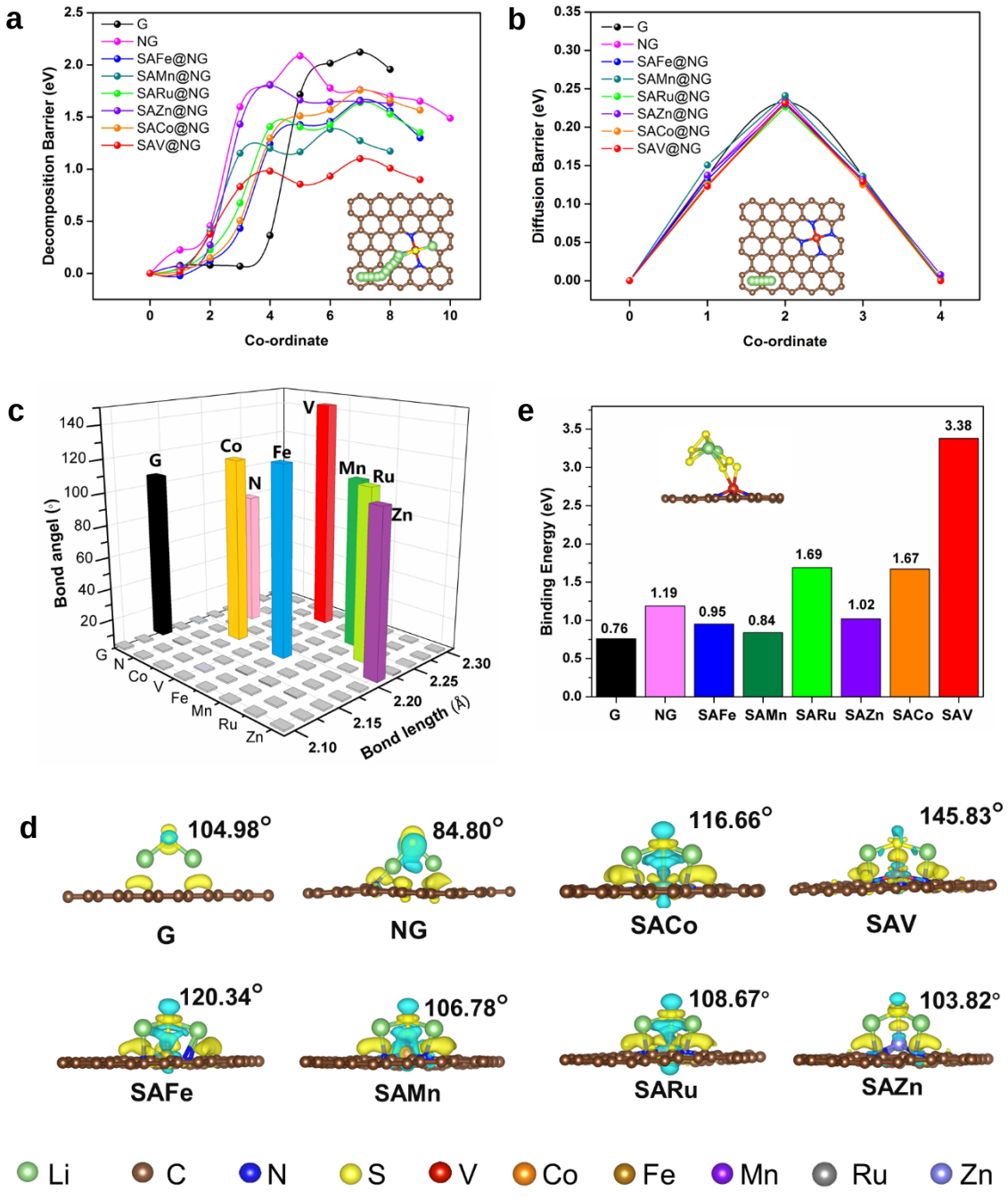

Figure 7.2 Theoretical understanding for Li_2S decomposition, Li ion diffusion and anchoring effect. a, Decomposition barriers of Li_2S and b, lithium ion diffusion barriers on different substrates

including graphene, NG, SAFe@NG, SAMn@NG, SARu@NG, SAZn@NG, SACo@NG and SAV@NG. The inset images in a and b are the detailed decomposition path of Li_2S and diffusion pathway of lithium atom on SAV@NG, respectively. c, Bond angel (Li-S-Li) of Li_2S, bond length (Li-S) of Li_2S and d, side view for charge density difference of Li_2S adsorption on the graphene, NG, SACo@NG, SAV@NG, SAFe@NG, SAMn@NG, SARu@NG and SAZn@NG, respectively. The yellow and blue sections represent the electron accumulate and lose region. The iso-surface is set to 0.003 eV/$Å^3$. e, Binding energy of Li_2S_6 on the graphene, NG, SACo@NG, SAV@NG, SAFe@NG, SAMn@NG, SARu@NG and SAZn@NG, respectively. The inset image is the side view for the Li_2S_6 cluster adsorption configurations on SAV@NG.

We considered the decomposition process from an intact Li_2S molecule into a LiS cluster and a single Li ion, which corresponds to the breaking of the Li-S bond. The decomposition pathway of Li_2S on different substrates are shown in Figure 7.2a (inset for SAV@NG). The results show that graphene possesses the greatest decomposition barrier (2.12 eV), much larger than the other seven cases. The decomposition barrier for SAV@NG, SACo@NG, SAFe@NG, SAMn@NG, SARu@NG, and SAZn@NG are 1.10, 1.76, 1.66, 1.38, 1.64 and 1.81 eV, respectively. Meanwhile, the lithium ion diffusion properties on the substrates were also important for studying the Li_2S decomposition performance. Fast lithium ion diffusion behavior facilitates the subsequent steps after the decomposition of Li_2S on the charging process and sulfur transformation chemistry on the discharging process. As shown in Figure 7.2b, the calculation results show that the diffusion barriers of lithium ion on all the substrates are around 0.23 eV. The detailed lithium diffusion pathway on these substrates are shown in the inset of Figure 7.2b (SAV@NG). Combining the decomposition energy barriers of Li_2S with lithium ion diffusion barriers on these substrates, it can be clearly seen that the dominant step for the decomposition process of Li_2S on the charging process is the bond breaking step between the Li and S atoms. SAV@NG exhibits the smallest decomposition barrier (1.10 eV) of Li_2S and can maintain the small lithium diffusion barrier, which shows the best potential for catalyzing the decomposition of Li_2S.

To further have an in-deep investigation for the different catalytic effect on decomposition of Li_2S on these substrates, the electronic structure and thermodynamic configuration analysis were performed. Considering that the bond length (Li-S) and bond angle (Li-S-Li) can reflect the bonding strength of the Li-S bond in the Li_2S, we measured the bond length and angle of Li_2S after

it was adsorbed on the substrates. As shown in Figure 7.2c, the bond length of Li-S on the graphene is the shortest with 2.19 Å and the bond angle of Li-S-Li on the NG is the smallest with 84.80°, while SAV@NG substrate possesses both a maximum bond length (2.28 Å, Li-S) and a maximum bond angle (145.83 °, Li-S-Li) among all substrates. The longer bond length and bigger bond angle of Li_2S on relative substrates mean the greater weakening of Li-S bond in the Li_2S molecules, which facilitate the decomposition of Li_2S. These results are agreement with our decomposition barrier calculation. Moreover, electronic transformation behavior between the Li_2S and substrates were also considered. As shown in Figure 7.2d, the charge density differences show the electron migration mainly accumulates between the Li atom and substrates for the graphene and NG materials. For the single atom substrates, in addition to the electron transfer between the Li atom and substrates, it can be clearly seen that there are also more electron transfer between the S atom and the metal atoms, which can further weaken the Li-S bond by forming the S-metal bond and thus, decrease the decomposition barriers of Li_2S.

Besides, the interaction between the polysulfides and substrates was also considered. Previous works have identified that the stronger chemical interaction between the substrates and polysulfides can effectively decrease the shuttle effect[35]. As shown in Figure 7.2e, the binding energy, E_b is computed to measure the binding strength between Li_2S_6 on these substrates. The binding energy is defined as $E_b = E_{Li2S6}$ (pure Li_2S_6 cluster) + E_{Sub} (pure substrate) – $E_{Li2S6+sub}$ (adsorbed system), while the positive and the larger value means the stronger anchoring effect of Li_2S_6 on the substrates. Based on the calculation results, the binding energy of Li_2S_6 on graphene, NG, SACo@NG, SAV@NG, SAFe@NG, SAMn@NG, SARu@NG and SAZn@NG are 0.76, 1.19, 1.67, 3.38, 0.95, 0.84, 1.69 and 1.02 eV respectively. The graphene exhibits the weakest chemical binding energy of 0.76 eV to Li_2S_6, while the NG and all of the single atom substrates can induce the bonding effect by N-Li or metal-S to increase the binding strength. Due to the directly bonding effect between the two S atoms of Li_2S_6 cluster and V atoms (inset of Figure 7.2e), the SAV@NG substrate possesses the biggest binding energy of 3.38 eV. This indicates that the SAV@NG material exhibits the best potential on mitigating polysulfide dissolution and suppressing shuttle effect in Li-S batteries. Combining the decomposition barrier, lithium ion diffusion barrier, structure stability performance and anchoring effect of the ten materials, the SAV@NG shows the best potential and was thus selected as an optimum catalyst for this study. Moreover, according to the different decomposition energy barrier gradients of Li_2S, similar

lithium ion diffusion barrier and different anchor effect level for Li_2S_6 on these substrates, graphene, NG and SACo@NG were also selected as the control electrodes.

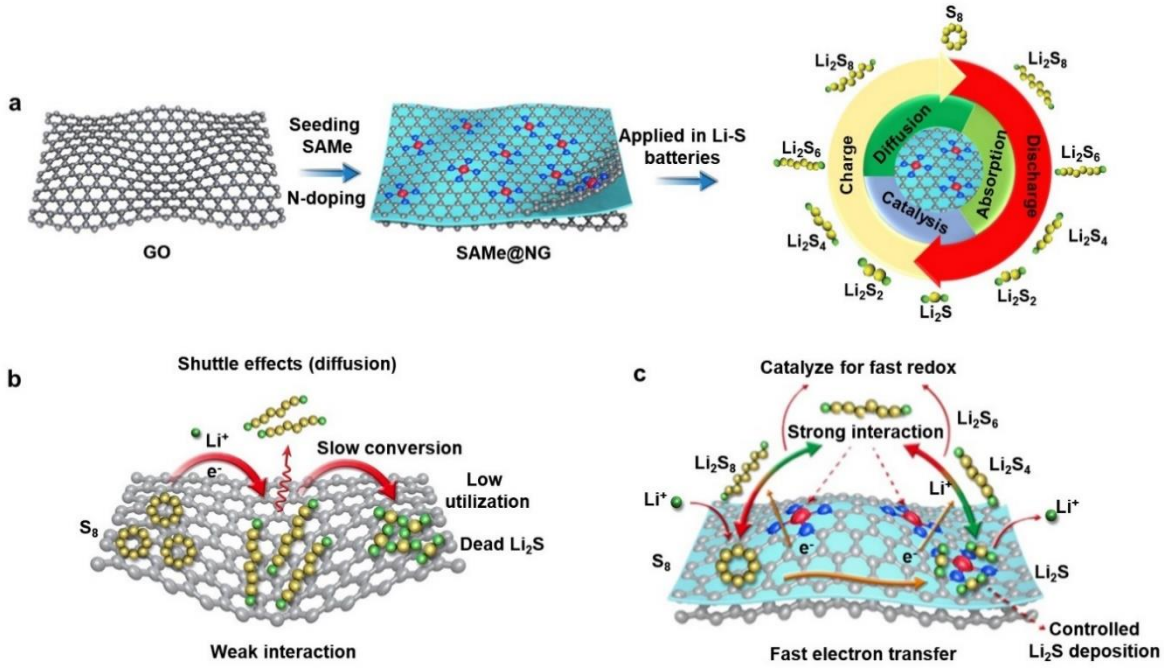

Figure 7.3 a, Schematics showing the seeding approach of single atom on graphene, the conversion process on b, graphene, and c, single atom seeded graphene for Li-S batteries.

Guided by the theoretical results, a seeding approach was proposed to synthesize the SACo@NG and SAV@NG samples, as shown in Figure7.3a. Briefly, the seeding approach involves three steps, *i.e.* the seed of single atom metal (Seed-SAMe) preparation, graphene surface modification and final seed. The surface modification layer was introduced on the surface of graphene oxide (GO), which bridged the connection between the GO and single atoms. The loading of seeds will be synthesized through absorbing and stabilizing the metal salts on the carbon nitrides. The components of the single atoms could be adjusted by changing the metal salts. Besides this, the content and loading are also controlled through changing the ratio between the seeds and supports. Finally, the specific loading of single atom seeds is testified by inductively coupled plasma-optical emission spectroscopy (ICP-OES) and then was added into the mixture based on the targeted design. The seeds will be almost decomposed completely during the annealing process and then single atom metal was bonded with the GO support. For instance, Seed-SACo and Seed-SAV were successfully synthesized through changing appropriate metal salts. Furthermore, they were

uniformly mixed with GO separately, followed by annealing treatments prior to the final single atom samples. GO hinders the aggregation of Seed-SAMe into nanoparticles and provides abundant sites, for the seed landing on the surface and then strongly bonded with GO. Benefiting from advantages of the single atom in the aspects of absorption, catalysis, and diffusion, the SAMe@NG based electrodes show great promise in Li-S batteries during charge-discharge processes in Figure7.3a Generally, due to weak interaction between graphene and LiPSs along with a slow conversion process, the shuttle effects cannot be refrained and dead Li_2S agglomerates during the cycling (Figure7.3b), resulting in a rapid capacity fading and low sulfur utilization. On the contrary, the multifunctional SACs can integrate the advantages of strong chemical adsorption of LiPSs, facilitated conversion among sulfur/lithium polysulfides/Li_2S, and controllable Li_2S deposition sites (Figure7.3c), which promote the realization of high capacity, fast kinetics and long-life Li-S batteries.

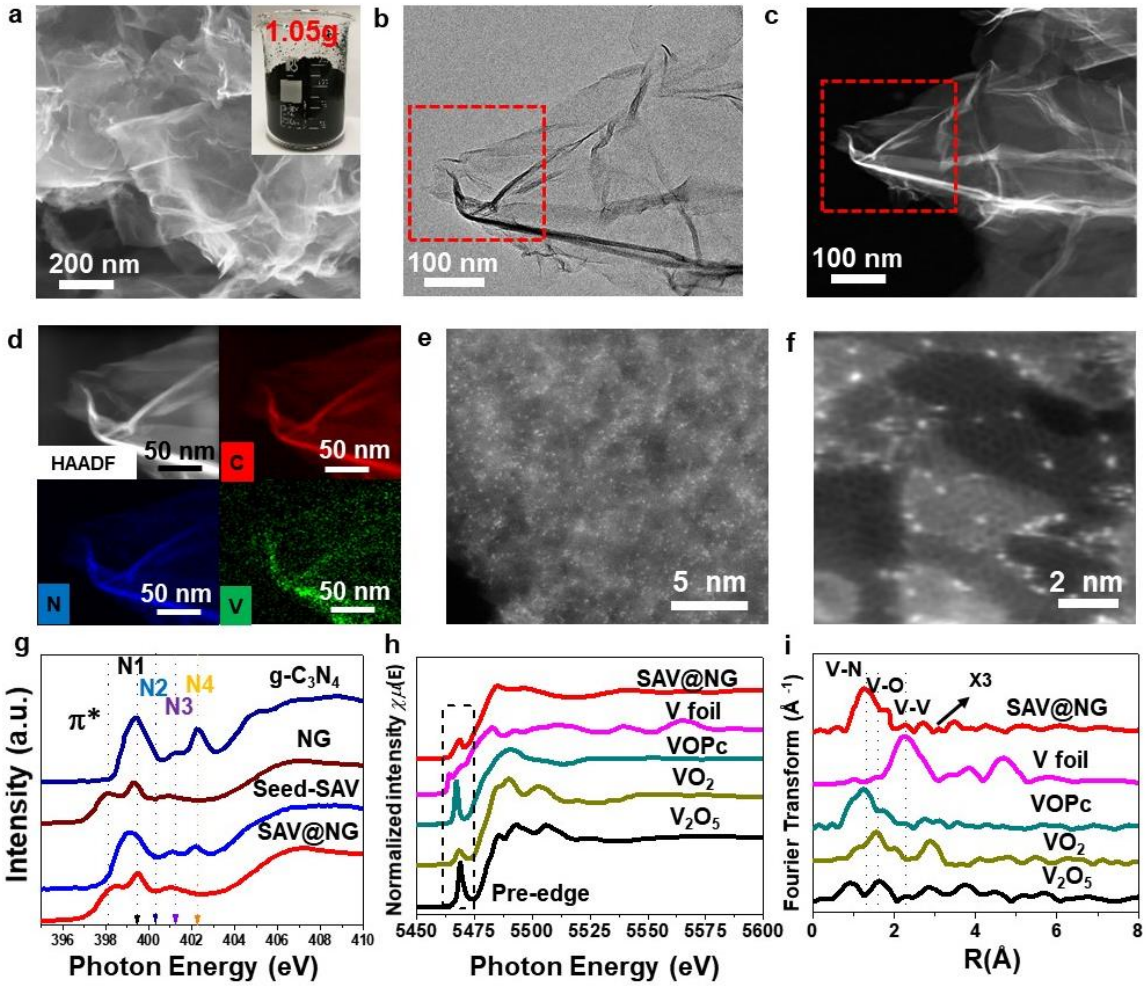

Figure 7.4 Structural characterizations of SAV@NG. (a), SEM image of SAV@NG, inset

image:1.05 g SAV@NG. (b), TEM image and (c), High-angle annular dark-field (HAADF)-STEM image of SAV@NG. (d), HAADF image and corresponding EDS mappings of SAV@NG. (e), (f), AC-STEM-ADF images of SAV@NG. (g), NEXAFS N K-edge of g-C_3N_4, NG, Seed-SAV and SAV@NG. (h), Vanadium K-edge X-ray absorption near edge structure (XANES) spectra of SAV@NG, V foil, VOPc, VO_2, and V_2O_5. (i), Fourier transform of vanadium K-edge EXAFS spectra of SAV@NG, V foil, VOPc, VO_2, and V_2O_5.

The SAV@NG and SACo@NG were prepared and scaled up as shown in the inset of Figure7.4a, allowing for significant commercial potential. The mass loading of vanadium and cobalt of SAV@NG and SACo@NG prepared was characterized by Thermogravimetric Analysis (TGA) and further confirmed by ICP-OES with values of around 4.3 wt% and 3.9 wt%, respectively (Figures 7.5a, b).

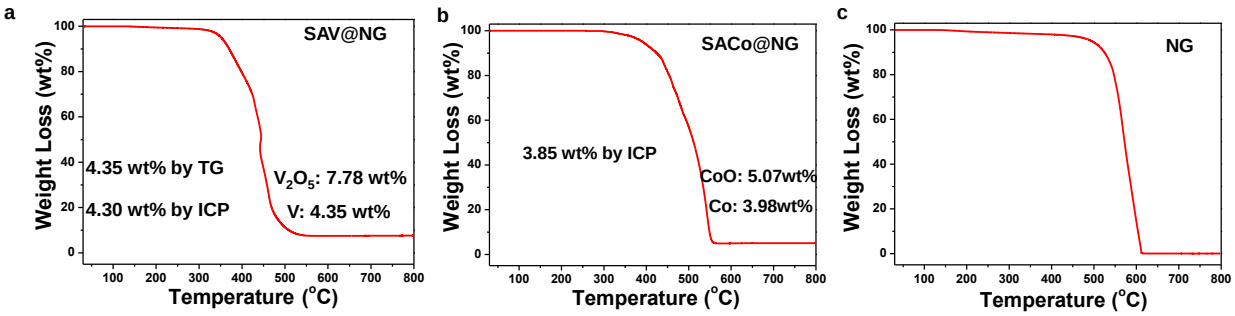

Figure 7.5 TG curves of (a) SAV@NG, (b) SACo@NG, and (c) NG.

The oxidation resistance temperature of NG, SACo@NG, and SAV@ NG are 558 °C, 500 °C, and 450 °C, respectively, and the reduced temperature indicates the catalytic effect of single atoms on the decomposition of NG in Figure 7.6a, b. Scanning electron microscopy (SEM) and transmission electron microscopy (TEM) images of SAV@NG and SACo@NG demonstrate curved graphene without nanoparticles observed on the surface (Figures 7.4a, b and Figures 7.6a, b).

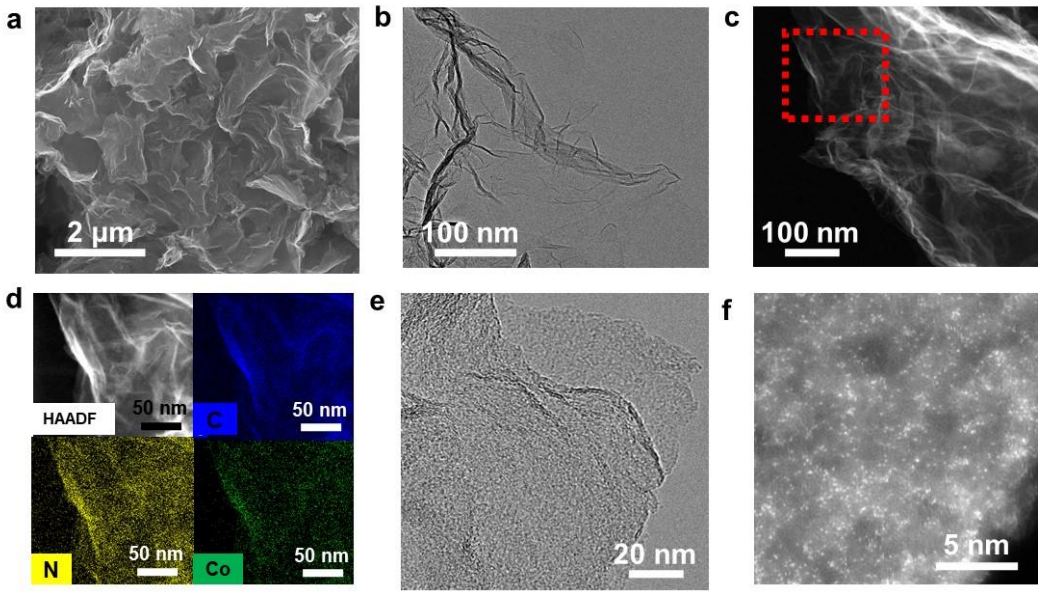

Figure 7.6 (a) SEM image of SACo@NG. (b) TEM image and (c) High-angle annular dark-field (HAADF)-STEM image of SACo@NG. (d) HAADF image and corresponding EDS mappings of SACo@NG. (e) HRTEM image and (f) AC-STEM-ADF image of SACo@NG.

SEM and TEM images of SACo@NG indicate the smooth morphology without the presence of nanoclusters (Figures 7.6a and b). Furthermore, EDS elemental mapping demonstrates that the C, N, Co elements are uniformly distributed throughout the SACo@NG (Figures 7.6c and d). HRTEM further indicates that there is no Co-derived nanoparticles or clusters detected on the surface (Figure 7.6e). AC-STEM-ADF image confirms individual Co atoms randomly dispersed on the graphene substrate (Figure 7.6f)

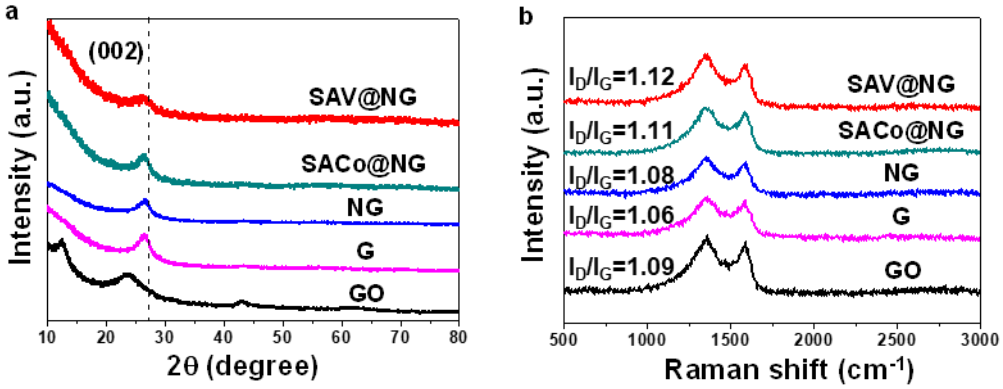

Figure 7.7 (a) XRD patterns and (b) Raman spectra of GO, G, NG, SACo@NG, and SAV@NG.

X-ray diffraction (XRD) patterns further confirm that there is no metallic vanadium or oxide

nanoparticles detectable in the products (Figure 7.7a), consistent with the TEM observations. Raman spectra indicate similar ratio of D and G band, which means the amorphous carbon derived from polyvinylpyrrolid (PVP) and poly ethyleneimine (PEI) does not change the basic sp^2 configuration of graphene (Figure 7.7b). Furthermore, the energy dispersive spectrum (EDS) elemental mapping images indicated that the C, N, V elements are uniformly distributed throughout the structure (Figure7.5c, d). Isolated single atoms were atomically dispersed on the substrate as shown by the aberration-corrected scanning transmission electron microscopy annular dark field (AC-STEM-ADF) images (Figure7.4e and f).

In order to understand the chemical environment of SAV@NG and SACo@NG, low energy X-ray photoelectron spectroscopy (XPS) and high energy X-ray absorption spectroscopy (XAS) were used to analyze the carbon, nitrogen and vanadium oxidation states (see more detail in Supplementary information). The nitrogen K-edge spectra reveal four characteristic resonances occurring at around 399.2, 400.4, 401.4 and 402.2 eV (Figure 7.4g), corresponding to aromatic C–N–C coordination in one tri-s-triazine heteroring (N1), terminal C–N–H (N2) bond, graphitic three-fold nitrogen atom N–3C (N3), and sp^3 N–3C bridging among the three tri-s-triazine moieties (N4), respectively[38]. By comparing with pure g-C_3N_4 of 399.5 eV, the peak of Seed-SAV shifts to lower energy of 399.0 eV, due to the introduction of V atoms in the g-C_3N_4 structure. The N near edge X-ray absorption fine structure (NEXAFS) indicates Seed-SAV largely maintaining the g-C_3N_4 structure (Figure 7.4g). In comparison, the SAV@NG and NG show an obvious peak at 398.4 eV, which can be assigned to the pyridinic N[39], and consistent with the XPS results (Figure 7.8).

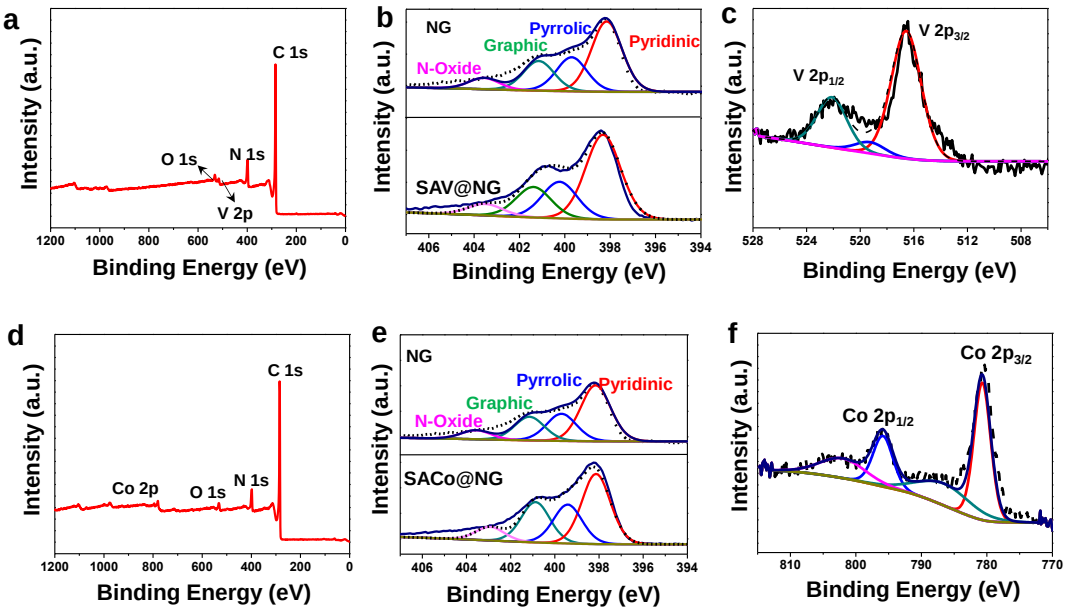

Figure 7.8 (a) The whole spectrum of SAV@NG. (b) Comparison of N 1s XPS spectra of NG and SAV@NG. (c) V 2p spectrum of SAV@NG. (d) The whole spectrum of SACo@NG. (e) Comparison of N 1s XPS spectra of NG and SACo@NG. (f) Co 2p spectrum of SACo@NG.

The whole and fine spectrum of XPS confirm the presence of V and Co in SAV@NG and SACo@NG, respectively (Figure7.8 a-f). Nitrogen atoms are present in the form of pyridinic, pyrrolic, graphitic, and oxidized N groups[40], as indicated in the high-resolution N 1s XPS spectra of SAV@NG, SACo@NG and NG. It is interesting to note that the strongest N 1s peak corresponds to pyridinic N (Figures7.8 b and e), indicating that Co and V atoms in the SACo@NG and SAV@NG are primarily bound to pyridinic N. The V 2p spectra was fitted assuming a single doublet for the V $2p_{3/2}$ and V $2p_{1/2}$ components, bringing about a spin−orbit splitting of 7.2 eV (Figure7.8c). Satellite lines due to the multiple structure can be described by one single broad peak at around 520.2 eV, which is closed to the V^{4+} position in the VOPc[41]. The Co 2p spectrum reveals that all the Co species in the presence of Co^{2+} around 780.4 eV other than metallic Co (0),[42] further confirming the isolated coordination configuration in SACo@NG.

In the Seed-SAV, the V form is predominant by V-N and slight low part of V-O, which may be due to the massive N protection in g-C_3N_4. Different from the rigorous inversion symmetry in VO, V_2O_5 and V metal, the pre-edge of SAV@NG shifts to higher energy, suggesting that the coordination symmetry is more distorted (Figure 7.4h)[43]. Turning to XAS, the extended X-ray absorption fine structure (EXAFS) (Figure 7.4i) profiles indicate the local atomic structure in

SAV@NG. The V in SAV@NG shows a lack of V-V bonding (2.24 Å) and is instead dominated by light element bonding, such as V-N (1.30 Å) and V-O (1.56 Å). SAV@NG shows similar structure with that of V in vanadium (IV) oxide phthalocyanine (VOPc), coordinating with two nitrogen atoms and one oxygen. The SAV@NG is dominated by V-N bonding with a smaller V-O contribution and consistent with XPS results (Figure7.8c). Similarly, the detailed results in Figure 7.8 f reveal that the Co in SACo@NG is also in the form of single atoms.

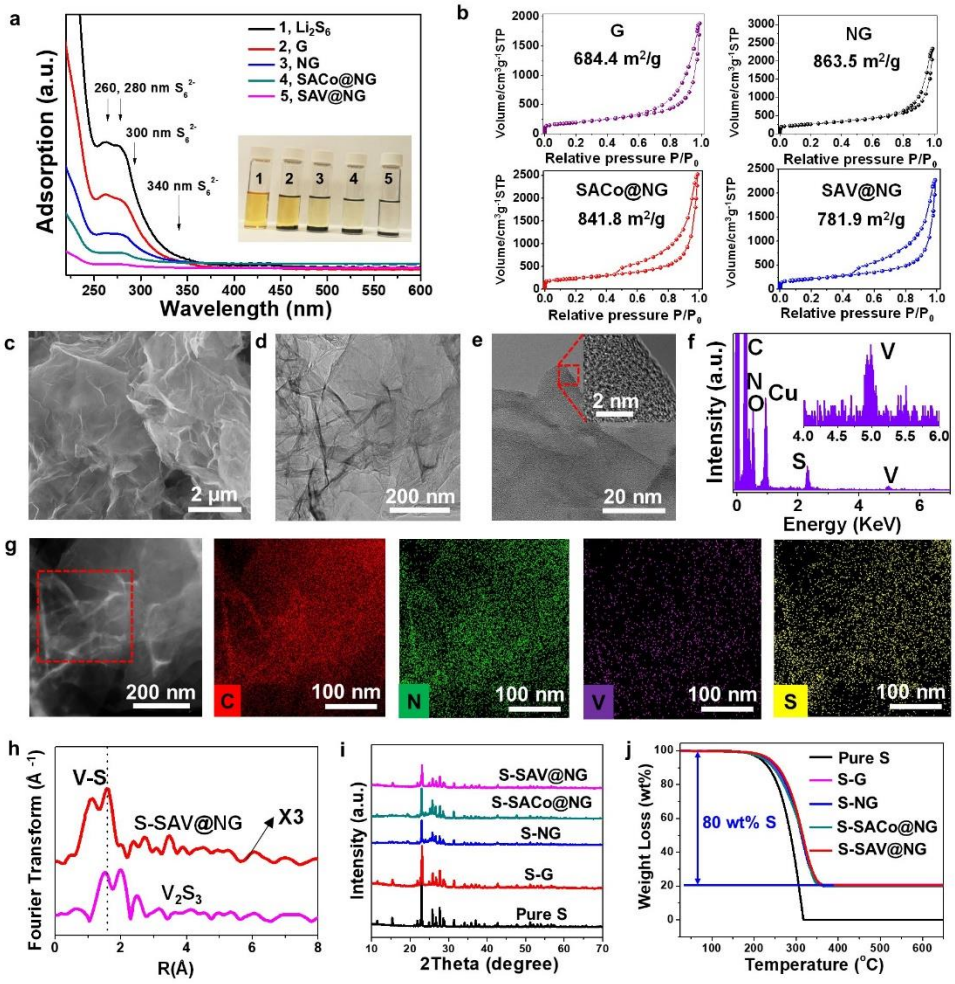

Figure 7.9 Polysulfide adsorption capability and structural characterizations of S-SAV@NG. (a), UV−vis spectra of the Li_2S_6 solution after exposure to graphene (G), NG, SACo@NG and SAV@NG and the inserted digital image of Li_2S_6 absorption test in 1,2-dimethoxyethane and 1,3-dioxolane solution (DOL/DME, 1:1 ratio, by volume). (b), Nitrogen adsorption–desorption isotherms of graphene, NG, SACo@NG, and SAV@NG. (c), SEM image of S-SAV@NG. (d), TEM and (e), HRTEM images of S-SAV@NG. (f), EDS spectroscopy of the red plotted area in

(g). (g), EDS mappings of S-SAV@NG. (h), Fourier transform of vanadium K-edge EXAFS spectra of S-SAV@NG and V_2S_3. (i), XRD patterns of pure S, S-G, S-NG, S-SACo@NG, and S-SAV@NG. (j), TGA curves of pure S, S-G, S-NG, S-SACo@NG, and S-SAV@NG.

To understand the LiPSs adsorption capability of these materials, Ultraviolet–visible (UV−vis) absorption spectroscopy was used to compare the concentration change of Li_2S_6 solution after adding graphene, NG, SACo@NG and SAV@NG (Figure7.9). The characteristic UV−vis peaks of the polysulfide solution located at 260, 280, 300 and 340 nm are assigned to the S_6^{2-} species.[40, 44] After the absorption for 1.5 h, it can be obviously observed that the absorption characteristic peaks of Li_2S_6 decrease for both graphene and NG, and almost disappear for SACo@NG and SAV@NG (inset of Figure 7.9a), which confirms better absorption capability for S_6^{2-} in SACo@NG and SAV@NG. Nitrogen adsorption/desorption isotherms were used to obtain the information of porous structure and surface area of the graphene, NG, SACo@NG and SAV@NG samples (Figure 7.9b), and the results indicate that there is a decrease in specific surface area of SACo@NG (841.8 $m^2 g^{-1}$) and SAV@NG (781.9 $m^2 g^{-1}$) compared with NG with a value of 863.5 $m^2 g^{-1}$, which may be attributed to the added metal that dilutes the value of surface area.

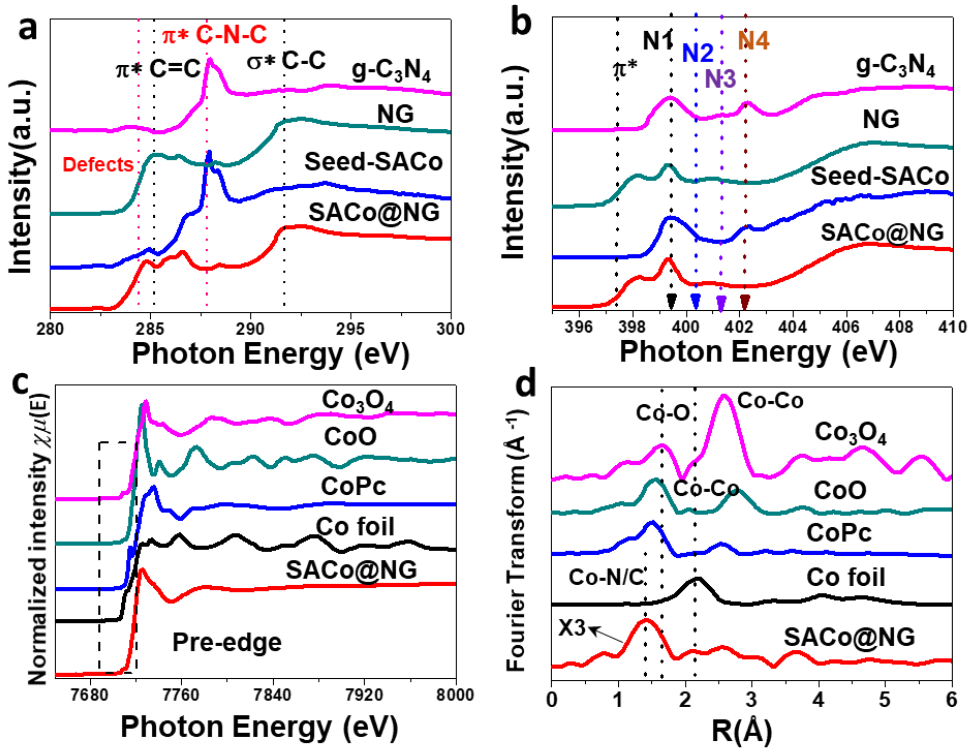

Figure 7.10 (a) C K-edge and (b) N K-edge of NEXAFS for SACo@NG, Seed-SACo, NG, and g-C_3N_4. (c) Fine Co L-edge of XANES for SACo@NG, Co foil, CoPc, CoO, and Co_3O_4. (d) Fourier transform of Co K-edge EXAFS spectra of SACo@NG, Co foil, CoPc, CoO, and Co_3O_4.

The C K-edge and N K-edge results of SACo@NG are similar to the NG and SAV@NG(Figures 7.10a and b). The pre-edge XANES of Co in SACo@NG is close to that for CoPc rather than the Co foil (Figure7.10c). As shown in the Fourier transforms of Co K-edge EXAFS, the peak at 1.42 Å in SACo@NG, corresponding to Co−N/C scattering paths, which is different from the peaks at 1.59 and 2.33 Å that corresponding to Co-O and Co−Co (Figure7.10d), respectively. Comparing this with the spectra of Co_3O_4, CoO and Co foil references, no Co−O and Co−Co scattering paths are detected in SACo@NG, revealing the presence of the Co−N local structure in the sample.

The strong chemical adsorption of SAC with LiPSs and large surface area of the composite are beneficial for constructing high performance sulfur electrodes in Li-S batteries. Therefore, four electrodes were produced through sulfur infiltration methods. Sulfur is uniformly dispersed on the surface of SAV@NG (S-SAV@NG, Figure7.9) and SACo@NG without obvious sulfur particle aggregates, which are different from S-G and S-NG.

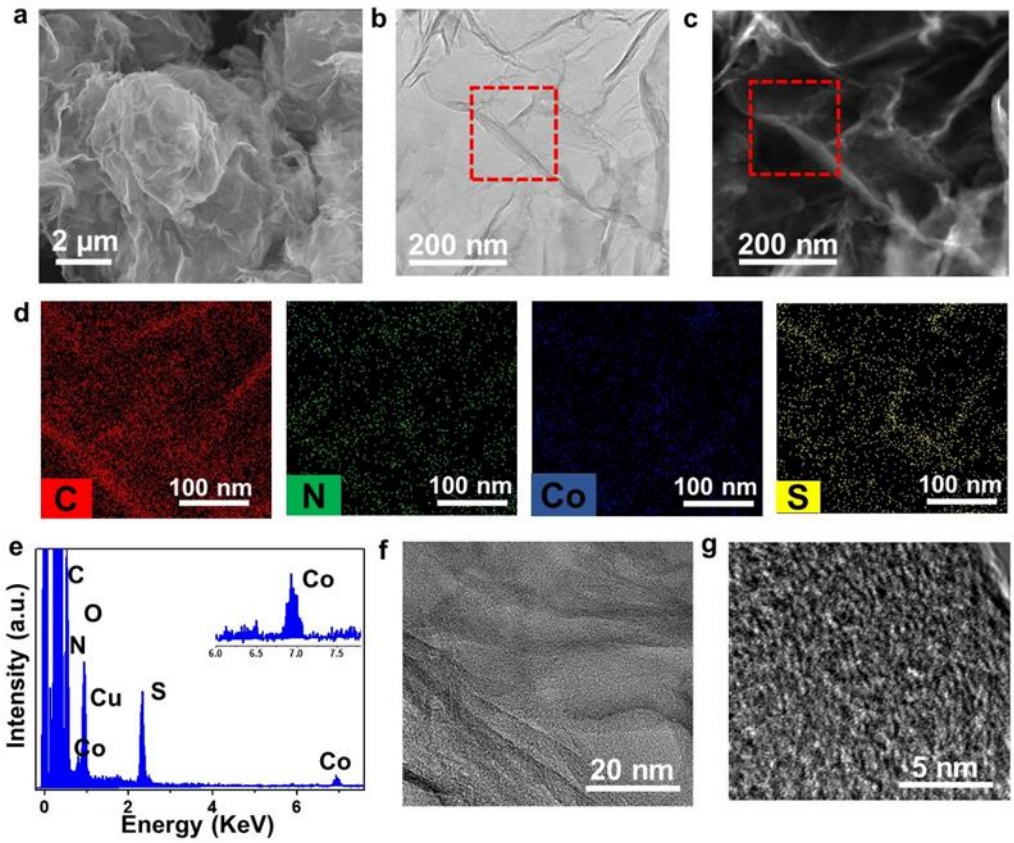

Figure 7.11 (a) SEM image of S-SACo@NG. (b) TEM image and (c) HAADF-STEM image of S-SACo@NG. (d) EDS mappings of S-SACo@NG. (e) EDS spectra of S-SACo@NG. (f, g) HRTEM images of S-SACo@NG.

Sulfur uniformly disperses on the surface of SACo@NG (Figure7.11a) without obvious sulfur particles. Furthermore, the TEM and corresponding HAADF images (Figures 7.11b and c) confirm the absence of obvious sulfur clusters. The uniform elemental distribution of C, N, Co, S reveals the good sulfur dispersion on SACo@NG (Figure 7.11d). The strong signals of 2.30 and 7.92 eV are attributed to the K_α of S and Co (Figure 7.11e). The HRTEM images (Figures 7.11f, g) confirm there are no sulfur particles, demonstrating good dispersion of sulfur on the S-SACo@NG.

In addition, HRTEM images in Figure 7.9e, e also confirms the absence of obvious sulfur clusters. The EDS signals at 2.30 and 4.95 KeV in Figure 7.10f indicate the presence of S and V in the S-SAV@NG. The uniform elemental distribution of C, N, V, and S reveals the good sulfur dispersion on the SAV@NG (Figure 7.9g). In addition, the EXAFS of S-SAV@NG and V_2S_3 (Figure 7.9h) were conducted to analyze the V state after sulfur infiltration. The first shell of V-S in V_2S_3 is very close to V-O around 1.53 Å, with a second shell of about 2.02 Å. It proves that the dextral bonding

near to V-S formed in the S-SAV@NG (Figure 7.9h). XRD patterns of S-G, S-NG, S-SACo@NG, S-SAV@NG and pristine sulfur exhibit similar characteristic diffraction peaks (Figure 7.10i), which can be indexed as a typical crystal structure of orthorhombic sulfur ((JCPDS) No. 08-0247). TGA is used to determine the sulfur content in the composite and the results indicate a high loading of sulfur in the above-mentioned samples with values up to 80 wt% (Figure 7.9j). All of these characteristics show great potential for applying single atom seeded graphene in Li-S batteries towards desirable electrochemical performance.

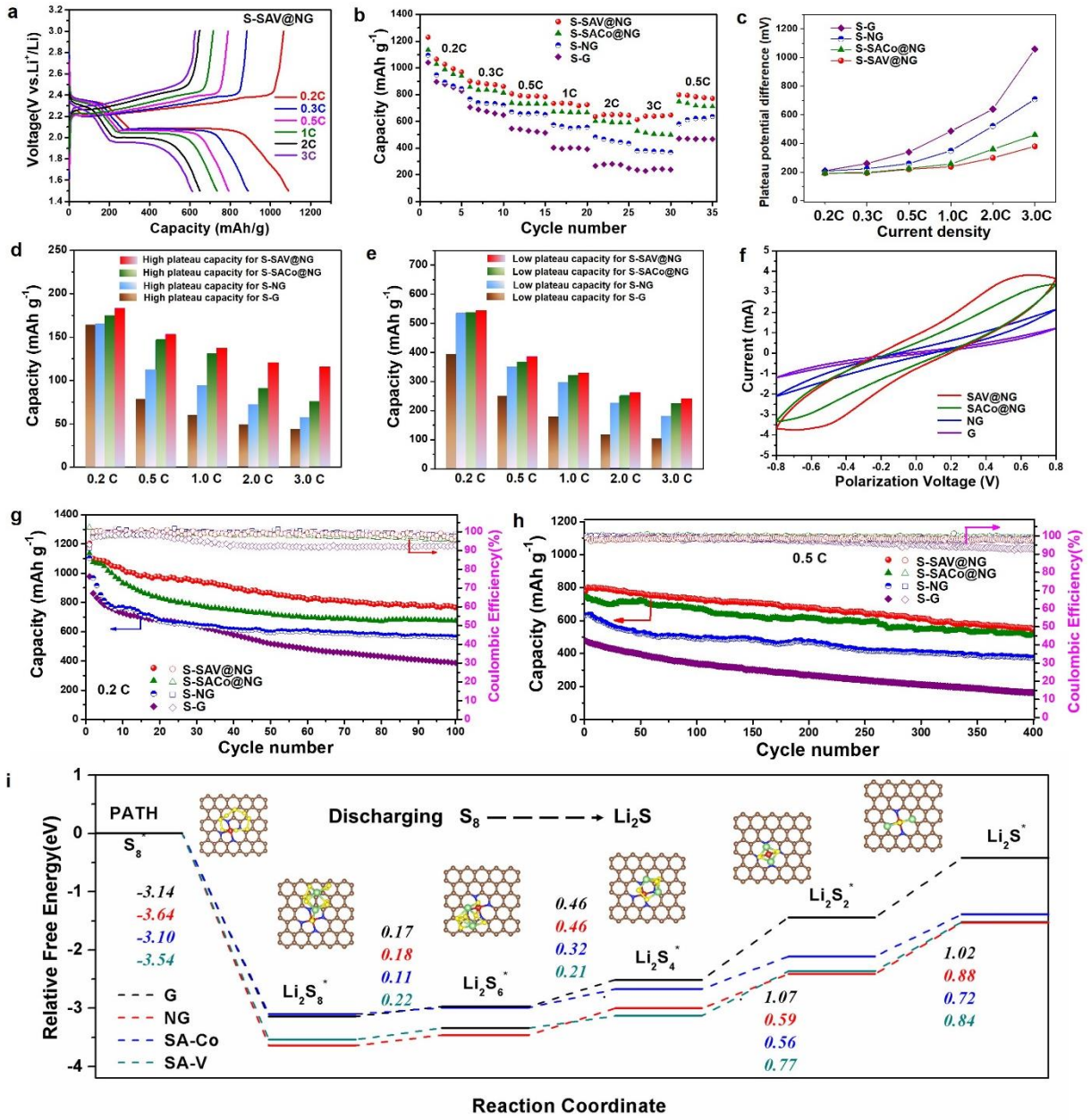

Figure 7.12 Electrochemical performance and mechanism understanding. (a), Charge−discharge

voltage profiles of S-SAV@NG electrode at current rates of 0.2, 0.3, 0.5, 1.0, 2.0, and 3.0 C. (b), Rate performance of the S-G, S-NG, S-SACo@NG and S-SAV@NG electrodes. (c), Comparison of the potential difference between the charge and discharge plateaus at different current densities for the S-G, S-NG, S-SACo@NG and S-SAV@NG electrodes. (d) and (e), High and low plateau capacity at different current densities for the S-G, S-NG, S-SACo@NG and S-SAV@NG electrodes. (f), CV curves of symmetric cells with the S-G, S-NG, S-SACo@NG and S-SAV@NG electrodes from −0.8 to 0.8 V. (g), Cycling performance and Coulombic efficiency of the S-G, S-NG, S-SACo@NG and S-SAV@NG electrodes at 0.2 C for 100 cycles. (h), Long-term cycling stability of the S-G, S-NG, S-SACo@NG and S-SAV@NG electrodes at 0.5 C for 400 cycles. (i), Energy profiles for the reduction of polysulfides on graphene, NG, SACo@NG and SAV@NG.

To substantiate the effective S/LiPSs/Li_2S catalysis conversion by single atoms in improving the performance of Li-S batteries, a series of electrochemical measurements of S-G, S-NG, S-SACo@NG and S-SAV@NG electrodes were conducted. From the charge/discharge profiles of the S-SAV@NG electrode (Figure7.12), it is clearly observed that two discharge/charge plateaus are well-retained even at a high rate of 3 C, indicating the excellent reaction kinetics. The S-SAV@NG electrode has an obvious higher discharge plateau at ~2.32 V (reduction of sulfur to long-chain LiPSs) and a longer plateau at ~2.10 V (formation of short-chain LiPSs) with corresponding charge plateaus between 2.20 and 2.40 V (transformation from Li_2S_2/Li_2S to long-chain LiPSs and then to sulfur)[45]. The efficient catalysis conversion of SAV enables the battery to deliver the highest capacity of 1230 mAh g^{-1} at 0.2 C rate, and the reversible discharge capacity could reach 645 mAh g^{-1} at a high current density of 3 C rate (Figure 7.13b). When the current rate was abruptly changed back to 0.5 C rate again, the electrode was able to recover to the original capacity, indicating the robustness and stable structure of the S-SAV@NG electrode.

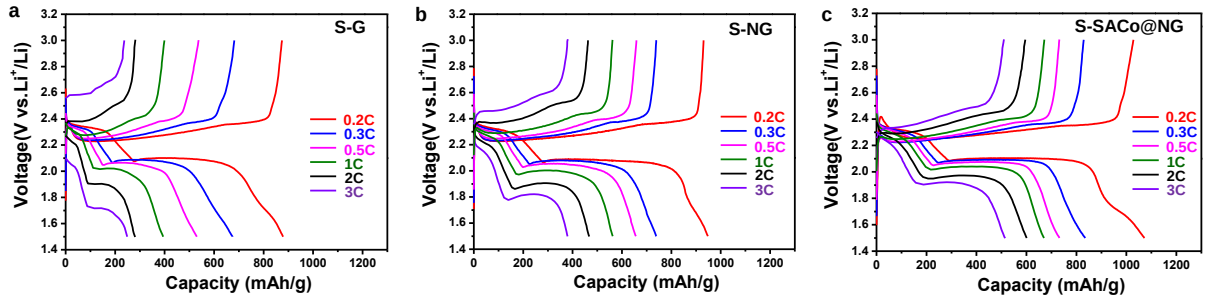

Figure 7.13 Galvanostatic charge–discharge curves of (a) S-G, (b) S-NG, and (c) S-SACo@NG electrodes at different rates.

Likewise, the S-SACo@NG electrode also exhibits good rate performance with well-defined charge/discharge plateaus, much better than S-G and S-NG electrodes with large polarization especially at high rates (Figure7.13 a-c). The polarization for the S-SAV@NG and S-SACo@NG electrodes is much lower compared to the S-G and S-NG electrodes at different current densities, *e.g.* the overpotential of S-SAV@NG and S-SACo@NG at 3.0 C is 380 and 460 mV respectively, much lower than that of S-NG (710 mV) and S-G (1060 mV) electrodes, demonstrating better redox reaction kinetics and good reversibility of single atom seeded sulfur electrodes (Figure7.12c). Moreover, the plateaus of the S-SAV@NG electrode are long and flat and are well-retained from 0.3 to 3 C rates between the charge/discharge processes. When comparing the capacity contribution between high and low plateau capacity at different current densities, it is worth noting that the S-SAV@NG has a larger capacity contribution from high and low plateau range especially at high current densities compared with the S-NG and S-SACo@NG electrodes (Figure7.12d, e). In sharp contrast, the capacity in high plateau of S-G electrode is only about one third of SAV@NG electrode at 3 C. Cyclic voltammetry (CV) tests in symmetric cells using an electrolyte containing 0.5 mol L^{-1} Li_2S_6 and 1 mol L^{-1} LiTFSI dissolved in DOL/DME (v/v = 1/1) were carried out to study the catalytic activity of G, NG, SACo@NG and SAV@NG electrodes within a potential window from −0.8 to 0.8 V (Figure7.12f). The SAV@NG and SACo@NG electrodes exhibit higher current under identical test conditions, indicating rapid polysulfide redox conversion reactions of polysulfides on the electrolyte/electrode surface compared to the other electrodes. The accelerated polysulfide redox reaction kinetics can be ascribed to the catalytic activity of SAV and SACo seeded on the graphene promoting the polysulfide conversion.

The cycling performance of these electrodes was measured at 0.2 C between 1.5 and 2.8 V for 100 cycles, as shown in Figure 7.12g. The S-SACo@NG and S-SAV@NG electrodes exhibit good cycling stability with nearly 100% Coulombic efficiency and reversible specific capacities of 675 and 770 mAh g^{-1} after 100 cycles, much higher than those of the S-G and S-NG with values of 388 and 560 mAh g^{-1}, demonstrating the effectiveness of the single atom structural design in confining sulfur species through a combined physical and chemical interaction. In addition, the long-term cyclic test at 0.5 C rate was carried out and the initial specific capacity is 780 and 749 mAh g^{-1} for S-SAV@NG and S-SACo@NG electrodes, respectively, and they stabilized at ~551 and 513 mAh g^{-1} after 400 cycles, respectively (Figure 7.12h).

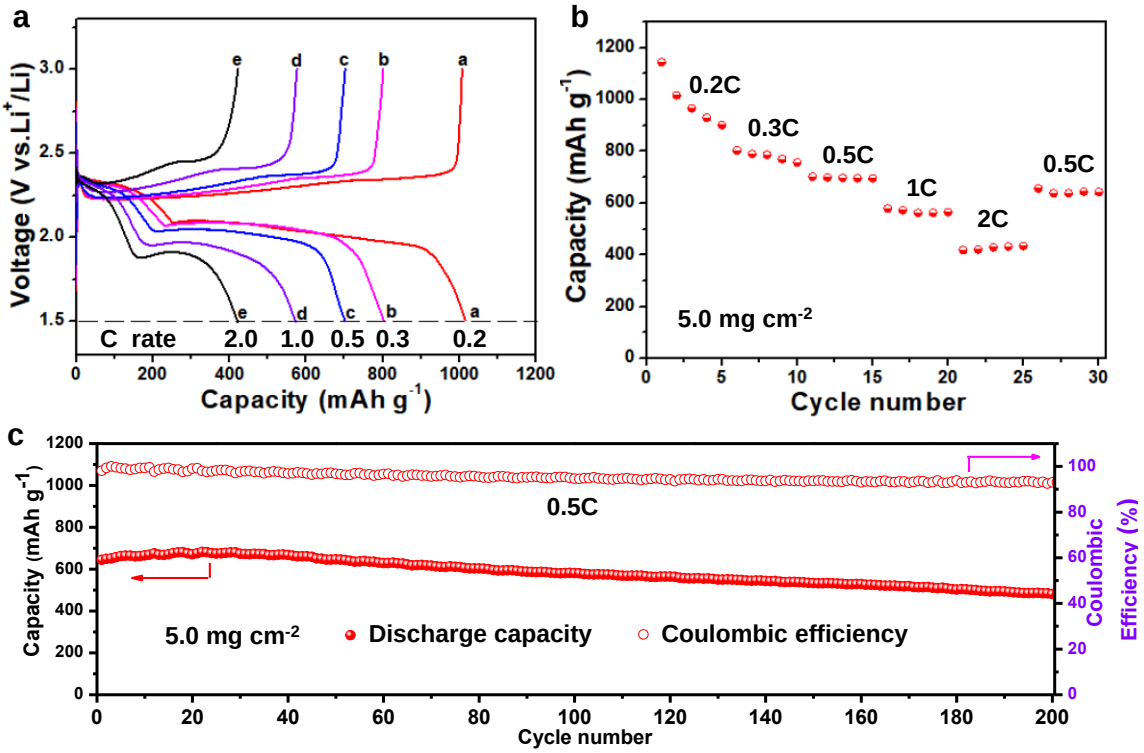

Figure 7.14 (a) Galvanostatic charge–discharge curves of S-SAV@NG electrode at different current densities. (b) Rate capability of S-SAV@NG electrode at 5.0 mg cm^{-2}. (c) Cycling stability and Coulombic efficiency of S-SAV@NG electrode at 0.5 C for 200 cycles.

The capacity decay is 0.073% and 0.079% per cycle for the S-SAV@NG and S-SACo@NG electrodes, much better than those of S-NG and S-G electrodes with decay rates of 0.101% and 0.165% per cycle, respectively. To further satisfy the requirements of high-energy batteries, the active sulfur loading of S-SAV@NG was increased to 5 mg cm^{-2}. It is obviously observed that the discharging/charging plateaus are still well-retained even at a high rate of 2.0 C (Figure7.14a), demonstrating that the reaction kinetic is not influenced by high sulfur loading. The single atom active site catalyst enables the battery to deliver a high initial capacity of 1143 mAh g^{-1} at 0.2 C, and 701, 580 and 430 mAh g^{-1} at higher cycling rates of 0.5, 1.0, and 2.0 C, respectively (Figure7.14b). In addition, a long-term cyclic test at 0.5 C rate was conducted and the initial specific capacity is 645 mAh g^{-1}, which stabilizes at ~485 mAh g^{-1} after 200 cycles (Figure7.14c). The significantly improved battery performance can be attributed to the merits of single atom seeded electrode configuration design including: (i) the single atom V effectively traps the dissolved LiPSs and provides more active sites for Li_2S deposition; (ii) the graphene substrate can

improve conductivity of the electrode and accommodate the volume change of the active sulfur and intermediate materials during cycling; (iii) the efficient catalytic conversion of Li_2S/LiPSs accelerates the reaction kinetics and prevents the loss of active material, thus realizing a high capacity, fast charging, and long cycling life Li-S battery.To attain an in-depth understanding of the reasons for the improved discharge reaction kinetics of the S-SACo@NG and S-SAV@NG cathodes, the overall reactions based on the reversible formation of Li_2S from S_8 and Li bulk were considered as shown in Figure 7.12i. The Gibbs free energies for all of the reaction steps were calculated and the evolution profile from S_8 to Li_2S species on all the substrates are exhibited.

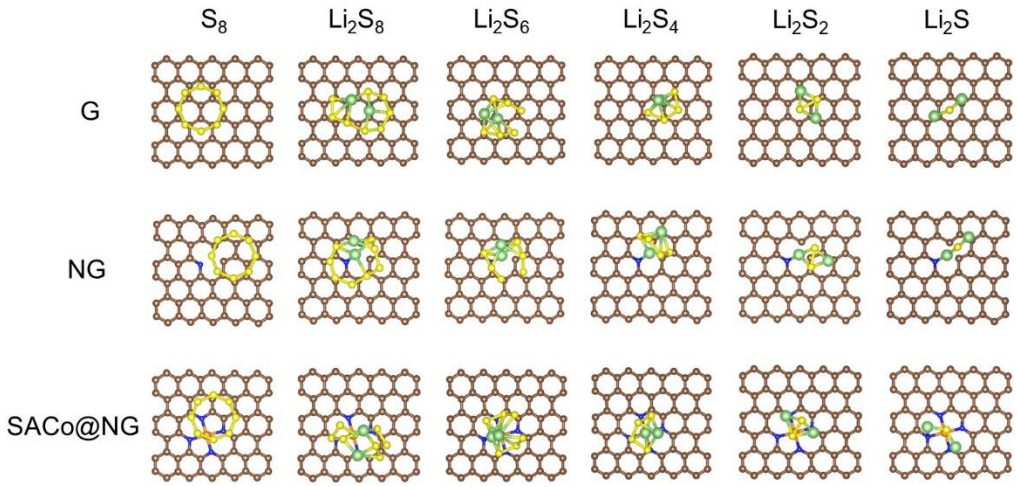

Figure 7.15 Detailed adsorption atomic configuration for the polysulfides on the G, NG, and SACo@NG.

The detailed optimized structures of the intermediates on the SAV@NG substrate were shown in the inset, while other atomic configurations can be seen in Figure7.15. It can be seen that the reduction step of S_8 to the Li_2S_8 shows a spontaneous exothermic reaction on all the substrates. The following four reduction steps, from Li_2S_6 to Li_2S, were an endothermic reaction, while the last two steps from Li_2S_4 to Li_2S_2 and Li_2S_2 to Li_2S exhibit the big positive Gibbs energy barrier comparing to other steps. The rate-limiting step in the graphene is the step from Li_2S_4 to Li_2S_2 with the value of 1.07 eV, but the rate-limiting step for the NG, SACo@NG and SAV@NG is the step from Li_2S_2 to the Li_2S. Considering the low positive Gibbs energy barrier of rate-limiting step on SACo@NG (0.72 eV) and SAV@NG (0.84 eV), the reduction process of sulfur is more convenient on these substrates during discharging and thus improves the electrochemical performance of Li-S batteries.

7.4 Conclusion

In summary, we have demonstrated a well-characterized and customizable method to synthesize SACs supported on graphene *via* a seeding strategy with scalable amount, controllable loading, and adjustable components. Based on the guidance of theoretical simulations, vanadium atom catalysts were chosen and prepared for high-performance Li-S batteries. The great improvement in the battery capacity, kinetics, and cycling life confirms the merits of SACs. The single vanadium active catalysis sites facilitate both the formation and decomposition of solid Li_2S in discharging and charging processes, which guarantee a high utilization of sulfur species. The precise synthesis of commercial quantities of SACs directly guided by theoretical calculations and our seeding fabrication approach provide tremendous opportunities for developing high energy/power density and long-life rechargeable batteries.

7.5 References

[1] P.G. Bruce, S.A. Freunberger, L.J. Hardwick, J.-M. Tarascon, Li-O_2 and Li-S batteries with high energy storage, Nat. Mater., 11 (2012) 19-29.

[2] Q. Pang, X. Liang, C.Y. Kwok, L.F. Nazar, Advances in lithium–sulfur batteries based on multifunctional cathodes and electrolytes, Nat. Energy, 1 (2016) 16132.

[3] Y. Liu, G. Zhou, K. Liu, Y. Cui, Design of Complex Nanomaterials for Energy Storage: Past Success and Future Opportunity, Acc. Chem. Res., 50 (2017) 2895-2905.

[4] A. Manthiram, Y. Fu, S.-H. Chung, C. Zu, Y.-S. Su, Rechargeable Lithium–Sulfur Batteries, Chem. Rev., 114 (2014) 11751-11787.

[5] G. Zhou, L. Xu, G. Hu, L. Mai, Y. Cui, Nanowires for Electrochemical Energy Storage, Chem. Rev., 119 (2019) 11042-11109.

[6] J.H. Yun, J.-H. Kim, D.K. Kim, H.-W. Lee, Suppressing Polysulfide Dissolution via Cohesive Forces by Interwoven Carbon Nanofibers for High-Areal-Capacity Lithium–Sulfur Batteries, Nano Lett., 18 (2018) 475-481.

[7] Z. Yuan, H.-J. Peng, T.-Z. Hou, J.-Q. Huang, C.-M. Chen, D.-W. Wang, X.-B. Cheng, F. Wei, Q. Zhang, Powering Lithium–Sulfur Battery Performance by Propelling Polysulfide Redox at

Sulfiphilic Hosts, Nano Lett., 16 (2016) 519-527.

[8] D. Liu, C. Zhang, G. Zhou, W. Lv, G. Ling, L. Zhi, Q.-H. Yang, Catalytic Effects in Lithium–Sulfur Batteries: Promoted Sulfur Transformation and Reduced Shuttle Effect, Adv. Sci., 5 (2018) 1700270.

[9] G.M. Zhou, Y. Zhao, C. Zu, A. Manthiram, Free-standing TiO2 nanowire-embedded graphene hybrid membrane for advanced Li/dissolved polysulfide batteries, Nano Energy, 12 (2015) 240-249.

[10] Y. Wang, R. Zhang, J. Chen, H. Wu, S. Lu, K. Wang, H. Li, C.J. Harris, K. Xi, R.V. Kumar, S. Ding, Enhancing Catalytic Activity of Titanium Oxide in Lithium–Sulfur Batteries by Band Engineering, Adv. Energy Mater., 9 (2019) 1900953.

[11] G. Zhou, H. Tian, Y. Jin, X. Tao, B. Liu, R. Zhang, Z.W. Seh, D. Zhuo, Y. Liu, J. Sun, J. Zhao, C. Zu, D.S. Wu, Q. Zhang, Y. Cui, Catalytic oxidation of Li_2S on the surface of metal sulfides for Li−S batteries, Proc. Natl. Acad. Sci. U.S.A., 114 (2017) 840-845.

[12] X. Liang, C. Hart, Q. Pang, A. Garsuch, T. Weiss, L.F. Nazar, A highly efficient polysulfide mediator for lithium–sulfur batteries, Nature Communications, 6 (2015) 5682.

[13] C. Zheng, S. Niu, W. Lv, G. Zhou, J. Li, S. Fan, Y. Deng, Z. Pan, B. Li, F. Kang, Q.-H. Yang, Propelling polysulfides transformation for high-rate and long-life lithium–sulfur batteries, Nano Energy, 33 (2017) 306-312.

[14] Y. Wang, R. Zhang, Y.-c. Pang, X. Chen, J. Lang, J. Xu, C. Xiao, H. Li, K. Xi, S. Ding, Carbon@titanium nitride dual shell nanospheres as multi-functional hosts for lithium sulfur batteries, Energy Storage Mater., 16 (2019) 228-235.

[15] X. Yang, X. Gao, Q. Sun, S.P. Jand, Y. Yu, Y. Zhao, X. Li, K. Adair, L.-Y. Kuo, J. Rohrer, J. Liang, X. Lin, M.N. Banis, Y. Hu, H. Zhang, X. Li, R. Li, H. Zhang, P. Kaghazchi, T.-K. Sham, X. Sun, Promoting the Transformation of Li2S2 to Li2S: Significantly Increasing Utilization of Active Materials for High-Sulfur-Loading Li–S Batteries, Adv. Mater., 31 (2019) 1901220.

[16] Z. Sun, J. Zhang, L. Yin, G. Hu, R. Fang, H.-M. Cheng, F. Li, Conductive porous vanadium nitride/graphene composite as chemical anchor of polysulfides for lithium-sulfur batteries, Nature Communications, 8 (2017) 14627.

[17] L. Li, L. Chen, S. Mukherjee, J. Gao, H. Sun, Z. Liu, X. Ma, T. Gupta, C.V. Singh, W. Ren, H.-M. Cheng, N. Koratkar, Phosphorene as a Polysulfide Immobilizer and Catalyst in High-Performance Lithium–Sulfur Batteries, Adv. Mater., 29 (2017) 1602734.

[18] X.-F. Yang, A. Wang, B. Qiao, J. Li, J. Liu, T. Zhang, Single-Atom Catalysts: A New Frontier in Heterogeneous Catalysis, Acc. Chem. Res., 46 (2013) 1740-1748.

[19] J. Liu, Catalysis by Supported Single Metal Atoms, ACS Catal., 7 (2017) 34-59.

[20] B. Qiao, A. Wang, X. Yang, L.F. Allard, Z. Jiang, Y. Cui, J. Liu, J. Li, T. Zhang, Single-atom catalysis of CO oxidation using Pt_1/FeO_x, Nat. Chem., 3 (2011) 634-641.

[21] C. Zhu, S. Fu, Q. Shi, D. Du, Y. Lin, Single-Atom Electrocatalysts, Angew. Chem. Int. Ed., 56 (2017) 13944-13960.

[22] A. Wang, J. Li, T. Zhang, Heterogeneous single-atom catalysis, Nat. Rev. Mater., 2 (2018) 65-81.

[23] H. Xu, D. Cheng, D. Cao, X.C. Zeng, A universal principle for a rational design of single-atom electrocatalysts, Nat. Catal., 1 (2018) 339-348.

[24] G. Kyriakou, M.B. Boucher, A.D. Jewell, E.A. Lewis, T.J. Lawton, A.E. Baber, H.L. Tierney, M. Flytzani-Stephanopoulos, E.C. Sykes, Isolated metal atom geometries as a strategy for selective heterogeneous hydrogenations, Science, 335 (2012) 1209.

[25] J. Wang, L. Jia, J. Zhong, Q. Xiao, C. Wang, K. Zang, H. Liu, H. Zheng, J. Luo, J. Yang, H. Fan, W. Duan, Y. Wu, H. Lin, Y. Zhang, Single-atom catalyst boosts electrochemical conversion reactions in batteries, Energy Storage Mater., 18 (2019) 246-252.

[26] Z. Du, X. Chen, W. Hu, C. Chuang, S. Xie, A. Hu, W. Yan, X. Kong, X. Wu, H. Ji, L.-J. Wan, Cobalt in Nitrogen-Doped Graphene as Single-Atom Catalyst for High-Sulfur Content Lithium–Sulfur Batteries, J. Am. Chem. Soc., 141 (2019) 3977-3985.

[27] J. Xie, B.-Q. Li, H.-J. Peng, Y.-W. Song, M. Zhao, X. Chen, Q. Zhang, J.-Q. Huang, Implanting Atomic Cobalt within Mesoporous Carbon toward Highly Stable Lithium–Sulfur Batteries, Adv. Mater., 31 (2019) 1903813.

[28] L. Zhang, D. Liu, Z. Muhammad, F. Wan, W. Xie, Y. Wang, L. Song, Z. Niu, J. Chen, Single

Nickel Atoms on Nitrogen-Doped Graphene Enabling Enhanced Kinetics of Lithium–Sulfur Batteries, Adv. Mater., 31 (2019) 1903955.

[29] A. Urban, D.-H. Seo, G. Ceder, Computational understanding of Li-ion batteries, Npj Comput. Mater., 2 (2016) 16002.

[30] X. Chen, H.-J. Peng, R. Zhang, T.-Z. Hou, J.-Q. Huang, B. Li, Q. Zhang, An Analogous Periodic Law for Strong Anchoring of Polysulfides on Polar Hosts in Lithium Sulfur Batteries: S- or Li-Binding on First-Row Transition-Metal Sulfides?, ACS Energy Lett., 2 (2017) 795-801.

[31] B. Ravel, M. Newville, ATHENA, ARTEMIS, HEPHAESTUS: data analysis for X-ray absorption spectroscopy using IFEFFIT, J. Synchrotron Rad., 12 (2005) 537-541.

[32] D. Aurbach, E. Pollak, R. Elazari, G. Salitra, C.S. Kelley, J. Affinito, On the Surface Chemical Aspects of Very High Energy Density, Rechargeable Li-Sulfur Batteries, Journal of The Electrochemical Society, 156 (2009) A694-A702.

[33] J. Klimeš, D.R. Bowler, A. Michaelides, Van der Waals density functionals applied to solids, Phys. Rev. B 83 (2011) 195131-195144.

[34] M. Methfessel, A.T. Paxton, High-precision sampling for Brillouin-zone integration in metals, Phys. Rev. B, 40 (1989) 3616-3621.

[35] Q. Zhang, Y. Wang, Z.W. Seh, Z. Fu, R. Zhang, Y. Cui, Understanding the Anchoring Effect of Two-Dimensional Layered Materials for Lithium–Sulfur Batteries, Nano Lett., 15 (2015) 3780-3786.

[36] S. Froyen, Brillouin-zone integration by Fourier quadrature: Special points for superlattice and supercell calculations, Phys. Rev. B, 39 (1989) 3168-3172.

[37] G. Henkelman, H. Jonsson, Improved tangent estimate in the nudged elastic band method for finding minimum energy paths and saddle points, J Chem Phys, 113 (2000) 9978-9985.

[38] K.S. Lakhi, D.-H. Park, G. Singh, S.N. Talapaneni, U. Ravon, K. Al-Bahily, A. Vinu, Energy efficient synthesis of highly ordered mesoporous carbon nitrides with uniform rods and their superior CO_2 adsorption capacity, J. Mater. Chem. A, 5 (2017) 16220-16230.

[39] H.B. Yang, J. Miao, S.-F. Hung, J. Chen, H.B. Tao, X. Wang, L. Zhang, R. Chen, J. Gao, H.M.

Chen, L. Dai, B. Liu, Identification of catalytic sites for oxygen reduction and oxygen evolution in N-doped graphene materials: Development of highly efficient metal-free bifunctional electrocatalyst, Sci. Adv., 2 (2016) e1501122.

[40] G.M. Zhou, E. Paek, G.S. Hwang, A. Manthiram, Long-life Li/polysulphide batteries with high sulphur loading enabled by lightweight three-dimensional nitrogen/sulphur-codoped graphene sponge, Nature Communications, 6 (2015) 7760-7770.

[41] H. Adler, M. Paszkiewicz, J. Uihlein, M. Polek, R. Ovsyannikov, T.V. Basova, T. Chassé, H. Peisert, Interface Properties of VOPc on Ni(111) and Graphene/Ni(111): Orientation-Dependent Charge Transfer, J. Phys. Chem. C, 119 (2015) 8755-8762.

[42] Y. Pan, R. Lin, Y. Chen, S. Liu, W. Zhu, X. Cao, W. Chen, K. Wu, W.-C. Cheong, Y. Wang, L. Zheng, J. Luo, Y. Lin, Y. Liu, C. Liu, J. Li, Q. Lu, X. Chen, D. Wang, Q. Peng, C. Chen, Y. Li, Design of Single-Atom Co–N_5 Catalytic Site: A Robust Electrocatalyst for CO_2 Reduction with Nearly 100% CO Selectivity and Remarkable Stability, J. Am. Chem. Soc., 140 (2018) 4218-4221.

[43] D. Haskel, Z. Islam, J. Lang, C. Kmety, G. Srajer, K.I. Pokhodnya, A.J. Epstein, J.S. Miller, Local structural order in the disordered vanadium tetracyanoethylene room-temperature molecule-based magnet, Phys. Rev. B 70 (2004) 054422.

[44] C. Barchasz, F. Molton, C. Duboc, J.C. Lepretre, S. Patoux, F. Alloin, Lithium/Sulfur Cell Discharge Mechanism: An Original Approach for Intermediate Species Identification, Anal Chem, 84 (2012) 3973-3980.

[45] G.M. Zhou, S. Pei, L. Li, D.-W. Wang, S. Wang, K. Huang, L.-C. Yin, F. Li, H.-M. Cheng, A Graphene–Pure-Sulfur Sandwich Structure for Ultrafast, Long-Life Lithium–Sulfur Batteries, Adv. Mater., 26 (2014) 625-631.

Chapter 8: Controlled synthesis of nickel single atoms embedded in carbon nanotube and graphene supports

Abstract

Single atom catalysts (SACs) have attracted much attentions due to the advantages of high catalysis efficiency and selectivity. However, the controllable, scalable and efficient synthesis of SACs remains a significant challenge. Herein, we report two feasible closely associated approaches to synthesize nickel single atoms on nitrogen doped carbon nanotube (NiSA-N-CNT) and nitrogen-doped graphene (NiSA-N-G). The formation of NiSA-N-CNT is due to the solid-to-solid rolling up mechanism during the high temperature pyrolysis from the stacked and layered g-C_3N_4-Ni structure to a bamboo-shaped tubular NiSA-N-CNT structure. Addition of citric acid interrupts the solid-to-solid rolling process, and result in NiSA-N-G. As for the synthesis of NiSA-N-G, the defective carbon anchoring mechanism was proposed to synthesize the single nickel atom on graphene. Finally, the CO_2 reduction reaction performance also have been compared for the two structures, which reveal that more exposed active sites owned in graphene structure achieves higher catalytic performance. The novel synthesis approaches and mechanism provides new understanding of single atom metal catalyst.

8.1. Introduction

Single atom catalysts (SACs) consist of individual atoms dispersed on and/or coordinated with the surface atoms of an appropriate support with high catalytic activity, selectivity and high atomic efficiency, and have been attracting increasing attention in recent years[1-6]. Because the single atoms are highly active and tend to form aggregates to reduce the Gibbs free energy, the atomic loading is generally very low, less than 3 wt%[1, 7]. Thus the development of facile and scalable synthesis method for the high SAC loading is critical for the practical application of SACs[8, 9]. The synthesized SACs should have a high loading and efficiently high active sites as the SACs embedded within the carbon supports may not be active for the electrocatalytic processes[10, 11]. To this end, many efforts have been explored to the synthesis of SACs with various approaches.

Due to the feasible preparation associated with the impregnation method, metal oxides,[12, 13] and metal or carbon nitride [14, 15] have been extensively studied as potential supports to achieve SACs. However, the large mass ratio and limited surface area of the support results in a restrained loading of SACs to generally less than 2-3 wt.%. Physical methods including atomic layer deposition (ALD) were applied to synthesize SACs[16, 17]. However, agglomeration of the single atom nanoclusters and particles is almost inevitable with loading lower than 2wt%. The theoretical calculation confirms than the nitrogen coordination to form the Me-pyridine/pyrrole-N4 is one powerful way to stabilize SACs. The relative research works have been reported in the series of carbon materials including carbon nanotubes(CNTs),[18-20] graphene,[7, 21-23] g-C_3N_4,[24] porous carbon,[25, 26] carbon fibers,[27] carbon spheres,[28] as well as MOF derived porous carbon[29-31]. The challenges still remain to control the synthesis process and to increase the SAC loading significantly. It is vital to open up possibilities to selectively design characteristic active sites for electrocatalysis and catalysis applications[32].

Most recently, we developed a facile one-pot pyrolysis method to synthesize carbon nanotube supported Ni SACs (NiSA-N-CNT) with loading as high as 20.3wt%[33]. The formation of NiSA-N-CNT is most likely through a rolling-up mechanism of the stacked and layered Ni single atom embedded g-C_3N_4 (g-C_3N_4-Ni) sheets to NiSA-N-CNT bamboo-shaped tubular structure activated by the high kinetic energy of embedded Ni single atoms[11]. The as-synthesized NiSA-N-CNT shows a high activity and selectivity for electrochemical CO_2 reduction (CO_2RR) to CO with depressed activity for H_2 evolution reaction (HER). However, we also found that the Ni SACs embedded with the inner tubes of CNTs are not active for the CO_2RR due to the shielding effect of the outer walls of CNTs. To avoid the embedded Ni SAC in CNTs, we introduce defective carbon species to restrain the solid-to-solid rolling-up process of g-C_3N_4-Ni sheets into CNTs structure. Instead, Ni single atoms embedded in graphene, NiSA-N-G is formed. The results indicate that NiSA-N-G has a lower Ni SAC loading but higher catalytic performance for CO_2RR, evidently due to the highly exposed active sites as compared with the Ni SACs enclosed CNTs. The current study demonstrates a facile and controllable synthesis method for SACs, an important aspect in the practical application of SACs.

8.2. Experimental section

8.2.1 Chemicals and synthesis of g-C_3N_4

Urea (CON_2H_4, Sigma Aldrich), nickel (II) acetylacetonate ($Ni(acac)_2$, Sigma Aldrich), $KHCO_3$, ($Ni(acac)_2$, Sigma Aldrich), citric Acid ($C_6H_8O_7$, Sigma Aldrich), nickel phthalocyanine (NiPc, Sigma Aldrich), CNTs (multi-walled CNTs, Shenzhen Nanotech Port Co. Ltd) were purchased and used without further treatment. The g-C_3N_4 was synthesized according to method reported[34]. Urea 100g was heated at 600 °C (ramp rate, 5 °C min^{-1}) for 2 h in a covered alumina crucible placed inside muffle furnace, forming g-C_3N_4.

8.2.2 Synthesis of CNT and G supported Ni SACs

Ni doped CNT (Ni-CNT) was synthesized through our previously reported microwave assistant method[35]. Briefly, CNTs was functionalized with PEI. Subsequently, PEI functionalized CNTs (100 mg) was ultrasonicated and dispersed in 100 mL ethylene glycol solution for 1 h, followed by the addition of 50 mg $Ni(acac)_2$. The dispersion was ultrasonicated for 20 min and then stirred for 1 h before being placed in a lab-use microwave oven (1000 W) in the fume cupboard and continuously heated for 6 min, followed by stirring for 10 h. The solution was then filtered using the membrane film and washed using the ethanol for 5 times. Thermally reduced graphene oxide (G) was prepared according to the reported methods previously[36]. The synthesis of Ni-G also follows the above procedure. The final Ni loading of Ni-CNT and Ni-G was 10 wt% and 7 wt%, assessed by TGA.

$Ni(acac)_2$ was dissolved into ethanol and acetone (with volume ratio of 4:1) solution, which was dropped into g-C_3N_4 and grinding to complete drying. The yellowish powder was heated to 660 ^oC at a ramp rate of 7 ^oC per min and kept for 1 h under argon Ar at a flow rate of 50 mL min^{-1}. After cooling down to room temperature, the product was successively leached at 70 °C in 2 M HCl for 12 h to remove nickel cluster species. The intermediate product was denoted as g-C_3N_4-Ni after drying for 10 h at 80 ^oC. The powder was heated again at 800 °C in Ar for 1 h at a ramp rate of 10 ^oC per min. During the annealing process, there is amount of gas and substance decomposed from g-C_3N_4-Ni. Therefore, the sample should be put into one inner tube to prevent the gas circuit blocking. The final product was denoted as NiSA-N-CNT.

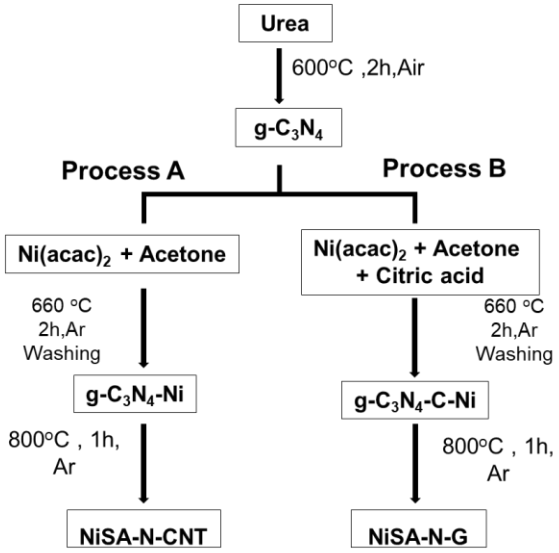

Figure 8.1 The synthesis procedure steps of NiSA-N-CNT and NiSA-N-G.

The $Ni(acac)_2$ was resolved into citric acid, ethanol and acetone solution (with Ni and citric acid molar ratio 1:10, 1:50, 1:100, 1:200), which was then dropped into g-C_3N_4 and grinding to complete drying. The mixture was annealing at 660 °C for 1 h and followed by washing via HCl for 12h. The as-annealed intermediate product after drying at 80 °C for 24 h was denoted as g-C_3N_4-Ni-C. After dying at 80 °C, the powder was heated again at 800 °C in Ar for 1 h at a ramp rate of 10 °C per min. The final product was denoted as NiSA-N-G. The synthesis procedure is shown in Fig 8.1.

8.2.3 Structure characterization

X-Ray Diffraction (XRD) data was collected with a Bruker D8 Advance diffractometer operated at 40 kV and 40 mA with Cu Kα (λ = 1.5406 Å) in the range of 10-80°. The specific surface area was calculated by the Brunauer–Emmett–Teller (BET) method. The inductively coupled plasma atomic emission spectroscopy (TJA RADIAL IRIS 1000, ICP-AES) was used to determine the mass content of Ni metal. Nitrogen adsorption/desorption characteristics were determined using a Micromeritics ASAP 2020 instrument at 77 K. The square resistance of the NiSA-N-CNT and NiSA-N-G was measured by a standard four-point-probe resistivity measurement system (RTS-9, Guangzhou, China). Before tests, the NiSA-N-CNT and NiSA-N-G were dispersed and filtered into film with mass of 0.1mg/cm^2. Five measurements were carried out at different positions on each sample, and the average resistivity value was calculated. Microstructure and morphology were obtained using scanning electron microscopy (SEM, Zeiss Neon 40 EsB) and high-resolution

transmission electron microscopy (HRTEM, FEI Titan G2 80-200 TEM/STEM).

High angle annular dark field scanning transmission electron microscopy (HAADF-STEM) imaging and element mapping were performed through ChemiSTEM Technology operating at 200 kV. The NiSA-N-CNT and NiSA-N-G were dispersed and deposited onto TEM sample grids using a high purity anhydrous ethanol solution. High-resolution aberration-corrected scanning transmission electron microscopy annular dark field images (AC-STEM-ADF) and annular bright field images (AC-STEM-ABF) were carried out by a Nion UltraSTEM100 microscope operating at 60 kV at a beam current of 60 pA. The recorded images were filtered through a Gaussian function (full width half maximum = 0.12 nm) to reduce high frequency noise. The convergence half angle of the electron beam was set to 30 mrad and the inner collection half angle of the ADF images was 51 mrad. The samples were dried at 160 ºC overnight before performing STEM. XPS patterns were conducted using a Kratos AXIS Ultra DLD system with monochromated Al Kα X-rays (1486.7 eV) operating at 225 W. The vacuum pressure of 1 x 10^{-9} mbar or better was kept throughout the experiment. The high-resolution spectra were collected with a pass energy of 160 eV for survey and 40 eV. The spectra were analyzed via CasaXPS software and further calibrated by shifting the main peak in the C 1s spectrum to 284.5 eV associated with SP2 carbon. Element loading of C, N, O, H was obtained by the elemental analyzer (Elementar, vario MICRO cube) at 950 ºC. Raman patterns tests were performed using one alpha300 RA Correlative Raman-AFM Microscope with a 532 nm He−Ne laser. The spectrum represents the average of 20 scans.

Near edge x-ray absorption structure (NEXAFS) spectroscopy measurements were performed at the Soft X-Ray beamline of the Australian Synchrotron[37].These measurements were conducted under ultra-high vacuum (UHV) conditions with a base pressure of 5 x 10^{-10} mbar or better. All spectra were obtained in partial electron yield (TEY) mode. All NEXAFS spectra were analyzed and normalized using the QANT software program developed at the Australian Synchrotron[38].X-ray absorption spectroscopy (XAS) experiments were carried out at the XAS Beamline (12ID) at the Australian Synchrotron. With the beamline optics employed (Si-coated collimating mirror and Rh-coated focusing mirror) the harmonic content of the incident X-ray beam was negligible. The samples were pressed into pellets via mechanical grinding with cellulose binder through a mortar/pestle for about 30 mins. Both fluorescence and transmission spectra were recorded based on the concentration of Ni in each sample. All XAS data were processed through the Athena software.

8.2.4 Computational methods

In this work, the density functional theory (DFT) calculations were performed by using the Vienna Ab-initio Simulation Package with the projector augmented wave[39] to describe the electron-ion interaction. The Perdew-Burke-Ernzerhof functional was used for the exchange-correlation term. The plane-wave cutoff was set to be 400 eV. A 2×2×1 g-C_3N_4 and a 6×6×1 graphene supercell with the vacuum thickness of 15 Å were used to calculate the binding energy of metal atom in the g-C_3N_4 and N-doped graphene, respectively. The Monkhorst-Pack (3×3×1) k-point was used to sample the Brillouin zone.

8.2.5 Electrochemical measurements

Electrochemical CO_2 reduction reaction (CO_2RR) experiments of NiSA-N-CNT and NiSA-N-G catalysts were performed in N_2 and CO_2 saturated 0.5 M $KHCO_3$ solution using linear scan voltammetry (LSV). The electrolyte was purified by electrolysis between two graphite rods at -0.15 mA for 24 h under CO_2 flow to remove any metal residual. LSV test was conducted with the catalysts loading of 0.2 mg cm^{-2}. The electrodes for CO_2RR were made via casting the catalysts-ethanol-Nafion solution (5 mg mL^{-1} catalysts, 1% Nafion) on carbon paper (1 cm^{-2}, Toray, Japan) with a gas diffusion layer and loading of 0.5 mg cm^{-2}. The CO_2RR was carried out in one gas tight electrochemical quartz cell under a series of potentials for 2 h (versus RHE). The final product was collected in the outlet with a gas bag for double channel gas chromatography (Shimadzu, GC-2014) analysis.

The rate of product yield is based on the average rate in 2 h. The Faradaic efficiency of CO production is calculated based on [40]:

$$FE\% = \frac{Qco}{Qtot} \text{x} 100 \quad (1)$$

And the j_{CO} is calculated by

$$j_{tot} = \frac{Qtot}{At} \text{x} 1000 \quad (2)$$

$$j_{CO} = FE\% \text{ x } j_{tot} \quad (3)$$

where Q_{CO} is the total number of electrons for CO production in the range of 2 hours, Q_{tot} the total number of electrons pass the electrode in 2 hours. j_{tot} (mA cm^{-2}) is the total average current density pass the electrode in 2 hours, A is the area of the electrode (1 cm^{-2}), and j_{CO} (mA cm^{-2}) is the current density contribute to the CO_2-to-CO reduction, and t (s) is sampling time.

The turn over frequency (*TOF*, mol CO mol^{-1} Ni h^{-1}) was calculated based on:[41]

$$TOF = \frac{Mjco}{NFm\omega} \quad (4)$$

j_{CO} is partial current for CO,

N: the number of electrons transferred for product formation, which is 2 for CO,

F: Faradaic constant, 96485 C mol^{-1},

m: catalyst mass in the electrode, g,

ω : Ni single atom loading in the catalyst, g,

M: atomic mass of Ni, 58.69 g mol^{-1}.

8.3. Results and discussion

8.3.1. Microstructure of NiSA-N-CNT and NiSA-N-G

Figure 8.2 shows the microstructure of g-C_3N_4 prepared from urea and heated at 600 ºC. The morphology of g-C_3N_4 synthesized in 600 ºC was characterized by irregular structure (stacked and layered structure). The size of g-C_3N_4 was around 2 μm. The morphology of g-C_3N_4 is consistent with that reported in the literature[42].

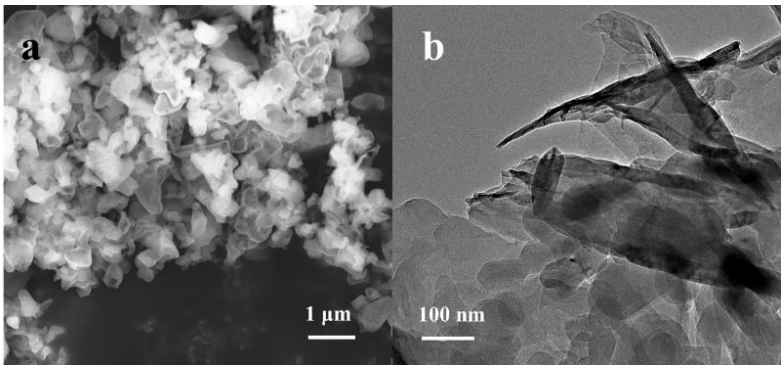

Figure 8.2 a) SEM and b) TEM micrographs of g-C_3N_4, synthesized from urea and heated at 600 °C.

Pristine g-C_3N_4 is not stable at high temperatures and will be decomposed completely at 660 ºC[11]. However, with the introduction of $Ni(acac)_2$ (the process A, Figure1), the microstructure of g-C_3N_4 remains intact after the heat treatment at 660ºC, forming g-C_3N_4-Ni. With further annealing at 800 ºC in Ar for 1 h, NiSA-N-CNt was obtained. Figure 8.3 shows microstructure and element distribution of g-C_3N_4-Ni before and after annealing at 800 ºC in Ar. g-C_3N_4-Ni is characterized

by irregular and layered nanosheets (Figure 8.3A). This indicates the presence of Ni stabilizes the g-C_3N_4 structure at high temperatures, consistent with previous study[11, 33]. The EDS results show the uniform distribution of Ni, N on the surface of g-C_3N_4 (Figure 8.3Ad). The high resolution TEM image confirmed there is no cluster or nanoparticles present in the structure after the HCl washing treatment (Figure 8.3Ae). Isolated single atoms were atomically dispersed on the substrate as shown by the AC-STEM image (Figure 8.3Af). This indicates the formation and uniform distribution of Ni single atoms in the layered g-C_3N_4 nanosheets.

After annealing at 800 ºC in Ar, the layered nanosheets disappear and bamboo-like CNTs were obtained (Figure 8.3B). The TEM confirms the formation of multi-walled CNTs with number of walls of 8 shown in Figure 8.3Be. The diameter of CNTs is 20-60 nm and the length of the individual section of the bamboo-like CNTs is 5-10 μm. The EDS mapping results confirm the uniform dispersion of Ni and N on the CNTs structure (Figure 8.3Bd). The AC-STEM images further indicate the presence of Ni single atoms and uniformly dispersed in the CNTs structure (Figure 8.3Bf). The density of distributed Ni single atoms appears very high, indicating the high loading of the NiSA-N-CNT, consistent with previous study[33].The transformation from stacked g-C_3N_4-Ni layered structure to Ni single atoms embedded CNTs occurs via the solid-to-solid rolling-up mechanism, activated by the kinetically active Ni single atoms embedded, as explained in our early papers[11].

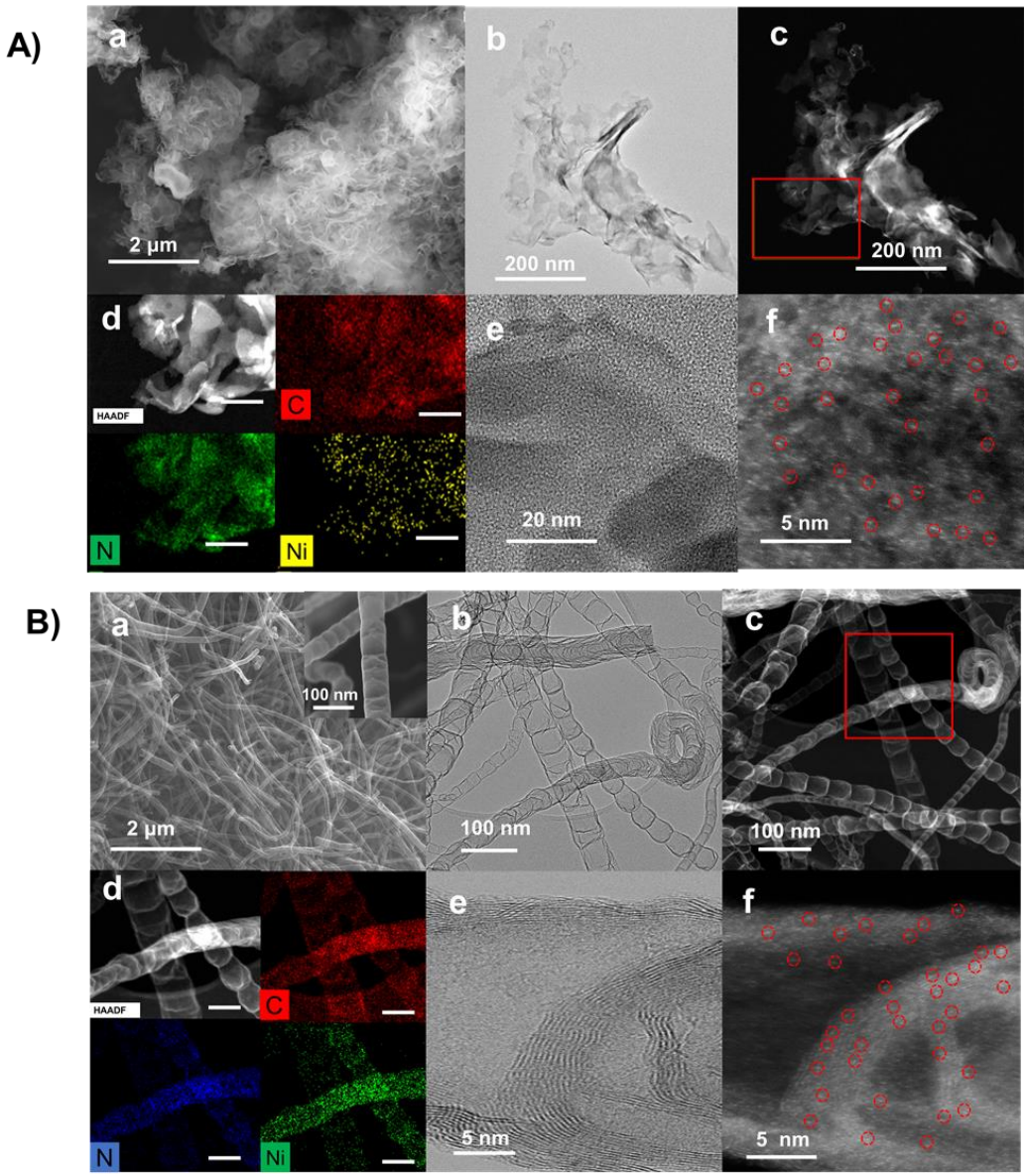

Figure 8.3 Microstructure and element distribution of (A) g-C_3N_4-Ni and (B) NiSA-N-CNT after annealing of g-C_3N_4-Ni at 800 ºC in Ar for 1 h. (a) SEM, (b) TEM, (c) AC-HAADF, (d) EDS patterns of the selected area in (c), (e) HRTEM, and (f) AC-STEM. In A), scale bar=50 nm and in B), scale bar=60 nm.

In the synthesis step B, citric acid was introduced in the synthesis of the Ni single atoms doped g-C_3N_4 stacked structure, g-C_3N_4-Ni-C (see Figure 8.1). Most interesting, with further annealing at 800 ºC in Ar for 1 h, identical conditions to g-C_3N_4-Ni, NiSA-N-G instead of NiSA-N-CNT was obtained. Figure 8.4 shows microstructure and element distribution of g-C_3N_4-Ni-C before and after annealing at 800 ºC in Ar. After introduction of citric acid, the intermediate product g-C_3N_4-

Ni-C shows similar nano-sheet layered structure like g-C_3N_4-Ni but the size of the stacked layer is 5 μm, larger than 2 μm measured on g-C_3N_4-Ni (Figure 8.4Aa-d). Similar to g-C_3N_4-Ni, the EDS results show the uniform distribution of Ni, N on the surface of g-C_3N_4-C (Figure 8.4Ad). The uniformly dispersed single Ni atoms were also obtained (Figure 8.4Bf). Most importantly, after annealing at the same high temperature of 800 ^oC as that used in g-C_3N_4-Ni, the planar graphene-like structure was formed rather than tubular structure (see Figure 8.5). The TEM image shows the number of layers of NiSA-N-G is about 3-5 with massive wrinkles (Figure 8.5e). The bright dots in Figure 8.5f indicate the atomically dispersed single Ni atoms embedded within the graphene structure.

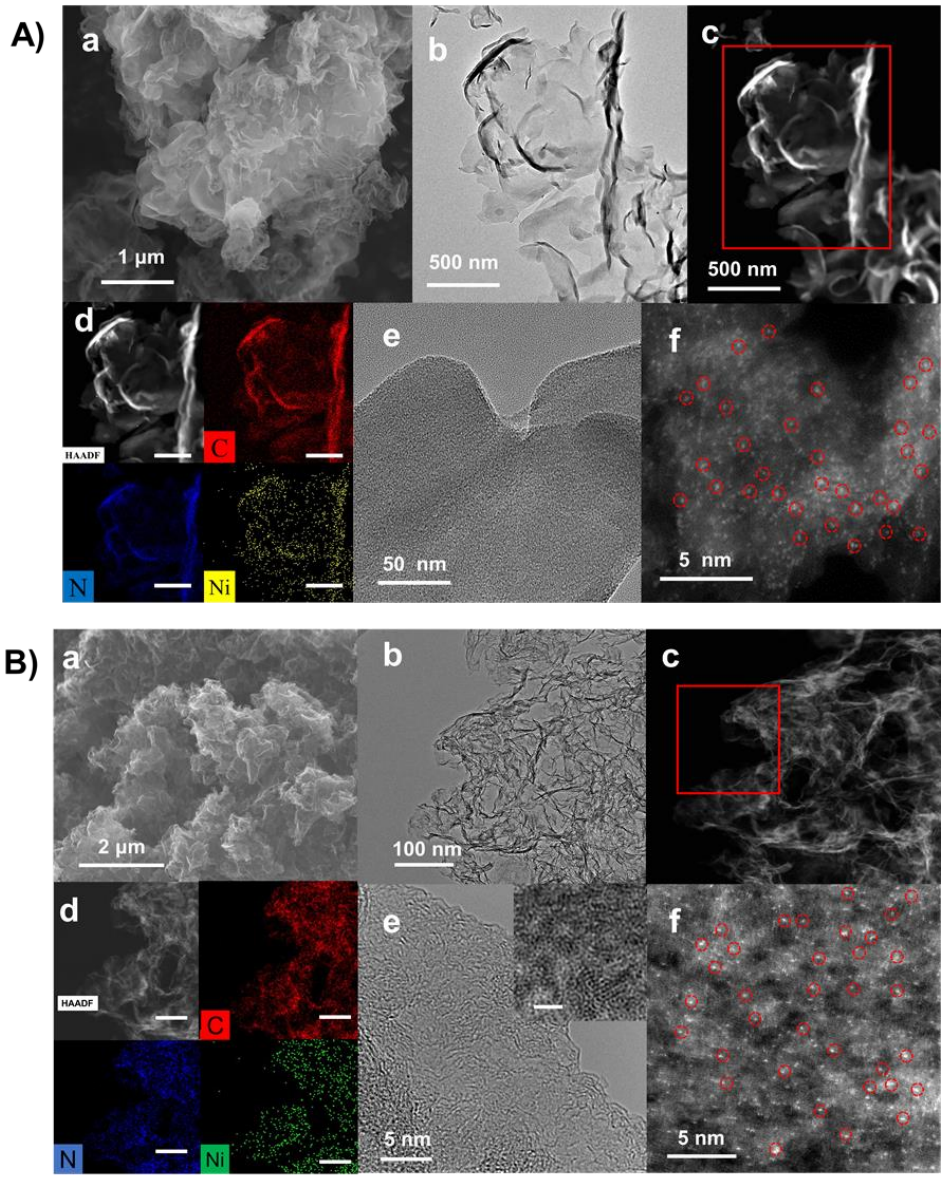

Figure 8.4 Microstructure and element mapping of (A) g-C_3N_4-Ni-C and (B) NiSA-N-G after annealing of g-C_3N_4-Ni at 800 ºC in Ar for 1 h. (a) SEM, (b) TEM, (c) AC-HAADF, (d) EDS element mapping of the selected area in (c), (e) HRTEM, and (f) AC-STEM. In A) scale bar=200 nm and in B) scale bar=40 nm.

The g-C_3N_4 is yellowish in color and with the presence of Ni single atoms, the color of g-C_3N_4-Ni changed into brown (Figure 8.5a). With the addition of citric acid, the g-C_3N_4-Ni-C formed after calcination at 660 ºC is black in color. This may indicate formation of the carbon film on the surface of g-C_3N_4-Ni due to the decomposition of citric acid. The XRD patterns confirm that g-C_3N_4-Ni and g-C_3N_4-Ni-C still basically remain the structure of g-C_3N_4. The two main peaks (100)

at 12.8° and (002) at 27.6° can be attributed to g-C_3N_4 (Figure 8.5b). The presence of Ni atoms could play a role in connecting the g-C_3N_4 into layered structure to reduce the surface energy due to strong Ni-N coordination. During the annealing process at 660 °C, the layer thickness of g-C_3N_4-Ni-C was reduced to obtain the graphene-like structure. This is supported by the fact that the surface area of g-C_3N_4-Ni and g-C_3N_4-Ni-C powder is 188 and 255 m^2 g^{-1}, respectively, much higher than 36 m^2 g^{-1} obtained on pristine g-C_3N_4 (see Table 8.1). This demonstrates that Ni single atoms in the g-C_3N_4 structure not only stabilize the carbide structure but also increase the surface area significantly. There is no characteristics associated with metallic Ni as shown in Ni-CNT and Ni-G for g-C_3N_4-Ni and g-C_3N_4-Ni-C (Figure 8.5c), consistent with the AC-STEM results (Figures 8.3B and 8.4B).

Sample	C%		N%		Ni%		O%		H%
	XPS	Elementar	XPS	Elementar	XPS	TGA /ICP	XPS	Elementar	Elementar
SANi-N-CNT	61.9	60.4	21	19.5	14.5	15.1/15.3	2.6	2.5	1.6
SANi-N-GO	75.5	77	16	17	4.5	6.1/5.9	4	5	1.7

Table 8.1 the elemental content analysis in the NiSA-N-CNT and NiSA-N-G.

The FTIR spectra of g-C_3N_4, g-C_3N_4-Ni, g-C_3N_4-Ni-C show a characteristic peak at around 820 cm^{-1} related to C–N heterocycles due to the triazine ring mode (Figure 8.5d). Another peak in the range of 1200–1600 cm^{-1}, attributed to the specific aromatic skeleton vibration of carbon nitride [43], was also observed. A broad band was evident in the range of 3000–3700 cm^{-1} corresponding to the stretching mode of $–NH_2$, which are uncondensed amine groups, or to N–H group vibrations present at the surface of carbon nitride [43]. The related peaks confirmed that the basic structure of g-C_3N_4 was retained in g-C_3N_4-Ni. However, FTIR results confirm that the introduction of citric acid during the formation of g-C_3N_4-Ni-C removed the characteristic peaks from 1200-1600 cm^{-1} in g-C_3N_4. This may indicate the presence of amorphous carbon on the surface of g-C_3N_4-Ni derived from citric acid at 660°C. The presence of an amorphous carbon derived from citric acid decomposition is also supported by the color change from brownish for g-C_3N_4-Ni to black for g-C_3N_4-Ni-C. The presence of such carbon film could increase the stability of the layered structure, which physically suppresses the solid-to-solid g-C_3N_4 rolling-up process into the tubular structure, leading to the formation of layered graphene structure.

The Raman patterns from NiSA-N-G shows I_g/I_d ratio of 0.7 higher than 0.4 obtained on NiSA-N-CNT. In the case of NiSA-N-CNT, D and G peaks are not clearly separated, which confirms the existence of abundant defects and poor carbon crystallinity. Based on the N_2 absorption spectrum curves, the surface area of NiSA-N-CNT and NiSA-N-G is 130 and 308 m^2 g^{-1}, respectively (Figure 8.5f). The transformation from layered structure to tubular CNT supports reduces the surface area, while the formation of graphene supports increases the surface area (Table 8.2). This indicates that the NiSA-N-G owns more exposed active sites than NiSA-N-CNT. The loading of Ni in the NiSA-N-CNT and NiSA-N-G are 15.1wt% and 6.1 wt%, respectively, as evaluated by TGA (Figure 8.5g), consistent with the ICP results (Table 8.1). The oxidation resistance temperature of NiSA-N-G is 470 ^oC, higher than 400 ^oC observed on NiSA-N-CNT, which is lower than traditional CNT and G of 800 ^oC[36, 44]. This indicates the higher graphitic structure of NiSA-N-G with the presence of amorphous carbon film, consistent with the Raman results. The square resistance of NiSA-N-CNT and NiSA-N-G are 106 and 35Ω/□ at room temperature which further indicates the higher conductivity of NiSA-N-G than NiSA-N-CNT.

Samples	g-C_3N_4	g-C_3N_4-Ni	g-C_3N_4-Ni-C	NiSA-N-CNT	NiSA-N-G
Surface area(m^2/g)	36	188	255	130	308

Table 8.2 the surface area comparison of the g-C_3N_4, g-C_3N_4-Ni, g-C_3N_4-Ni-C, NiSA-N-CNT, NiSA-N-G.

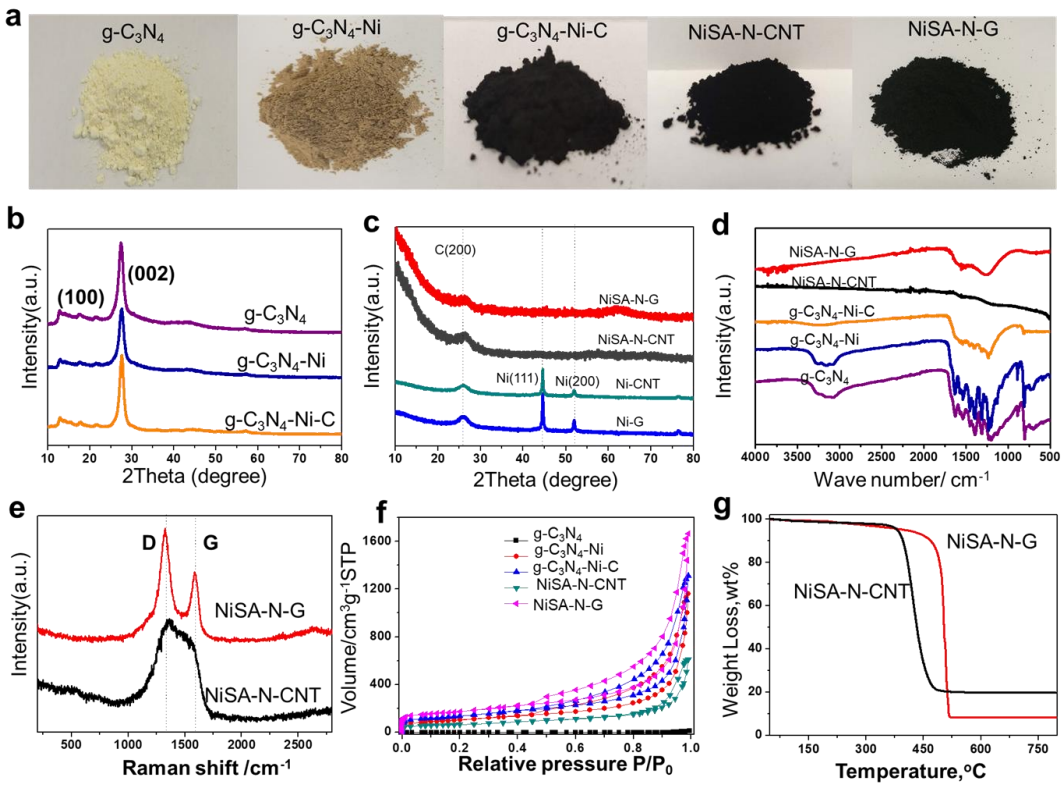

Figure 8.5 Color and structural Characterization of g-C_3N_4, g-C_3N_4-Ni, g-C_3N_4-Ni-C, NiSA-N-CNT and NiSA-N-G. (a) optical image, (b) and (c) XRD pattern, (d) FTIR spectrum of different intermediates, (e) Raman spectrum, (f) N_2 absorption and desorption curves, and (g) TGA curves.

The transformation of layered g-C_3N_4 to planar graphene structure rather than tubular CNT depends on the ratio of Ni (or g-C_3N_4) to citric acid. Figure 6 shows microstructure of the powder product after the final annealing at 800 ºC of g-C_3N_4-Ni-C as a function of Ni/citric acid ratio. When the citric acid content is not high enough, both CNTs and graphene are formed (see Figure 8.6a-c). However, the relative content of graphene structure increases with the increase of citric acid content. When the Ni/citric acid mass ratio reaches 1:1, the transformation of layered g-C_3N_4-Ni-C to graphene structure is complete, indicating the restrained formation of tubular CNT (Figure 8.6d). The change in the distribution of CNT and graphene supports in the final powder after annealing at 800 ºC confirms the important role of citric acid in the control of the microstructure and morphology of the supports for the embedded Ni single atoms. The results indicate the feasibility in the control of the microstructure of the supports for SACs.

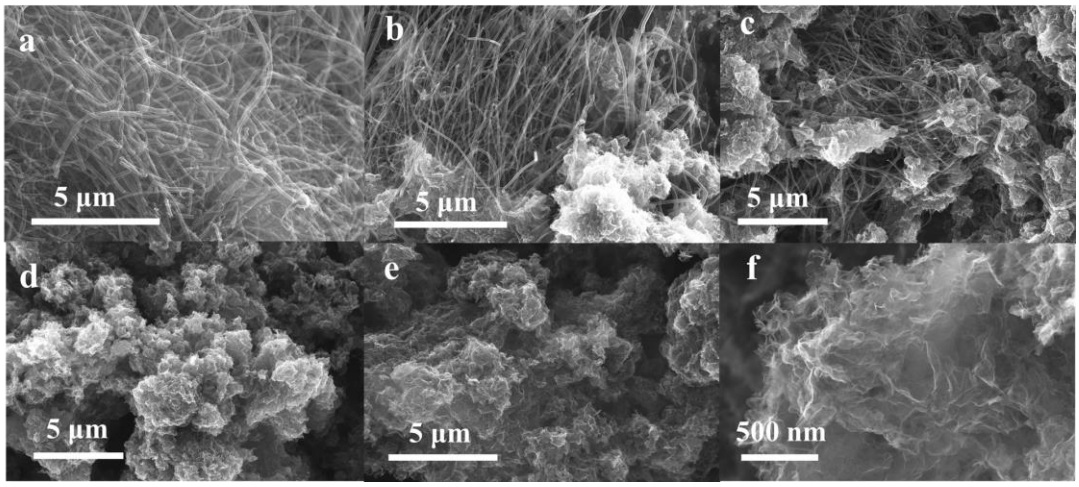

Figure 8.6 SEM micrographs of the powder products after the final annealing at 800 ºC of g-C_3N_4-Ni-C as a function of Ni/citric acid ratio. (a) 1:0 (i.e., NiSA-N-CNT), (b) 1:0.25, (c) 1:0.5, (d) 1:1, (e) 1:2 and (f) higher magnification of (e).

8.3.2 Ni SACs on CNT and G

The chemical environments of NiSA-N-CNT and NiSA-N-G were investigated through X-ray absorption spectroscopy (Figure 8.7). The Ni L-edge shows typically two groups of peaks around 850-855eV (L3-edge) and 868-874 eV (L2-edge) corresponding to the splitting of the Ni 2p orbitals (Figure 8.7a). The Ni L3-edge of the NiSA-N-CNT and NiSA-N-G own a major peak at around 854.7 eV. The main peaks in NiSA-N-CNT and NiSA-N-G are at ~854.2 eV and 854.1 eV respectively, which are very close to that of NiPc, ~854.3 eV, different from Ni in Ni foil (852.7 eV), NiO (853.0 eV) and Ni $(OH)_2$ (853.2 eV).

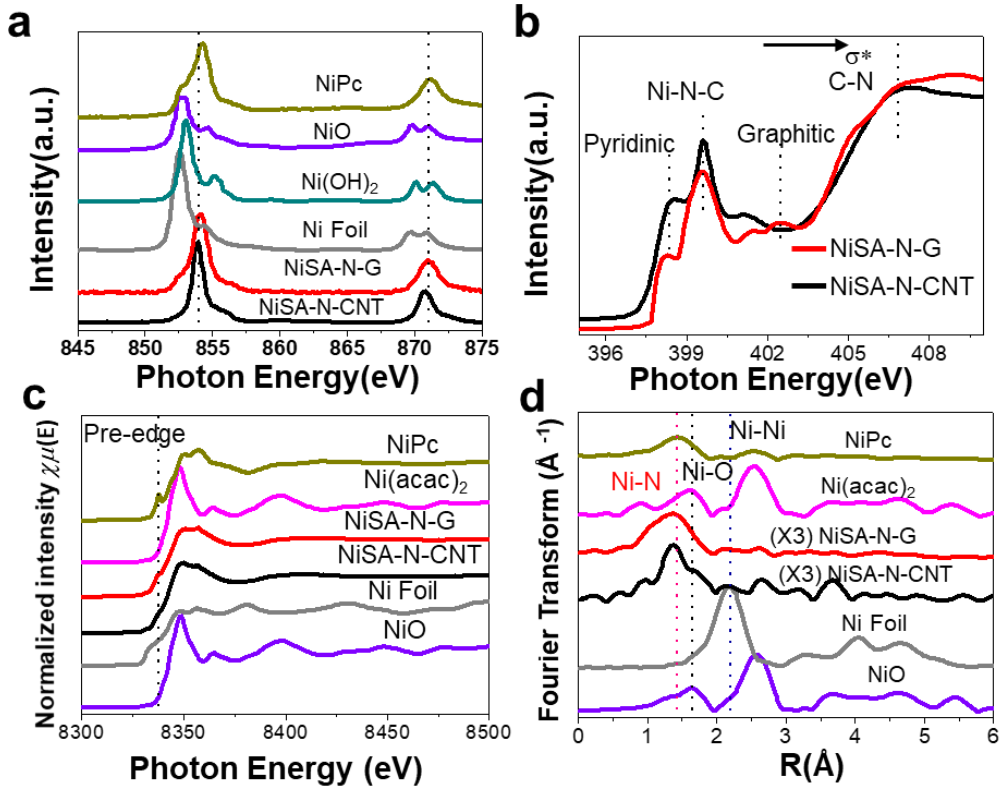

Figure 8.7 Chemical environment of NiSA-N-CNT and NiSA-N-G as invested via X-ray absorption spectroscopy. (a) Ni L-edge spectra. (b) N K-edge spectra of NEXAFS spectra. (c) pre-edge of Ni in EXAFS. (d) Fourier transform of the EXAFS spectra from NiPc, NiSA-N-CNT, NiSA-N-G, $Ni(acac)_2$, Ni Foil, NiO.

Furthermore, the Ni 2p XPS spectrum (Figure 8.8) indicates the Ni is in the form of 2^+ but not the metallic Ni^0. This evidently proves that the Ni in NiSA-N-CNT and NiSA-N-G is mainly coordinated with N but not in the form of Ni-Ni, Ni-O or Ni-OH [23]. The N K-edge of NiSA-N-CNT shows two main peaks at 398.6 eV and 401.5 eV (Figure 8.7b), assigned to pyridinic and graphitic N, respectively. Different from NiSA-N-CNT, the notable peak at 402.5ev appears in NiSA-N-G which is consistent with the graphitic N. It confirms that the introduction of defective carbon has influenced the N structure in the carbon lattice. The peaks centered at 399.4 eV can be assigned to Ni-N-C species [45]. Compared to a Ni foil, the pre-edge of Ni K-edge XANES spectra shift to higher energies (Figure 8.7c). The Fourier-transformed extended X-ray absorption fine structure reveals that NiPc shows a sharp peak centering at 1.43 Å (Figure 8.7d), consistent with the well-defined Ni-N4 species [46]. However, the intensity of the peak at 1.42 Å is lower than that of NiPc, likely because of the formation of unsaturated Ni-N2, Ni-N3 and well-defined Ni-N4

species. Further, the broad peaks at 2.30 Å is likely contributed by the presence trace amount of Ni NPs in NiSA-N-CNT, but the peak was not found in NiSA-N-G.

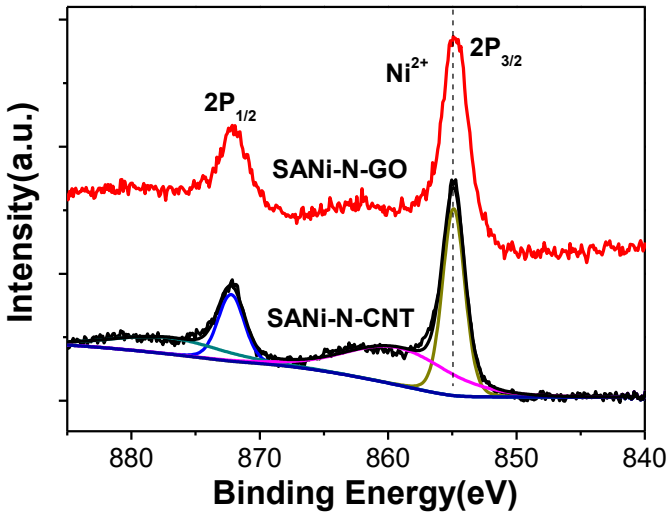

Figure 8.8 the XPS spectrum of Ni2p in SANi-N-CNT and SANi-N-GO.

3.3 Formation mechanism of CNT and graphene supports for Ni SACs

Before the evaluation of the transformation mechanism of the layered g-C_3N_4 structure to tubular CNT or planar graphene structure during the high temperature annealing, computational first-principle calculations were performed. For the purpose of calculation, the structure of pure g-C_3N_4 with Ni single atom was constructed and optimized. The results indicate that the two-dimensional (2D) structure of the g-C_3N_4 suffers a deformation after the introduction of Ni atoms (Figure 8.9a-b). The original planar structure of g-C_3N_4 has undergone a large structure fluctuation of 1.48 Å along the *z* direction. This deformation of the structure may lead to the crimp or rolling-up of the layered g-C_3N_4 during the high temperature annealing process. However, the situation is different with the introduction of a graphene carbon source to g-C_3N_4.

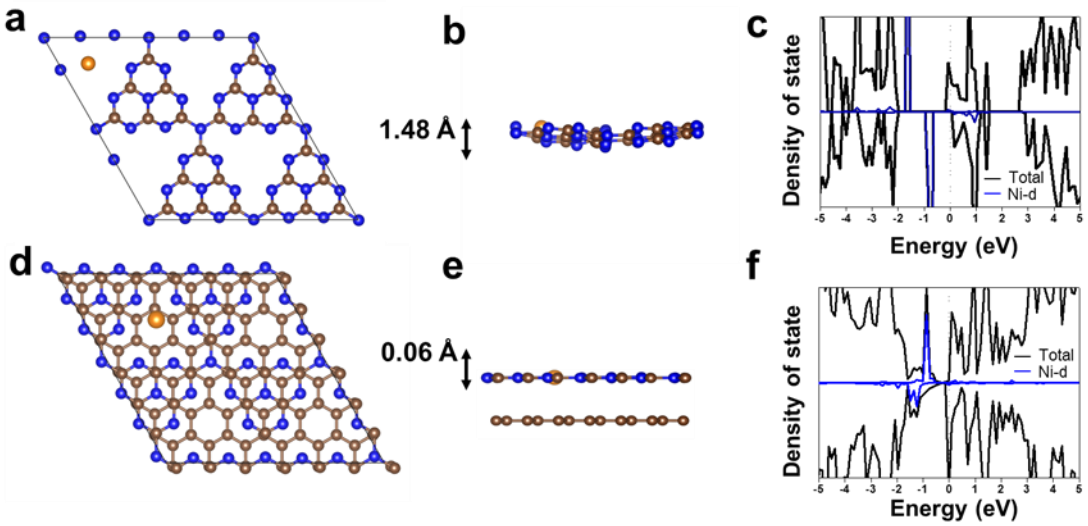

Figure 8.9 (a) Top view and (b) side view of Models simulating the g-C_3N_4-Ni structure after geometric optimization, (c) Density of states of the g-C_3N_4-Ni structure, (d) top view and (e) side view of Models simulating the g-C_3N_4-Ni/Graphene structure after geometric optimization, and (f) Density of states of the g-C_3N_4-Ni/Graphene composite.

In this case, a heterojunction structure of Graphene/g-C_3N_4 was constructed to simulate the effect of carbon source formed by decomposition of citric acid on g-C_3N_4-Ni. As shown in Figure 8.10, the heterojunction structure of Graphene/g-C_3N_4 possesses the well structure stability after the structure is optimized that both graphene and g-C_3N_4 are in planar. Based on this heterojunction materials, the structure stability was investigated when the Ni atom was introduced. As shown in Figs. 8.9d-e, the Graphene-g-C_3N_4 heterojunction structure maintains the planar properties with the presence of Ni atoms. The structure fluctuation of g-C_3N_4-Ni in this case is within 0.06 Å, substantially smaller than 1.48 Å along the *z* direction calculated for the g-C_3N_4-Ni. The theoretical calculation indicates that the presence of additional carbon source has a significant influence on the structure fluctuation of g-C_3N_4-Ni intermediates, which in turn has important implication to the evaluation and transformation of the microstructure of carbon-based supports for the Ni SACs.

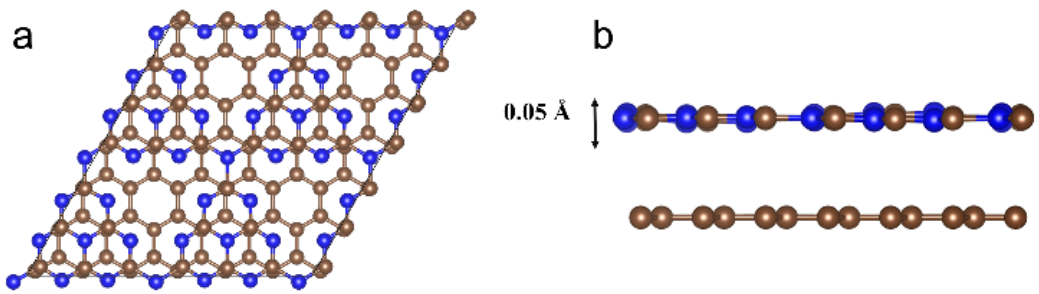

Figure 8.10 (a) Top view and (b) side view of Models simulating the g-C_3N_4/Graphene structure after geometric optimization.

Moreover, the electronic structure of these two structures were also calculated. As shown in Figure 8.9c and 8.9e, there are more states near the Fermi-level in the heterojunction structure of Graphene/g-C_3N_4-Ni which represents the better electronic conduction. The *d*-orbit of the Ni atom in the heterojunction structure is closer to the Fermi level compare to the pure g-C_3N_4-Ni, which means that the higher catalytic activity. In summary, the defect carbon introduction not only maintains the planar structure stability of the g-C_3N_4-Ni in synthesis process, but also improve the catalytic activity of the single Ni atoms, which is beneficial for the electrochemical activity of the Ni SACs.

Based on the experimental and theoretical calculations, a controlled synthesis of Ni SACs embedded in CNT and graphene carbon supports can be proposed, as shown in Figure 8.11. The presence of Ni single atoms stabilizes the layered g-C_3N_4 structure at a high temperature of 660 ^oC. However, without the introduction of carbon source or layer, significant fluctuation of the layered g-C_3N_4-Ni structure occurs. Such structural fluctuation would lead the curving and eventually rolling-up mechanism during the high temperature annealing process, forming tubular CNT supports for Ni SACs. The fundamental reason is due to the high mobility and activation energy of Ni single atoms. With the introduction of citric acid, amorphous carbon layers are formed on the surface of g-C_3N_4-Ni due to the decomposition of citric acid at low temperature annealing at 660 ^oC, as showing by the FTIR (Figure 8.5d). The presence of amorphous carbon source forms graphene/g-C_3N_4-Ni-like heterojunction structure, substantially reducing the structure fluctuation and preventing the rolling-up mechanism during the high temperature annealing for the precursor with Ni/citric acid ratio of 1:1 or higher.

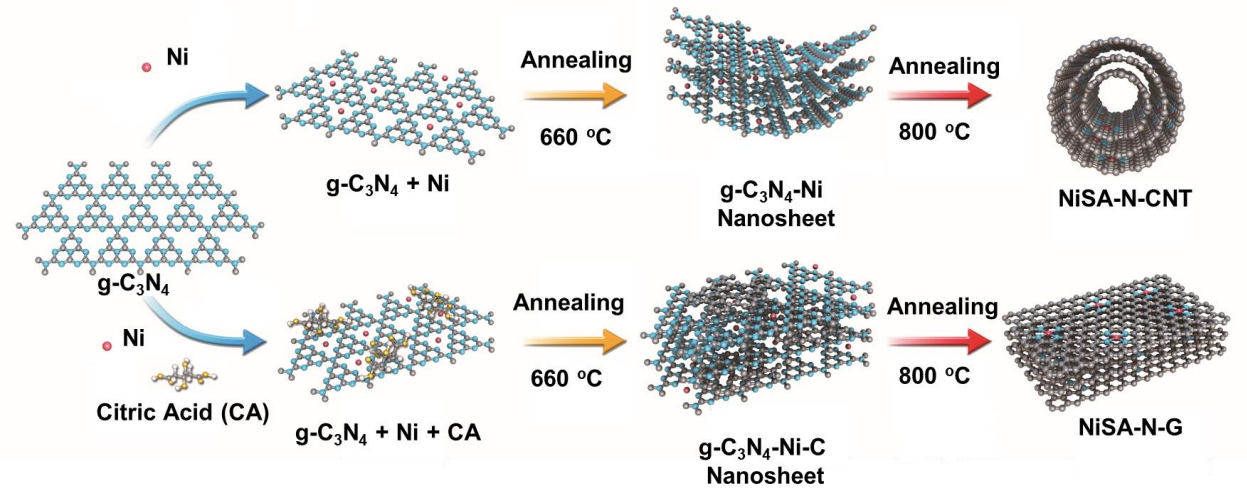

Figure 8.11 Controlled synthesis of NiSA-N-CNT and NiSA-N-G.

3.4 CO2RR electrochemical performance

The electrochemical performance of NiSA-N-CNT and NiSA-N-G for CO_2RR were conducted in N_2- and CO_2-saturated 0.5 M $KHCO_3$ solution and the results are shown in Figure 10. A significantly higher current density was obtained in CO_2-saturated solution as compared to that in N_2-saturated solution for NiSA-N-CNT and NiSA-N-G with an onset potential of -0.27 and -0.25V vs RHE. Glassy carbon showed negligible CO2RR activity (Figure 8.12a).

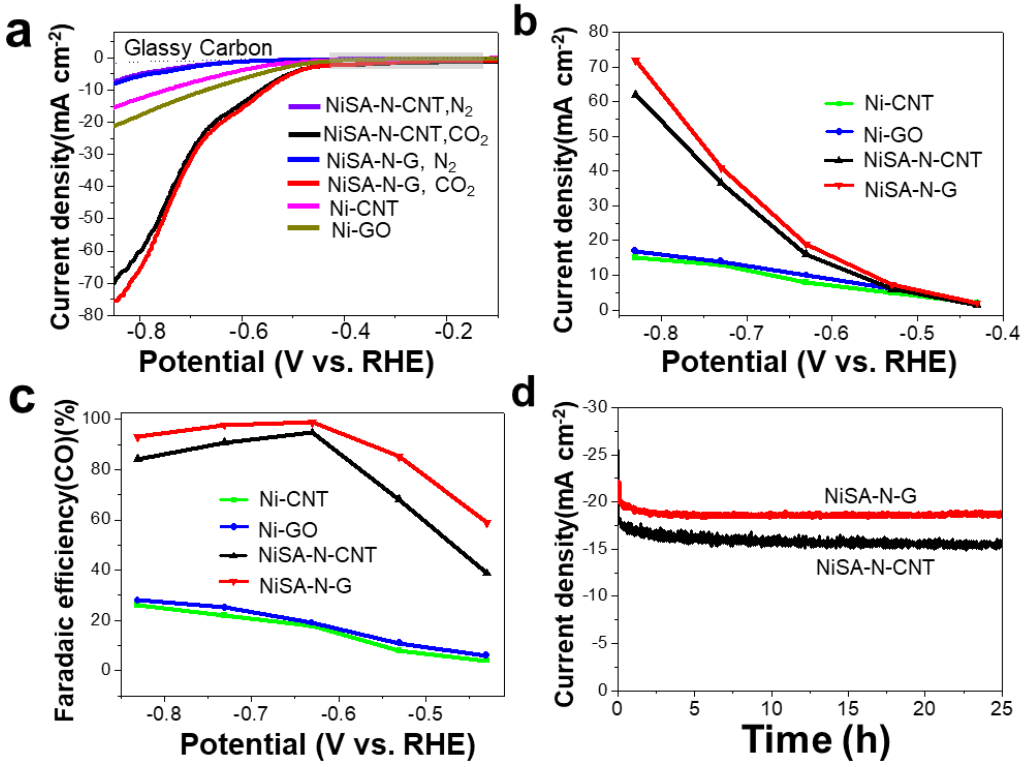

Figure 8.12 CO2RR performance. (a) Linear scan voltammetry (LSV) curves, (b) plots of j of Ni-CNT, Ni-G, NiSA-N-CNT, NiSA-N-G, (c) Faradaic efficiency, and (d) initial stability of NiSA-N-CNT and NiSA-N-G electrodes, measured in CO2 saturated 0.5 m $KHCO_3$ solution.

The Ni-G and Ni-CNT were synthesized as shown in Figure 8.13 for performance comparison. Ni-G and Ni-CNT showed the improved activity, but the performance is much less than NiSA-N-CNT and NiSA-N-G. The NiSA-N-G and NiSA-N-CNT show a much better activity for CO2RR with suppressed H_2 evolution as compared to Ni-CNT and Ni-G (Figs.8.12b, 12c). The CO yield increases with the increase of cathodic potentials (Figure 8.12b). The NiSA-N-G and NiSA-N-CNT have obvious advantages of the selective reduction of CO_2 to CO as compared to Ni-G and Ni-CNT. Furthermore, the NiSA-N-G and NiSA-N-CNT have outperformed the counterparts shown in Table 8.3. The Faraday efficiency (FE, Figure 8.12c) of NiSA-N-CNT is 94% at -0.63V slightly lower than 96% of NiSA-N-G.

Catalyst	Medium and Electrolyte	Product	Overpotential (V vs RHE)	Current density (mA/cm2)	FE (%)(product CO)	Stability	Refs
Au NP	Aq. 0.5 M KHCO3	CO	-0.55	N/A	97	N/A	[47]
Nano Cu	Aq. 0.5 M KHCO3	CO, HCO_2H	-0.38	2.7	40	7 h,74 %	[48]
Nano porous Ag	Aq. 0.5 M KHCO3	CO	-0.6	19.5	92	N/A	[49]
Au nanotip	Aq. 0.5 M KHCO4	CO	-0.35	15	95	N/A	[50]
Au NP	Aq. 0.1 M KHCO3	CO	-0.46	3	83	2 h, N/A	[51]
Nano Ag	Aq. 0.1 M KHCO3	CO	-0.8	1.02	89	2 h, 95 %	[52]
NiN-GS	Aq. 0.1 M $KHCO_3$	CO	-0.7	19	90	20 h,98 %	[53]
NiSG	Aq. 0.5 M KHCO3	CO	-0.61	36.5	97	100 h,98 %	[23]
CoPc-CNT	Aq. 0.1 M	CO	-0.52	15	95	1 h,95 %	[54]
Co-MOF	Aq. 0.1 M KHCO3	CO	-0.6	1	76	7 h, 1 mA/cm2	[55]
NiSA-N-CNT	Aq. 0.5 M KHCO3	CO	-0.63	19.1	94	25h, 90 %	This Study
NiSA-N-G	Aq. 0.5 M KHCO3	CO	-0.63	16.3	96	25h,97%	This Study

Table 8.3 Summarized data for the reported CO_2RR performance of catalysts.

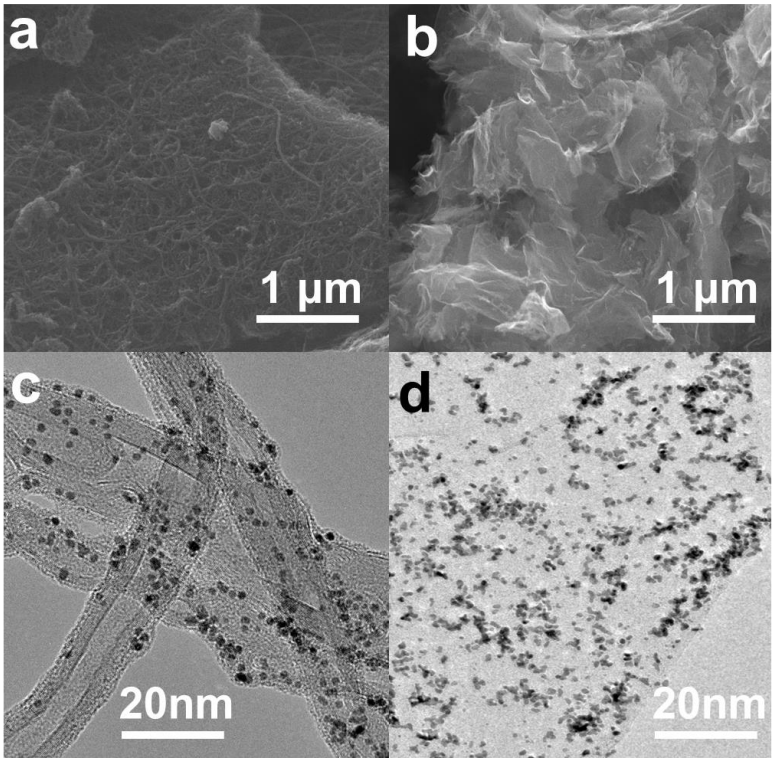

Figure 8.13 the SEM and TEM images of Ni-CNTs (a,c) and Ni-GO(b,d). The diameter of Ni nanoparticles on Ni-GO and Ni-CNTs are 2 nm and 3 nm respectively. The loadings of Ni in Ni-CNTs and Ni-GO are 10 wt% and 7 wt% assessed by TGA.

The preliminary stability of NiSA-N-CNT and NiSA-N-G for CO2RR was tested at -0.63 V (Figure 8.12d). The initial current density for CO2RR was ~19.1 and 16.2 mA cm^{-2} for NiSA-N-G and NiSA-N-CNT respectively, and decreased slightly by 3% and 10% after polarization for 25 h. After the polarization the FE for elctrochemical CO_2-to-CO conversion was 87% on NiSA-N-CNT and 93% on NiSA-N-G. These results furthermore confirm that the stability of NiSA-N-G is higher than NiSA-N-CNT due to more efficient active sites and higher sructural durability. The remarkable CO2RR performance of NiSA-N-G shows the significance and superiority of the planar graphene supports for Ni SACs.

8.4. Conclusion

In conclusion, we have demonstrated a well-characterized and controlled method to synthesize

NiSA-N-CNT and NiSA-N-G through introducing citric acid to stabilize the layered g-C_3N_4-Ni and interrupt the solid-to-solid rolling process. The DFT results identify the introduction of defective carbon in g-C_3N_4 plays important role on restraining rolling up into CNT but obtaining G structure, which is consistent with the experimental data. The higher CO2RR performance of NiSA-N-G than NiSA-N-CNT even with lower SACs loading, which confirms that the exposed active sites are more significant in the electrochemical reduction process. Our results provide the feasibility to achieve controllable synthesis of carbon-based SACs catalysts.

8.5 References

[1] C. Zhu, S. Fu, Q. Shi, D. Du, Y. Lin, Single-Atom Electrocatalysts, Angewandte Chemie International Edition, 56 (2017) 13944-13960.

[2] A. Wang, J. Li, T. Zhang, Heterogeneous single-atom catalysis, Nature Reviews Chemistry, 2 (2018) 65-81.

[3] H. Xu, D. Cheng, D. Cao, X.C. Zeng, A universal principle for a rational design of single-atom electrocatalysts, Nature Catalysis, 1 (2018) 339-348.

[4] B.T. Qiao, J.X. Liang, A.Q. Wang, J.Y. Liu, T. Zhang, Single atom gold catalysts for low-temperature CO oxidation, Chin. J. Catal., 37 (2016) 1580-1587.

[5] A.P. O'Mullane, From single crystal surfaces to single atoms: investigating active sites in electrocatalysis, Nanoscale, 6 (2014) 4012-4026.

[6] L.T. Cui, L.R. Cui, Z.J. Li, J. Zhang, H.N. Wang, S.F. Lu, Y. Xiang, A copper single-atom catalyst towards efficient and durable oxygen reduction for fuel cells, Journal of Materials Chemistry A, 7 (2019) 16690-16695.

[7] H. Fei, J. Dong, Y. Feng, C.S. Allen, C. Wan, B. Volosskiy, M. Li, Z. Zhao, Y. Wang, H. Sun, P. An, W. Chen, Z. Guo, C. Lee, D. Chen, I. Shakir, M. Liu, T. Hu, Y. Li, A.I. Kirkland, X. Duan, Y. Huang, General synthesis and definitive structural identification of MN4C4 single-atom

catalysts with tunable electrocatalytic activities, Nature Catalysis, 1 (2018) 63-72.

[8] X.-F. Yang, A. Wang, B. Qiao, J. Li, J. Liu, T. Zhang, Single-Atom Catalysts: A New Frontier in Heterogeneous Catalysis, Accounts of Chemical Research, 46 (2013) 1740-1748.

[9] J. Liu, Catalysis by Supported Single Metal Atoms, ACS Catalysis, 7 (2017) 34-59.

[10] X.P. Qin, S.Q. Zhu, F. Xiao, L.L. Zhang, M.H. Shao, Active Sites on Heterogeneous Single-Iron-Atom Electrocatalysts in CO2 Reduction Reaction, Acs Energy Letters, 4 (2019) 1778-1783.

[11] S. Zhao, Y. Cheng, J.-P. Veder, B. Johannessen, M. Saunders, L. Zhang, C. Liu, M.F. Chisholm, R. De Marco, J. Liu, S.-Z. Yang, S.P. Jiang, One-Pot Pyrolysis Method to Fabricate Carbon Nanotube Supported Ni Single-Atom Catalysts with Ultrahigh Loading, ACS Applied Energy Materials, 1 (2018) 5286-5297.

[12] B. Qiao, A. Wang, X. Yang, L.F. Allard, Z. Jiang, Y. Cui, J. Liu, J. Li, T. Zhang, Single-atom catalysis of CO oxidation using Pt1/FeOx, Nat Chem, 3 (2011) 634.

[13] S.F.J. Hackett, R.M. Brydson, M.H. Gass, I. Harvey, A.D. Newman, K. Wilson, A.F. Lee, High-Activity, Single-Site Mesoporous Pd/Al2O3 Catalysts for Selective Aerobic Oxidation of Allylic Alcohols, Angewandte Chemie International Edition, 46 (2007) 8593-8596.

[14] P. Liu, Y. Zhao, R. Qin, S. Mo, G. Chen, L. Gu, D.M. Chevrier, P. Zhang, Q. Guo, D. Zang, B. Wu, G. Fu, N. Zheng, Photochemical route for synthesizing atomically dispersed palladium catalysts, Science, 352 (2016) 797-800.

[15] G.P. Gao, Y. Jiao, E.R. Waclawik, A.J. Du, Single Atom (Pd/Pt) Supported on Graphitic Carbon Nitride as an Efficient Photocatalyst for Visible-Light Reduction of Carbon Dioxide, J. Am. Chem. Soc., 138 (2016) 6292-6297.

[16] S. Sun, G. Zhang, N. Gauquelin, N. Chen, J. Zhou, S. Yang, W. Chen, X. Meng, D. Geng, M.N. Banis, R. Li, S. Ye, S. Knights, G.A. Botton, T.-K. Sham, X. Sun, Single-atom Catalysis

Using Pt/Graphene Achieved through Atomic Layer Deposition, Scientific Reports, 3 (2013) 1775.

[17] H. Yan, Y. Lin, H. Wu, W. Zhang, Z. Sun, H. Cheng, W. Liu, C. Wang, J. Li, X. Huang, T. Yao, J. Yang, S. Wei, J. Lu, Bottom-up precise synthesis of stable platinum dimers on graphene, Nature Communications, 8 (2017) 1070.

[18] Y. Zheng, Y. Jiao, Y. Zhu, Q. Cai, A. Vasileff, L.H. Li, Y. Han, Y. Chen, S.-Z. Qiao, Molecule-Level g-C3N4 Coordinated Transition Metals as a New Class of Electrocatalysts for Oxygen Electrode Reactions, Journal of the American Chemical Society, 139 (2017) 3336-3339.

[19] J.-C. Li, Z.-Q. Yang, D.-M. Tang, L. Zhang, P.-X. Hou, S.-Y. Zhao, C. Liu, M. Cheng, G.-X. Li, F. Zhang, H.-M. Cheng, N-doped carbon nanotubes containing a high concentration of single iron atoms for efficient oxygen reduction, Npg Asia Materials, 10 (2018) e461.

[20] Y. Cheng, S. He, J.P. Veder, R. De Marco, S.Z. Yang, S. Jiang, Atomically Dispersed Bimetallic FeNi Catalysts as Highly Efficient Bifunctional Catalysts for Reversible Oxygen Evolution and Oxygen Reduction Reactions, Chemelectrochem, 6 (2019) 3478-3487.

[21] P. Su, K. Iwase, S. Nakanishi, K. Hashimoto, K. Kamiya, Nickel-Nitrogen-Modified Graphene: An Efficient Electrocatalyst for the Reduction of Carbon Dioxide to Carbon Monoxide, Small, 12 (2016) 6083-6089.

[22] X. Li, X. Huang, S. Xi, S. Miao, J. Ding, W. Cai, S. Liu, X. Yang, H. Yang, J. Gao, J. Wang, Y. Huang, T. Zhang, B. Liu, Single Cobalt Atoms Anchored on Porous N-Doped Graphene with Dual Reaction Sites for Efficient Fenton-like Catalysis, Journal of the American Chemical Society, 140 (2018) 12469-12475.

[23] H.B. Yang, S.-F. Hung, S. Liu, K. Yuan, S. Miao, L. Zhang, X. Huang, H.-Y. Wang, W. Cai, R. Chen, J. Gao, X. Yang, W. Chen, Y. Huang, H.M. Chen, C.M. Li, T. Zhang, B. Liu, Atomically dispersed Ni(i) as the active site for electrochemical CO2 reduction, Nature Energy, 3 (2018) 140-147.

[24] X. Li, W. Bi, L. Zhang, S. Tao, W. Chu, Q. Zhang, Y. Luo, C. Wu, Y. Xie, Single-Atom Pt as Co-Catalyst for Enhanced Photocatalytic H2 Evolution, Advanced Materials, 28 (2016) 2427-2431.

[25] D. Zhang, W. Chen, Z. Li, Y. Chen, L. Zheng, Y. Gong, Q. Li, R. Shen, Y. Han, W.-C. Cheong, L. Gu, Y. Li, Isolated Fe and Co dual active sites on nitrogen-doped carbon for a highly efficient oxygen reduction reaction, Chemical Communications, 54 (2018) 4274-4277.

[26] Q. Li, W. Chen, H. Xiao, Y. Gong, Z. Li, L. Zheng, X. Zheng, W. Yan, W.-C. Cheong, R. Shen, N. Fu, L. Gu, Z. Zhuang, C. Chen, D. Wang, Q. Peng, J. Li, Y. Li, Fe Isolated Single Atoms on S, N Codoped Carbon by Copolymer Pyrolysis Strategy for Highly Efficient Oxygen Reduction Reaction, Advanced Materials, 30 (2018) 1800588.

[27] Y. Zhu, W. Sun, W. Chen, T. Cao, Y. Xiong, J. Luo, J. Dong, L. Zheng, J. Zhang, X. Wang, C. Chen, Q. Peng, D. Wang, Y. Li, Scale-Up Biomass Pathway to Cobalt Single-Site Catalysts Anchored on N-Doped Porous Carbon Nanobelt with Ultrahigh Surface Area, Advanced Functional Materials, 28 (2018) 1802167.

[28] Y. Pan, R. Lin, Y. Chen, S. Liu, W. Zhu, X. Cao, W. Chen, K. Wu, W.-C. Cheong, Y. Wang, L. Zheng, J. Luo, Y. Lin, Y. Liu, C. Liu, J. Li, Q. Lu, X. Chen, D. Wang, Q. Peng, C. Chen, Y. Li, Design of Single-Atom Co–N5 Catalytic Site: A Robust Electrocatalyst for CO2 Reduction with Nearly 100% CO Selectivity and Remarkable Stability, Journal of the American Chemical Society, 140 (2018) 4218-4221.

[29] X.D. Chen, N. Wang, K. Shen, Y.K. Xie, Y.P. Tan, Y.W. Li, MOF-Derived Isolated Fe Atoms Implanted in N -Doped 3D Hierarchical Carbon as an Efficient ORR Electrocatalyst in Both Alkaline and Acidic Media, Acs Applied Materials & Interfaces, 11 (2019) 25976-25985.

[30] F. Xiao, G.L. Xu, C.J. Sun, M.J. Xu, W. Wen, Q. Wang, M. Gu, S.Q. Zhu, Y.Y. Li, Z.D. Wei, X.Q. Pan, J.A. Wang, K. Amine, M.H. Shao, Nitrogen-coordinated single iron atom catalysts derived from metal organic frameworks for oxygen reduction reaction, Nano Energy, 61 (2019) 60-68.

[31] L. Jiao, G. Wan, R. Zhang, H. Zhou, S.H. Yu, H.L. Jiang, From Metal-Organic Frameworks to Single-Atom Fe Implanted N-doped Porous Carbons: Efficient Oxygen Reduction in Both Alkaline and Acidic Media, Angew. Chem.-Int. Edit., 57 (2018) 8525-8529.

[32] G. Zhang, Y. Jia, C. Zhang, X. Xiong, K. Sun, R. Chen, W. Chen, Y. Kuang, L. Zheng, H. Tang, W. Liu, J. Liu, X. Sun, W.-F. Lin, H. Dai, A general route via formamide condensation to prepare atomically dispersed metal–nitrogen–carbon electrocatalysts for energy technologies, Energy & Environmental Science, 12 (2019) 1317-1325.

[33] Y. Cheng, S.Y. Zhao, B. Johannessen, J.P. Veder, M. Saunders, M.R. Rowles, M. Cheng, C. Liu, M.F. Chisholm, R. De Marco, H.M. Cheng, S.Z. Yang, S.P. Jiang, Atomically Dispersed Transition Metals on Carbon Nanotubes with Ultrahigh Loading for Selective Electrochemical Carbon Dioxide Reduction, Adv. Mater., 30 (2018) 1706287.

[34] P. Niu, L. Zhang, G. Liu, H.-M. Cheng, Graphene-Like Carbon Nitride Nanosheets for Improved Photocatalytic Activities, Advanced Functional Materials, 22 (2012) 4763-4770.

[35] S. Wang, S.P. Jiang, X. Wang, Microwave-assisted one-pot synthesis of metal/metal oxide nanoparticles on graphene and their electrochemical applications, Electrochimica Acta, 56 (2011) 3338-3344.

[36] C.-M. Chen, Q. Zhang, M.-G. Yang, C.-H. Huang, Y.-G. Yang, M.-Z. Wang, Structural evolution during annealing of thermally reduced graphene nanosheets for application in supercapacitors, Carbon, 50 (2012) 3572-3584.

[37] B.C.C. Cowie, A. Tadich, L. Thomsen, The Current Performance of the Wide Range (90–2500 eV) Soft X-ray Beamline at the Australian Synchrotron, AIP Conference Proceedings, 1234 (2010) 307-310.

[38] E. Gann, C.R. McNeill, A. Tadich, B.C.C. Cowie, L. Thomsen, Quick AS NEXAFS Tool (QANT): a program for NEXAFS loading and analysis developed at the Australian Synchrotron, Journal of Synchrotron Radiation, 23 (2016) 374-380.

[39] J. Klimeš, D.R. Bowler, A. Michaelides, Van der Waals density functionals applied to solids, Physical Review B, 83 (2011) 195131.

[40] C.S. Chen, A.D. Handoko, J.H. Wan, L. Ma, D. Ren, B.S. Yeo, Stable and selective electrochemical reduction of carbon dioxide to ethylene on copper mesocrystals, Catalysis Science & Technology, 5 (2015) 161-168.

[41] C. Zhao, X. Dai, T. Yao, W. Chen, X. Wang, J. Wang, J. Yang, S. Wei, Y. Wu, Y. Li, Ionic Exchange of Metal–Organic Frameworks to Access Single Nickel Sites for Efficient Electroreduction of CO2, Journal of the American Chemical Society, 139 (2017) 8078-8081.

[42] Y. Liu, X. Xu, J. Zhang, H. Zhang, W. Tian, X. Li, M.O. Tade, H. Sun, S. Wang, Flower-like MoS2 on graphitic carbon nitride for enhanced photocatalytic and electrochemical hydrogen evolutions, Applied Catalysis B: Environmental, 239 (2018) 334-344.

[43] S.C. Yan, Z.S. Li, Z.G. Zou, Photodegradation Performance of g-C3N4 Fabricated by Directly Heating Melamine, Langmuir, 25 (2009) 10397-10401.

[44] H. Zhang, C.H. Sun, F. Li, H.X. Li, H.M. Cheng, Purification of Multiwalled Carbon Nanotubes by Annealing and Extraction Based on the Difference in van der Waals Potential, The Journal of Physical Chemistry B, 110 (2006) 9477-9481.

[45] Y. Cheng, S. Zhao, B. Johannessen, J.-P. Veder, M. Saunders, M.R. Rowles, M. Cheng, C. Liu, M.F. Chisholm, R. Marco, H.-M. Cheng, S.-Z. Yang, S.P. Jiang, Atomically Dispersed Transition Metals on Carbon Nanotubes with Ultrahigh Loading for Selective Electrochemical Carbon Dioxide Reduction, Advanced Materials, 30 (2018) 1706287.

[46] L.A. Avakyan, A.S. Manukyan, A.A. Mirzakhanyan, E.G. Sharoyan, Y.V. Zubavichus, A.L. Trigub, N.A. Kolpacheva, L.A. Bugaev, Atomic structure of nickel phthalocyanine probed by X-ray absorption spectroscopy and density functional simulations, Optics and Spectroscopy, 114 (2013) 347-352.

[47] W. Zhu, R. Michalsky, Ö. Metin, H. Lv, S. Guo, C.J. Wright, X. Sun, A.A. Peterson, S. Sun, Monodisperse Au Nanoparticles for Selective Electrocatalytic Reduction of CO2 to CO, Journal of the American Chemical Society, 135 (2013) 16833-16836.

[48] C.W. Li, M.W. Kanan, CO2 Reduction at Low Overpotential on Cu Electrodes Resulting from the Reduction of Thick Cu2O Films, Journal of the American Chemical Society, 134 (2012) 7231-7234.

[49] Q. Lu, J. Rosen, Y. Zhou, G.S. Hutchings, Y.C. Kimmel, J.G. Chen, F. Jiao, A selective and efficient electrocatalyst for carbon dioxide reduction, Nature Communications, 5 (2014) 3242.

[50] M. Liu, Y. Pang, B. Zhang, P. De Luna, O. Voznyy, J. Xu, X. Zheng, C.T. Dinh, F. Fan, C. Cao, F.P.G. de Arquer, T.S. Safaei, A. Mepham, A. Klinkova, E. Kumacheva, T. Filleter, D. Sinton, S.O. Kelley, E.H. Sargent, Enhanced electrocatalytic CO2 reduction via field-induced reagent concentration, Nature, 537 (2016) 382.

[51] Z. Cao, D. Kim, D. Hong, Y. Yu, J. Xu, S. Lin, X. Wen, E.M. Nichols, K. Jeong, J.A. Reimer, P. Yang, C.J. Chang, A Molecular Surface Functionalization Approach to Tuning Nanoparticle Electrocatalysts for Carbon Dioxide Reduction, Journal of the American Chemical Society, 138 (2016) 8120-8125.

[52] M. Ma, B.J. Trześniewski, J. Xie, W.A. Smith, Selective and Efficient Reduction of Carbon Dioxide to Carbon Monoxide on Oxide-Derived Nanostructured Silver Electrocatalysts, Angewandte Chemie International Edition, 55 (2016) 9748-9752.

[53] K. Jiang, S. Siahrostami, A.J. Akey, Y. Li, Z. Lu, J. Lattimer, Y. Hu, C. Stokes, M. Gangishetty, G. Chen, Y. Zhou, W. Hill, W.-B. Cai, D. Bell, K. Chan, J.K. Nørskov, Y. Cui, H. Wang, Transition-Metal Single Atoms in a Graphene Shell as Active Centers for Highly Efficient Artificial Photosynthesis, Chem, 3 (2017) 950-960.

[54] X. Zhang, Z. Wu, X. Zhang, L. Li, Y. Li, H. Xu, X. Li, X. Yu, Z. Zhang, Y. Liang, H. Wang, Highly selective and active CO2 reduction electrocatalysts based on cobalt phthalocyanine/carbon

nanotube hybrid structures, Nature Communications, 8 (2017) 14675.

[55] N. Kornienko, Y. Zhao, C.S. Kley, C. Zhu, D. Kim, S. Lin, C.J. Chang, O.M. Yaghi, P. Yang, Metal–Organic Frameworks for Electrocatalytic Reduction of Carbon Dioxide, Journal of the American Chemical Society, 137 (2015) 14129-14135.

Chapter 9 Conclusions and Recommendations for Future Work

9.1 Conclusions and achievements

The aim of this thesis is to develop novel synthesis methods of SACs for electrochemical applications. It has been successfully achieved by the development of one-pot approach and seeding methods to synthesize highly controllable SACs with high atomic loading. The main achievements from the present study are listed below and Table.9.1.

1), Carbon nanotube supported Ni single atom catalysts, NiSA-N-CNT, with Ni single atom loadings as high as 20.3 wt% have been successfully synthesized using a new one-pot pyrolysis approach. The synthesized NiSA-N-CNT catalysts displayed a high electrochemical efficiency for the CO2RR with suppressed activity for HER as compared to carbon nanotube supported Ni NPs. The CNT stabilized Ni SACs formed by the rolling-up of layered Ni-g-C_3N_4 sheets represent an attractive path to realize the SACs with high catalysts loadings for a wide range of practical applications.

2), We successfully tailored the edge structures of porous carbon with Ni single atoms. The porous structure provided large number of anchor sites for single Ni atoms and the nanopores (<6 nm) also help prevent aggregation and stabilize the single atom Ni-N species during high temperature annealing. The unsaturated edge anchored Ni single sites with loading as high as 6.9 % show a mass activity of 53.6 mA mg^{-1} and a high selectivity of 92.1% at an overpotential of 0.59 V for CO2RR. The DFT results identify that the edge-anchored unsataured three nitrogen coordinated Ni single atoms exibit better activity for CO2RR compared with in-plane structures, and the high CO2RR activity originates from the high loading of unsaturated Ni single atoms on edges.

3), The controllable method to synthesize a series of single metal atom catalysts on two-dimensional materials was achieved. The seeding strategy is versatile and has been demonstrated on Ni, Co, Fe, Cu, Ag, Pd single atoms as well as binary NiCu atoms supported on 2D materials including GO, MoS_2 and BN nanosheets. The applicability of the synthesized SA-2D catalysts has been illustrated on the high activity and selectivity of SANi-GO for CO_2RR. The seeding approach described in this paper may serve as an enabling technology for multiple applications.

4), The application of SACs for Li-S batteries was obtained under the guidance of theoretical

calculation. The dual between forward and reverse catalytic reaction were firstly taken into consideration to design the efficient catalyst vanadium and coblat, based on the guidance of experiments and DFT calculations. The significantly improved battery performance has been obtained benefited from the great catalytic effects, consistent with the DFT theoretical calculations.

5), The two feasible closely associated approaches to synthesize nickel single atoms on nitrogen doped carbon nanotube (NiSA-N-CNT) and graphene (NiSA-N-G). The formation of NiSA-N-CNT is due to the solid-to-solid rolling up mechanism to form a bamboo-like tubular structure. Addition of citric acid interrupts the solid-to-solid rolling process, and result in NiSA-N-G. The CO2RR performance reveals that more exposed active sites owned in graphene structure achieves higher catalytic performance. The novel synthesis approaches and mechanism provides new understanding of single atom metal catalyst.

Chapter	SACs Supports	Metal Atoms	Synthesis methods	Loading(wt.%)	Catalysis Reaction
4	N-CNT	Ni	One pot	20.3	CO2RR
5	MEGO	Ni	Impregnation @ annealing	6.9	CO2RR
6	2D Materials(GO, MoS2, BN)	Ni,Fe,Co, Pd, Ag	Seeding strategy	2.8-7.9	CO2RR
7	NG	Vanadium, Cobalt	Seeding strategy	4.3(V)/3.9(Co)	Li-S battery
8	N-CNT	Ni	One pot	15.3(SANi-N-CNT)	CO2RR
	N-GO	Ni	One pot	5.9(SANi-N-GO)	CO2RR

Table 9.1 The list of the work done in this thesis.

9.2 Recommendations for future work

The development of SACs embedded in 1D and 2D supports opens new opportunities in the development of new electrocatalysts for energy conversion and storage applications. Based on the current synthesis approaches, future work should be carried out in areas including ORR, HER and OER and so on. In addition, further studies are required in areas as follows.

(a) How to achieve highly dense coordinated sites to obtain more isolated atom centers. The more active sites, the higher efficiency. In order to improve the loading of SACs, the different strategies could be combined for integral design to overcome the limitations of solo approach.

(b) How to reduce the cost and simplify the synthesis process of SACs. Prior to any practical application, the price of an advanced technique is always the highest priority. Therefore, the more feasible approaches are left to explore to achieve the synthesis of SACs with lower cost and higher environmental friendliness, for example employing the environmental rich biomass, natural waste as SACs supports.

(c) How to explore different atoms coordinated with center metal atom. For instance, the catalytic activity could be tunable through changing the most used coordination nitrogen atom into oxygen, sulfur, phosphorous and so on. These researches also help us to design specific catalyst for target reaction and further get one deep understanding of the intrinsic properties of SACs.

(d) How to achieve multifunctional SACs such as bifunctional or even tri-functional application. As for this application, we should combine different types SACs on one support to explore the possibilities of multifunctional applications.

Appendix: Permission of Reproduction from the Copyright Owner

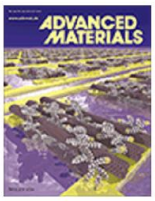

Title: Single-Atom Pt as Co-Catalyst for Enhanced Photocatalytic H2 Evolution

Author: Xiaogang Li, Wentuan Bi, Lei Zhang, et al

Publication: Advanced Materials

Publisher: John Wiley and Sons

Date: Jan 29, 2016

Order Completed

Thank you for your order.

This Agreement between Shiyong Zhao ("You") and John Wiley and Sons ("John Wiley and Sons") consists of your license details and the terms and conditions provided by John Wiley and Sons and Copyright Clearance Center.

Your confirmation email will contain your order number for future reference.

printable details

License Number	4679111113355
License date	Sep 30, 2019
Licensed Content Publisher	John Wiley and Sons
Licensed Content Publication	Advanced Materials
Licensed Content Title	Single-Atom Pt as Co-Catalyst for Enhanced Photocatalytic H2 Evolution
Licensed Content Author	Xiaogang Li, Wentuan Bi, Lei Zhang, et al
Licensed Content Date	Jan 29, 2016
Licensed Content Volume	28
Licensed Content Issue	12
Licensed Content Pages	5
Type of use	Dissertation/Thesis
Requestor type	University/Academic
Format	Print and electronic
Portion	Figure/table
Number of figures/tables	1
Original Wiley figure/table number(s)	Figure 1
Will you be translating?	No
Title of your thesis / dissertation	Synthesis, Characteristics and Application of Single Atom Catalysts

Expected completion date	Jan 2020
Expected size (number of pages)	200
Requestor Location	Shiyong Zhao Grose Ave 60-B602 Perth-cannington, WA 6107 Australia Attn: Shiyong Zhao
Publisher Tax ID	EU826007151
Total	0.00 USD

Would you like to purchase the full text of this article? If so, please continue on to the content ordering system located here: Purchase PDF

If you click on the buttons below or close this window, you will not be able to return to the content ordering system.

ORDER MORE CLOSE WINDOW

Order Completed

Thank you for your order.

This Agreement between Shiyong Zhao ("You") and Springer Nature ("Springer Nature") consists of your license details and the terms and conditions provided by Springer Nature and Copyright Clearance Center.

Your confirmation email will contain your order number for future reference.

printable details

License Number	4679130751954
License date	Sep 30, 2019
Licensed Content Publisher	Springer Nature
Licensed Content Publication	Nature Chemistry
Licensed Content Title	Single-atom catalysis of CO oxidation using Pt1/FeOx
Licensed Content Author	Botao Qiao et al
Licensed Content Date	Jul 22, 2011
Type of Use	Thesis/Dissertation
Requestor type	non-commercial (non-profit)
Format	print and electronic
Portion	figures/tables/illustrations
Number of figures/tables/illustrations	1
High-res required	no
Will you be translating?	no
Circulation/distribution	30 - 99
Author of this Springer Nature content	no
Title	Synthesis, Characteristics and Application of Single Atom Catalysts
Institution name	n/a
Expected presentation date	Jan 2020
Portions	Figure 1
Requestor Location	Shiyong Zhao Grose Ave 60-B602 Perth-cannington, WA 6107 Australia Attn: Shiyong Zhao

Title: Single-Atom Catalysts: A New Frontier in Heterogeneous Catalysis

Author: Xiao-Feng Yang, Aiqin Wang, Botao Qiao, et al

Publication: Accounts of Chemical Research

Publisher: American Chemical Society

Date: Aug 1, 2013

PERMISSION/LICENSE IS GRANTED FOR YOUR ORDER AT NO CHARGE

This type of permission/license, instead of the standard Terms & Conditions, is sent to you because no fee is being charged for your order. Please note the following:

- Permission is granted for your request in both print and electronic formats, and translations.
- If figures and/or tables were requested, they may be adapted or used in part.
- Please print this page for your records and send a copy of it to your publisher/graduate school.
- Appropriate credit for the requested material should be given as follows: "Reprinted (adapted) with permission from (COMPLETE REFERENCE CITATION). Copyright (YEAR) American Chemical Society." Insert appropriate information in place of the capitalized words.
- One-time permission is granted only for the use specified in your request. No additional uses are granted (such as derivative works or other editions). For any other uses, please submit a new request.

If credit is given to another source for the material you requested, permission must be obtained from that source.

Title:	Design of Single-Atom Co–N5 Catalytic Site: A Robust Electrocatalyst for CO2 Reduction with Nearly 100% CO Selectivity and Remarkable Stability
Author:	Yuan Pan, Rui Lin, Yinjuan Chen, et al
Publication:	Journal of the American Chemical Society
Publisher:	American Chemical Society
Date:	Mar 1, 2018

PERMISSION/LICENSE IS GRANTED FOR YOUR ORDER AT NO CHARGE

This type of permission/license, instead of the standard Terms & Conditions, is sent to you because no fee is being charged for your order. Please note the following:

- Permission is granted for your request in both print and electronic formats, and translations.
- If figures and/or tables were requested, they may be adapted or used in part.
- Please print this page for your records and send a copy of it to your publisher/graduate school.
- Appropriate credit for the requested material should be given as follows: "Reprinted (adapted) with permission from (COMPLETE REFERENCE CITATION). Copyright (YEAR) American Chemical Society." Insert appropriate information in place of the capitalized words.
- One-time permission is granted only for the use specified in your request. No additional uses are granted (such as derivative works or other editions). For any other uses, please submit a new request.

If credit is given to another source for the material you requested, permission must be obtained from that source.

Appendix - Co-author attribution statement

1.Chapter 4.Paper "One-pot Pyrolysis Method to Fabricate Carbon Nanotube Supported Ni Single Atom Catalysts with Ultrahigh Loading", ACS Applied Energy Materials, 2018,10.1021/acsaem.8b00903.

	Conception and design	Experiments conduction & data acquisition	Data processing & analysis	interpretation & discussion	Manuscript writing, revision and finalisation	Final approval
Dr. Yi Cheng	×	×	×		×	×
	I acknowledge that these represent my contribution to the above result output. Signed. [redacted]					
Dr. Jean-Pierre Veder	×	×		×	×	×
	I acknowledge that these represent my contribution to the above result output. Signed. [redacted]					
Dr. Bernt Johannessen	×	×	×	×	×	×
	I acknowledge that these represent my contribution to the above result output. Signed. [redacted]					
Dr. Martin Saunders			×		×	×
	I acknowledge that these represent my contribution to the above result output. Signed. [redacted]					
Dr. Lianji Zhang			×	×	×	×
	I acknowledge that these represent my contribution to the above result output. Signed. [redacted]					
Dr. Chang Liu	×		×		×	×
	I acknowledge that these represent my contribution to the above result output. Signed. [redacted]					
Dr. Roland De Marco			×	×	×	×
	I acknowledge that these represent my contribution to the above result output. Signed. [redacted]					
Dr. Shi-Ze Yang	×		×	×	×	×
	I acknowledge that these represent my contribution to the above result output. Signed. [redacted]					
Dr. San Ping Jiang	×		×	×	×	×
	I acknowledge that these represent my contribution to the above result output. Signed. [redacted]					

2. Chapter5. Paper" Unsaturated Edge-anchored Ni Single Atoms on Porous Microwave Exfoliated Graphene Oxide for Electrochemical CO2 Reduction" Applied Catalysis B: Environmental.2018, 2018,243, 294-303.

	Conception and design	**Experiments conduction & data acquisition**	**Data processing & analysis**	**interpretation & discussion**	**Manuscript writing, revision and finalisation**	**Final approval**
Dr. Yi Cheng	×	×	×		×	×
	I acknowledge that these represent my contribution to the above result output. Signed.					
Dr. Jean-Pierre Veder	×	×		×	×	×
	I acknowledge that these represent my contribution to the above result output. Signed.					
Dr. Bernt Johannessen	×	×	×	×	×	×
	I acknowledge that these represent my contribution to the above result output. Signed.					
Dr. Martin Saunders			×		×	×
	I acknowledge that these represent my contribution to the above result output. Signed.					
Dr. Haobo Li			×	×	×	×
	I acknowledge that these represent my contribution to the above result output. Signed.					
Dr. Chang Liu	×		×		×	×
	I acknowledge that these represent my contribution to the above result output. Signed.					
Dr. Shanfu Lu	×			×	×	×
	I acknowledge that these represent my contribution to the above result output. Signed.					
Dr. Shuai He			×	×	×	×
	I acknowledge that these represent my contribution to the above result output. Signed.					
Dr. Jian Pan			×	×	×	×
	I acknowledge that these represent my contribution to the above result output. Signed.					
Dr. Shi-Ze Yang	×		×	×	×	×
	I acknowledge that these represent my contribution to the above result output. Signed.					
Dr. San Ping Jiang	×		×	×	×	×
	I acknowledge that these represent my contribution to the above result output. Signed.					

3.Chapter6. Paper"A Universal Seeding Strategy to Synthesis Single Atom Catalysts on 2D Materials for Electrocatalytic Applications". Advanced Functional Materials.2019, adfm.201906157.

	Conception and design	**Experiments conduction & data acquisition**	**Data processing & analysis**	**interpretation & discussion**	**Manuscript writing, revision and finalisation**	**Final approval**
Dr. Jean-Pierre Veder	×	×		×	×	×
	I acknowledge that these represent my contribution to the above result output. Signed. JP					
Dr. Bernt Johannessen	×	×	×	×	×	×
	I acknowledge that these represent my contribution to the above result output. Signed.					
Dr. Martin Saunders			×		×	×
	I acknowledge that these represent my contribution to the above result output. Signed. M. Saunders					
Dr. Lianji Zhang			×	×	×	×
	I acknowledge that these represent my contribution to the above result output. Signed. Lianji Zhang					
Dr. Chang Liu	×		×		×	×
	I acknowledge that these represent my contribution to the above result output. Signed.					
Dr. Roland De Marco			×	×	×	×
	I acknowledge that these represent my contribution to the above result output. Signed. Roland De Marco					
Dr. Shi-Ze Yang	×		×	×	×	×
	I acknowledge that these represent my contribution to the above result output. Signed. Shize Yang					
Dr. San Ping Jiang	×		×	×	×	×
	I acknowledge that these represent my contribution to the above result output. Signed.					

4. Chapter7. Paper" Theoretical calculation guided design of single-atom catalysts towards fast kinetic and long-life Li-S batteries" 2020,10.1021/acs.nanolett.9b04719.

	Conception and design	**Experiments conduction & data acquisition**	**Data processing & analysis**	**Interpretation & discussion**	**Manuscript writing, revision and finalisation**	**Final approval**
Dr. Guangmin Zhou	×	×	×		×	×
	I acknowledge that these represent my contribution to the above result output. Signed [redacted]					
Dr. Tianshuai Wang	×	×		×	×	×
	I acknowledge that these represent my contribution to the above result output. Signed. [redacted]					
Dr. Bernt Johannessen	×	×	×	×	×	×
	I acknowledge that these represent my contribution to the above result output. Signed. [redacted]					
Dr. Martin Saunders			×		×	×
	I acknowledge that these represent my contribution to the above result output. Signed. [redacted]					
Dr. Hao Chen			×	×	×	×
	I acknowledge that these represent my contribution to the above result output. Signed. [redacted]					
Dr. Chang Liu	×		×		×	×
	I acknowledge that these represent my contribution to the above result output. Signed. [redacted]					
Dr. Qianfan Zhang	×			×	×	×
	I acknowledge that these represent my contribution to the above result output. Signed. [redacted]					
Dr. Shi-Ze Yang	×		×	×	×	×
	I acknowledge that these represent my contribution to the above result output. Signed. [redacted]					
Dr. San Ping Jiang	×		×	×	×	×
	I acknowledge that these represent my contribution to the above result output. Signed. [redacted]					

5. Chapter8. Paper" Controlled One-pot Synthesis of Nickel Single Atoms Embedded in Carbon Nanotube and Graphene Supports with High Loading".ChemNanoMat, 2020, doi:10.1002/cnma.202000223.

	Conception and design	**Experiments conduction & data acquisition**	**Data processing & analysis**	**interpretation & discussion**	**Manuscript writing, revision and finalisation**	**Final approval**
Dr. Tianshuai Wang	×	×	×		×	×
	I acknowledge that these represent my contribution to the above result output. Signed. [redacted]					
Dr.Jean-Pierre Veder	×	×		×	×	×
	I acknowledge that these represent my contribution to the above result output. Signed. [redacted]					
Dr.Bernt Johannessen	×	×	×	×	×	×
	I acknowledge that these represent my contribution to the above result output. Signed. [redacted]					
Dr.Martin Saunders			×		×	×
	I acknowledge that these represent my contribution to the above result output. Signed. [redacted]					
Dr.Qianfan Zhang			×	×	×	×
	I acknowledge that these represent my contribution to the above result output. Signed. [redacted]					
Dr.Chang Liu	×		×		×	×
	I acknowledge that these represent my contribution to the above result output. Signed. [redacted]					
Dr.Lianji Zhang	×			×	×	×
	I acknowledge that these represent my contribution to the above result output. Signed. [redacted]					
Dr.Roland De Marco			×	×	×	×
	I acknowledge that these represent my contribution to the above result output. Signed. [redacted]					
Dr.Shi-Ze Yang	×		×	×	×	×
	I acknowledge that these represent my contribution to the above result output. Signed. [redacted]					
Dr.San Ping Jiang	×		×	×	×	×
	I acknowledge that these represent my contribution to the above result output. Signed. [redacted]					